January 2016

WHITE ROSE

K41: Reservoir Engineering Field Report

Category: Storage

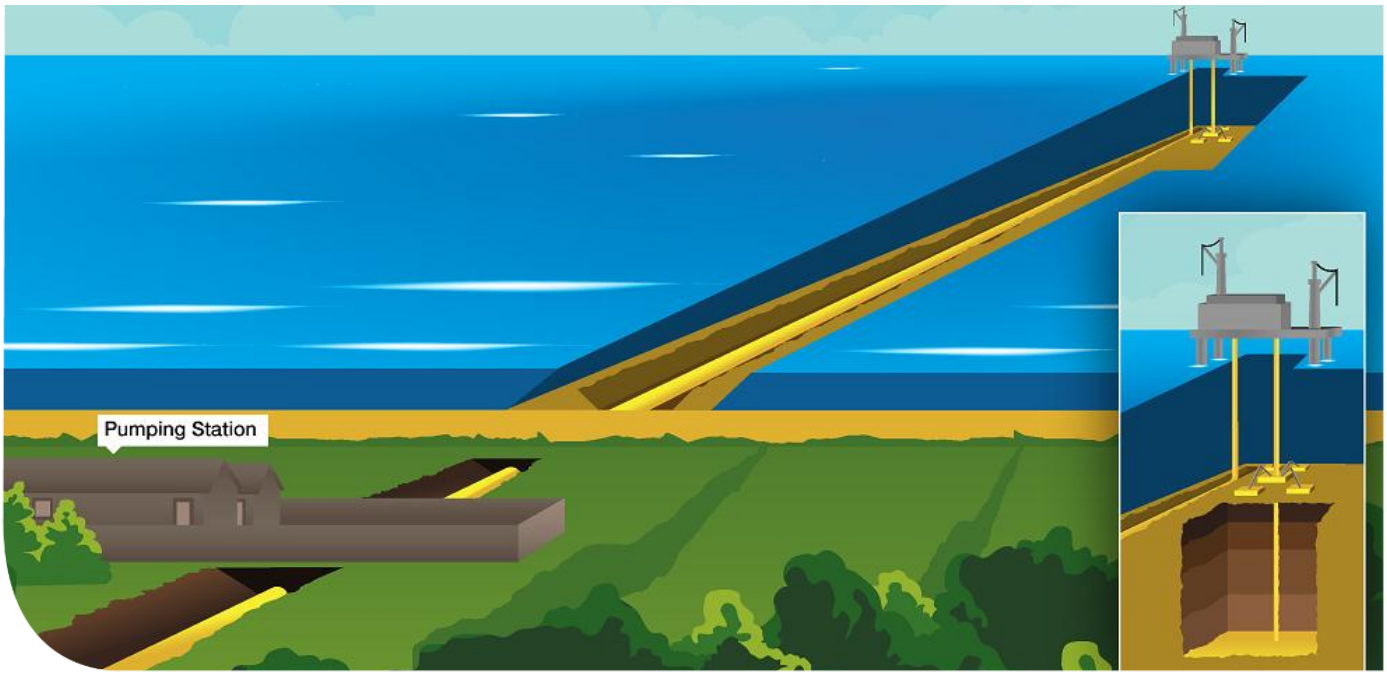

CAPTURE POWER

drax

BOC
A Member of The Linde Group

nationalgrid

IMPORTANT NOTICE

The information provided further to UK CCS Commercialisation Programme (the Competition) set out herein (the Information) has been prepared by Capture Power Limited and its sub-contractors (the Consortium) solely for the Department of Energy and Climate Change in connection with the Competition. The Information does not amount to advice on CCS technology or any CCS engineering, commercial, financial, regulatory, legal or other solutions on which any reliance should be placed. Accordingly, no member of the Consortium makes (and the UK Government does not make) any representation, warranty or undertaking, express or implied, as to the accuracy, adequacy or completeness of any of the Information and no reliance may be placed on the Information. In so far as permitted by law, no member of the Consortium or any company in the same group as any member of the Consortium or their respective officers, employees or agents accepts (and the UK Government does not accept) any responsibility or liability of any kind, whether for negligence or any other reason, for any damage or loss arising from any use of or any reliance placed on the Information or any subsequent communication of the Information. Each person to whom the Information is made available must make their own independent assessment of the Information after making such investigation and taking professional technical, engineering, commercial, regulatory, financial, legal or other advice, as they deem necessary.

Contents

Key Words

Key Word	Meaning or Explanation
Carbon	An element, but used as shorthand for its gaseous oxide, Carbon Dioxide (CO_2)
Capture	Collection of CO_2 from power station combustion process or other facilities and its process ready for transportation
Key knowledge	Information that may be useful if not vital to understanding how some enterprise may be successfully undertaken
Reservoir	A unit or volume of rock which has both porosity and permeability and can store, produce or receive fluids, by injection in the case of Carbon Capture and Storage (CCS). In the context of CCS, the reservoir forms the main storage facility for CO_2 injected into the store
Storage	The containment of CO_2 in a store for an indefinite period of time. The store is composed of porous rock, with the pores initially containing saline water, but as CO_2 injection commences the pores will contain CO_2 and water. With respect to the White Rose project, the storage site comprises the BSF (Bunter Sandstone Formation) within the Endurance structure. The lithologies above and below Bunter Sandstone are mainly shales and evaporites, hence they are all envisaged to have a good sealing quality. The areal dimensions of the storage site are taken from the most likely Top Bunter depth map which closes at 1460m True Vertical Depth Sub-Sea (TVDSS)
Subsurface	Pertaining to the rocks below the seabed, for an offshore development. Also, in the context of disciplines, can mean the activities of individuals, such as geologist, geophysicists and petrologists who perform technical work related to defining and analysing the rocks and fluids below the seabed
Well	A structure which forms a conduit from surface to a storage reservoir (in the case of CCS). The structure is formed by concentric tubes or pipes, decreasing in diameter from surface to the reservoir depth. The outermost tubes are known as casings, and are inserted into drilled holes and cemented in place. The innermost pipe is known as the tubing, and conveys the CO_2 transported by pipeline from onshore and into the store

Executive Summary

This report is one of a series of reports; these “key knowledge” reports are issued here as public information. These reports were generated as part of the Front End Engineering Design (FEED) contract agreed with the Department of Energy and Climate Change (DECC) as part of the White Rose Project.

White Rose seeks to deliver a clean coal-fired power station using oxy-fuel technology fitted with Carbon Capture and Storage (CCS), which would generate up to 448MWe (gross) while capturing at least 90% of the carbon dioxide emissions. CCS technology allows the carbon dioxide produced during combustion to be captured, processed and compressed before being transported in dense phase to storage. The dense phase carbon dioxide would be kept under pressure while it is pumped through an underground pipeline to the seashore and then through an offshore pipeline to be stored in a specially chosen rock formation under the seabed. This Key Knowledge Deliverable (KKD) provides a description of the flows and processes associated with the overall system.

The structure of interest (identified as Endurance) is a four-way dip-closure straddling quadrants 42 and 43. This structure is a saline aquifer, approximately 22km long, 7km wide and over 200m thick. The crest of the reservoir is located at a depth of approximately 1020m below the seabed. Reservoir datum, at 1300m True Vertical Depth Sub-Sea (TVDSS), pressure and temperature were determined as 140.0bar and 55.9°C, respectively. A layer of mudstone called the Röt Clay provides the primary cap rock or seal. This in turn is overlain by more than 90m of a salt layer known as the Röt Halite which is anticipated to provide additional seal capability.

A pressure, volume and temperature report was undertaken to analyse the phase behaviour of CO_2 and formation brine during CO_2 injection into the Endurance reservoir. The typical purity level of the White Rose CO_2 stream is 99.7 %, this means that the phase behaviour of CO_2 entering the Endurance reservoir can be approximated by established methods and algorithms which have been developed for pure CO_2. A comprehensive analysis of Endurance water samples recovered at several depths by the appraisal well indicated highly saline brine with sodium chloride as the dominant mineral constituent. Compositional, physicochemical, microbiological or radiological analyses did not show any clear trends with depth nor was there any measureable concentration of associated gas within the samples. Brine within Endurance is therefore expected to exhibit uniform properties across the reservoir at temperature and pressure conditions anticipated for the White Rose CO_2 injection.

Static geological modelling was undertaken to investigate the impact of varying cemented facies types on reservoir quality incorporating the results from analytical studies and from the appraisal programme, resulting in current models for subsequent phases of the project. Simulation should concentrate on the most likely and extreme model cases. It is possible that the Bunter reservoir is of such good quality relative to the properties of super critical CO_2 that the extreme models have little significant impact on CO_2 plume development. Once injection operations have commenced it is recommended that simulation studies be undertaken to investigate the likely Net To Gross (NTG) ratio cut-off for injected CO_2. It is believed that the NTG cut-off is a dynamic parameter for CO_2 storage given the relatively short period of injection as compared to time involved in hydrocarbon migration and storage. When detailed well planning is undertaken it is recommended that both the low and high case Top Bunter reservoir structure maps, that provided input to the structural uncertainty work, be taken into consideration.

The current P5 platform location is well constrained by surrounding well control. If, however, the development plan were to be extended beyond the current first phase development, particularly in the east of Endurance, mitigation planning against structural uncertainty may be important.

There is no evidence of compartmentalisation or the presence of lateral or vertical persistent barriers to flow likely to cause either static or dynamic pressure compartmentalisation during White Rose CO_2 injection. All available evidence suggests that Endurance is a single homogeneous hydraulic system with a moderate reservoir property variation with depth that is fully accounted for by authigenic digenetic processes.

Standard pore pressure prediction techniques are not required for the Endurance structure; the pressure gradient within Endurance is well behaved and can be approximated as 0.1147bar/m across the Bunter Sandstone reservoir.

Analytical and full field simulation models were used as well as regional information to assess the capacity, injectivity, hydrodynamics and containment of the Endurance structural closure for the safe and permanent storage of White Rose CO_2. The dynamic modelling confirms that Endurance is an extremely strong candidate for a CO_2 store. The modest Phase 1 loading into such a large structure with what is thought to be a large and strong connected volume will allow the operator to gain invaluable experience of CO_2 storage operations that can be shared with operators of similar projects in the future.

1 Introduction

National Grid Carbon Limited (NGC) is a wholly owned subsidiary of the National Grid group of companies. Capture Power Limited (CPL) is a special purpose vehicle company, which was formed by a consortium consisting of General Electric (GE), Drax and BOC, to pursue the White Rose Carbon Capture and Storage (CCS) Project (the White Rose Project).

CPL has entered into an agreement (the Front End Engineering Design (FEED) Contract) with the UK Government's Department of Energy and Climate Change (DECC) pursuant to which it will carry out, among other things, the engineering, cost estimation and risk assessment required to specify the budget necessary to develop and operate the White Rose Assets. The White Rose Assets are an end-to-end electricity generation and carbon capture and storage system comprising, broadly: a coal fired power station utilising oxy-fuel technology, carbon dioxide capture, processing, compression and metering facilities; transportation pipeline and pressure boosting facilities; offshore carbon dioxide reception and processing facilities, and injection wells into an offshore storage reservoir.

CPL and NGC have entered into an agreement, the Key Sub-Contract (KSC), pursuant to which NGC will perform the White Rose Transport and Storage (T&S) FEED Project which will meet that part of CPL's obligations under the FEED Contract which are associated with the T&S Assets. The T&S Assets include, broadly: the transportation pipeline and pressure boosting facilities; offshore carbon dioxide reception and processing facilities, and injection wells into an offshore storage reservoir.

A key component of the White Rose T&S FEED Project is the Key Knowledge Transfer process. A major portion of this is the compilation and distribution of a set of documents termed Key Knowledge Deliverables, of which this document represents one example.

This document summarises work undertaken to characterise flow behaviour of CO_2 and brine during CO_2 injection into the subsurface formation designated as the White Rose Storage Endurance Site (previously 5/42).

2 Purpose

The purpose of this document is to provide a summary description of the reservoir engineering involved in characterising the Endurance saline aquifer. It includes the following:

- a snapshot of the pressure, volume and temperature report which analyses the phase behaviour of CO_2 and brine in aquifer conditions;
- static model (field) report;
- CO_2 storage capacity estimate;
- pore pressure prediction report;
- evidence or otherwise of reservoir compartmentalisations/barriers to vertical flow; and
- dynamic modelling output report (including any cross sections or fine scale sectional modelling) and full field simulation report.

3 Overview

The White Rose CCS Project is to provide an example of a clean coal-fired power station of up to 450MW gross output, built and operated as a commercial enterprise.

The project comprises a state-of-the-art coal-fired power plant that is equipped with full CCS technology. The plant would also have the potential to co-fire biomass. The project is intended to prove CCS technology at a commercial scale and demonstrate it as a competitive form of low-carbon power generation and an important technology in tackling climate change. It would also play an important role in establishing a CO_2 transportation and storage network in the Yorkshire and Humber area. Figure 3.1 below gives a geographical overview of the proposed CO_2 transportation system.

Figure 3.1: Geographical Overview of the Transportation Facility

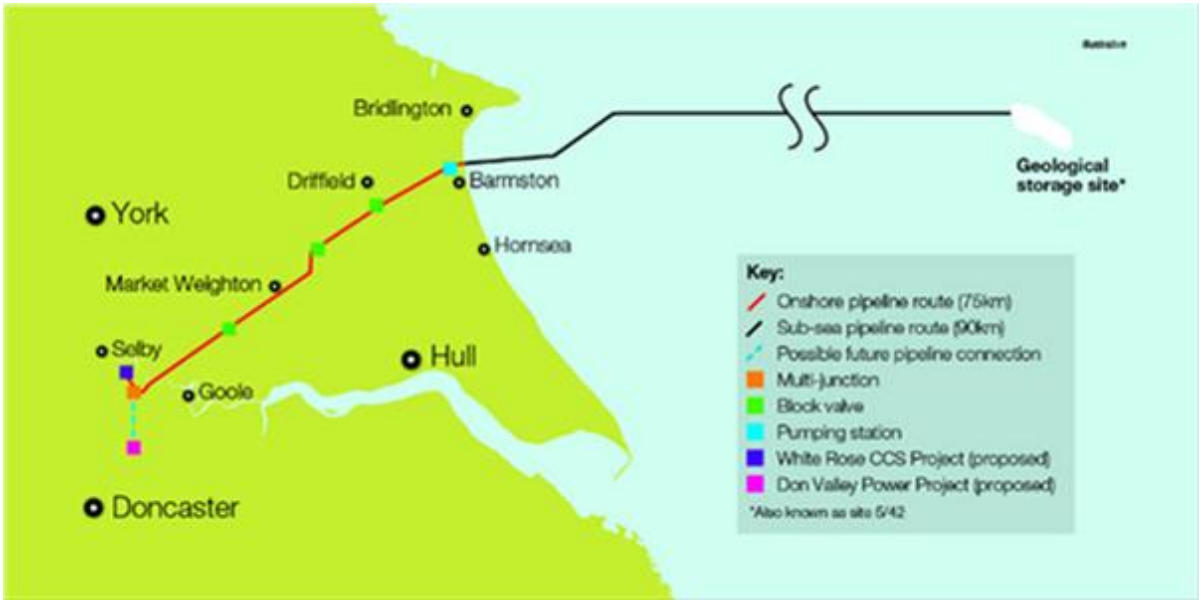

The standalone power plant would be located at the existing Drax Power Station site near Selby, North Yorkshire, generating electricity for export to the electricity transmission network (the "Grid") as well as capturing approximately two million tonnes of CO_2 per year, some 90% of all CO_2 emissions produced by the plant. The by-product CO_2 from the Oxy Power Plant (OPP) would be compressed and transported through an export pipeline for injection into an offshore saline aquifer (the reservoir) for permanent storage.

The power plant technology, which is known as Oxyfuel combustion, burns fuel in a modified combustion environment with the resulting combustion gases being high in CO_2 concentration. This allows the CO_2 produced to be captured without the need for additional chemical separation, before being compressed into dense phase and transported for storage.

The overall integrated control of the end-to-end CCS chain would have similarities to that of the National Grid natural gas pipeline network. Operation of the transport and storage system would be undertaken by NGC. However the transportation of carbon dioxide presents different concerns to those of natural gas; suitable specific operating procedures would be developed to cover all operational aspects including start-up, normal and abnormal operation, controlled and emergency

shutdowns. These procedures would include a hierarchy of operation, responsibility, communication procedures and protocols. Figure 3.2 below provides a schematic diagram of the overall end-to-end chain for the White Rose CCS Project.

Figure 3.2: End To End Chain Overall Schematic Diagram

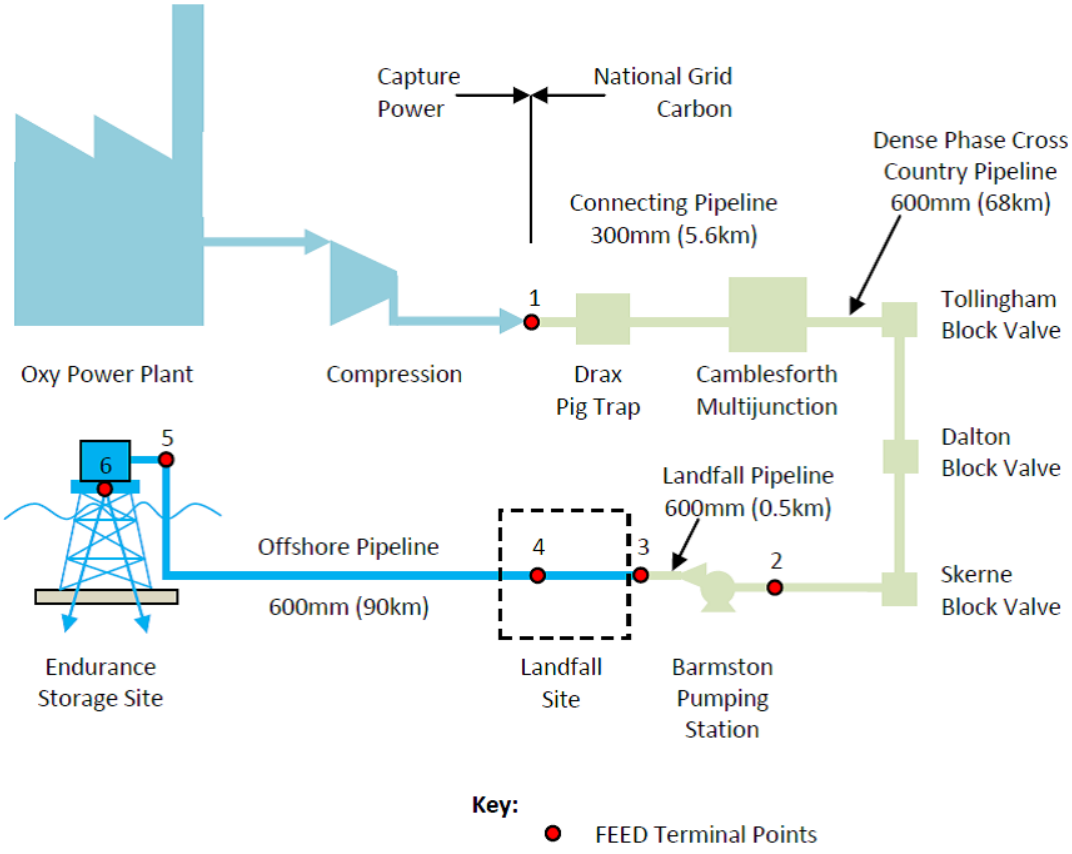

Endurance is a four-way dip-closure straddling quadrants 42 and 43. This structure is a saline aquifer, approximately 22km long, 7km wide and over 200m thick. The crest of the reservoir is located at a depth of approximately 1020m below the seabed. A layer of mudstone called the Röt Clay provides the primary cap rock or seal. This in turn is overlain by more than 90m of a salt layer known as the Röt Halite which is anticipated to provide additional seal capability.

4 Temperature CO_2 and Brine PVT and Phase Behaviour

A Pressure, Volume and Temperature (PVT) report has been undertaken which analyses the phase behaviour of CO_2 and formation brine during CO_2 injection into the Endurance saline aquifer (reservoir). This is summarised in the following sections.

4.1 PVT and Phase Behaviour of Free Phase CO_2

The physical properties of CO_2 can vary according to temperature and pressure. It can be a gas, solid, liquid or can exist in a 'supercritical' state, where it behaves as a gas but has the viscosity of a liquid. CO_2 is described as 'dense phase' in either the supercritical or liquid stage.

Pure CO_2 is a gas with a density of approximately 1.98 kg/m^3 at standard ambient temperature and pressure conditions of 25°C and 1barg respectively; this density is approximately 1.67 times that of air.

The CO_2 phase diagram in Figure 4.1 shows the conditions at which thermodynamically distinct phases can occur. The diagram shows lines of equilibrium or phase boundaries, which mark conditions under which multiple phases can coexist at equilibrium. Note that phase transitions occur along lines of equilibrium.

The critical point shown on the phase diagram is the point at which the phase boundary between liquid and gas terminates.

The triple point shown on the phase diagram is the temperature and pressure at which the three phases (gas, liquid, and solid) coexist in thermodynamic equilibrium.

Figure 4.1: Phase Diagram of Pure CO_2

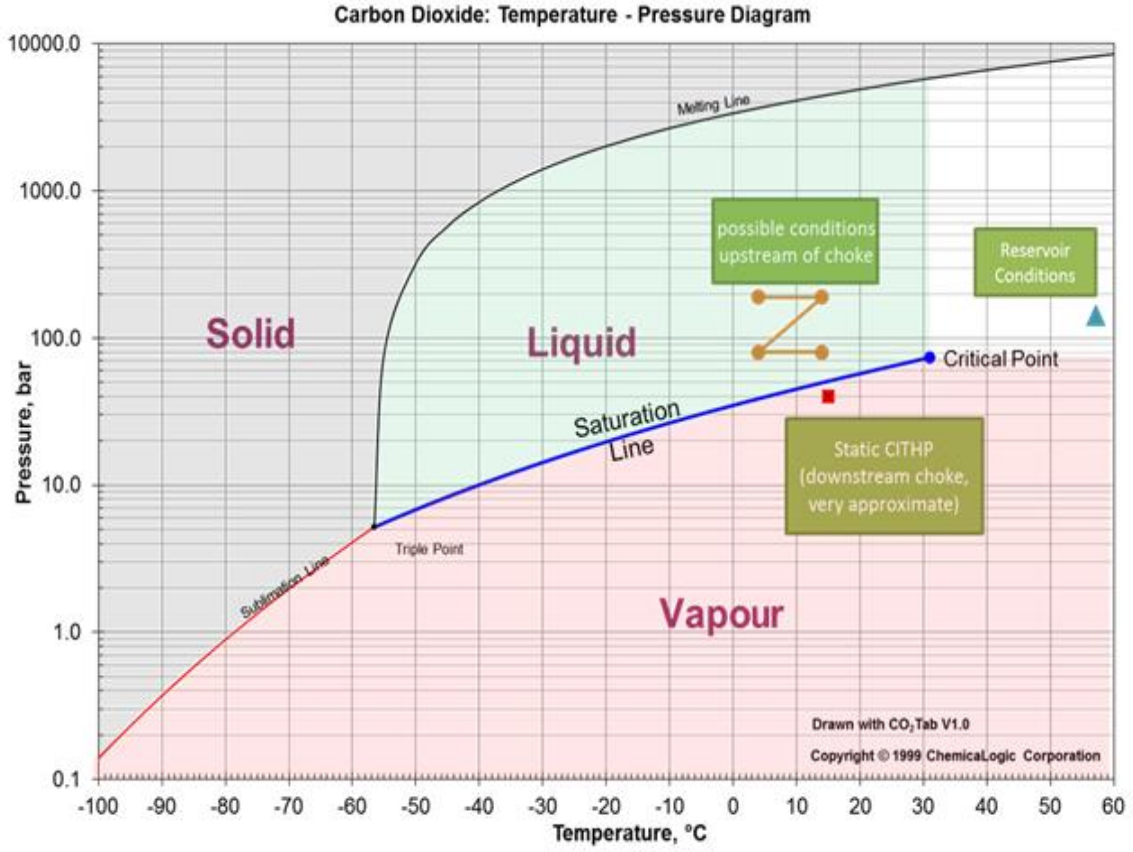

CITHP Closed-In Tubing Head Pressure

The compositional specification of the CO_2 that will be injected into the Endurance aquifer is outlined in Table 4.1. The specification characterises the CO_2 as a near-pure stream which will exhibit phase behaviour similar to that of pure CO_2.

Table 4.1: CO_2 Arrival Properties

Property	Value	Unit	Notes
Maximum Arrival Rate	2.68	MTPA	White Rose only (139.6mmscf/day)
Minimum Arrival Rate	0.58	MTPA	White Rose only (30.4mmscf/day)
Maximum Arrival Pressure	182	barg	Design Pressure = 200barg
Minimum Arrival Pressure	90	barg	
Maximum Purity	99.7	%	0.3% N_2+Ar, 10 ppmv O_2
Typical Purity White Rose	99.7	%	
Typical (Generic) Purity	97.4	%	2% N_2, 0.6% Ar, 10 ppmv O_2
Minimum Purity	96	%	4% N_2+O_2+H_2 + CH_4 + Ar
Maximum Arrival Temperature	16 / 24	°C	Winter/Summer
Minimum Arrival Temperature	3 / -7	°C	Summer/Winter

MMscf/day: Million standard cubic feet per day

The pipeline pressure and temperature are selected to be able to meet the design injection capacity of 2.68MTPA and transport the CO_2 in a liquid state.

The arrival temperature of the CO_2 at the platform varies according to seasonal variations in the temperature of the sea and the 90km segment of pipeline along the seabed. Given the design temperature range, Figure 4.1 shows that CO_2 can be kept in a liquid state as long as the pipeline pressure is above 50; this pressure is much lower than the pipeline minimum operating pressure of 90barg.

As the CO_2 leaves the pipeline and enters the well, the inherent operational cooling and heating effects may cause it to transform from a liquid to a gas state. To inhibit this transition, and reduce the flow instabilities associated with density fluctuations, the pressure of the CO_2 will be controlled during start-up and normal operating conditions.

The injected CO_2 will be liquid phase at the well perforations and during injection, where its temperature is substantially below critical point.

Once the CO_2 is inside the reservoir and injection is stopped, its temperature will increase as it moves into dense phase.

4.2 Phase Behaviour of Brine under Reservoir Condition

Water samples were collected as part of the well appraisal programme and categorised according to date and location of sample.

A comprehensive analysis of the water samples was undertaken to provide the following:

- quantification of Total Dissolved Solid (TDS), the ionic composition, and density;
- quantification of ph and resistivity;
- quantification of heavy metals and trace metals;
- quantification of radionuclides, and isotopes of carbon, oxygen (hydrogen) and strontium;
- quantification of the chemical tracer 2-fluorobenzoic acid to establish the level of mud invasion;
- an assessment of the microbial content to establish the type of bacteria populations present;
- an appraisal of selected pesticides; and
- the composition of any associated gas (if present).

4.2.1 Sample Removal and Appearance

The samples were collected using a Büchner flask and a Tedlar bag as shown in Figure 4.2. Prior to the sample removal the Büchner flask and tubing were purged with air-free helium and the Tedlar sampling bag was emptied by vacuum. The fluids produced were collected with the stabilised liquid kept in a Büchner flask and the associated gas in a Tedlar sampling bag.

Figure 4.2: Schematic of the Sample Removal Set-up

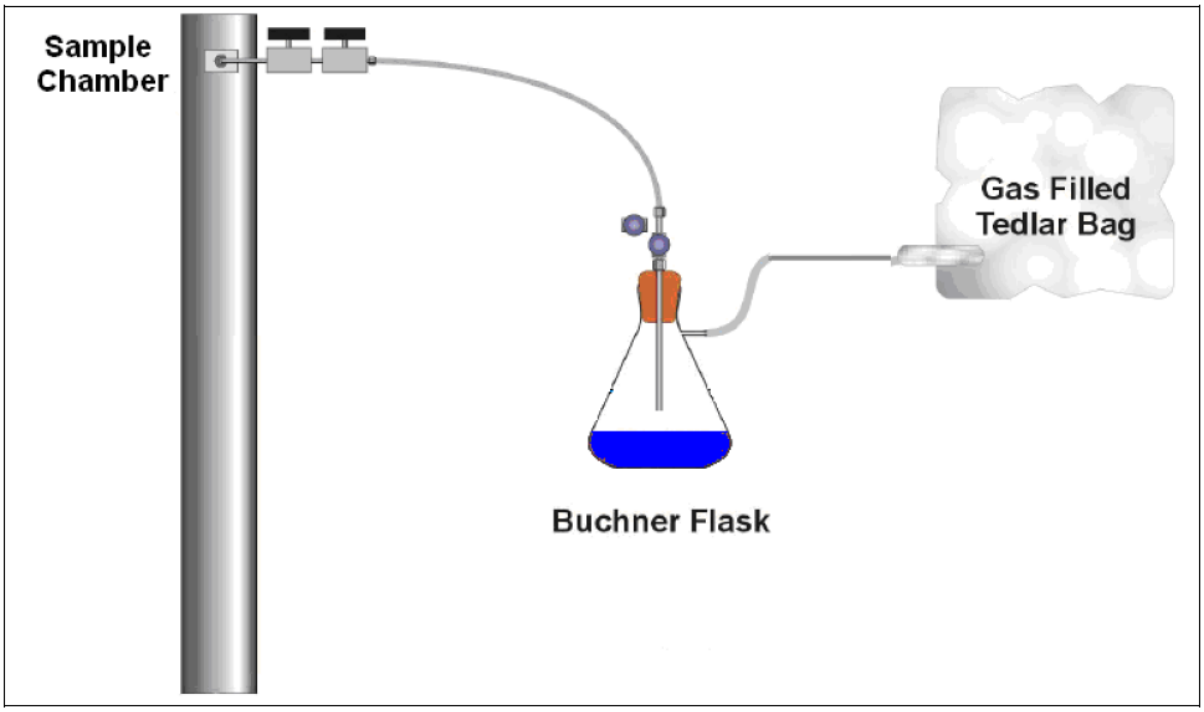

All pressurised water samples were kept refrigerated to keep the storage temperature sufficiently low to maintain the sample integrity.

After removal from the sample chamber all samples were initially cloudy then, within minutes, clear and colourless. It is assumed that the sudden change in pressure and temperature, on removing the sample from the cylinder, may have caused temporary precipitation of halite salts in suspension that then quickly redissolved.

4.2.2 Sample Preparation and Analysis

Samples were filtered through a 25mm syringe filter prior to analysis except for the determination of total organic carbon, barium and iron, soluble and total mercury, radionuclides, microbiology and pesticides.

All dilutions were carried out on a mass basis, so that the data obtained relates back directly to a concentration in mg/kg. Where analysis was carried out on a non-diluted sample and the data

relates to a concentration in mg/L, the original data has been divided by the measured density to convert to mg/kg.

4.2.3 Physicochemical Parameters

The physicochemical parameters are dependent on the joint action of both physical and chemical processes, those that have been measured are:

- density by means of a density meter; and
- total dissolved solids by evaporation/gravimetry. Note that gravimetry is an analytical method in which the analytical signal is a measurement of mass or a change in mass.

4.2.3.1 Density

Density was measured at 20.0°C ± 0.08°C in accordance with IP365 (modified) using a densitometer calibrated with deionised water.

4.2.3.2 Total Dissolved Solids

TDS are the inorganic and organic substances contained in water that can pass through a 2 micron filter.

To obtain the TDS measurements, a known mass of filtered sample was evaporated then dried to constant mass; the TDS was then calculated from the mass ratio of sample residue to sample taken.

For comparison purposes, TDS was also calculated from the sum of the dissolved substances determined. Table 4.2 below gives a comparison of the measured and calculated TDS for five samples recovered from four sampling depths.

Table 4.2: Total Dissolved Solids Measurements for Selected Samples

Sample Reference	1.04	1.09	1.13	2.10	2.14
Total Dissolved Solids at 0.2µm by Mass (mg/kg)					
TDS Measured	256146	247659	247730	259680	258925
TDS Calculated	253426	242549	241832	254014	254988
Total Dissolved Solids at 0.2 µm by Volume (mg/L)					
TDS Measured	306299	294244	294006	310993	310089
TDS Calculated	303047	288173	287007	304207	305374
Total Dissolved Solids at 0.2 µm by Volume (mg/L) Corrected for MDT Dilution					
TDS Measured	315980	307595	307483	310993	310089
TDS Calculated	312625	301248	300163	304207	305374

MDT: Modular Dynamic Tester

The measured TDS was in agreement with the TDS calculated from the ionic composition. The resistivity and density of all samples were in good agreement with the calculated TDS, using models based on NaCl solutions for comparison. These observations are good indications that the samples

can be approximated to NaCl solutions and that no non-ionic additives, such as glycol used in drilling fluids or contaminants that can act as insulators such as hydrocarbons, were significantly present.

The results of the TDS measurements indicated some variation of brine salinity with depth; an extrapolation has shown that it is unlikely to be a simple linear variation.

4.2.4 Ionic Composition

The ionic compositions of the samples of brine were determined using a number of methods:

- potentiometric titration to determined chloride;
- ion selective electrode to determined fluoride;
- ion chromatography to separate the anions (negative ions) of interest: bromide, nitrate, phosphate, sulphate and iodide;
- inductively coupled plasma optical emission spectrometry to determine cations (positive ions) of interest: metals, vanadium, arsenic, boron, phosphorus, silicon and sulphur; and
- acidification on a shaken unfiltered portion of sample to determine total barium and total iron.

Note that it was assumed that the deionised water used for washing was ion-free and had no contamination effect on the ionic composition of the respective samples other than dilution.

The ratio between chloride (Cl) and bromide (Br) concentrations was included as an indicator of contamination and the nature of brine. Most natural brines have a Cl to Br ratio in the range 100 to 350. If a brine has a high ratio, it may be an indication that the brine is artificial and made from purified chloride salt, or contaminated with a chloride-based drilling fluid. Similarly, if the ratio is lower than 100, it may be an indication of contamination from drilling fluid where bromide is commonly used.

The Cl:Br ratio for the samples fell in the range 323 to 355. This is close to the upper limit normally associated with naturally occurring brines, but there is no supporting evidence of any contamination. The close agreement between the samples taken from different depths is a strong indication that all samples are derived from a single natural source. This also suggests that the Bunter Sandstone within Endurance is fully connected and not compartmentalised.

4.2.5 The Composition of any Associated Gas

Typically, pressurised water samples yield a relatively low volume of associated gas, the volume is usually, but not always, linked to the concentration of associated hydrocarbon material.

A precaution was taken that the sample removal setup, as shown in Figure 4.2, was optimised to minimise headspace and the final dilution of the gas subsample. Despite this, the volume of gas associated with all samples was very low (<50mL) and the gas collected was too heavily diluted with helium from the displaced headspace to allow meaningful analysis. As a result no gas composition data was obtained.

As there is very little gas associated with the water, then, depending on the gas composition and the environment in which the gas will reside or pass through, the impact of such gas may be negligible.

Sufficient gas may be obtained for analysis by combining the gas from multiple cylinders and considering the optimum use of the numbers of (water) samples available for the whole analysis programme; however the time and cost implications of such an exercise would have to be considered against the benefits.

For water samples where there is associated hydrocarbon material present, the major components of the gas are usually a mixture of methane, nitrogen and carbon dioxide with ethane, propane and butane as minor components.

However for these samples it was evident that there was:

- no evidence of hydrocarbon material;
- no organic acid anions present that, under certain conditions, may be precursors to natural gas components; and
- no appreciable levels of any bacteria that may produce gaseous products such as hydrogen sulphide and methane.

It can be concluded that any gas associated with the water would be devoid of significant concentrations of hydrocarbon gases or volatile sulphur components. It was assumed that any gas associated with the water comprises mainly nitrogen.

4.3 PVT Behaviour of the CO_2-Brine System at Reservoir Conditions

The phase behaviour of the CO_2-brine (H_2O+NaCl) system was described using a thermodynamic model called the “black oil” model, where the simultaneous flow of brine and CO_2 is described; CO_2 may dissolve in the brine, but the brine is not allowed to vaporise into the CO_2 phase. The model uses a simple algorithm to generate the black oil PVT data required for flow simulation of CO_2 storage in saline aquifers, such as solubility/formation volume factor, molecular diffusion coefficient, compressibility factor, viscosity and so on.

The black oil model accounts for CO_2-brine phase partitioning at given aquifer temperature and pressure conditions. Comparison with experimental data shows the model to be accurate at temperatures of between 12°C and 300°C, pressures of between 1bar and 600bar, and salinities of between 0 and 6 mNaCl (the Bunter Sandstone Formation has a salinity of approximately 4.3 mNaCl, equivalent to 250,000 ppm by mass). Figure 4.3 shows a range of CO_2 and brine PVT data calculated using the model and in Reference 1 in Section 9.

Figure 4.3: CO_2 and Brine PVT Data as Functions of Pressure for 150,000 ppm Salinity at 50°C

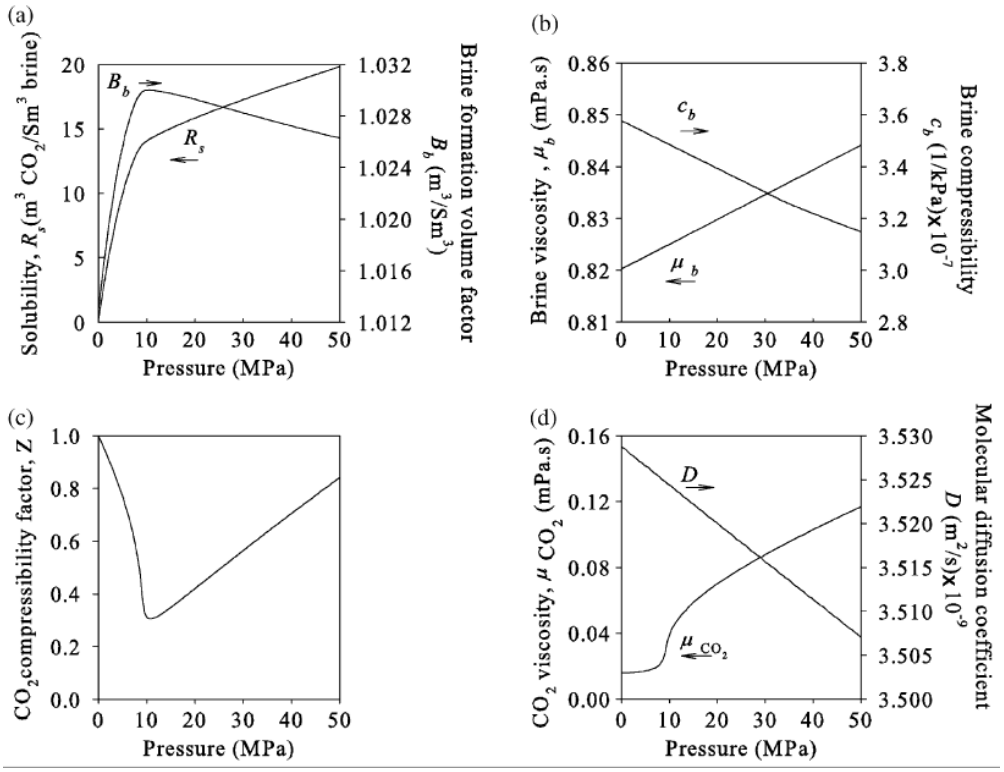

Key: (a) CO_2 solubility and brine formation volume factor
(b) Brine compressibility and viscosity
(c) CO_2 compressibility factor
(d) CO_2 viscosity and CO_2molecular diffusion coefficient in brine

4.4 Conclusion

The typical purity level of the White Rose CO_2 stream is 99.7 %, this means that the phase behaviour of CO_2 entering the Endurance reservoir/aquifer can be approximated by established methods and algorithms which have been developed for pure CO_2. This has been the approach adapted for predicting CO_2, brine and CO_2-brine PVT properties during dynamic simulation of White Rose CO_2 injection.

A comprehensive analysis of Endurance water samples recovered at several depths by the 42/25d-3 appraisal well indicate a highly saline brine with sodium chloride as the dominant mineral constituent. Compositional, physicochemical, microbiological or radiological analyses did not show any clear trends with depth nor was there any measureable concentration of associated gas within the samples. Brine within Endurance is therefore expected to exhibit uniform properties across the reservoir at temperature and pressure conditions anticipated for the White Rose CO_2 injection.

5 Static Geological Modelling

Geological modelling work on the Endurance White Rose storage site and complex was conducted after the drilling of the 42/25d-3 appraisal well in July 2013. A summary of interim model updates, which were made as new data from the 42/25d-3 well became available follows. The primary aim of this work was to provide a comprehensive model revision that could be used for subsequent project phases including FEED. The current model incorporates post appraisal well studies including chemostratigraphy, Routine conventional Core Analysis (RCA), revised petrophysical analysis, sedimentology and petrography.

The current models have very fine resolution in order to capture the CO_2 plume evolution in the simulation model. Capturing a good representation of vertical permeability was seen as particularly important as it controls how quickly CO_2 migrates to the cap rock and ultimately to the crest of the structure. Additionally, the current work has established a number of alternative models to define the large scale cementation changes inferred from the seismic data. Information from these models has been used to understand the key static model uncertainties and update the estimated range of NPV for the Endurance structure.

The large size of the structure (22km x 7km) and the desire for finer scale detail inevitably has led to larger models which become more cumbersome in simulation. Consequently, “tartan-style” simulation grids have been developed which focus on specific development concepts to reduce grid sizes. This has involved up-scaling from the geological grid into the simulation grid. Examples of “tartan-style” simulation grids are given in Figure 8.31.

The starting point of this modelling work was a regional structural model that incorporates the full stratigraphic column both above and below the reservoir.

5.1 Post 42/25D-3 Modelling Status

A total of four post-42/25d-3 model updates have been made since the well was drilled, including the current models described in this section. The modelling methodology is broadly similar to the pre-well modelling work.

The models make use of the seismic phase reversal polygon, which is interpreted to define the boundary between a region of largely uncemented rock over the Endurance anticline from cemented rock on the anticline margins. Cemented facies of varying porosities are preferentially placed within the cemented and uncemented areas based on trends observed from 16 wells in the greater Endurance area. The four model updates are summarised below.

5.1.1 November 2013

The November 2013 model incorporated the early data from the 42/25d-3 appraisal well, namely facies, provisional pre-RCA, porosity logs and a revised depth map. This early stage Top Bunter depth map and resulting model did not include the Bunter Sandstone outcrop that lies 14km to the east south-east.

Facies are based on raw log data and have remained largely unchanged until the current model (August 2014). The Top Bunter depth map was created using a depth-conversion that incorporated the northerly flank wells 43/21-2 and 43/21-3 as well as the new appraisal well. Previously 43/21-2

and 43/21-3 were thought to contain anomalous velocities and were excluded. The revised depth and model yielded an increased NPV of 5.6 x10^9 m^3, 30% larger than the pre-drill model. The model continued to use the Schlumberger permeability transform since RCA data was not available at that early stage.

The November 2013 model update was described in the April 2014 modelling report along with the pre-appraisal well model.

5.1.2 January 2014

An assessment of the likely GRV range for Endurance structure (Wright2 2014) indicated that the Top Bunter depth map used in the November 2013 model was a high case. It was not felt appropriate to base the simulation of injected CO_2 into the structure on a high case map and model. Consequently the model was rebuilt with a version of the pre-drill map that excluded the two northerly flanking wells, 43/21-2 and 43/21-3 from the depth conversion. This map represents a low case map which resulted in a model NPV volume of 4.79 x$10^9$$m^3$.

The use of the P50 depth map from the structural uncertainty modelling was considered but rejected as it could not be linked back to an actual seismic interpretation. The Top Bunter interpretation and model was extended to include the outcrop in the geological model. However, the outcrop was excluded from the up-scaled simulation model to minimise the number of cells and optimise simulator run times.

This model build provided the reservoir component of the current geomechanical model.

5.1.3 July 2014

The July 2014 update was made to incorporate a revised porosity log for 42/25d-3 that had been calibrated to the now available RCA data. Additionally, the model included a more optimistic permeability based on the RCA data. The model continued to use the low case depth map, as used in the previous model. Following learning from previous work, a coarser simulation, tartan style, simulation model was built that now included the outcrop.

5.1.4 Current Model

The current model build continues to use the low case Top Bunter depth structure map and incorporates late stage analytical data from the appraisal well. Specifically, this includes a revised reservoir zonation of the appraisal well based on chemostratigraphy and modified facies based on petrographic analysis. Additionally, an optimised permeability transform has been used based on the RCA data. A series of models has been built that has fed information into a revised assessment of the Endurance NPV volumetric range.

5.2 Depositional Setting and Sedimentological Summary

The Bunter Sandstone was deposited in a broad, land locked and gradually subsiding basin situated between 20° and 30° north of the equator. The climate was semi-arid with rivers and streams draining into the basin from surrounding highs and terminating in a playa (dry) lake situated within the

basin centre. During drier periods, aeolian processes redistributed the sands, and mudstones were desiccated. Expansion of the playa lakes during wetter periods resulted in deposition similar to that of the underlying Bunter Shale Formation and presumably also similar to that of the overlying Röt Clay. Figure 5.1 illustrates the depositional environment in the region of the 42/25d-3 well. Well 44/26-1 for example lies farther south than 42/25d-3 and consists exclusively of siltstones, very fine sandstones and minor mudstones and therefore represents a more distal location.

Sedimentological interpretation from the short core (16 m) recovered from well 42/25-1, the closest well to 42/25d-3, show sandstones that comprise finely interbedded sequence of sand sheet, playa margin, aeolian and fluvial laminated facies. The absence of well-developed finer-grained facies in 42/25d-3 has hindered the subdivision of the Bunter Sandstone into lower-order stratigraphic units based on sedimentology. This has, however, been achieved using chemostratigraphy, where the Bunter Sandstone formation has been divided into three main units (L1, L2 and L3 from the base up, equivalent to P1, P2 and P3).

The 42/25d-3 core log has been split into six facies successions which include fluvial deposits (mainly sheetfloods) subject to occasional aeolian reworking. The dominant lithology is very-fine to fine-grained sandstone. The only Mudstone bed seen in 42/25d-3 is about 0.35 ft (10 cm) thick, comprising muddy siltstones with irregular top and base, and interpreted as laterally inextensive. A bed of presumed reworked ooids from the underlying Rögenstein section is thought to be regionally extensive, and forms a distinct calcareous horizon several feet thick. Nodular anhydrite cement is common at numerous horizons.

Although the depositional interpretation has centred around the 42/25d-3 appraisal well, data and analysis from wells around the Endurance structure, have been used to constrain the interpretation.

Figure 5.1: Schematic Representation of Bunter Sandstone Depositional Environments in the Region Around the 42/25d-3 Well

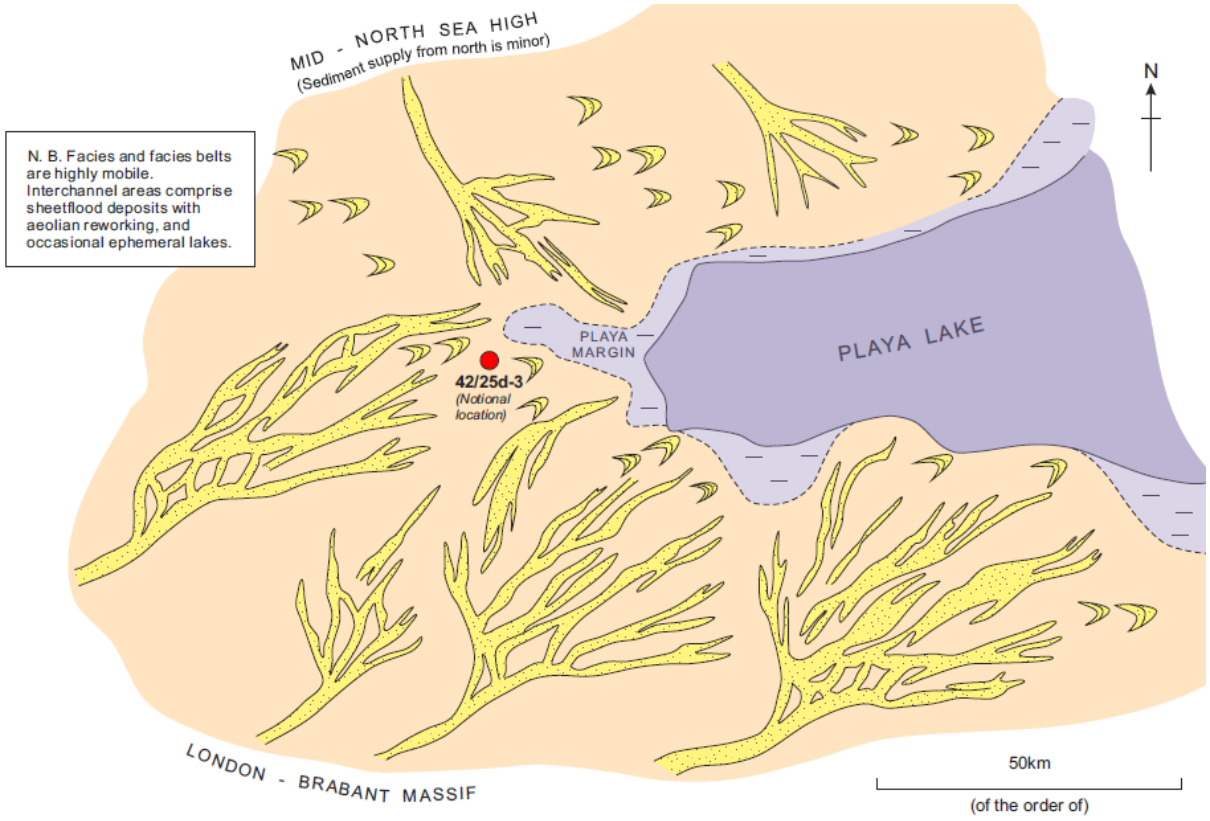

Figure 5.2: Location Map

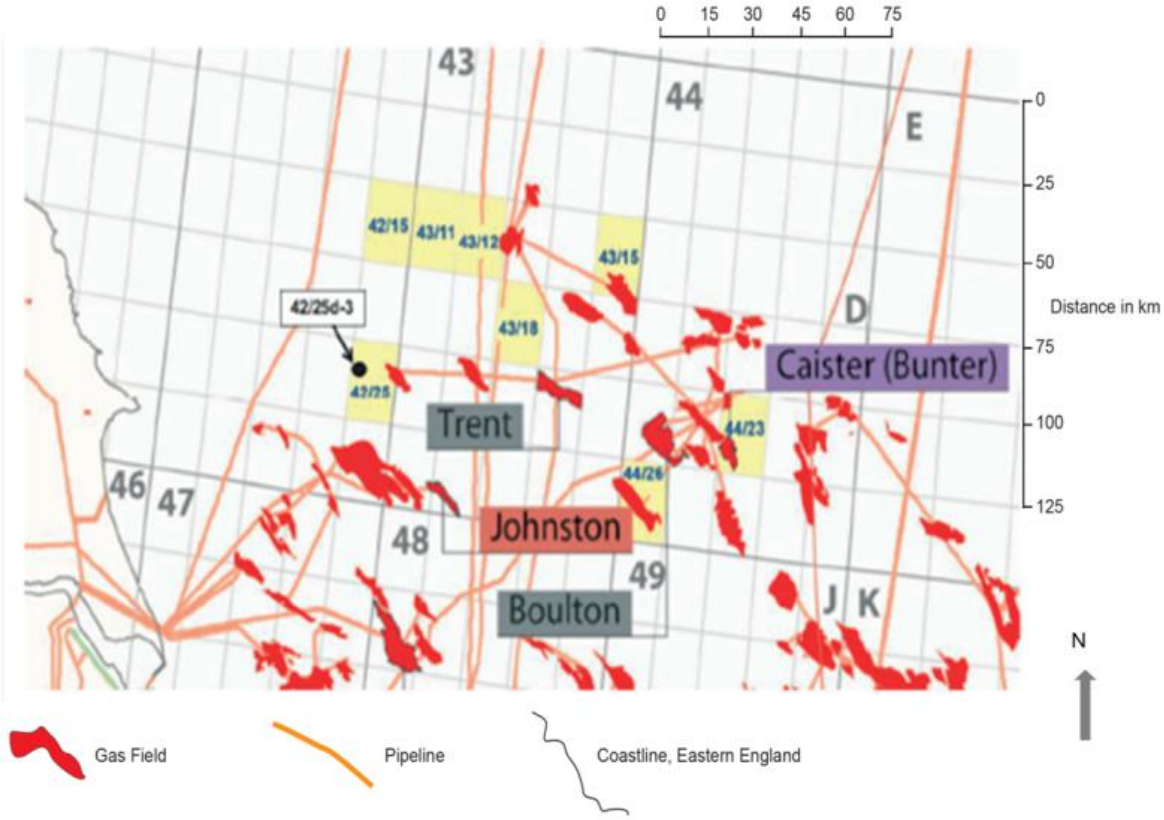

The location map shown in Figure 5.2 is an extract highlighting the blocks (in yellow) showing wells include in the sedimentology study.

5.3 Reservoir Quality Summary

The average porosity of the extensively cored appraisal well 42/25d-3 ranges from 17% in the Lower Bunter to 24% in the Upper Bunter with corresponding estimated average permeabilities of 100mD and 800mD. Similar values are observed in the crestal wells 42/25-1 and 43/21-1. The distribution of facies porosity from 42/35d-3 core shows that reservoir quality is independent of depositional facies, shown in Figure 5.3. The lack of relationship between sedimentary facies and reservoir quality from ten cores in the greater Endurance area and the high porosity and permeability may be interpreted as a product of dissolution of detrital grains (most notably feldspars) and halite cements. Although the reservoir lies at a relatively shallow level, 1000m to 1500m, it is well documented that the Bunter Sandstone in the southern North Sea was buried to a much deeper depth prior to being inverted in the late Cretaceous to early Tertiary (see Reference 2 in Section 9).

Figure 5.3: Log Porosity Distribution of the 42/25d-3 Cored Interval by Sedimentary Facies (Number of Observations vs. Porosity)

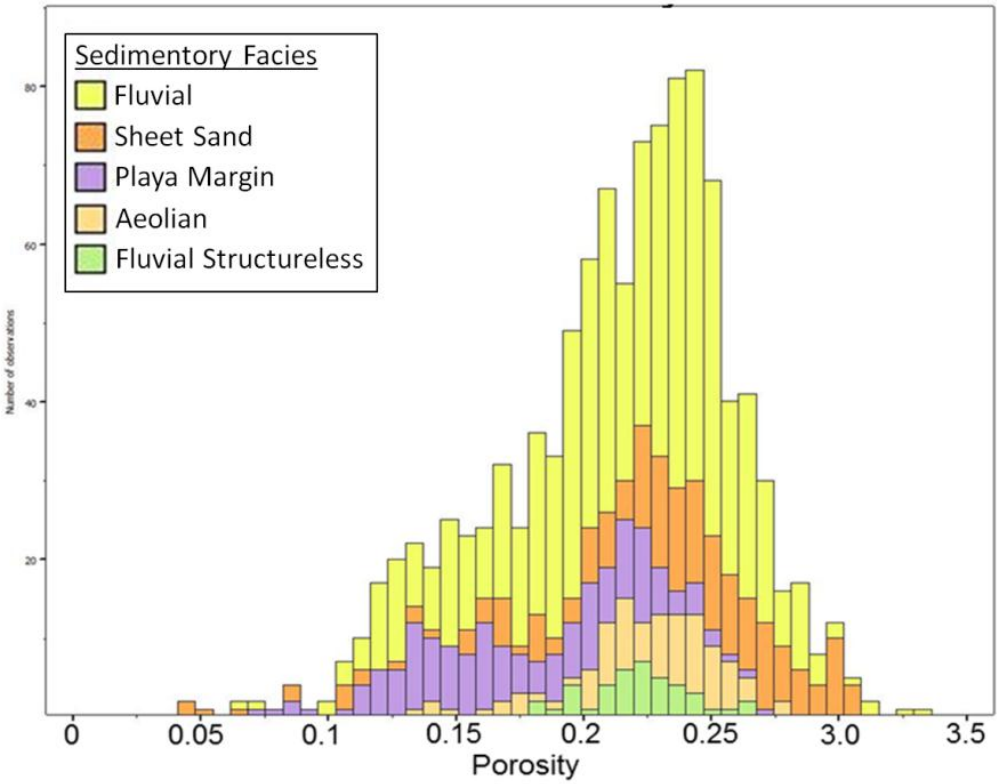

The overriding control on reservoir quality appears to be diagenetic, related to post-depositional cementation and possibly dissolution. Anhydrite, dolomite and halite have all been recognised as potential cementing phases. Wells with cemented sandstone occur on the margin of the Endurance anticline where porosity ranges from being completely occluded to very low (5%). This cementation appears to be more strongly developed at the top of the reservoir and creates a strong phase reversal on seismic data at the Top Bunter level.

The phase reversal boundary is approximately conformant with the Endurance structure, lying close to the structural spill at least at the western end of the structure. The phase reversal boundary has been used to limit the extent of good reservoir quality rock in this modelling work. The cemented sandstone margin of the Endurance structure is commonly referred to as the hardground.

5.4 Reservoir Correlation

The reservoir has been subdivided into three main zones, L1 at the base, L2 in the middle and L3 at the top of the Bunter Sandstone. Each of the three main zones have been subdivided into two sub-zones; a lower “a” zone and an upper “b” zone. The zonation is based on chemostratigraphic analysis of six wells over the Endurance structure, including 42/25d-3.

Chemostratigraphy provides the best means of correlating Triassic sandstone packages in the absence of microfossils, obvious regional shale breaks and repeatable log character. The correlation has been expanded by interpolation to the wells without chemostratigraphic analysis (Figure 5.6).

5.5 Area of Interest

The Area of Interest (AoI) covered by the geological model is shown on the Top Bunter Sandstone reservoir map shown in Figure 5.6. The area is 44km x 47km in size and designed to include 16 surrounding Bunter Sandstone well penetrations. Due to missing or incomplete log data sets, rock properties have been interpreted in 13 of these wells, whilst the remaining three have been used for correlation only. Additionally, the AoI includes the Bunter Sandstone seabed outcrop that overlies a Zechstein salt diapir, 14km south-west of the Endurance structure. This has been included to investigate the possibility of connate water flow at the outcrop during phases of CO_2 injection.

The AoI was extended southward to capture the well 42/30-6. This well was included as it is one of the six wells which have chemostratigraphic zonation. The well only has a Gamma-Ray (GR) log over the Bunter Sandstone interval. Previous models accounted for the 42/30-6 well chemostratigraphic zonation by correlation to neighbouring well 42/30-5.

Figure 5.4: Endurance Top Bunter Depth Surface with Wells and PRP (Phase Reversal Polygon)

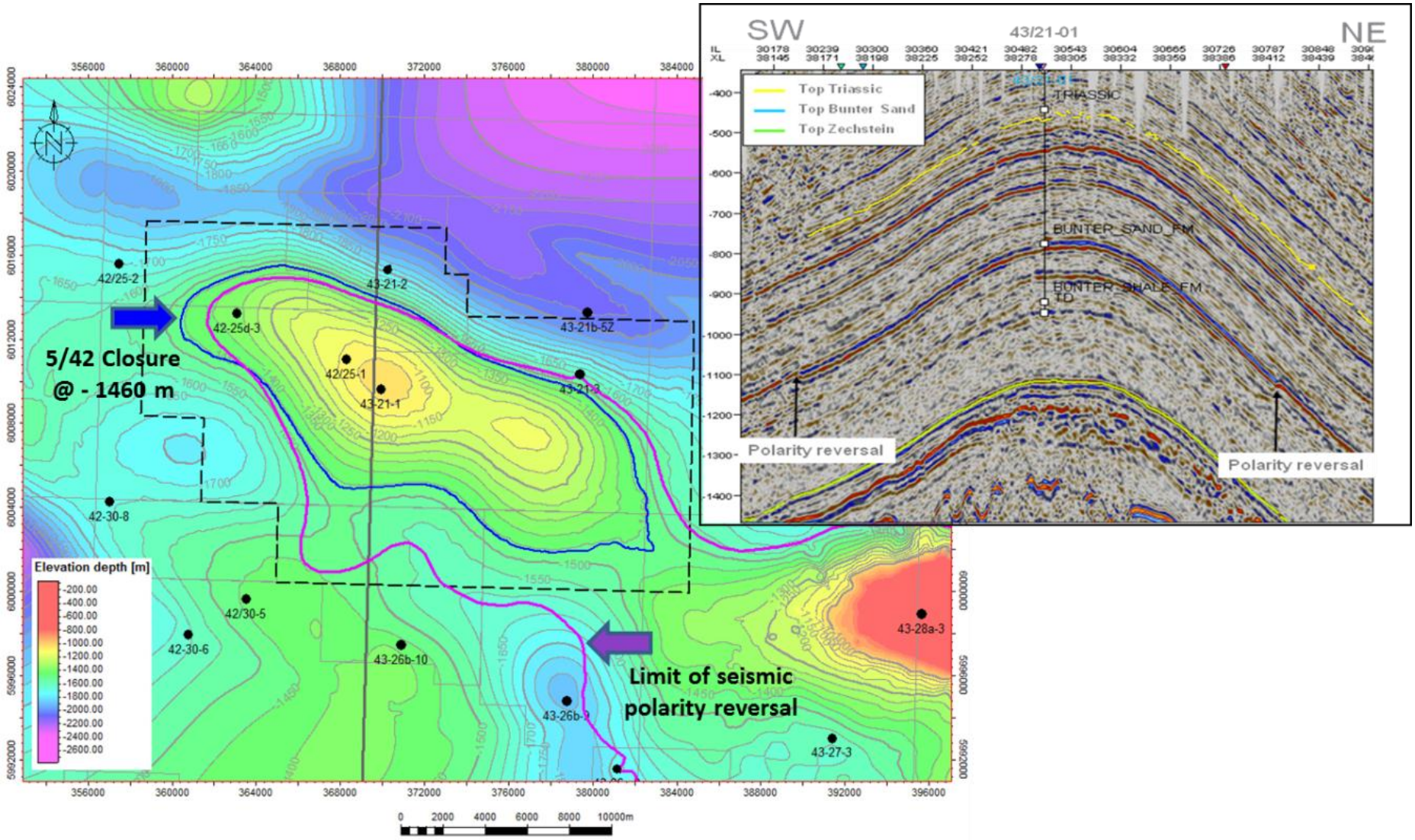

Figure 5.5: Top Bunter Depth Structure Illustrating the Model AoI

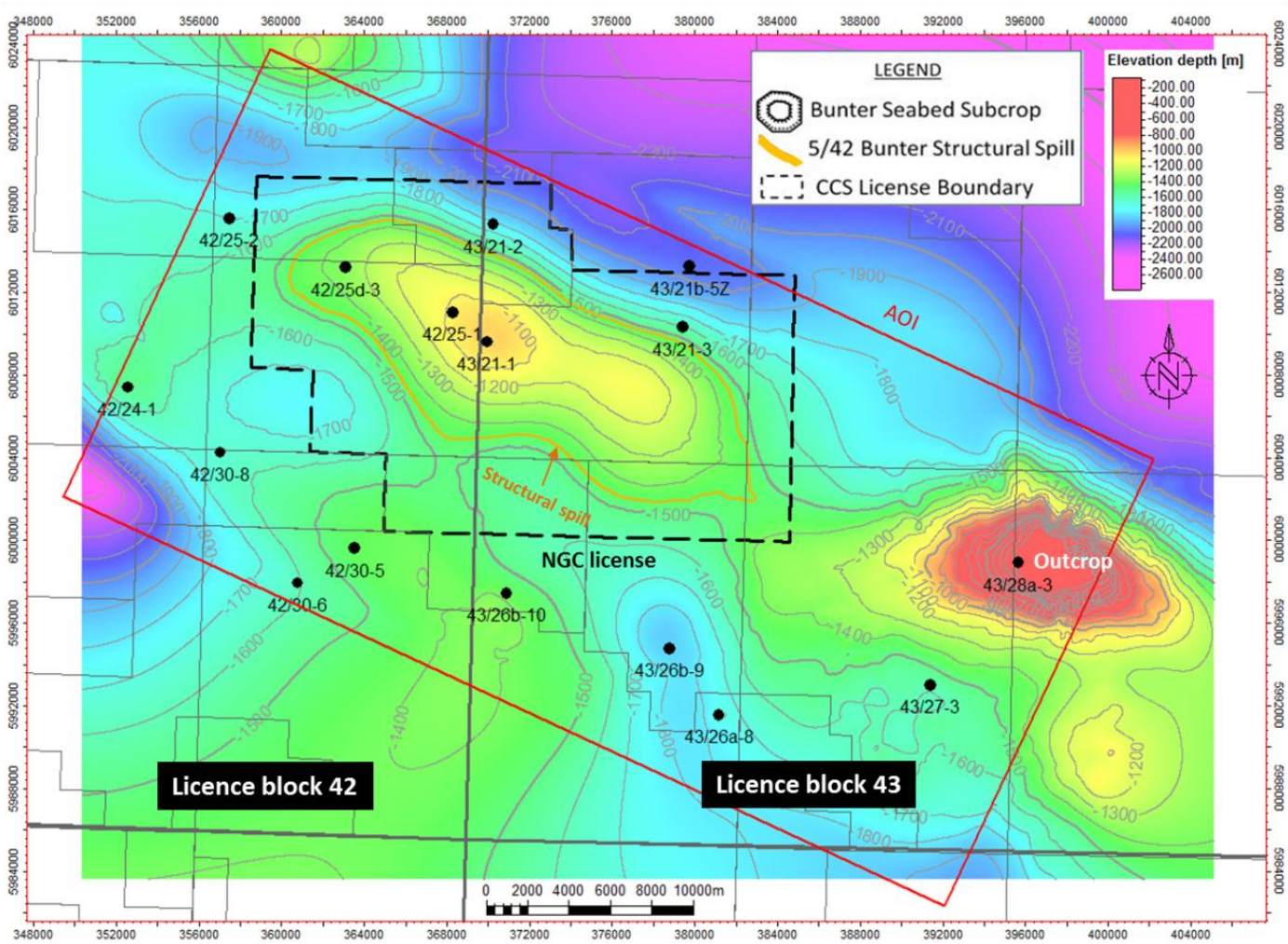

Figure 5.6: Endurance Area Bunter Sandstone Well Correlation

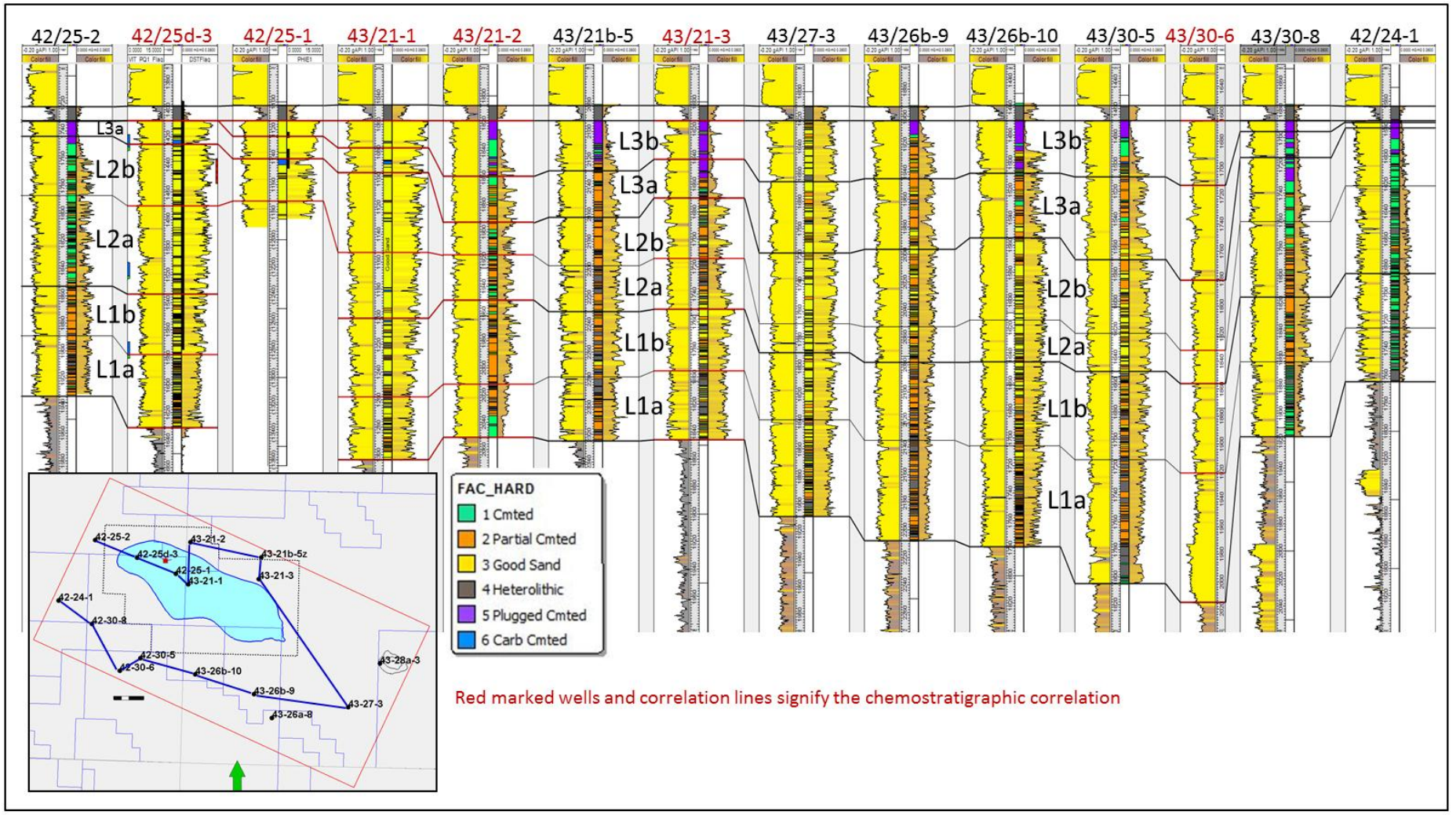

5.6 Stratigraphic and Structural Framework Model

A Regional Structural Framework Model (RSFM) was built to provide structure horizons over the full stratigraphic column from seabed to Top Rotliegend. This provides a common link between the different models that are likely to be built, the geological model, simulation model and geomechanical model. Although a geomechanical model has not been built in this update the RSFM allows later geomechanical models to be constructed if required.

The current RSFM has been built using the Build Simple Model process in the Schlumberger software application, Petrel, without faults (Figure 5.7). Faults have not been included as the geomechanical modelling software (Visage) requires an unfaulted model with faults input separately as surfaces.

The RSFM has lateral cells dimensions of 100m x 100m within the 44km x 47km AoI and is rotated by -25° to be parallel to the Endurance structural grain. No layering was applied so each zone is in effect one layer thick.

Figure 5.7: Petrel Make Horizon Process for the RSFM

Index	Horizon name	Color	Calculate	Horizon type	Conform to another horizon		Status	Well tops	Input #1
1	Seabed		Yes	Conformable	No	1	Done	Seabed (Tops_Aug14_LA	Seabed
2	Base_Quat		Yes	Erosional	No	1	Done		Base_Quaternary
3	Chalk_Grp		Yes	Base	No	1	Done	Chalk_Grp (Tops_Aug14_	Top_Chalk
4	Base_Chal		Yes	Base	No	1	Done	Base_Chalk_Grp (Tops_A	Base_Chalk
5	BCU		Yes	Erosional	No	1	Done	BCU (Tops_Aug14_LATE	BCU
6	Corralian_		Yes	Base	No	1	Done	Corralian_Lmst (Tops_Aug	Corralian_Lmst
7	Base_Corr		Yes	Base	No	1	Done	Base_Corralian_Lmst (Top	Base_Corralian_Lmst
8	Mid_Jurass		Yes	Base	No	1	Done	Mid_Jurassic (Tops_Aug1	Mid_Jurassic
9	Lias_Gp		Yes	Base	No	1	Done	Lias_Gp (Tops_Aug14_LA	Liassic
10	TRIASSIC		Yes	Base	No	1	Done	TRIASSIC (Tops_Aug14_	Triassic
11	Haisboroug		Yes	Base	No	1	Done	Haisborough_Gp (Tops_A	Haisborough_Gp
12	Top_Keup		Yes	Base	No	1	Done	Top_Keuper_Anhydrite_M	Top_Keuper_Anhydrite_Mbr
13	Base_Keu		Yes	Base	No	1	Done	Base_Keuper_Anhydrite_	Base_Keuper_Anhydrite_Mbr
14	DUDGEON		Yes	Base	No	1	Done	DUDGEON_FM (Tops_Au	Dudgeon_Fm
15	DOWSING		Yes	Base	No	1	Done	DOWSING_FM (Tops_Au	Dowsing_Fm
16	Top_Musc		Yes	Base	No	1	Done	Top_Muschelkalk_Halite_	Top_Muschelkalk_Halite_Mbr
17	Base_Mus		Yes	Base	No	1	Done	Base_Muschelkalk_Halite	Base_Muschelkalk_Halite_Mbr
18	Rot_Halite		Yes	Base	No	1	Done	Rot_Halite_3 (Tops_Aug1	Rot_Halite_3
19	Rot_Halite		Yes	Base	No	1	Done	Rot_Halite_2 (Tops_Aug1	Rot_Halite_2
20	Rot_Halite		Yes	Base	No	1	Done	Rot_Halite_1 (Tops_Aug1	Rot_Halite_1
21	Rot_Clay_		Yes	Base	No	1	Done	Rot_Clay_Mbr (Tops_Aug	Rot_Clay_Mbr
22	BUNTER_		Yes	Erosional	No	1	Done	BUNTER_L3b (Tops_Aug	Buntetr_L3
23	BUNTER_		Yes	Base	No	1	Done	BUNTER_SHALE_FM (To	Buntetr_Shale_Fm_corr_4328a3
24	PERMIAN		Yes	Base	No	1	Done	PERMIAN (Tops_Aug14_L	Permian
25	Rotliegene		Yes	Base	No	1	Done	Rotliegenes (Tops_Aug14	Rotliegend

The seismically derived Top Bunter Sandstone input surface is given in Figure 5.4. The other key seismically derived input structures of Top Triassic, Top Zechstein and Top Rotliegend are given in Appendix A. A cross-section through the RSFM is given in Figure 5.8.

Figure 5.8: Cross Section through the Regional Structural Framework Model

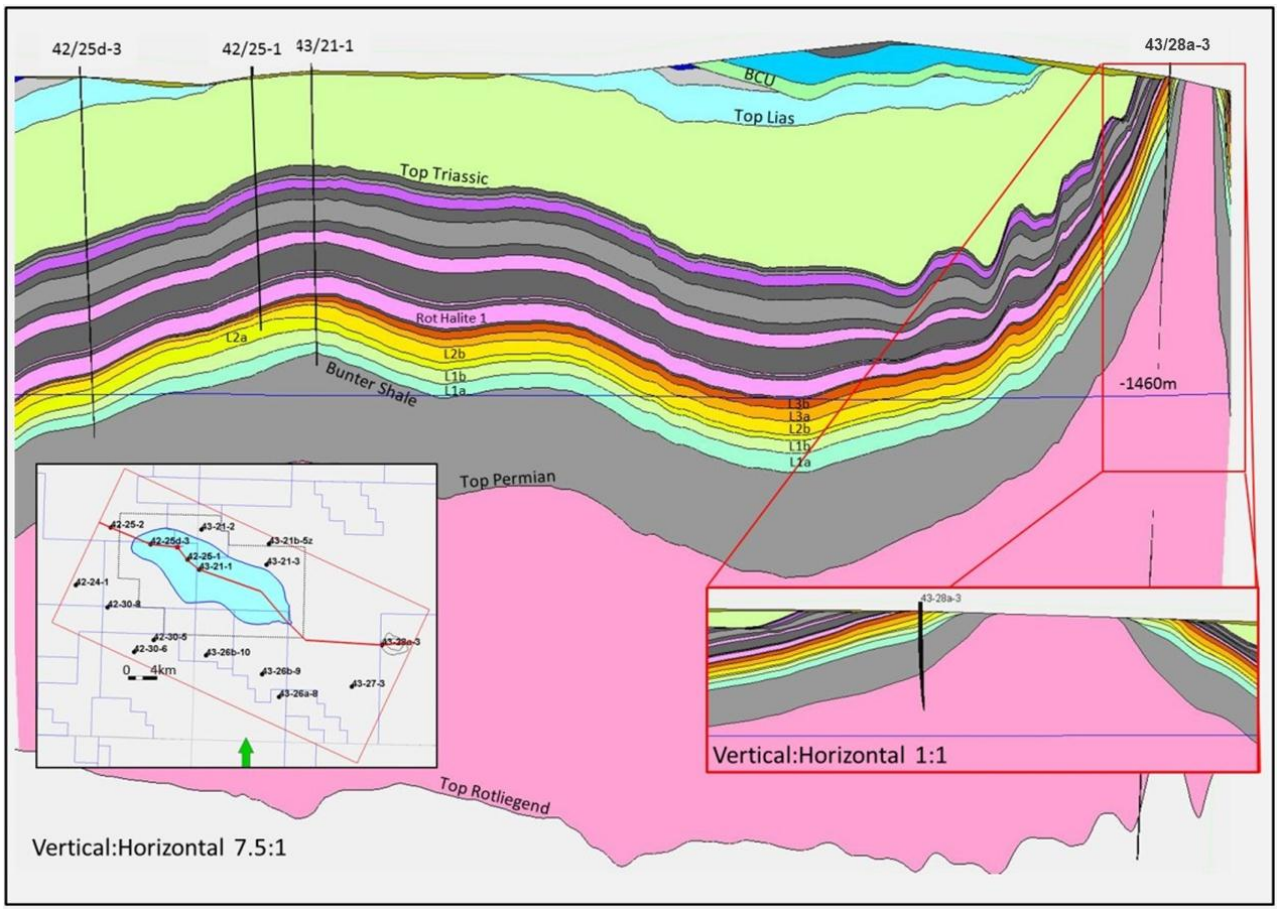

The new addition of a Base Quaternary surface and the updated reservoir zonation are discussed below.

5.6.1 Base Quaternary Surface

Only very limited Base Quaternary data was available from the pre-appraisal well site surveys, the pipeline route survey and the seabed outcrop survey. This data was mapped using Gaussian Random Function Simulation (GRFS) with an anisotropic variogram (15000m x 5000m X -23°) to attempt to mimic the degree of structural variation observed from survey data to the greater Endurance AoI (Figure 5.9). Away from the survey data the confidence in the Base Quaternary surface will be significantly reduced.

Figure 5.9: Base Quaternary Depth Surface

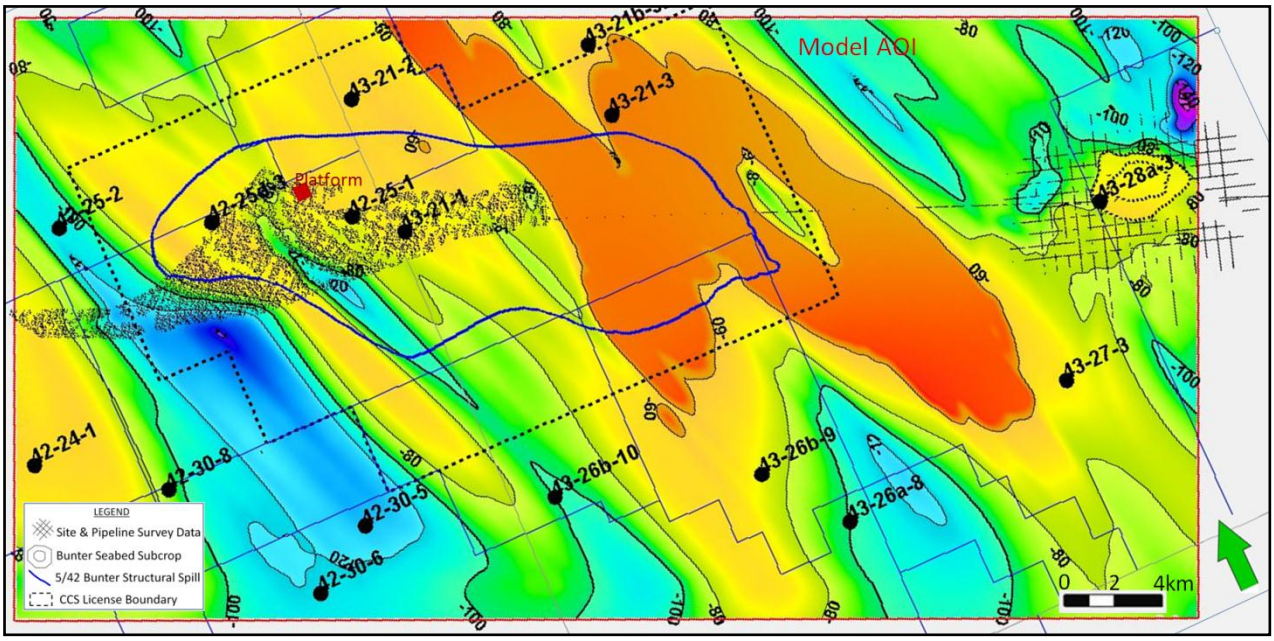

5.6.2 Bunter Sandstone Reservoir Zonation

A threefold zonation (L1 to L3) was used for previous model builds that have included the 42/25d-3 well (November 2013, January 2014, July 2014 and July 2014 updates). This zonation was based on the existing chemostrat well data at the time (42/25-1, 43/21-1, 43/21-2, 43/21-3, 42/20-6) extrapolated to the non-chemostrat wells.

The new 42/25d-3 chemostrat data has shown a significant thinning of the upper L3 zone to the west that has warranted a complete isochore update. Specifically, the uppermost L3b chemostratigraphic subzone pinches out between wells 42/25-1 and 42/25d-3, see Figure 5.10. To capture this variation in the model the two fold chemostratigraphic subdivision of the L3 into upper L3b and lower L3a has been incorporated into the RSFM and Geological Models. Additionally, the two fold subdivisions of the L2 and L3 have also been incorporated into the RSFM to allow for future modelling should it be required.

The isochores were created by first mapping the chemostratigraphic isochore thicknesses in Petrel using the gross Bunter Isochore as a trend. These mapped Isochores were fitted into the Bunter Sandstone envelope by using ratios of each mapped isochore to the sum of mapped isochores as shown below:

$$\frac{\text{Mapped Isochore}}{\text{Gross Bunter Trend}} \times \text{Gross Bunter Isochore} = \text{Fitted Isochore}$$

Total Mapped Isochore Gross Bunter Trend

The new RSFM isochores are illustrated in Figure 5.10.

Figure 5.10: Bunter Sandstone Zonal Isochores

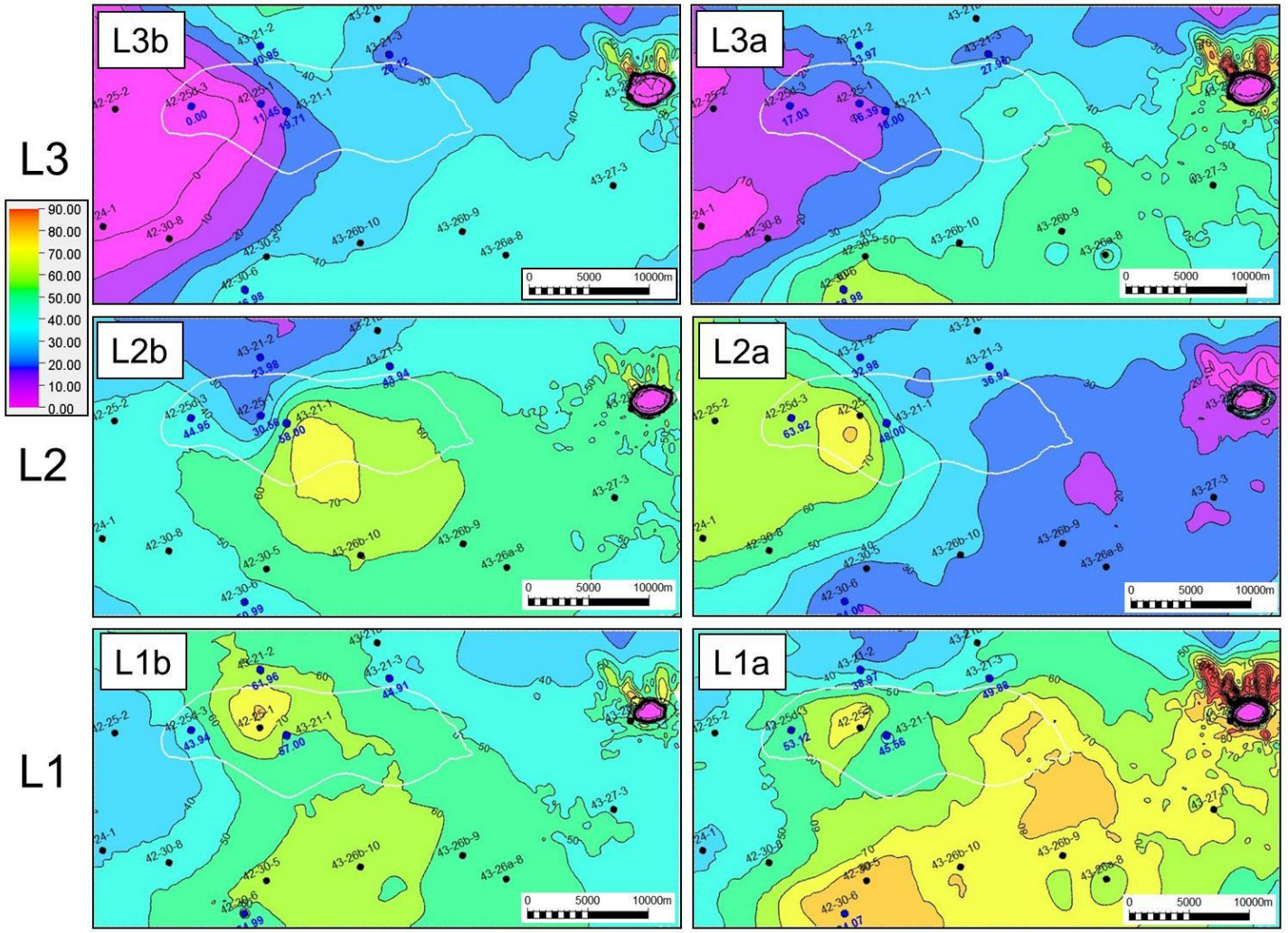

Figure 5.11: Geological Model Make Horizons Process in Petrel

Index	Horizon name	Color	Calculate	Horizon type	Conform to another horizon		Status	Smooth iterations	Use horizon -fault lines	Well tops	Input #1
1	Rot_Halite		Yes	Conformable	No	1	Done	0	Yes	Rot_Halite_1 (Tops_Aug14_LAT	Rot_Halite_1
2	Rot_Clay_		Yes	Conformable	No	1	Done	0	Yes	Rot_Clay_Mbr (Tops_Aug14_LA	Rot_Clay_Mbr
3	BUNTER_		Yes	Erosional	No	1	Done	0	Yes	BUNTER_L3b (Tops_Aug14_LAT	Buntetr_L3
4	BUNTER_		Yes	Base	No	1	Done	0	Yes	BUNTER_L3a (Tops_Aug14_LAT	BUNTER_L3a
5	BUNTER_		Yes	Base	No	1	Done	0	Yes	BUNTER_L2b (Tops_Aug14_LAT	BUNTER_L2b
6	BUNTER_		Yes	Base	No	1	Done	0	Yes	BUNTER_L1b (Tops_Aug14_LAT	BUNTER_L1b
7	BUNTER_		Yes	Base	No	1	Done	0	Yes	BUNTER_SHALE_FM (Tops_Au	Buntetr_Shale_Fm_corr_4328a3

5.6.3 Geological Model Grid Design

The Geological model was built using the Make Simple Grid process, without faults, using the same input horizons as the RSFM for the Make Horizons process; Röt Halite 1, Röt Clay, Top Bunter, Bunter Shale. Additionally, the internal reservoir horizons for the top L3a, L2b and L1b from the RSFM were also used as input into Horizon Modelling (Figure 5.11).

The Geological Model is consistent with the RSFM in that it has the same lateral cell dimensions of 100m x 100m, it is rotated by the same angle of -25° and has coincident cells. The L3b and L3a subzones have been adopted in the geological model to capture the pinch-out of the topmost L3a subzone in the west of the Endurance structure. The lower zones, L2 and L1 have not been sub-dived into their constituent subzones (L2b, L2a, L1b and L1a) in the geological model. It was felt that including these zones would over complicate the model and could be detrimental to the use of facies trends.

The top two model zones, comprising the Röt Halite 1 and underlying Röt Clay, are both 1 layer thick. The reservoir layering has been designed to be approximately 1 m thick.

Table 5.1: Geological Model Layering Summary

Zone	Average Zone Thickness (m)	Number of Layers	Layer Numbers	Average Layer Thickness (m)	Layering Method
Röt Halite	76	1	0	76	Single layer
Röt Clay	1	1	1	10.9	Single layer
L3b	28	100	2-101*	1	Base up 1 m thick
L3a	31	143	102-244*	1	Base up 1 m thick
L2	100	100	245-344	1	Proportional
L1	122	122	345-466	1	Proportional

* Simbax layers

The top two reservoir layers, L3b and L3a, are thin and truncated to the west. A base-up layering system has been adopted for these layers with 1 m thick cells. This method causes cells to truncate against their topmost bounding surface in an unconformable fashion. It is questionable whether the Top Bunter (L3b) and L3a horizons are unconformities. The high proportion of re-worked ooids close to the L3a/L2 boundary may be an indication of unconformities within the Bunter Sandstone or at least in areas bounding the basin margin. The base-up layering method was primarily used to avoid generating large numbers of very thin cells close to the pinched out margins, as would be the case in a proportional layering method. Large numbers of thins cells can cause computation problems in the Schlumberger software application, Eclipse simulator, leading to excessively long run times.

A proportional layering method was used for the remaining L2 and L3 zones since these zones maintain significant thickness across the AoI.

Simulation grid design is discussed in Section 8.3.2.1.

5.7 Facies Definition

5.7.1 Objective of Facies Modelling

The objective for defining facies was to create a set of facies that relate to reservoir quality, which could be used for property distribution in the static model. No attempt was made to model the sedimentological facies identified in the sedimentological interpretation since they bear no meaningful relationship to reservoir quality (Figure 5.12). Consequently, a set of "electro facies" was defined based on wireline log data alone. Facies were interpreted in 13 wells in the greater Endurance area, including 42/25d-3. These were investigated for trends that could be used in modelling.

5.7.2 Facies Definition Summary

Six electro facies were picked on the three common logs that were available in all wells, namely gamma-ray, sonic and resistivity (Table 5.2). The facies are interpreted to relate primarily to post-depositional diagenetic processes that created varying degrees of cementation and porosity reduction. Figure 5.13 illustrates porosity distributions of the six facies types. Four of the six facies represent varying degrees of cemented sand, and two are uncemented facies.

Table 5.2: Electro-facies Wireline Log Criteria and Porosity Ranges

Facies No.	Description	Facies Definition	Mean Porosity	Porosity Range
Facies 1	Cemented sand	RT>0.2 ohmm	6.27	0.47 to 15.59
Facies 2	Partially cemented sand	Remainder of uncharacterised sand	12.12	2.16 to 18.77
Facies 3	Good sand	DT>80 us/ft	20.66	13.28 to 36.04
Facies 4	Heterolithic	GR_Norm>0.3 (clay rich)	11.8	0 to 30.12
Facies 5	Plugged cemented sand	Very high resistivity, zero-very low porosity	2.88	0 to 14.87
Facies 6	Dolomite cemented sand	Very low GR, variable porosity	11.61	2.43 to 23.89

Good Sands (Facies 3) and Heterolithics comprising clay rich sand (Facies 4) are interpreted to be uncemented. Good Sands have the best porosity and Heterolithics variable porosity. Plugged Cemented Sands have the lowest porosity (Facies 5), whilst Cemented Sands (Facies 1) and Partially Cemented Sands (Facies 2) show progressively better porosity. Carbonate Cemented Sands (Facies 6) have variable porosity.

The Heterolithic distribution shown in Figure 5.13 is truncated at 17% porosity from the distribution generated from the electrofacies criteria alone. The truncation was applied following the results of the 42/25d-3 core sedimentology which showed that the bulk of the low porosity facies (<17%) are playa margin facies (Figure 5.14). Playa margin facies are interpreted as sands that have been influenced by periodic flooding from a desert lake. The sands include fine clay particles derived from

the lake and consequently have lower porosities. The high porosity tail from the original electrofacies distribution has been amalgamated with the good sand facies as illustrated in Figure 5.15.

In the previous model report (Wright 2014) Facies 6, Dolomite Cement, was described as carbonate cement. The clarification applied here follows the results of petrography in well 42/25d-3, which clearly demonstrates that this facies is dolomite cemented sandstone (Figure 5.16). Similarly, the new petrography also provides some clarification on the Partially Cemented facies which comprise both dolomite and anhydrite cements. Unfortunately the petrography provides no indications for the mineral content of the Cemented Plugged and Cemented facies since they were not penetrated in well 42/25d-3.

Figure 5.12: Porosity Distribution of Electrofacies Heterolithics over the 42/25d-3 Cored Interval, Coloured by Sedimentary Facies

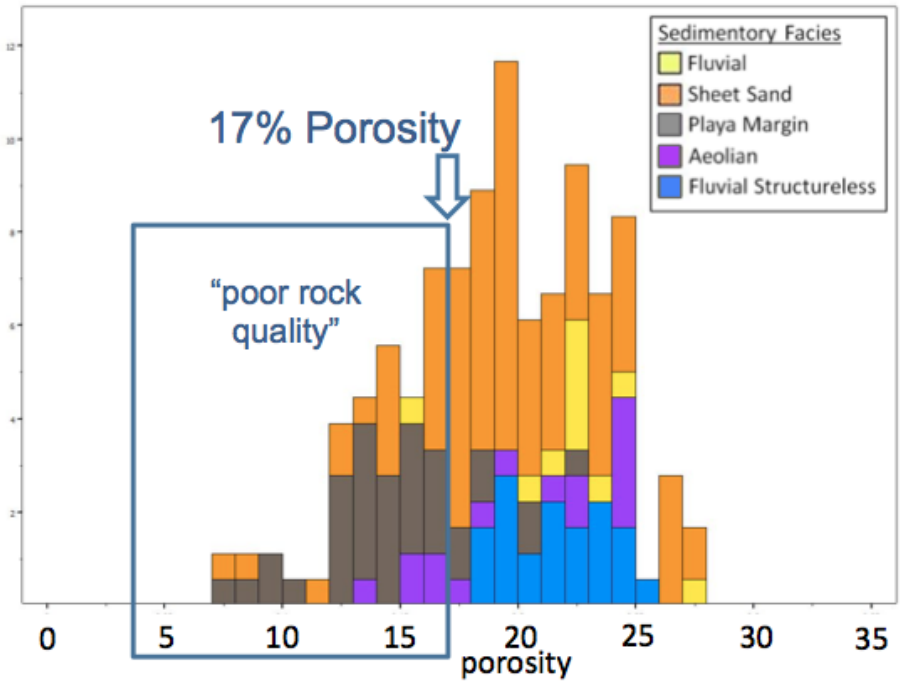

Figure 5.13: Facies Porosity Distributions

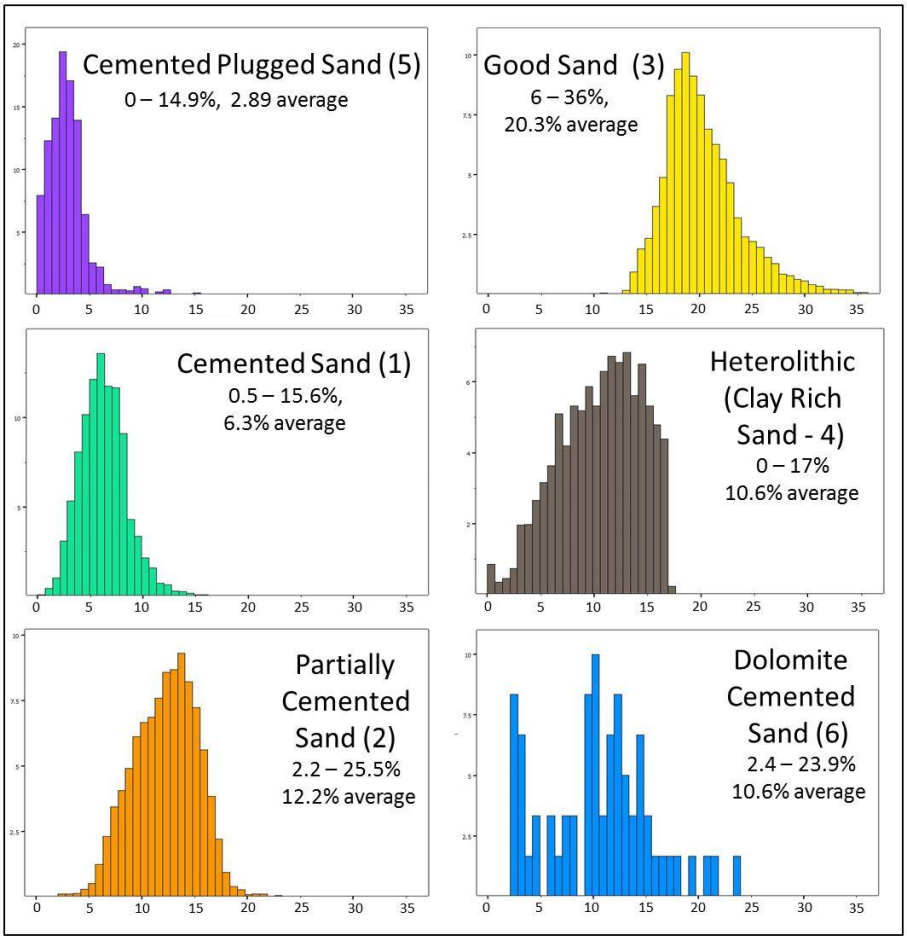

A mineral characterisation of the Bunter Sandstone suggests that halite is more prevalent in cemented wells (42/25-2 and 43/21-3) than in uncemented wells (42/25d-3 and 43/21-1, Figure 5.16). A small proportion of halite is still present in the uncemented wells. Blackbourn's Thermohaline Circulation Model proposes an explanation for the absence of significant halite cement over the Endurance structure, within the seismic phase reversal polygon. The model envisages convection currents of lower salinity brine preferentially removing halite by dissolution. These convection currents are driven by differential heating of the reservoir from the underlying Permian salt pillow.

Figure 5.14: Raw Heterolithic Fraction (Top), Split into a Refined Heterolithic Fraction (<17% Porosity, Bottom Left) and the Good Sand Facies (Bottom Right)

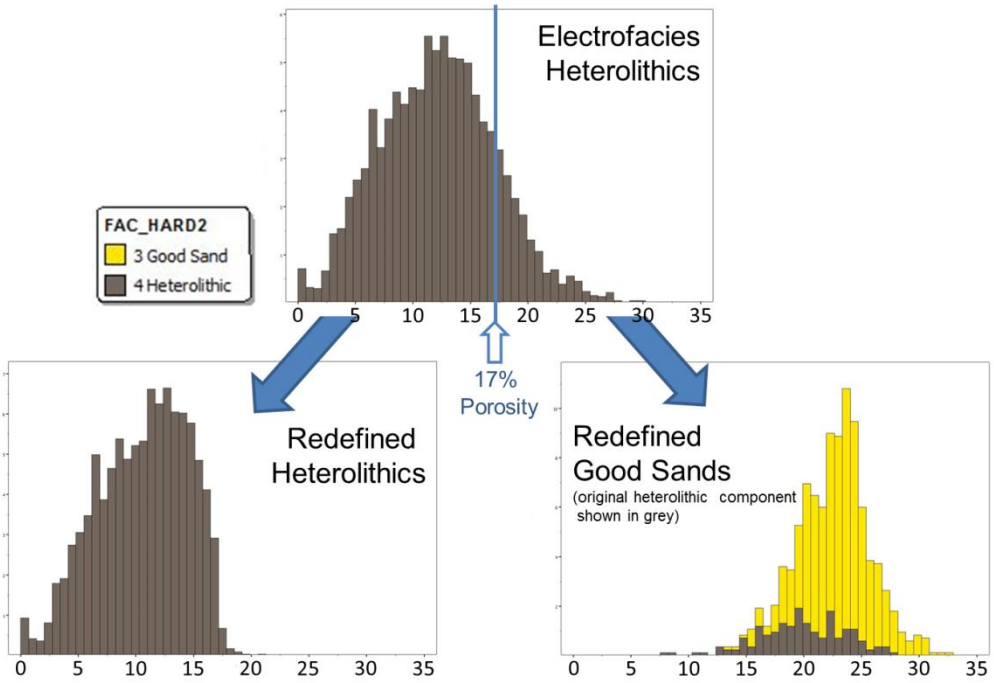

Figure 5.15: GR, Porosity and Electrofacies Over the 42/25d-3 Cored Interval Compared to the Proportions of Dolomite and Anhydrite Cements from Petrographic Analysis

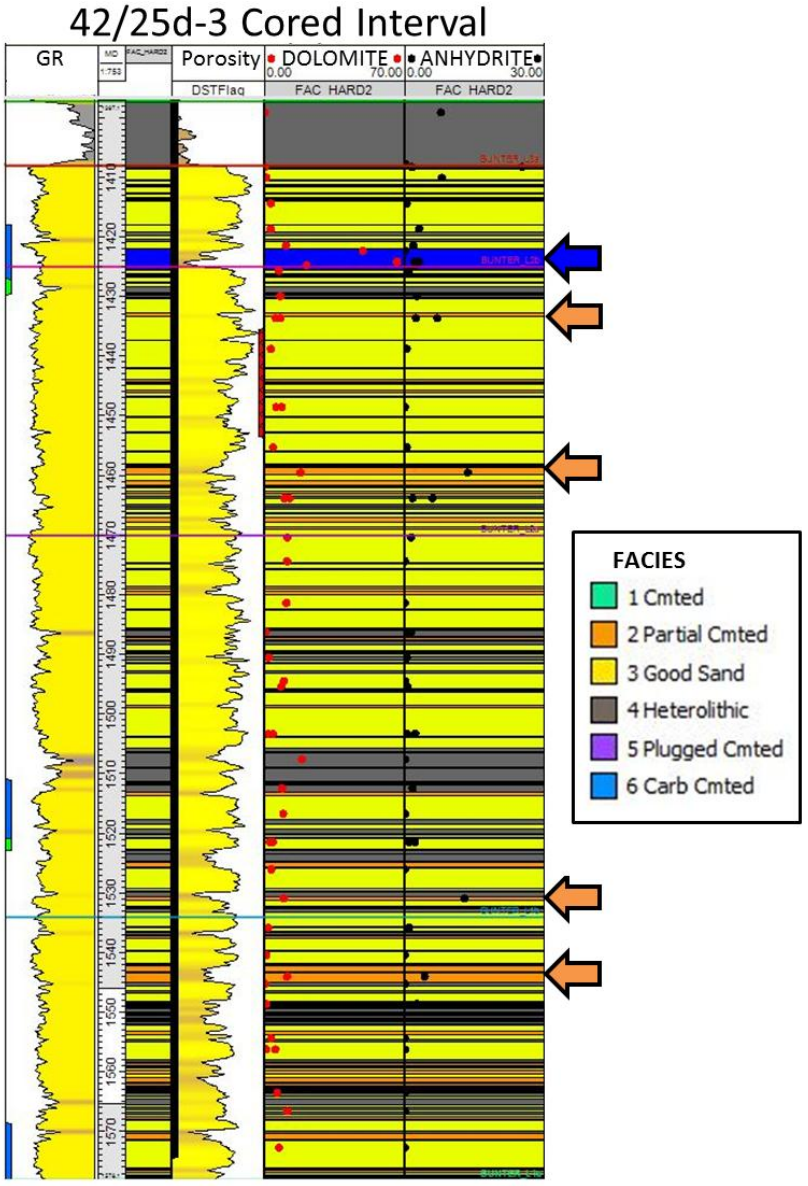

Electrofacies displayed in Track 3 and repeated in Tracks 5 and 6 for comparison to Dolomite and Anhydrite points.

Figure 5.16: Proportions of Halite, Anhydrite and Carbonate Cement from XRF Mineral Analysis of Cuttings and Core Samples

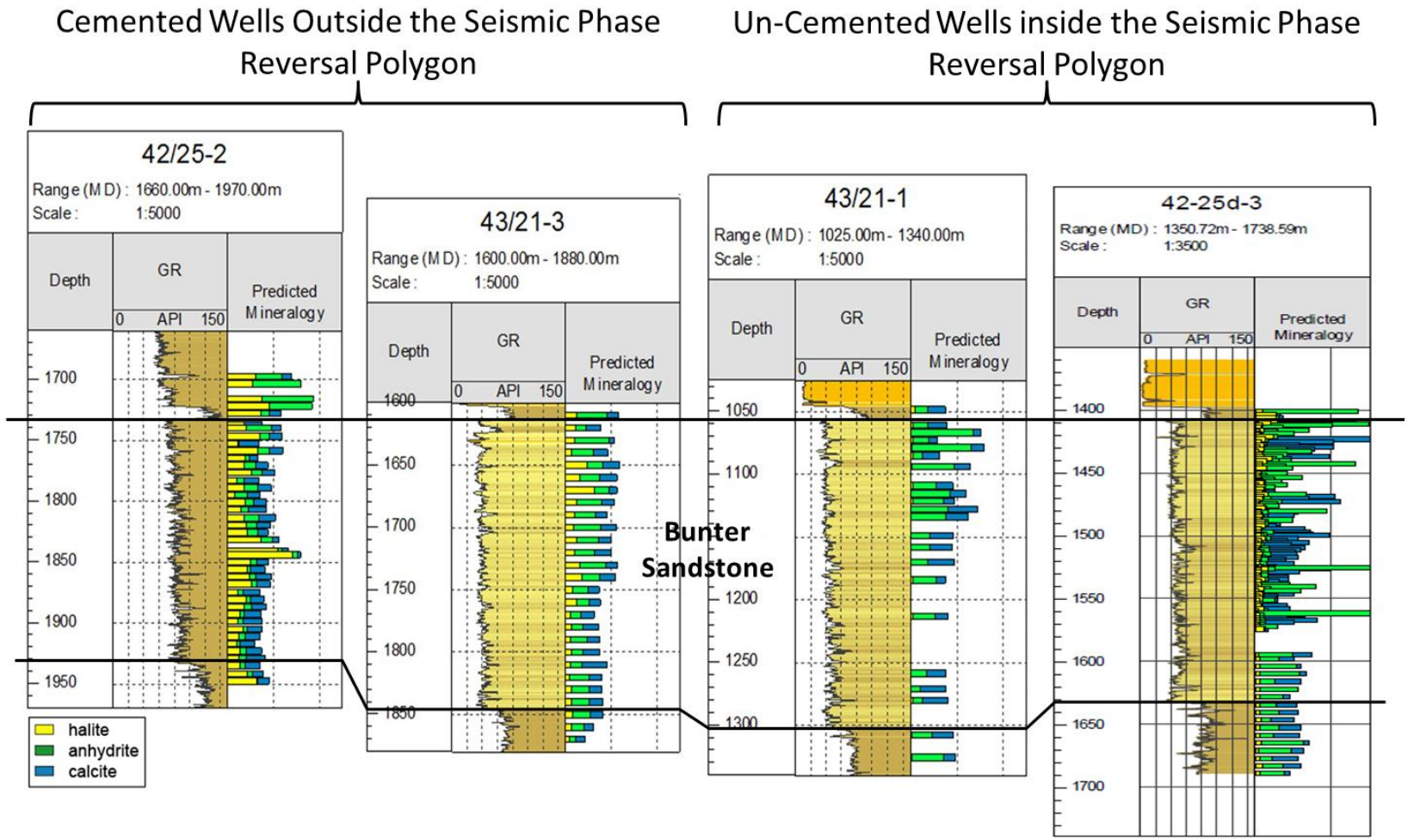

5.8 Facies Trends

Thirteen wells (out of the total well stock of sixteen) containing wireline logs have been investigated for areal and vertical trends such that they can be incorporated into the modelling process. The observed facies trends are described below.

5.8.1 Gross Facies Trends Related to the Seismic Phase Reversal Boundary

Good Sand facies occur almost exclusively in wells within the seismic phase reversal boundary in wells 42/25-1, 42/25d-3, 43/21-1 and 43/27-3 (Figure 5.17). Plugged Cemented and Cemented Sands lie in wells outside the seismic phase reversal boundary. Partially Cemented and Heterolithic Facies are common in wells inside and outside the phase reversal boundary. Dolomite Cemented Facies occur in the three wells, 42/25-1, 42/25d-3 and 43/21-1, in discrete intervals close to the top of the reservoir. It is probable that these cements also occur in wells outside the phase reversal boundary where the log response is dominated by other cemented facies.

5.8.2 Plugged Cemented Trend

This facies appears to be restricted to wells outside the phase reversal boundary and at the top of the reservoir although cementation becomes more pronounced to the south-west of the field at all levels in the reservoir. The Vertical Proportion Curve (VPC) in Figure 5.18, which is based on all 13 wells, demonstrates that Plugged Cemented Sands are restricted to the top of the Bunter formation.

5.8.3 Cemented Sand Trend

Mapping of facies proportions in the wells has highlighted that Cemented Sands are most abundant in the west of the area and least common in the east (Figure 5.19). This trend probably relates to depth of burial, which is interpreted to have been deeper in the west. Deeper burial is inferred from absence of post- Base Cretaceous Unconformity (BCU) sediments in the west, and from the observation of increasing westward velocity within the Röt Clay formation suggesting increasing compaction. These post-BCU sediments are interpreted to have been eroded by a later Late Cretaceous and Tertiary inversion and uplift events focused toward the west. This inversion has been well documented as the Sole Pit Inversion (see Reference 2 in Section 9).

Figure 5.17: GR, Electrofacies and Porosity Logs of 3 Cemented Wells Outside the PRP (42/25-2, 43/21-3 and 43/26b-9 and Two Wells Inside the PRP (42/25d-3 and 43/21-1)

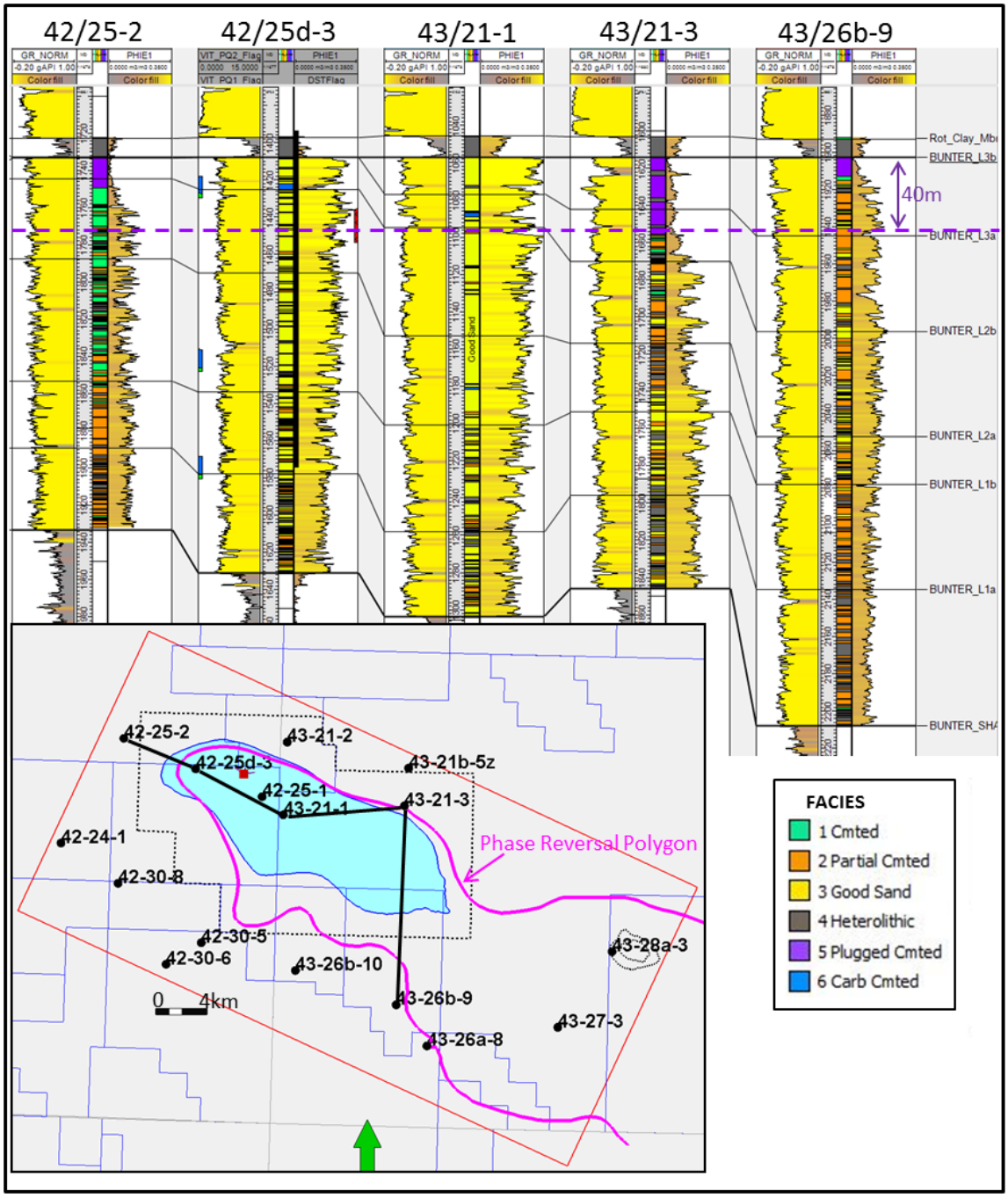

Figure 5.18: Vertical Proportion Curves from the Greater Endurance Wells Compared to Vertical Facies Functions for the Plugged Cemented and Heterolithic Facies

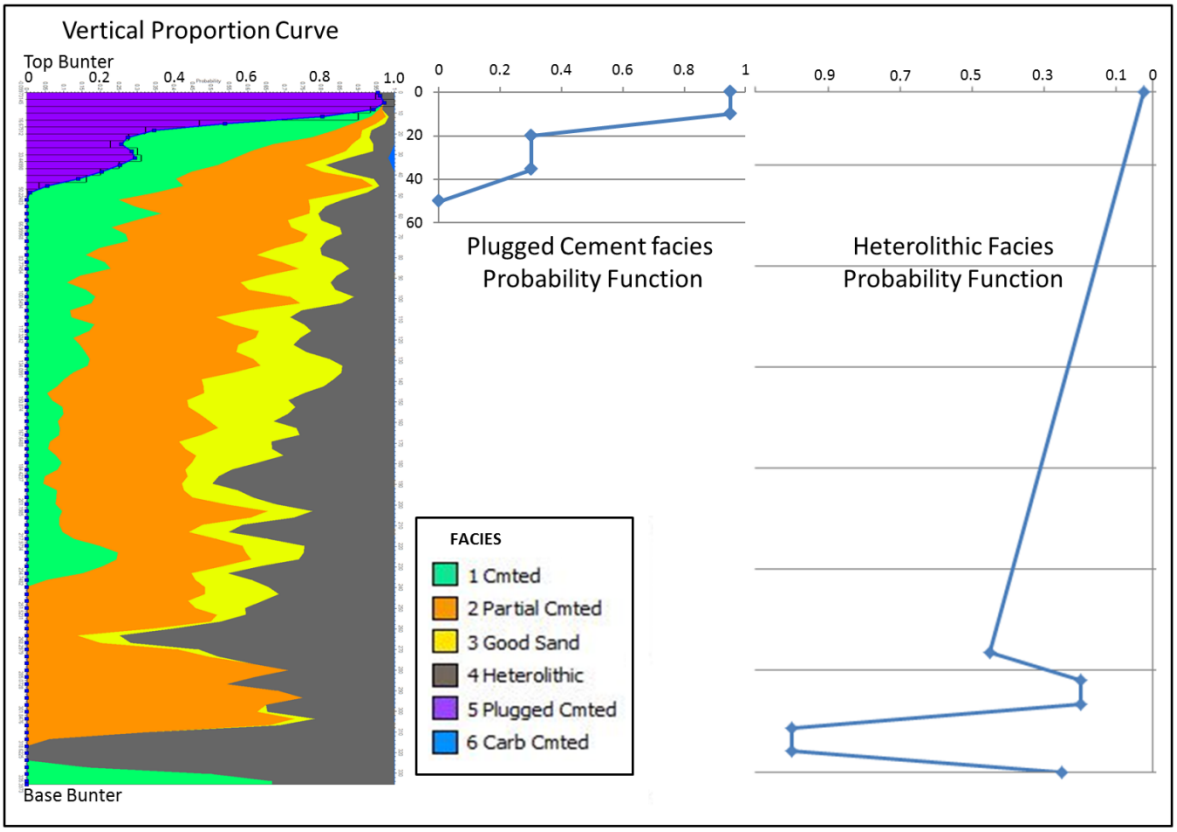

Figure 5.19: East-west Trend Surface Illustrating the Increased Proportion of Cemented Facies

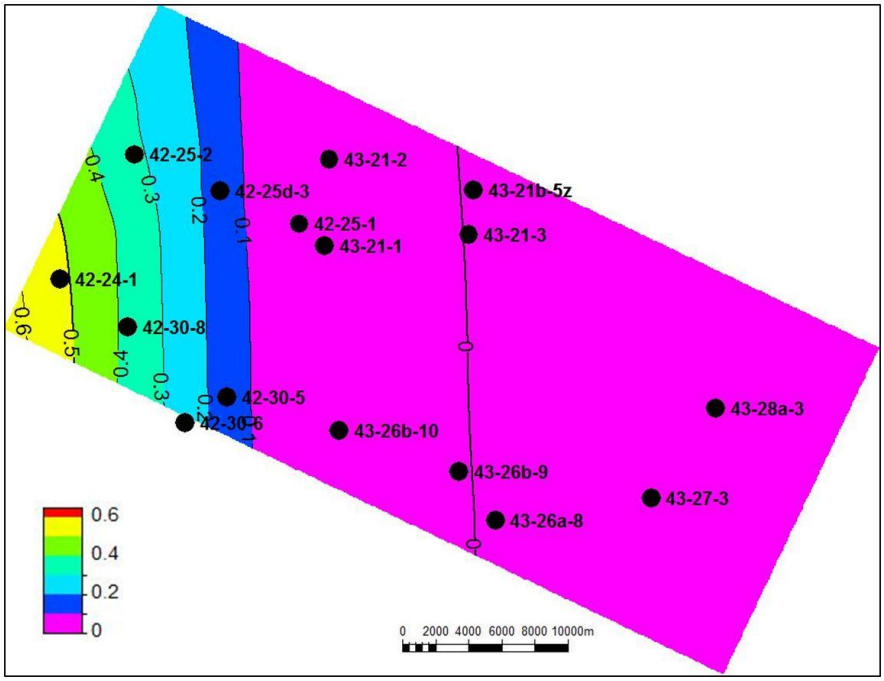

5.8.4 Dolomite Cemented Sand Trend

Seismic modelling of well based synthetic seismic logs suggests that a strong seismic amplitude anomaly within the phase reversal boundary is related to the presence of thin dolomite cemented sands near the top of the reservoir (Figure 5.20). The amplitude anomaly, which is not related to the main seismic phase anomaly, but rather is an intra-reservoir event, highlights the distribution of such sands elsewhere over the Endurance structure. It does not however give any indication as to whether the dolomite cemented interval is a single event or a concentration of numerous events at approximately the same elevation. Chemostratigraphy over wells 42/25d-3, 42/25-1 and 43/21-1 (Figure 5.6) suggests that these cemented sands are not stratigraphically related, but cut across the L3b/L2a boundary. However, there is the possibility that this dolomite cemented interval may be of depositional origin, in that it contains reworked oolithic material, and could be a continuous event based on petrographic data.

5.8.5 Heterolithic Trend

The vertical proportion curve in Figure 5.18 illustrates that heterolithics increase in frequency with depth below Top Bunter. As noted previously, heterolithics occur in wells on both sides of the seismic phase reversal boundary and are interpreted to be uncemented.

Figure 5.20: Top Bunter Sandstone Seismic Amplitude Anomaly

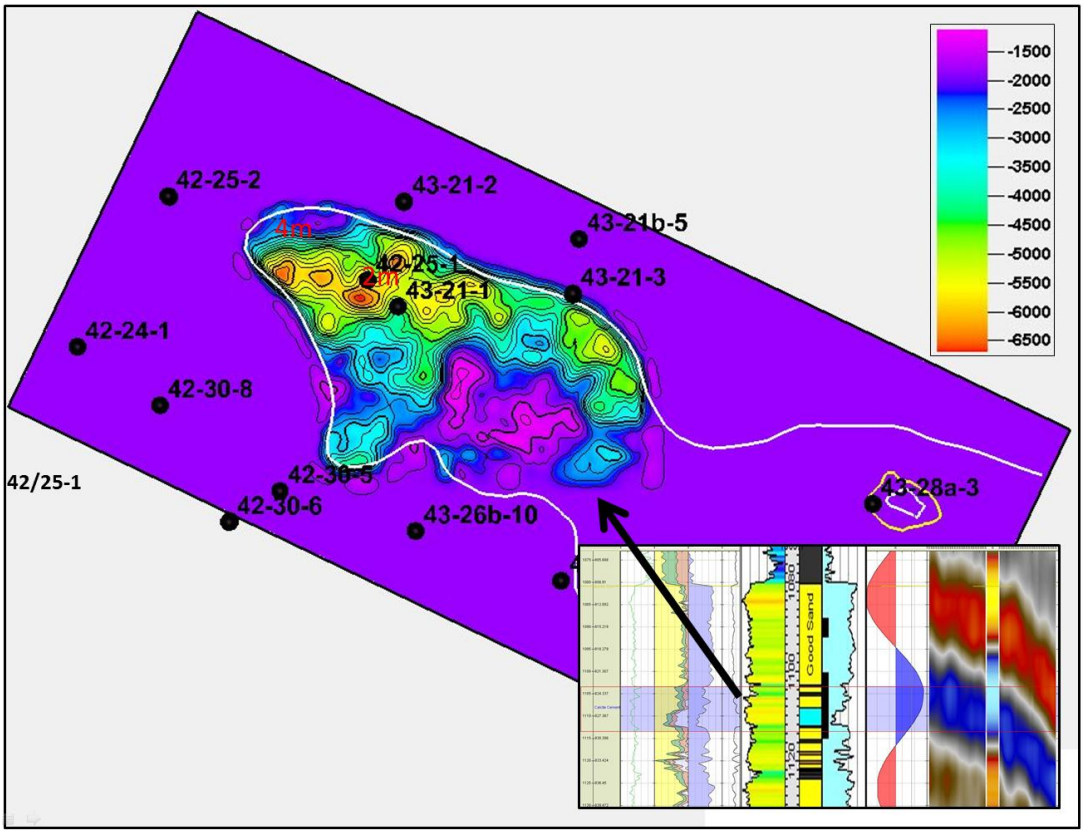

5.9 Facies Modelling

The primary aim in facies modelling was to capture the seismic phase reversal boundary that appears to control the distribution of cemented facies as discussed above. All other facies trends are secondary to this major trend. Facies modelling follows four steps:

1. Creation of a Hardground Region Parameter that captures the phase reversal boundary which is used in step 2 to distribute the facies types. This parameter determines where the different cemented and non-cemented facies types can occur based on the observation discussed in Section 5.8.
2. Distribution of sand facies types within the cemented/uncemented areas of the Hardground Region. The individual facies trends discussed in Section 5.8 are included in this step.
3. Distribution of Heterolithic Facies which are independent of the Hardground Region. Heterolithic Facies are not cemented and their presence is related to original depositional trends and unrelated to the diagenetic cementation.
4. Combination of the sand facies model created in step 2 and the Heterolithic model created in step 3.

The four facies steps are described in more detail below.

5.9.1 Hardground Region Parameter

The Hardground parameter was designed to place most of the cemented facies on the flanks of the Endurance structure outside the seismic phase reversal boundary, and the uncemented facies over the anticline's core area inside the boundary. Five hardground parameters were created in order to capture some level of facies model uncertainty:

5.9.1.1 Vertical Hard Region

The Vertical Hardground region Model (VHM) was created using geometrical modelling in Petrel, with the seismic phase reversal polygon defining a "cookie cutter" style region of uncemented rock surrounded by cemented rock. A similar approach was considered during the earlier scoping phases of the Endurance project.

5.9.1.2 Diffuse Vertical Hardground Region

Diffuse Vertical Hardground region Model (DVHM): This is similar to the VHM except that it has a fuzzy margin (Figure 5.21B). This model acknowledges the fact that good sands exit outside the phase reversal polygon in small proportions that get smaller away from the polygon. The model was created by distributing an uncemented sand flag using Truncated Gaussian Simulation (TGS) with a trend parameter that shows the proportion of good sands diminishing away from the phase reversal polygon (Figure 5.22). The TGS process used an anisotropic variogram with ranges 500m x 500m x 10m. To honour the phase reversal polygon the top 40m of the model was made to be the same as the VHM.

Figure 5.21: Hardground Facies Models

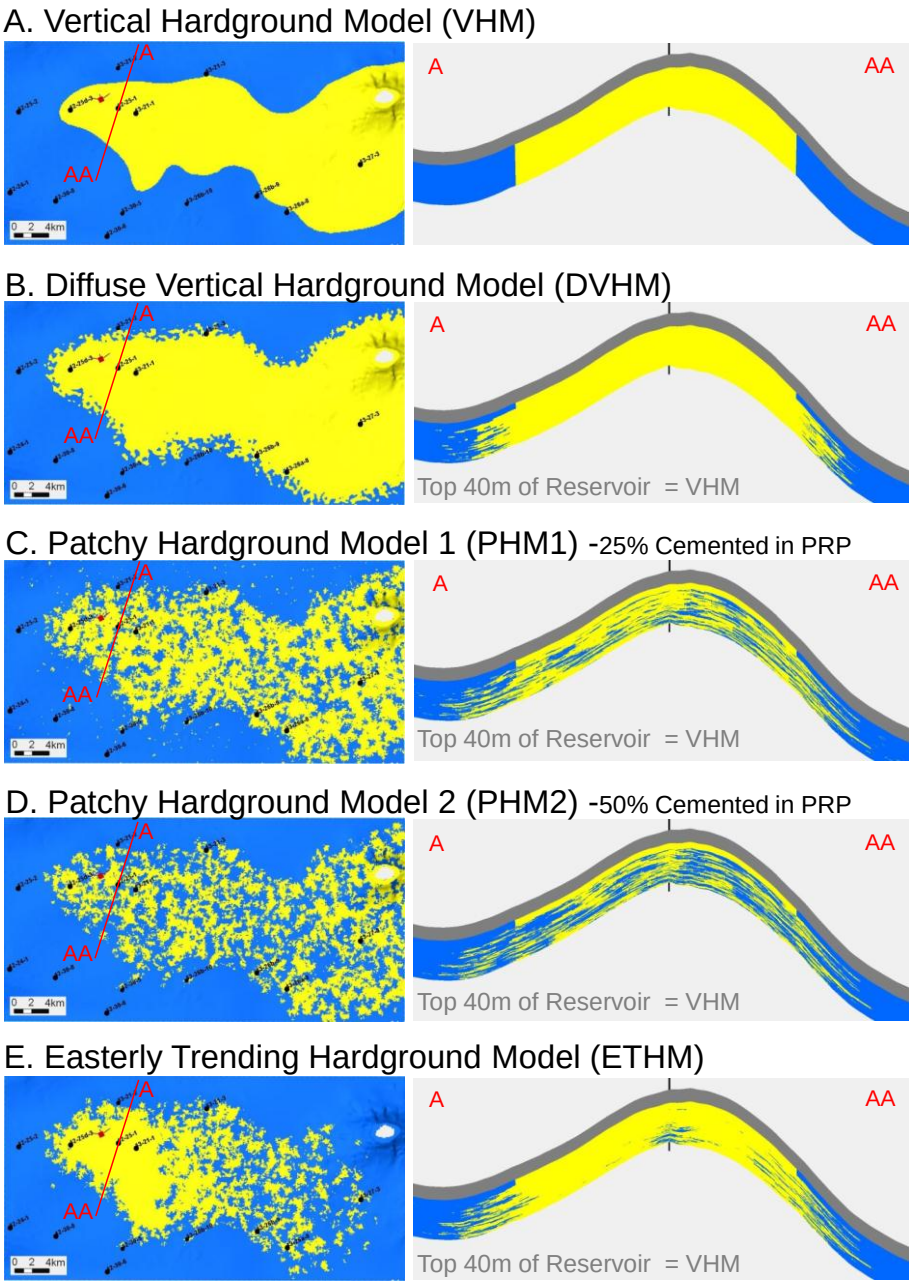

5.9.1.3 Patchy Hardground Model 1

This Patchy Hardground Model (PHM) distributes patches of cemented sand within the phase reversal polygon (Figure 5.21C). The model was created by distributing a cemented sand flag using Sequential Indicator Simulation (SIS) with a trend probability parameter that shows the 25% probability of cemented sand with the phase reversal polygon (Figure 5.23). The SIS process used an anisotropic variogram with ranges 750m x 750m x 10m. To honour the phase reversal polygon the top 40m of the model was made to be the same as the VHM.

5.9.1.4 Patchy Hardground Model 2

This model is similar to the PHM1 except the probability parameter used to distribute patches of cemented sand was increased to 50% within the phase reversal polygon. It places a higher proportion of cemented sand in the phase reversal polygon (Figure 5.21D). Similar to the previous models, the top 40m of the model was made to be the same as the VHM to honour the phase reversal polygon.

Figure 5.22: Lateral Trend Parameter Used in Petrel for the VHM

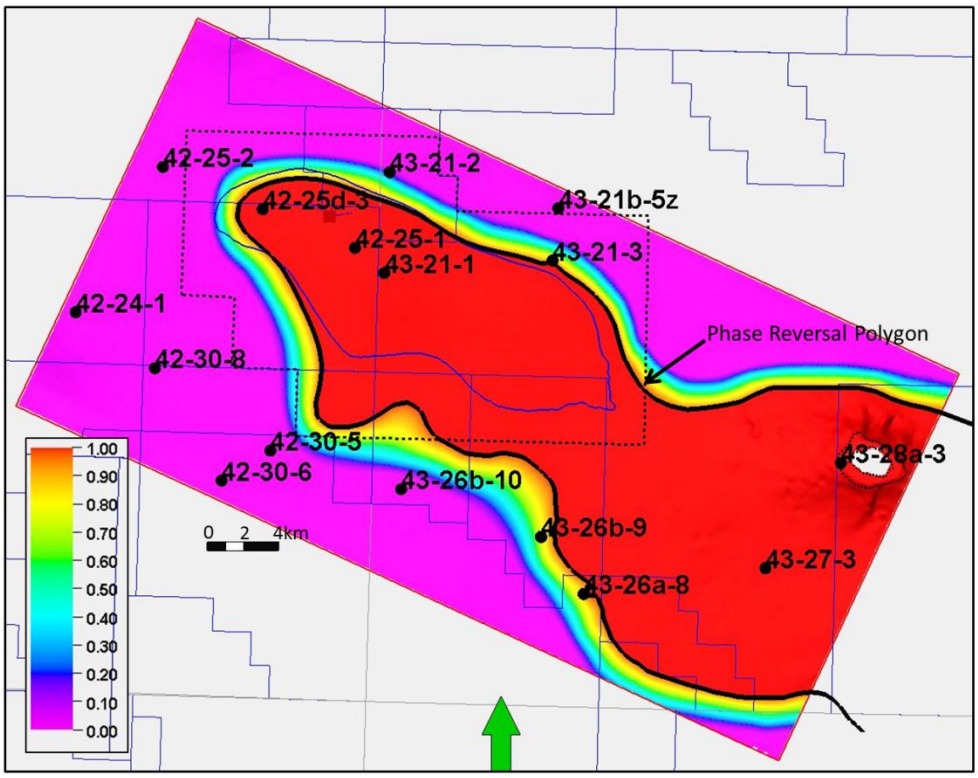

5.9.1.5 Easterly Trending Hardground Model

The Easterly Trending Hardground Model (ETHM) distributes progressively higher proportions of cemented sand toward the east of the AoI (Figure 5.21E). It follows the same process as the patchy hardground models in that it distributes a cemented sand flag using SIS with a trend probability parameter. The trend probability parameter increases the probability of having cemented sands from zero in the west, around the 42/25d-3 and 43/21-1 wells, to 1 in the east (Figure 5.24). Once again the top 40m of the model was made to be the same as the VHM to honour the phase reversal polygon.

Figure 5.23: Lateral Trend Parameter Used in Petrel for the PHM1

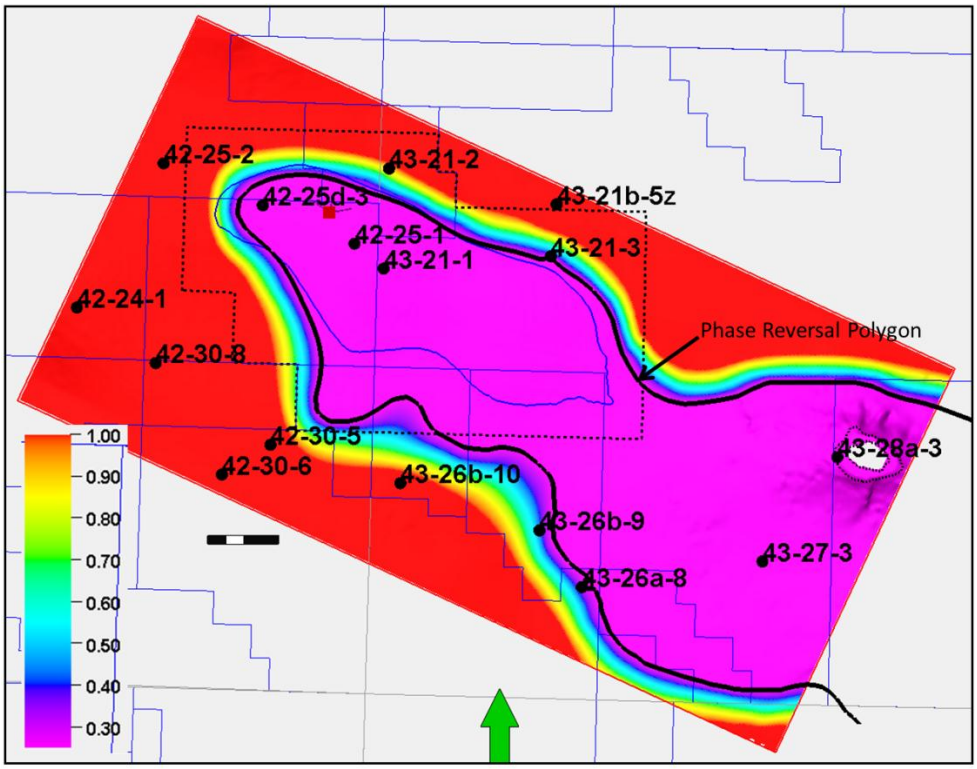

Figure 5.24: Lateral Trend Parameter Used in Petrel for the ETHM

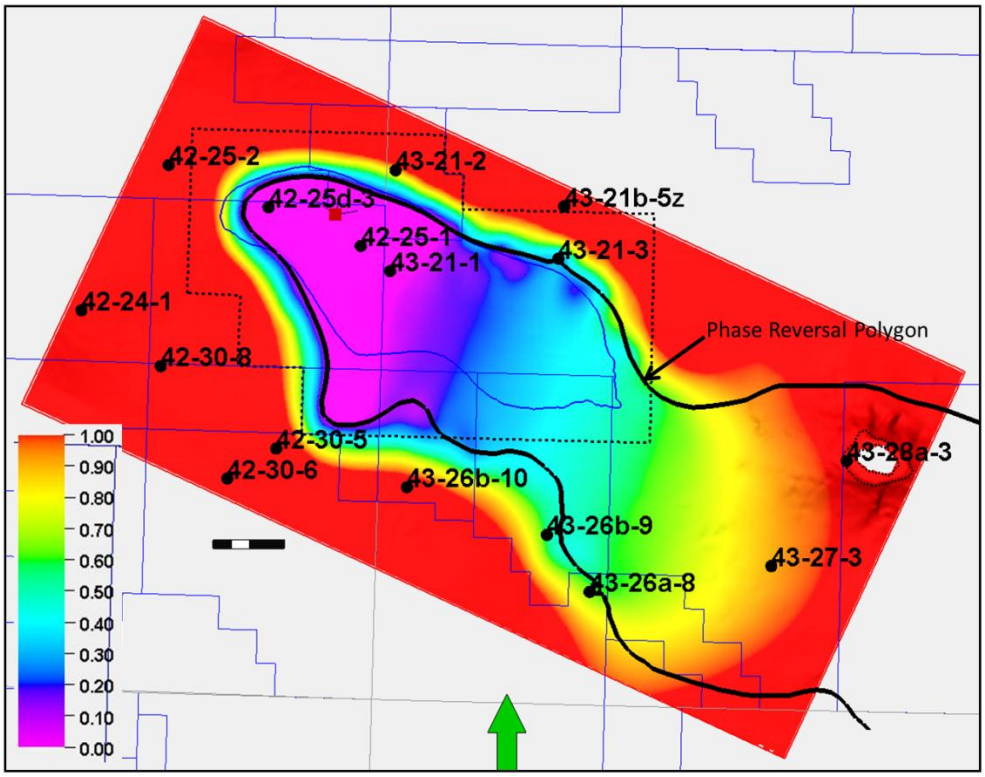

5.9.2 Distribution of Sand Facies within the Hardground Region

Sand facies types are distributed using SIS within Hardground Regions described above. The Hardground Regions are used as a "facies" within the Facies Modelling process. Good, Partially Cemented, Cemented and Cemented Plugged Sands are distributed in the cemented zone whilst Good, Partially Cemented and Carbonate Cemented Sands are distributed in the uncemented zone.

The SIS process uses variograms to control the spatial similarity and distribution of data (see Reference 3 in Section 9). There is insufficient data in the well to extract lateral variograms, consequently the five sand facies types have be given the same lateral facies range estimate of 1000m x 750m (Table 5.3). All variograms are orientated east-west (90°) parallel to the perceived axis of deposition. Analysis of cross beds from image logs from 42/25d-3 strongly indicates an east-west depositional trend. This confirms previous east-west estimates based on the thickening of plugged cemented sands, which are presumed to represent a palaeo fairway axis of channel sands (Figure 5.25). The wells provide sufficient data in the vertical direction for vertical variograms to be determined by facies (Figure 5.26).

The proportion of facies has been taken from well control in the cemented and uncemented zones of the Hardground Region, respectively. The proportion of facies gets modified in the modelling process by the introduction of trends for the Cemented Plugged Sands and Cemented. Despite this, the comparison between upscaled log facies and model facies was good (Figure 5.27).

An additional model was made using the DVHM where good sand facies proportions were forced to be between 90-95% in the uncemented zone at the expense of the other sand facies. Heterolithic proportions for this case were forced to be less than 5%. This model represents an extreme upside case and has been labelled *DVHM_upside*.

For the Cemented Plugged sand facies the vertical proportion function discussed in Section 5.8 and illustrated in Figure 5.18 has been used to preferentially place this facies at the top of the Bunter Formation in zone L3. For the Cemented Facies the increasing east to west trend map, illustrated in Figure 5.19, has been used to preferentially place this facies toward the west in all Bunter Formation zones.

Figure 5.25: Thickness Map of the Plugged Cemented Facies at the Top of the Bunter Reservoir, Outside the PRP, Illustrating a Potential East-West Trend

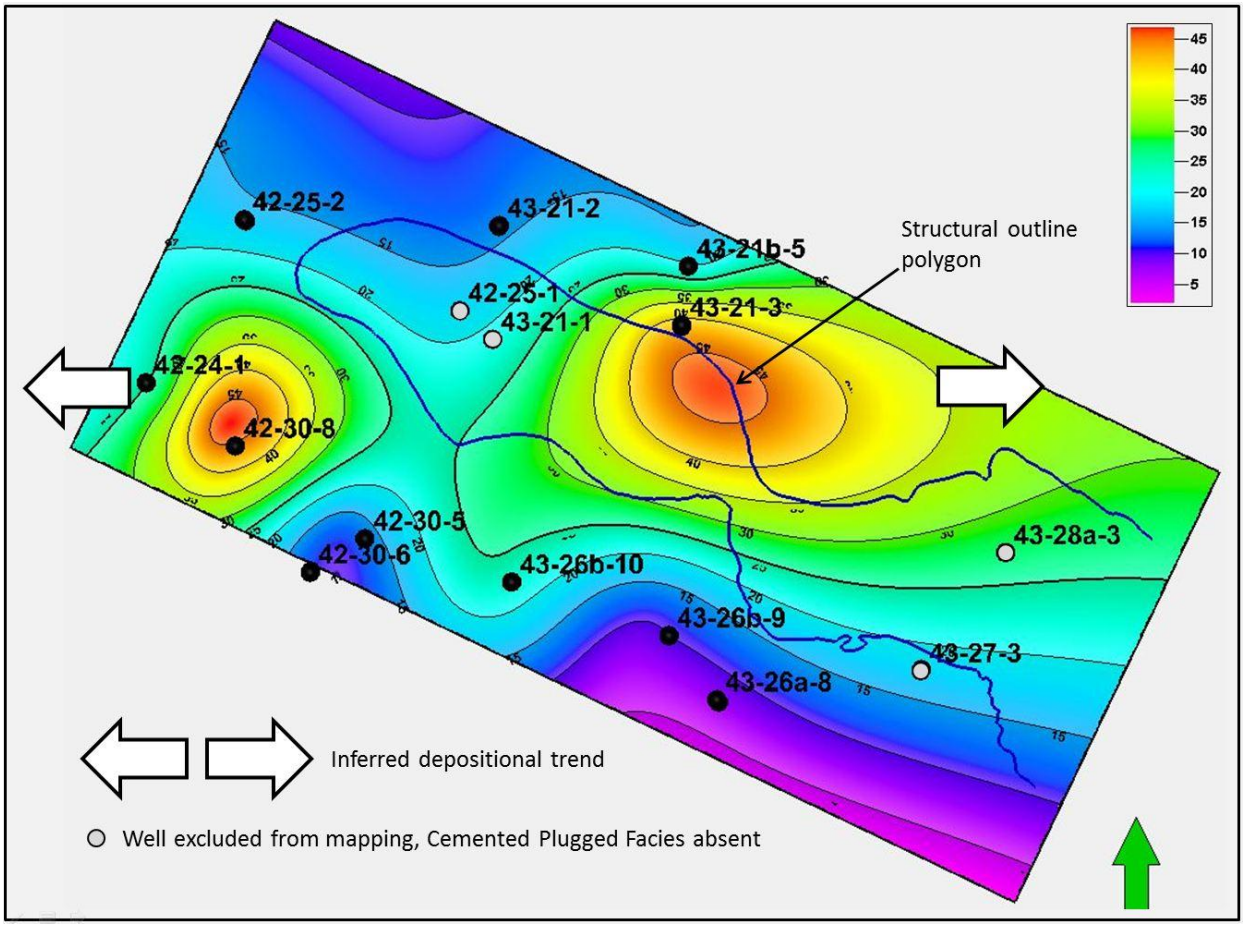

Table 5.3: Facies Variogram Ranges

Facies	Hardground Region		Modelling Method	Variogram			Orientation
	Uncemented	Cemented		Lateral X	Lateral Y	Vertical	
Good sand	Yes	Yes	SIS	1000	750	1	90
Partially cemented sand	Yes	Yes	SIS	1000	750	2	90
Cemented sand	No	Yes	SIS	1000	750	3	90
Cemented plugged sand	No	Yes	SIS	1000	750	3	90
Dolomite cemented sand	Yes	No	SIS	1000	750	3.7	90
Heterolithic	Yes	Yes	TGS	2000	1000	1.9	0

Figure 5.26: Experimental Vertical Variograms

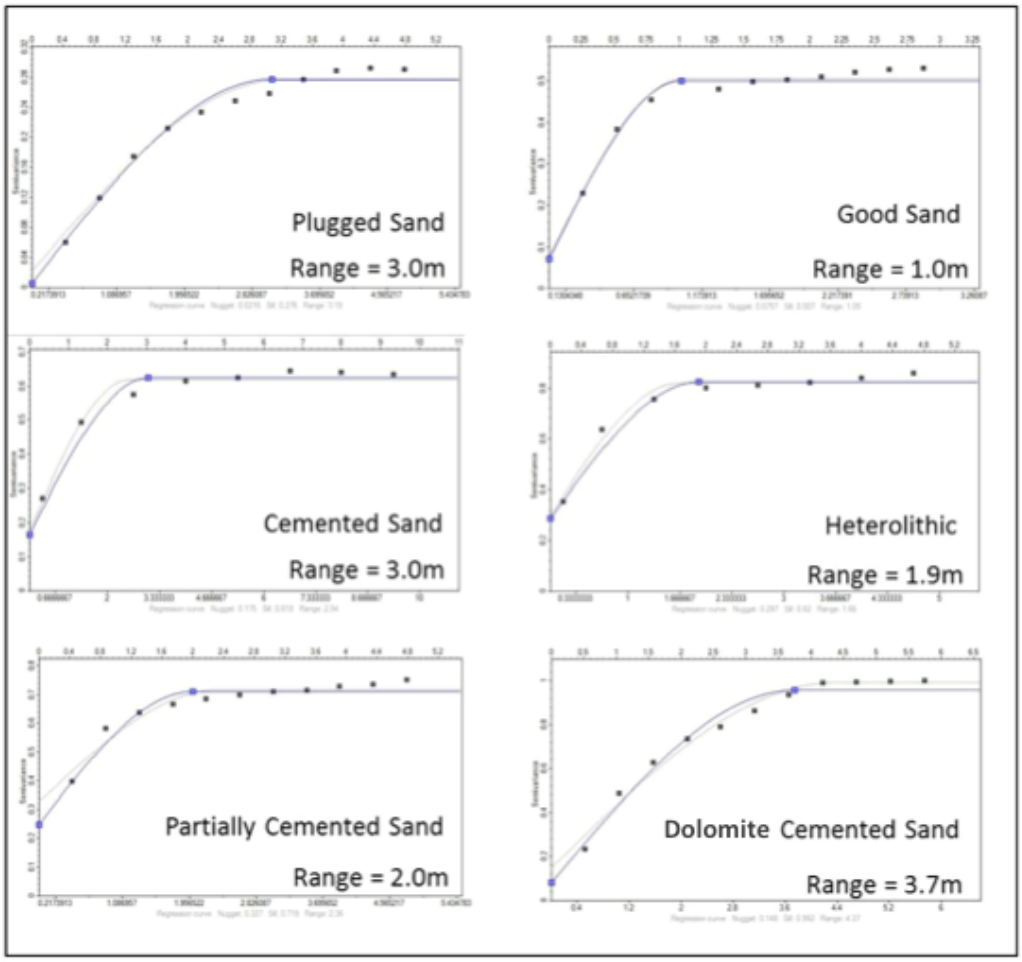

The distribution of Dolomite Cemented Sand in the uncemented zone is controlled by a probability parameter that is based on the Top Bunter seismic amplitude anomaly illustrated in Figure 5.20 and described in Section 5.8. A normalised version of the amplitude anomaly within the uncemented zone was made within a narrow 15 m depth interval lying between 25 m and 40m from the top of the Bunter (Figure 5.28(A)). The interval is based on the location of Dolomite Cemented Sand in the crestal wells 42/25d-3, 42/25-1 and 43/21-1. The dolomite cemented interval is interpreted to be independent of the zonation partly lying within zones L3b, L3a and the uppermost part of L2.

The seismic anomaly was normalised between 0.13 and 1.0 with the higher values reflecting a greater chance of distributing Dolomite Cemented Sand. The remainder of the uncemented zone was given a 0.13 probability, reflecting a lower chance of distributing Carbonate Cemented Sand. Figure 5.28B provides areal and cross sectional views illustrating the distribution of Carbonate Cemented Sands.

Figure 5.27: Facies Proportions by Facies Models

VHM	Code	Name	Un-Cemented Zone		Cemented Zone	
			Model	Raw Wells	Model	Raw Wells
	1	Cmted Sand	0.0%	0.0%	17.0%	15.7%
	2	Partially Cmtd	15.7%	15.2%	42.6%	38.4%
	3	Good Sand	67.0%	72.7%	16.0%	13.9%
	4	Heterolithic*	15.7%	10.6%	16.6%	23.8%
	5	Plugged Cmtd	0.0%	0.0%	7.8%	8.2%
	6	Dolomite Cmtd	1.6%	1.5%	0.0%	0.1%
		Total	*1.0*	*1.0*	*1.0*	*1.0*
ETHM	Code	Name	Un-Cemented Zone		Cemented Zone	
			Model	Raw Wells	Model	Raw Wells
	1	Cmted Sand	0.0%	0.0%	18.7%	16.4%
	2	Partially Cmtd	15.7%	7.1%	50.8%	42.9%
	3	Good Sand	67.0%	87.8%	6.9%	4.7%
	4	Heterolithic*	15.7%	3.9%	16.6%	27.3%
	5	Plugged Cmtd	0.0%	0.0%	7.0%	8.5%
	6	Dolomite Cmtd	1.6%	1.2%	0.0%	0.1%
		Total	*1.0*	*1.0*	*1.0*	*1.0*
)VHM	Code	Name	Un-Cemented Zone		Cemented Zone	
			Model	Raw Wells	Model	Raw Wells
	1	Cmted Sand	0.0%	0.0%	20.9%	18.1%
	2	Partially Cmtd	14.2%	13.8%	49.4%	42.7%
	3	Good Sand	68.6%	76.0%	4.4%	3.0%
	4	Heterolithic*	16.0%	9.1%	16.4%	26.7%
	5	Plugged Cmtd	0.0%	0.0%	8.9%	9.4%
	6	Dolomite Cmtd	1.2%	1.1%	0.0%	0.1%
		Total	*1.0*	*1.0*	*1.0*	*1.0*
PHM1	Code	Name	Un-Cemented Zone		Cemented Zone	
			Model	Raw Wells	Model	Raw Wells
	1	Cmted Sand	0.0%	0.0%	18.8%	16.4%
	2	Partially Cmtd	7.4%	7.1%	50.2%	42.9%
	3	Good Sand	75.9%	87.8%	6.8%	4.9%
	4	Heterolithic*	15.6%	3.9%	16.6%	27.3%
	5	Plugged Cmtd	0.0%	0.0%	7.5%	8.5%
	6	Dolomite Cmtd	1.2%	1.2%	0.0%	0.1%
		Total	*1.0*	*1.0*	*1.0*	*1.0*
PHM2	Code	Name	Un-Cemented Zone		Cemented Zone	
			Model	Raw Wells	Model	Raw Wells
	1	Cmted Sand	0.0%	0.0%	18.5%	16.3%
	2	Partially Cmtd	7.4%	7.1%	50.4%	42.7%
	3	Good Sand	76.5%	87.8%	7.4%	5.3%
	4	Heterolithic*	15.0%	3.9%	16.7%	27.2%
	5	Plugged Cmtd	0.0%	0.0%	7.0%	8.5%
	6	Dolomite Cmtd	115.0%	0.0%	0.0%	0.1%
		Total	*2.1*	*1.0*	*1.0*	*1.0*
HMup	Code	Name	Un-Cemented Zone		Cemented Zone	
			Model	Raw Wells	Model	Raw Wells
	1	Cmted Sand	0.0%	0.0%	24.0%	18.1%
	2	Partially Cmtd	7.7%	13.8%	59.4%	42.7%
	3	Good Sand	89.5%	76.0%	5.2%	3.0%
	4	Heterolithic	2.5%	9.1%	2.3%	26.7%
	5	Plugged Cmtd	0.0%	0.0%	9.2%	9.4%
	6	Dolomite Cmtd	0.3%	1.1%	0.0%	0.1%
		Total		*1.0*		*1.0*

Figure 5.28: Comparison between the Normalised Top Bunter Seismic Amplitude Anomaly (A) and Model Carbonate Cement NTG (B)

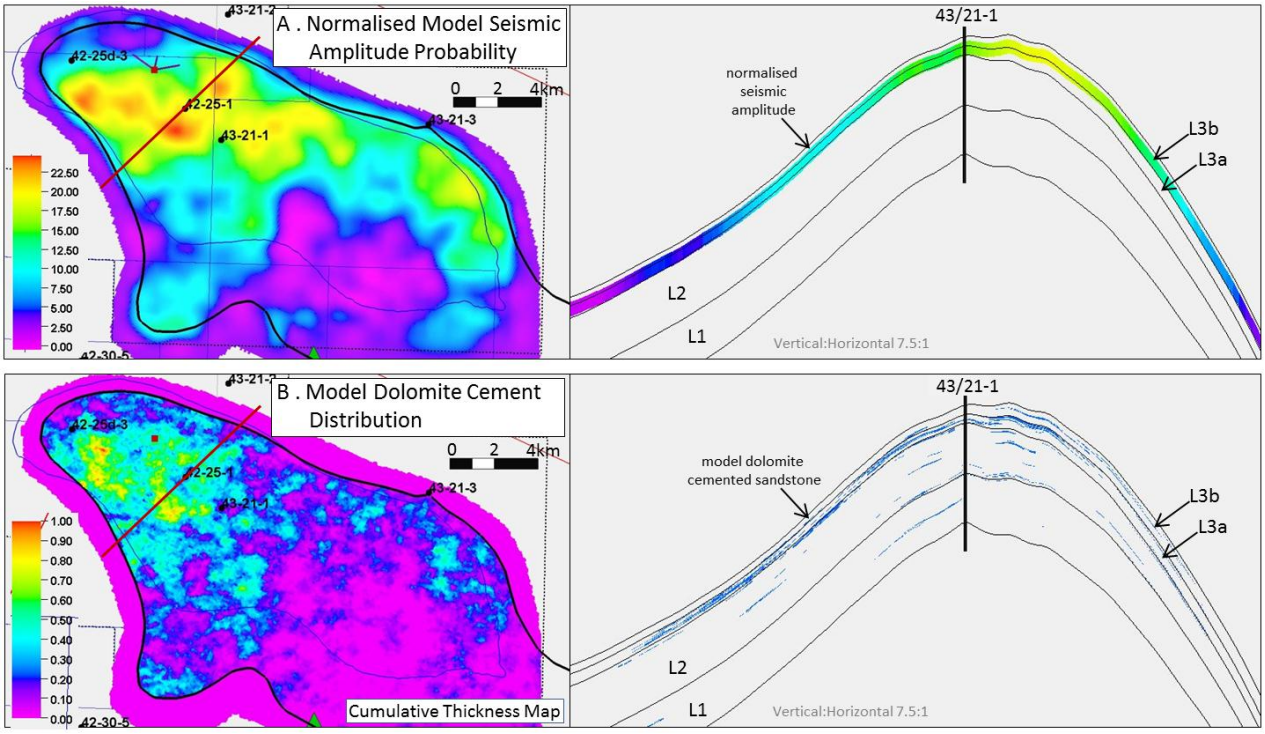

5.9.3 Heterolithic Facies Modelling

Heterolithics are distributed separately to sandstone facies as they are largely unaffected by diagenetic cementation and independent of the Hardground Region. They are distributed using Truncated Gaussian Distribution. This method was preferred to SIS as it creates more continuous and connected bodies, reflecting the fact that the heterolithics do represent original sedimentological facies, unlike the sandstone "facies", which are dominated by diagenetic cementation. Heterolithics are progressively more abundant with depth. The vertical proportion function discussed in Section 5.8 and illustrated in Figure 5.18 has been used to control the vertical distribution of Heterolithics in the reservoir. Heterolithics variograms are orientated perpendicular to the depositional trend to mimic the likely orientation of a lake margin. The cross section in Figure 5.29B illustrates the Heterolithics distribution.

5.9.4 Final Facies Model – Combination of Sand and Heterolithic Facies

The sandstone and heterolithic models described above were combined using the Property Calculator in Petrel. In this process Heterolithic facies were allowed to overwrite sandstone "facies". Figure 5.29C provides an illustration of the combined final facies model.

Figure 5.29: South-West to North-East Cross Section Across the Endurance Model Illustrating the Sand "Facies" Model (A), the Heterolithic Model (B) and the Combined Facies Model (C)

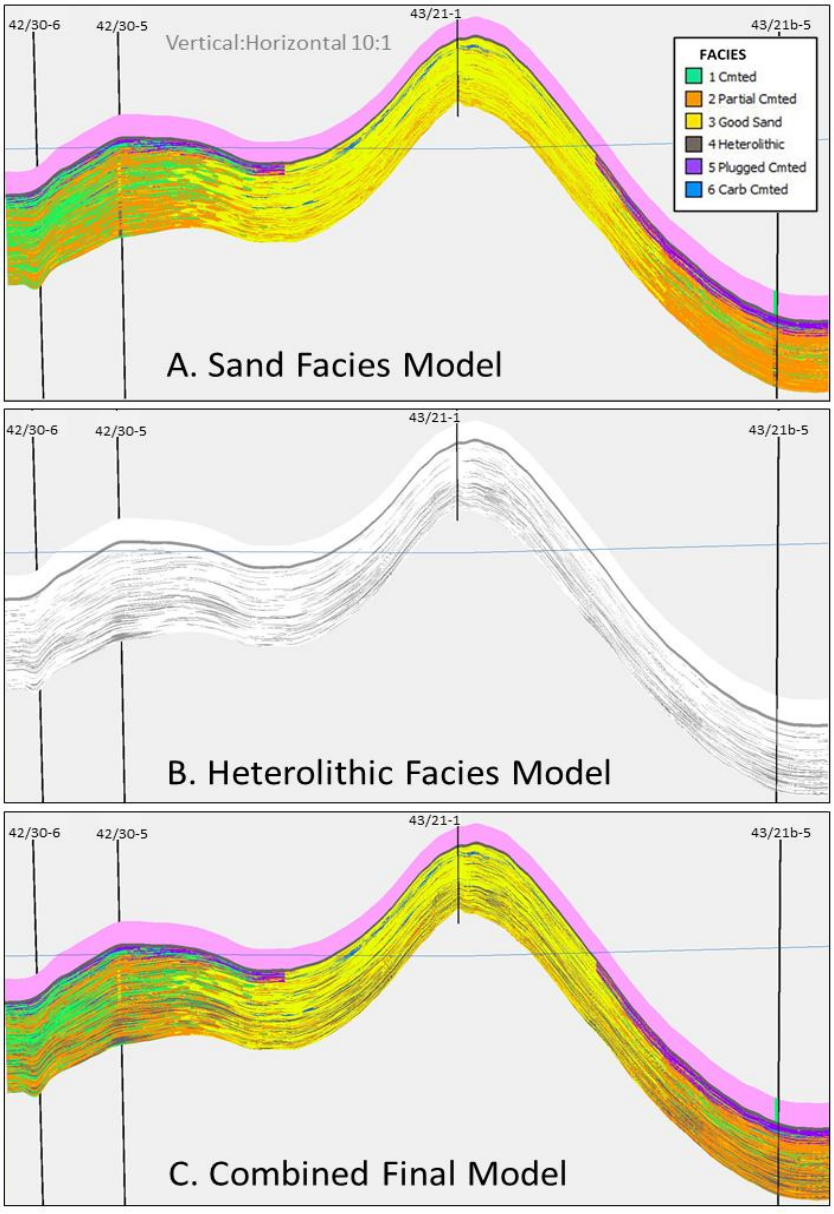

5.10 Property Modelling

5.10.1 Porosity

Porosity was distributed by facies using GRFS in the petrophysical module in Petrel. Porosity variogram ranges have been made to be half the range used for facies (Table 5.4). Variograms were orientated in the same direction as facies. Good sands across the whole Bunter interval, Heterolithics and Partially Cemented facies in L1 have compaction trends that show porosity decreasing with increasing depth (Figure 5.30). Consequently, porosity depth trends were applied for these facies during the simulation process.

Table 5.4: Facies Porosity Variogram Ranges and Orientations

Facies	Modelling Method	Porosity Depth Trend	Variogram Measurements			Orientation
			Lateral X	Lateral Y	Vertical	
Good sand	GRFS	All layers	500	375	0.5	90
Partially cemented sand	GRFS	No	500	375	1	90
Cemented sand	GRFS	No	500	375	1.5	90
Cemented plugged sand	GRFS	L1 only	500	375	1.5	90
Dolomite cemented sand	GRFS	No	500	375	1.85	90
Heterolithic	GRFS	L1 only	750	500	0.95	0

Figure 5.30: Facies Porosity Variogram Ranges and Orientations

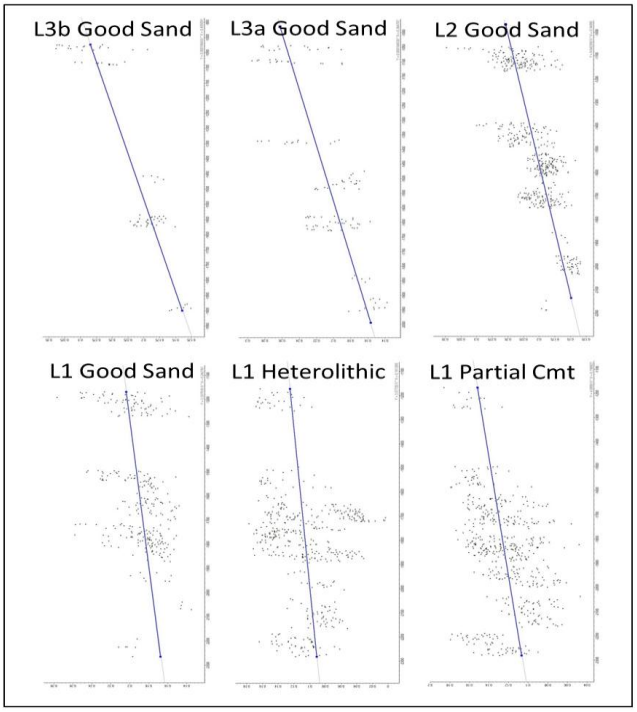

5.10.2 Permeability

Permeability has been based on RCA data from 42/25d-3 and 42/25-1. Klinkenberg corrected permeability was binned into porosity groups and the binned data used to create a porosity-permeability function (Figure 5.31A). Binned data on a semi-log plot yields a statistically more accurate means of fitting a curve through the data than using the raw data cloud. The power function was chosen as it gives a reasonable fit to the very low permeability as compared to a conventional linear function (Figure 5.31B). The permeability function formula is:

$$\text{Permeability} = 2E6 \times \text{Porosity}^{4.4833}$$

Figure 5.31: RCA Porosity vs Permeability Plots with Trend Function

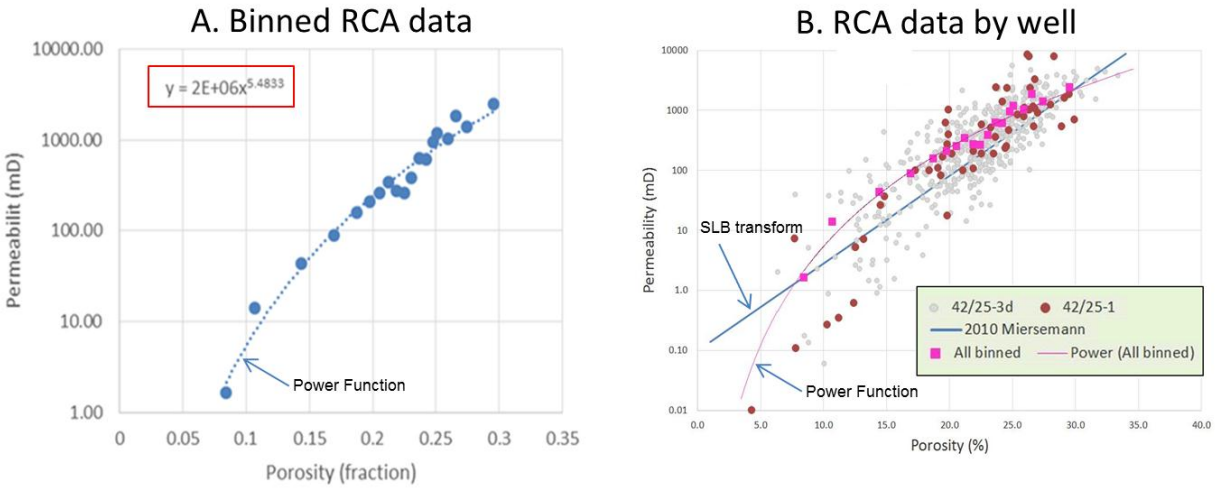

The linear function shown in Figure 5.31B is the Schlumberger linear function used for the November 2013 and January 2014 Model updates and this is based on regional well data excluding 42/25d-3. The July 2014 model update used two linear transforms of the binned RCA permeability data; one for heterolithic rock and one for non-heterolithic rock (Figure 5.32).

Figure 5.32: RCA Porosity vs Permeability Plot Coloured by Electrofacies

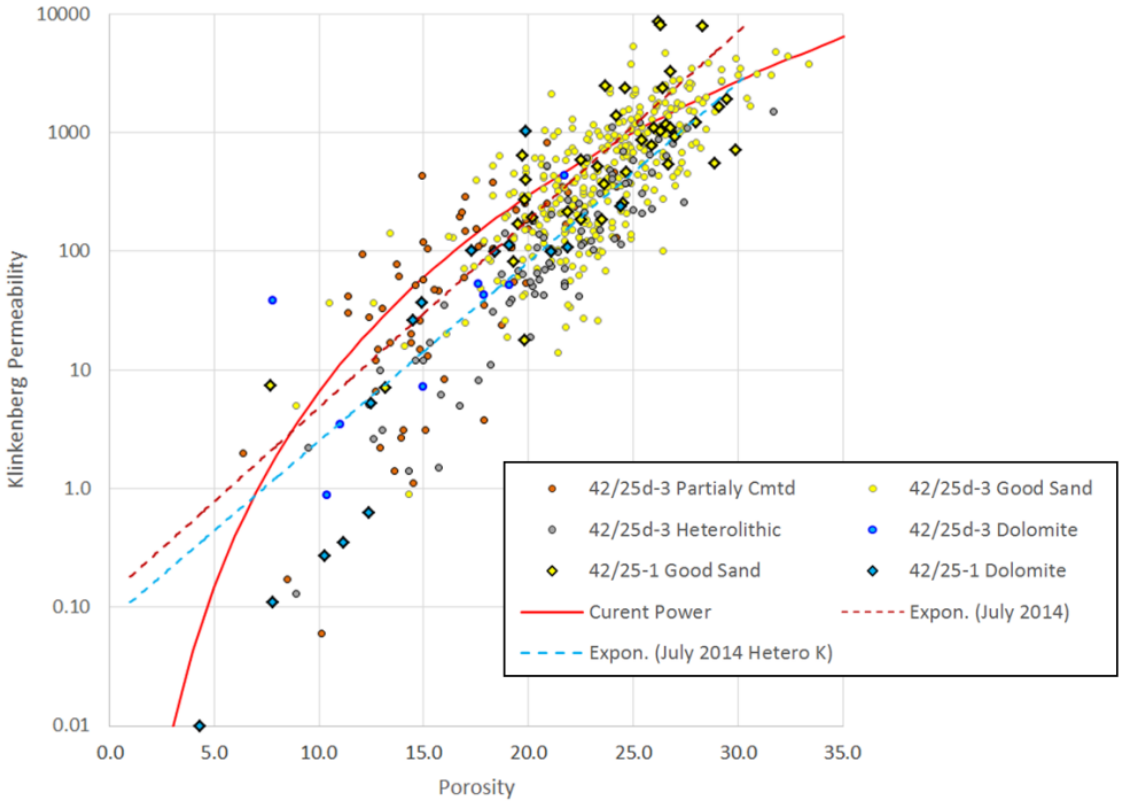

5.10.3 Net:Gross

The NTG cut-off is uncertain in CO_2 storage given the short period of injection compared to hydrocarbon charge. This uncertainty was captured using a range of porosity cut-offs, following established standards in oil and gas exploration using the poro-perm power function shown in Figure 5.32:

- 4.56% (0.1 mD) – equivalent to typical light natural gas threshold;
- 7% (1 mD) – equivalent to a typical light oil threshold; and
- 12% (17.9 mD) – defined as being a threshold above which the reservoir volumes are insensitive.

5.11 Volumetrics

The NPV from the seven models and three porosity cut-offs cases are illustrated in Table 5.5. The NPV ranges from 3.6 x10^9 m^3 to 5.1 x10^9 m^3 with an average of 4.6 x10^9 m^3. The DVHM is regarded as the most likely case model with a mid-case porosity cut-off at (7%) NPV of 4.6 x10^9 m^3. The uncertainty workflows calculated the spill point for each of the 500 maps generated. The current model spill is -1460m whilst the range coming out of the workflow is -1416 m to -1553 m.

The DVHM is regarded as a most likely case because it distributes predominantly uncemented rock throughout the model within the Phase Reversal Polygon (PRP). This is consistent with the four

wells inside the PRP (42/25d-3, 42/25-1, 43/21-1 and 43/37-3) in that their Bunter intervals are largely uncemented. The DVHM is preferred as a base case to the VHM since it appears more geologically reasonable, albeit that it is not based on a precise diagenetic model.

Table 5.5: Deterministic Model Volumetrics and Average Properties

Model	Cut-off (%)	GRV x10^9 m^3	NRV x10^9 m^3	NRV x10^9 m^3	NTG	Por
DVHM_up	4.7	24.6	24.4	5.097	0.993	0.209
DVHM_up	7.0	24.6	24.2	5.087	0.987	0.210
DVHM_up	12.0	24.6	23.4	4.999	0.951	0.214
VHM	4.7	24.6	24,2	4.629	0.987	0.191
VHM	7.0	24.6	23.7	4.596	0.964	0.194
VHM	12.0	24.6	21.2	4.347	0.863	0.205
DVHM	4.7	24.6	24.2	4.654	0.986	0.192
DVHM*	7.0	24.6	23.7	4.621	0.964	0.195
DVHM	12.0	24.6	21.3	4.384	0.866	0.206
ETHM	4.7	24.6	24.1	4.583	0.981	0.190
ETHM	7.0	24.6	23.2	4.517	0.947	0.194
ETHM	12.0	24.6	20.7	4.267	0.842	0.206
PHM1	4.7	24.6	24.0	4.380	0.976	0.183
PHM1	7.0	24.6	23.1	4.326	0.940	0.187
PHM1	12.0	24.6	19.9	4.011	0.810	0.202
PHM2	4.7	24.6	23.7	4.098	0.964	0.173
PHM2	7.0	24.6	22.5	4.026	0.915	0.179
PHM2	12.0	24.6	18.5	3.636	0.752	0.197
Min			18.5	3.636	0.752	0.173
Max			24.4	5.097	0.993	0.214
Average			22.8	4.459	0.927	0.196

* Most likely case

Given that the area within the PRP is very large and only penetrated by four wells, most of the modelling has focused on downside scenarios where poorer quality cemented sands could be present away from the wells. The fact that three downside models (PHM1, PHM2 and ETHM) have been created does not reflect an increased probability. These models were simply created to investigate possible scenarios. The PHM2 model that yields a NPV of 3.6 x10^9 m^3 with a low case porosity cut-off (12%) is regarded as an extreme low case.

The DVHM_upside model is regarded as an extreme upside case given that the facies proportions for this model have been forced to have extremely high values within the PRP. This yields an NPV of 5.1 x10^9 m^3 with the high case porosity cut-off of 4.65%.

Table 5.6 shows a NPV comparison with other recent models that use a common porosity cut-off of 12%. It is clear that GRV is a significant volumetric uncertainty as the contrast between the high case map scenario (Nov 13, 5.59 x10^9 m^3) and the other low case map, post-42/25d-3, scenarios

(4.38-4.83 x10^9 m^3) is large. Clearly, the range of volumes would be larger if different structural scenarios were to be used.

Table 5.6: Comparative Volumetrics of Recent Models

Model Update	Model Input Summary	Structural Closure (m)	NPV x10^9 m^3
Nov 13	Pre 42/25d-3, low case map	-1455	4.32
Nov 13	Post 42/25d-3, high case map, preliminary porosity	-1520	5.59
Jan 14	Post 42/25d-3, low case map, preliminary porosity	-1460	4.76
Jul 14	Post 42/25d-3, low case map, RCA porosity	-1460	4.83
Aug 14	Post 42/25d-3, low case map, RCA porosity, revised zones and facies	-1460	4.38

The reduction in volume between the July 2014 update model and the current model (4.38 vs 4.83 x10^9 m^3) is related to the new Chemostrat zonation that distributes less good quality L3 rock in the west of the structure. The gross L3 isochore thins toward the west whereas previously it maintained a uniform thickness. Additionally, the July model had over-optimistic facies proportions that preferentially distributed more good quality reservoir sands whilst the current models are more closely tied to the well facies proportions with the exception of the DVHM_upside model.

5.12 Conclusions (Static Model)

The static modelling incorporates the results from analytical studies and from the appraisal programme of 42/25d-3 well. Specifically, it includes the final well logs, petrophysical analysis, chemostratigraphic analysis, conventional core analysis, core sedimentology and petrography. A number of interim model updates were made as analytical results from the 42/25d-3 became available. The current modelling work documented in this report has now superseded these models. The current models form the input for subsequent phases of the project including the FEED.

Diagenetic cementation is the key factor that controls reservoir quality in the Bunter Sandstone in the Endurance area. Six facies models have been created to investigate the impact of varying cemented facies types on reservoir quality. The models have been created purely to match the phase reversal observed on seismic at the Top Bunter horizon and the sparse well control within it. They have been constructed independently of any diagenetic model.

Five of the models are regarded as being broadly consistent with Thermohaline Circulation Model (TCM), which predicts better quality sand in the Upper Bunter. The ETHM does not fit the TCM in that it distributes disproportionately higher volumes of cemented rock to the east and good quality sands in the west. The TCM suggest that the upper part of the Bunter should be free of cementation due to the dissolution of cements by convection currents caused by heating from the underlying Permian salt pillow. Despite the misfit, it is recommended that the ETHM should be retained; recognising the fact that the TCM model is not conclusive and the process of cementation could be more complex. It should also be noted that any significant amounts of cementation, if present within

the upper part of the reservoir, should be visible on the seismic data, for example the cemented layer which has been mapped from the seismic and which is already used in the model.

The six facies models have been combined with three NTG cut-off scenarios to create eighteen deterministic models that have an NPV range of 3.636 $x10^9$ m^3 to 5.097 $x10^9$ m^3.

The most likely deterministic case is interpreted to be the DVHM, 7% porosity cut-off NTG scenario, with a NPV of 4.6121 $x10^9$ m^3. The NPV range has been expanded to take account of structural uncertainty. Average properties from the deterministic range have been used to create distributions of NTG and porosity which have themselves been combined with the previously established GRV distribution to estimate the NPV range at Endurance. This range yields P90, P50 and P10 values of 4.182, 4.793 and 5.398 $x10^9$ m^3 respectively. Top Bunter reservoir structure, facies model, and average porosity have the greatest impact on the NPV range. NTG and gross Bunter isochore thickness are less significant. The NPV range reported here should form the basis for estimation of Endurance storage capacity.

It is not recommended that all eighteen deterministic models should be simulated; rather simulation should concentrate on the most likely and extreme model cases. It is entirely possible that the Bunter reservoir is such good quality relative to the properties of super critical CO_2 that the extreme models have little significant impact on CO_2 plume development.

Once injection operations have commenced it is recommended that simulation studies be undertaken to investigate the likely NTG cut-off for injected CO_2. It is believed that NTG cut-off is a dynamic parameter for CO_2 storage given the relatively short period of injection as compared to time involved in hydrocarbon migration and storage.

When detailed well planning is undertaken it is recommended that both the low and high case Top Bunter reservoir structure maps, that provided input to the structural uncertainty work, be taken into consideration. The current P5 platform location is well constrained by surrounding well control. If, however, the development plan were to be extended beyond the current first phase development, particularly in the east of Endurance, mitigation planning against structural uncertainty may be important.

6 Reservoir Compartmentalisation

6.1 Endurance Fault Interpretation using Seismic Data

Compartmentalisation is the partitioning of reservoir into multiple pressure units that are sealed within impermeable or semi-permeable geological boundaries. The sealing boundaries are broadly categorised as static or dynamic based on the degree of sealing provided. Whilst static boundaries, such as faults and shale layers, provide pressure segregation over geological time scales, dynamic boundaries, such as permeability heterogeneities at stratigraphic interfaces, function more as flow barriers that allow pressure equilibration across the boundary over time.

Faulting within a reservoir interval is widely regarded as the most dominant cause of reservoir compartmentalisation. A review of mechanisms that control reservoir compartmentalisation in the gas fields of the Permian Rotliegend Group concluded that faulting accounted for approximately 75% of the compartment boundaries (see Reference 12 in Section 9). Any indication of faulting within Endurance would therefore provide a serious cause for concern about possible compartmentalisation. On the other hand, the absence of faults would greatly diminish the probability of finding isolated pressure compartments within 5/2. The fault interpretation study performed on the Endurance structure using 2D and 3D seismic data suggests that the presence of faults within the Endurance reservoir is highly unlikely.
The deepest fault picks on the high resolution Polarcus 3D seismic data were shown to be above the Röt Halite reflector, whilst fault interpretation on the lower quality Ocean Bottom Cable (OBC) 3D seismic data showed the faults extending deeper into the RötHalite and terminating above the Top Bunter seismic horizon, see Figure 6.1.

Figure 6.1: Comparison of Endurance Fault Interpretation Using Polarcus and OBC 3D Seismic Data Sets: (a) Polarcus and (b) OBC 3D Seismic Data Sets

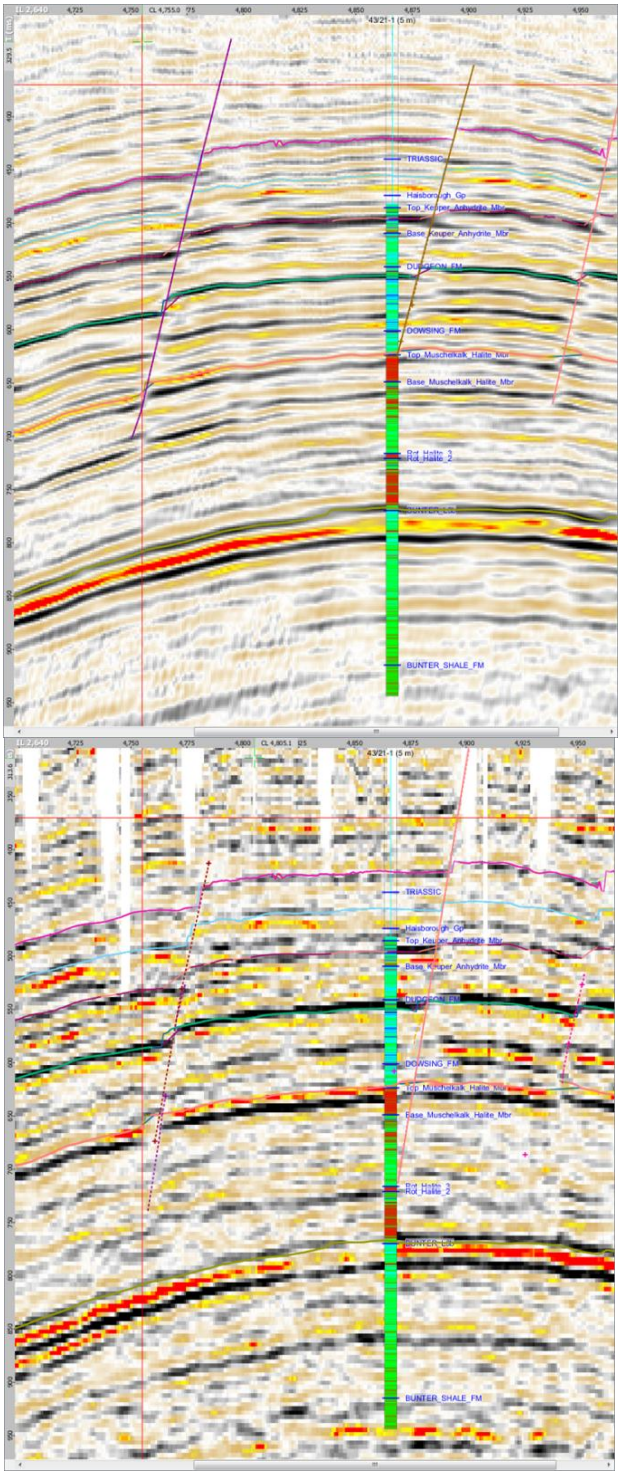

The deepest fault interpreted with the better quality Polarcus data “soled out” above the Röt Halite whilst interpretation of the same fault using the lower quality OBC data shows it “soling out” within the Röt Halite. The important point is that no faults were interpreted to penetrate the Bunter Sandstone).

The following sections review all the available Endurance characterisation data that could enable an assessment of whether or not pressure compartments exist within the Endurance structure.

6.2 Endurance Reservoir Quality from Sedimentological Analysis

The sedimentological and depositional setting of Endurance has already been described in Section 5.2. Apart from an overall slight reduction in reservoir quality downwards through the sequence, which results primarily from a reduction in grain size and an increase in the proportion of impermeable mudstone beds, sedimentological logging in the appraisal well suggests that the Bunter Sandstone reservoir is remarkably uniform at large scales. The formation as a whole can be approximated to a single “tank”, with occasional laterally impersistent barriers to vertical permeability associated with thin mudstone horizons, and more widespread baffles associated either with cemented horizons and concentrations of mudstones, such as within playa margin facies.

Figure 6.2 gives a stylised depiction of the probable geometry of the Bunter Sandstone reservoir at a relatively large-scale. It is clear from the figure that there are no significant barriers to neither horizontal nor vertical flow that could result in pressure compartmentalisation. The only impermeable barriers to vertical flow are mudstone beds, although they are considered unlikely to extend laterally for more than around 100m and in some cases not wholly impermeable. Thin beds rich in mudstone rip-up clasts are common within the succession, although these usually lie within permeable sands and would act only as baffles to vertical flow rather than impermeable barriers.

In the appraisal well 42/25d-3, a calcareous ooid-rich horizon lies close to the top of the Bunter Sandstone and it is probably laterally extensive, see Figure 6.2, since it appears to occur also in the crestal 42/25-1 well which is approximately 5km away. This may comprise the most extensive lower-permeability horizon within the Endurance reservoir. It is interpreted as a depositional horizon, but whether a sheetflood or channelised sand, it is unlikely to be uniform in thickness throughout. Although displaying a relatively low permeability, the sample from 4670.0 ft which contains over 65% carbonate still retains a permeability of 44 mD and so will therefore form a significant baffle, but not a barrier, to vertical flow.

Figure 6.2: Illustrative Cross Section Through Part of The Bunter Sandstone in The 42/25d-3 Area, Depicting Possible Geometry of Permeability Barriers and Baffles

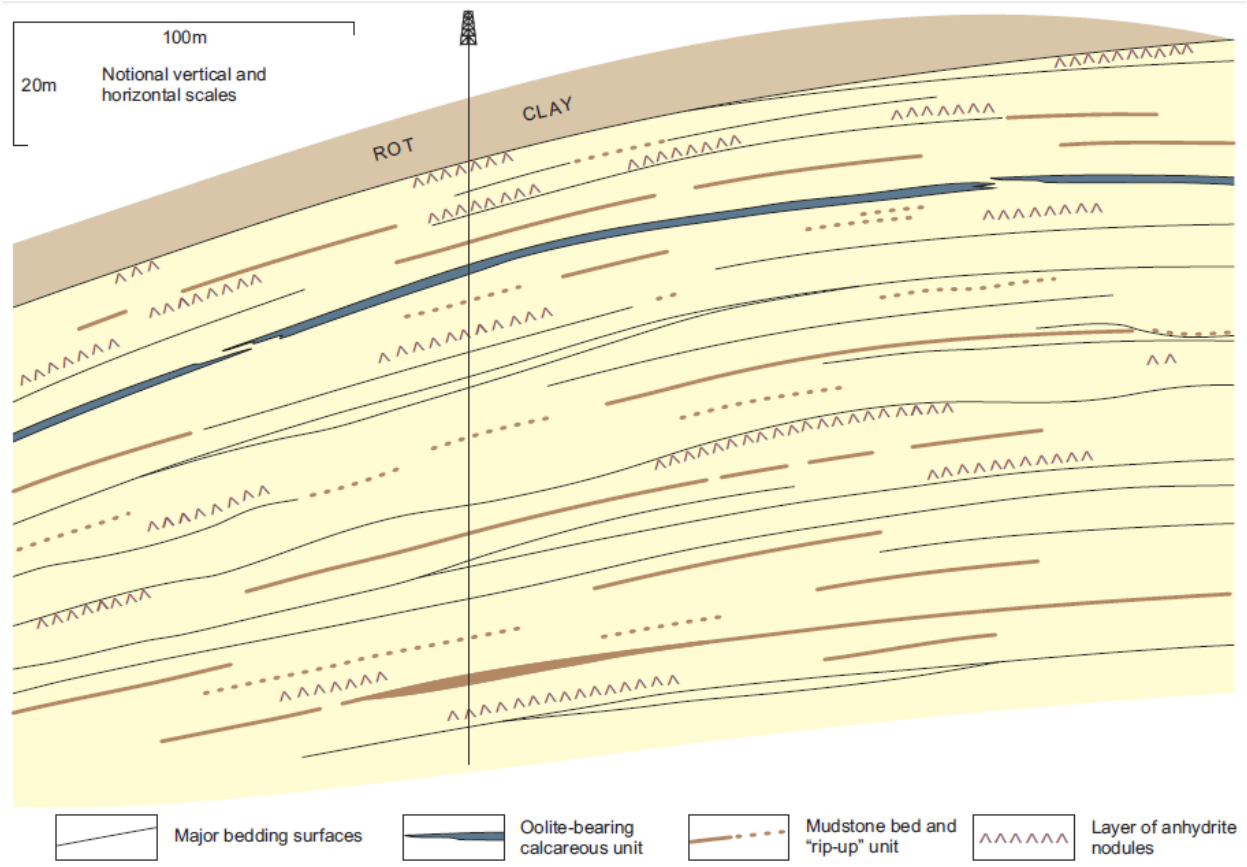

6.3 Well Test Interpretation

As part of the data gathering programme in the 42/25d-3 appraisal well, a well test was completed over the interval 1396.3 m to 1414.3 m True Vertical Depth Sub-Sea (TVDSS). However, the test was designed as a limited entry test over a perforated interval that covered a small fraction of the Bunter Sandstone and therefore offered no clear evidence of laterally extensive barriers to flow across the full Bunter Sandstone interval within the Endurance structure. The volume investigated by the test extended to a radius of only 1.2km and there was no evidence of boundaries within this radius.

6.4 Formation Water Analysis Studies

A comprehensive water chemistry analysis was performed on samples collected from the 42/25d-3 appraisal well during the MDT (Modular Formation Dynamic Testing tool) run and from the Drill Stem Test (DST). The overall sampling spanned a total depth interval of approximately 163 m (1412.4 m to 1575.0m TVDSS), making it possible to identify changes in water composition with depth and assess potential for reservoir compartmentalisation.

The results show no evidence to suggest that the five samples from different depth intervals that were subjected to analysis originated from isolated fluid compartments within the reservoir. There was an overall close similarity of chloride to bromide concentration ratios (Cl:Br) between the samples which strongly suggest that all samples are derived from a single natural source; this is generally a good indicator of contamination, but could also be used to distinguished waters from different sources. Further, most of the isotopic data exhibited very good agreement between samples, although some significant variation in the carbon thirteen (^{13}C) data was observed; however, the concentrations of inorganic carbon were low in all samples so these variations may not be particularly relevant.

In summary, no compositional, physicochemical, microbiological or radiological trends with sample depth were identified. All samples were found to be highly saline (TDS ~300,000 ± 10,000mg/L) sodium chloride dominated brines with significant concentrations of common rock constituents, calcium, magnesium and sulphate.

6.5 Information from Analogous Reservoirs

The best reservoir analogues to the Endurance storage site are gas fields developed within the Bunter Sandstone Formation (BSF) in the southern North Sea. Production performance of these fields have been analysed in the context of their geological characteristics to enable a better understanding of the future dynamic performance of Endurance and the underlying Greater Bunter aquifer.

A review of the depletion characteristics of the Caister gas field, to the east of Endurance, and the Esmond Complex (comprising Esmond, Forbes, and Gordon gas fields), to the north, indicates that primary depositional and diagenetic characteristics provide the main control on production performance. Pressure and geological data from Caister suggests that internal barriers to vertical flow (siltstones and cemented sands) confine pressure communication to individual layers within the gas accumulation. This is to be contrasted with the more homogeneous Esmond reservoir which records a uniform pressure distribution. Comparison of the gross gamma ray log character in the appraisal well 43/21-1 on the crest of Endurance with those in wells at Caister and Esmond field suggests a greater similarity in reservoir properties between Endurance and Esmond (which in turn suggests similar dynamic performance) than with Caister.

Review of Esmond production performance suggests a good hydraulic connection to a Greater Bunter aquifer that extends over an area approximately 20,000km^2 and which is bounded by the Dowsing Fault Zone to the east and the thinning to the east across of the Base Cretaceous Unconformity on the Cleaver Bank High in the Dutch sector of the southern North Sea (Figure 6.3). There is a strong reason to suggest that the Endurance reservoir is also connected to this regional aquifer. Comparison of bottom hole pressure measurements in the 42/25-1 exploration well drilled in 1990 whilst Esmond was still in production and the 42/25d-3 CO_2 appraisal well drilled in 2013 shows that pressure in Endurance fell by 0.7bar in 23 years, probably as a result of gas offtake from the Esmond field about 50km north-east of Endurance and the subsequent expansion of the aquifer to replace this void space. The assumption implicit in this analysis is that both wells, about 5km apart, occupy the same pressure compartments within the Endurance structure.

Figure 6.3: Approximate Areal Extent of the Greater Bunter Aquifer that is Hydraulically Connected to Endurance, Esmond and other Surrounding Gas Fields

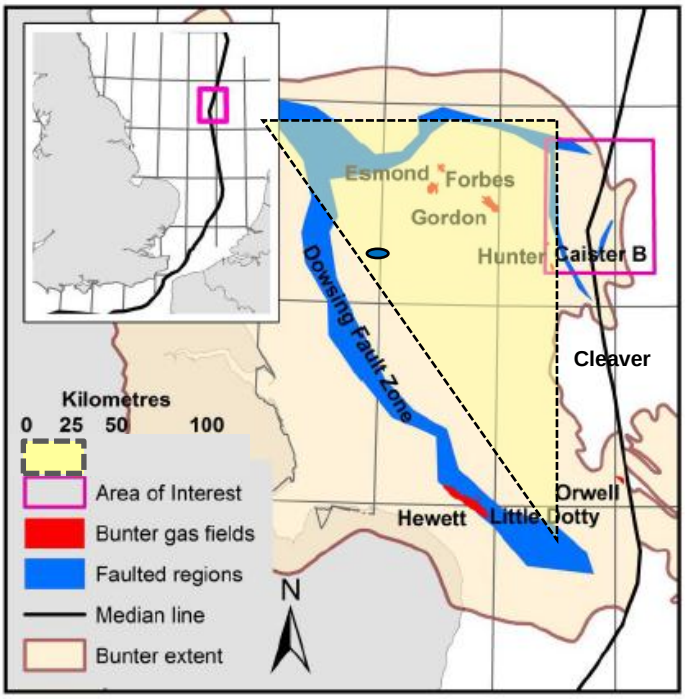

6.6 Summary and Conclusion (Information from Analogous Reservoirs)

To summarise the conclusions of this chapter, a review of multiple strands of evidence, analogue and Endurance specific data, has revealed no evidence of compartmentalisation or the presence of lateral or vertical persistent barriers to flow likely to cause either static or dynamic pressure compartmentalisation during White Rose CO_2 injection. All available evidence suggests that Endurance is a single homogeneous hydraulic system with a moderate reservoir property variation with depth that is fully accounted for by authigenic digenetic processes.

7 Pore Pressure Prediction

This Chapter presents the methodology for predicting pore pressure within the Endurance structure.

7.1 Endurance Pore Pressure

Knowledge of formation pressure is used to anticipate potential bore hole stability problems and to design suitable mitigation measures. For formations that have not been penetrated by wells, a number of methods have been developed for inferring pore pressures. These usually fall into two broad approaches:

1. direct methods: the use of crossplots (see Reference 4 in Section 9) or overlays (see Reference 5 in Section 9) to estimate pore pressure deviation from a designated normal pressure trend liner; or
2. Effective Stress methods: based on the interpretation of stress change effects for example compaction and changes in elastic wave velocities, as only a function of the vertical effective stress (σ) according to the relation:

$$\sigma = S - P$$

Where:

σ is the vertical effective stress
S is the total vertical stress
P is the pore pressure (see References 6 and 7 in Section 9).

The Endurance structure has been penetrated by three wells, two of which have had direct pore pressure measurements taken. All available information from Endurance suggest that it is highly unlikely that the Bunter Sandstone is compartmentalised. Standard pore pressure prediction techniques are not required for the Endurance structure, instead, the combined plot of the RFT pressure data from well 42/25-1 and the long duration MDT pressure data from well 42/25d-3 in Figure 7.1 below shows that the pressure gradient within Endurance is well behaved and can be approximated as 0.1147bar/m across the Bunter Sandstone reservoir.

From Figure 7.1 the functional form of the most recent pore pressure measurement; the MDT pressure data can be stated as:

$$P = 0.1147Z - 8.7057$$

where:

P is the pore pressure [bar] at a given depth Z [m TVDSS].

Therefore, the pore pressure at 1405.3 m TVDSS (the midpoint of perforations for the well test performed in the 42/25d-3 appraisal well) is calculated as 152 ±0.5bar. This is in agreement with the calculated final pressure at the end of the well test build-up period of 151.8bar at the same depth.

A comparison of the MDT and well test pressure data is shown in Figure 7.2.

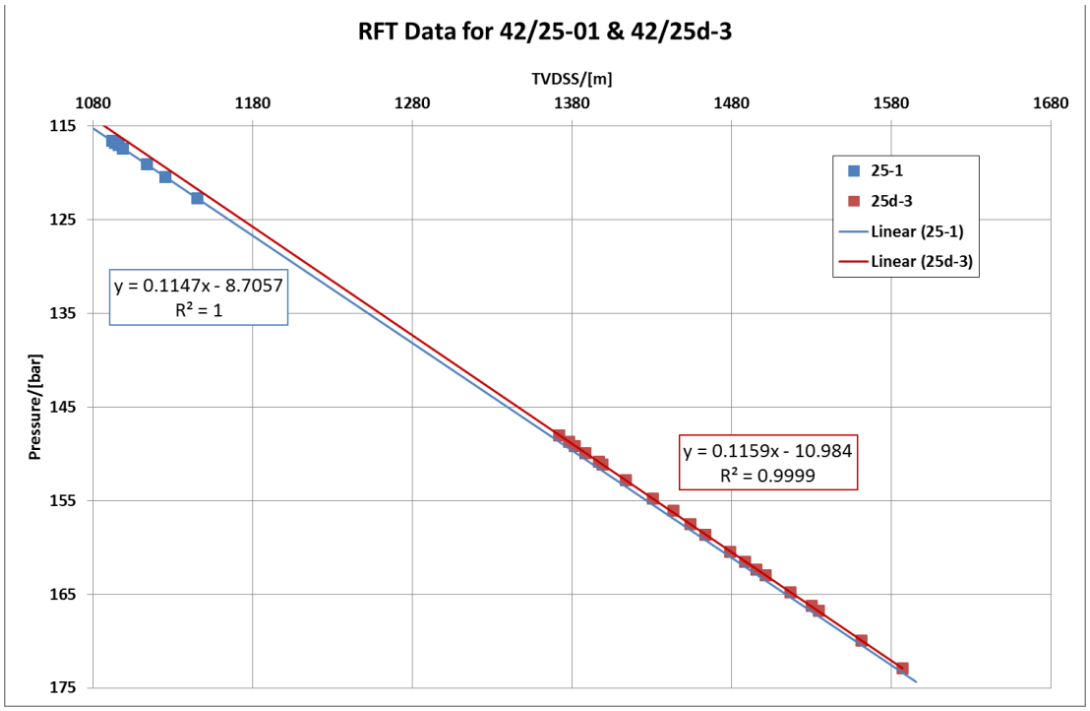

Figure 7.2: Comparison of Well Test and MDT Pressure Data

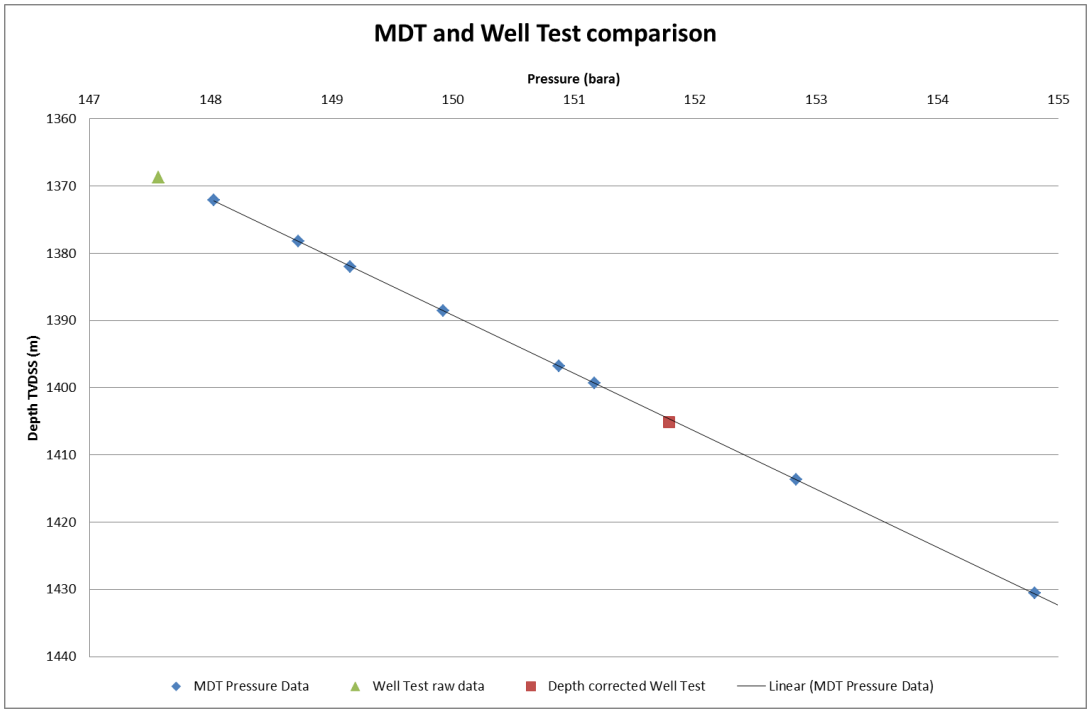

8 Dynamic Modelling

Analytical and full field simulation models were used as well as regional information to assess the capacity, injectivity, hydrodynamics and containment of the Endurance structural closure for the safe and permanent storage of White Rose CO_2

CO_2 enters the formation through perforations in the pipe as a horizontal flow. The density of CO_2 in the brine field in the aquifer at reservoir conditions; will be considerably less than the native brine, so buoyancy will force the CO_2 to migrate upward until it reaches the cap rock.

Once at the cap rock, the CO_2 will flow along the top of the Bunter Sandstone formation until it reaches the crest of the brine in the aquifer where it will start to form a secondary gas cap.

There are many important aspects associated with the injection of CO_2 into a saline aquifer, not least of which is the effect on reservoir pressure. If pressure is not managed correctly, there will be a risk of fracture of the reservoir and cap rock that would compromise the integrity of the store.

Other important aspects are the different types of trapping mechanism which can occur:

- Structural and Stratigraphic, which is largely a function of the geology of the reservoir and its cap rock;
- Residual, a function of relative permeability;
- Solubility, which depends on the CO_2/brine phase behaviour; and
- Mineral trapping.

The first three mechanisms listed above will be considered in this section. The fourth, mineral trapping is largely down to geochemical reactions which are thought to take place over the timescale of hundreds to thousands of years and have not been considered in this study.

8.1 Appraisal of Endurance Structure with Well 42/25D-3

To obtain a storage permit application from the UK regulator, DECC, National Grid Carbon will have to satisfy the relevant legislation to meet the requirements of Directive 2009/31/EC of the European Parliament and of the Council of 23 April 2009 on the geological storage of carbon dioxide and amending Council Directive 85/337/EEC, European Parliament and Council Directives 2000/60/EC, 2001/80/EC, 2004/35/EC, 2006/12/EC, 2008/1/EC and Regulation (EC) No 1013/2006.

A key statement within the guidance is: *The goal of the characterisation of the storage site and complex is to assess the site's capacity, injectivity, hydrodynamics, containment and ability to be monitored in order to ensure safe and permanent storage of* CO_2.

This statement drove the objectives of the appraisal of well 42/25d-3; the data gathering programme is summarised in Figure 8.1 following.

Figure 8.1: Bunter Sandstone Formation Stratigraphy and 42/25d-3 Appraisal Well Data Gathering Programme

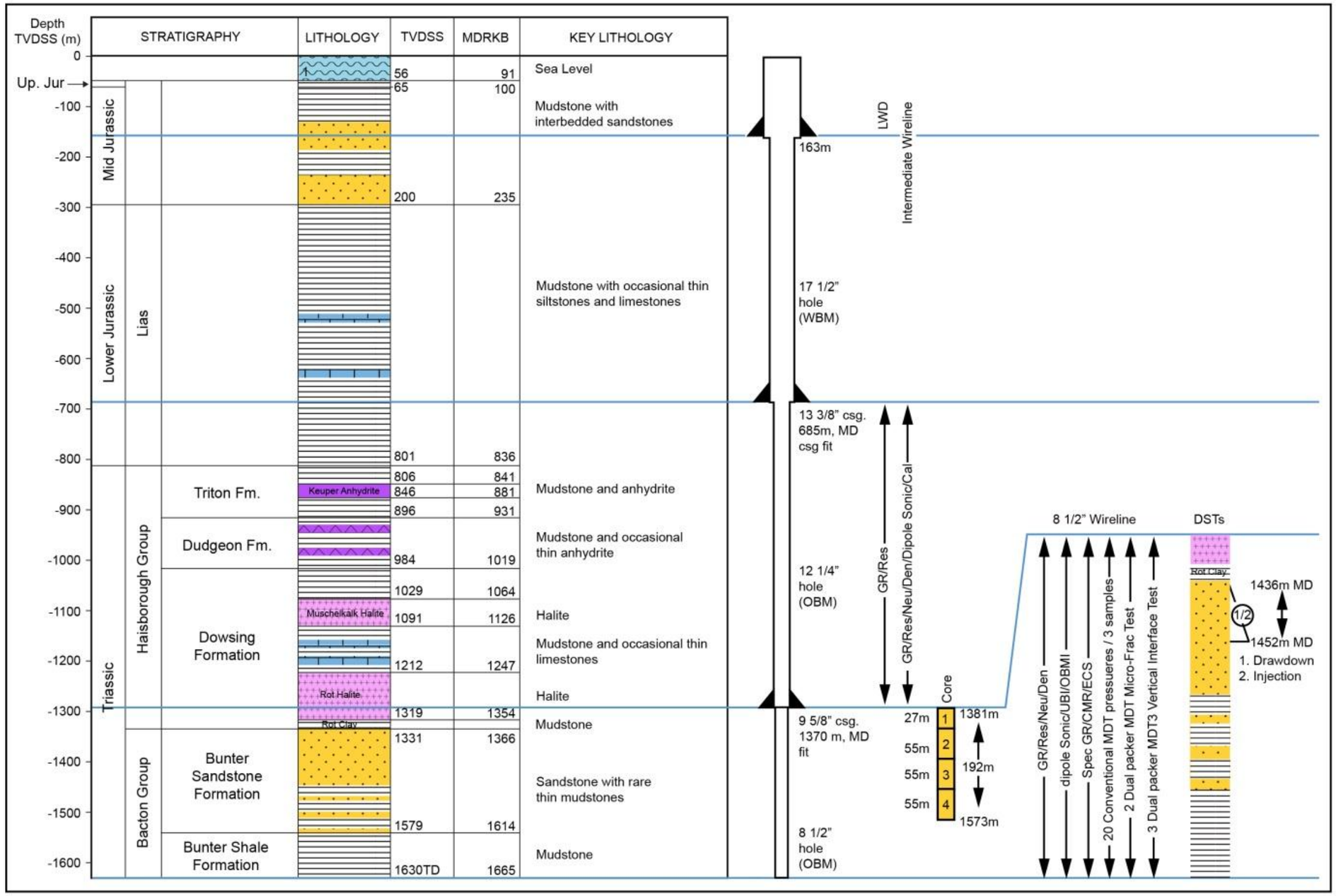

The following list some of the data gathered and how they address the objectives:

- Capacity: the static capacity of the reservoir, as measured by the pore volume, helps define the Net To Gross (NTG) ratio and porosity measurements from the gamma ray and neutron logs;
- Injectivity: a multi-rate injection test was undertaken following on from the production flow test to prove injectivity. Filtered sea-water was used as the injectant as a substitute for dense phase supercritical $CO_{2;}$
- Hydrodynamics: the key parameters affecting hydrodynamics are the absolute and relative permeability of the CO_2 and brine. The relationship between absolute permeability and porosity was refined through logs and core measurements whilst relative permeability was measured for the first time by special core analysis of some of the core samples;
- Containment: a number of activities have proved containment:
  - the parallel geomechanical modelling study completed in February 2015;
  - specialist logs for data gathering; and
  - testing of the cap rock and reservoir core sample for data gathering; and
- Monitoring: a four dimensional (4D) seismic tools was employed to monitor plume development. The data from some of the specialist logs, such as dipole sonic, produced images of the reservoir as it is filled.

The key components of well 42/25d-3 appraisal programme are summarised in the following sections.

8.1.1 Core Analysis

Four cores were recovered from well 42/25d-3 totalling a length of 192.51 m (631.6 ft), see Figure 8.2.

Core 1 (84.6 ft.; 25.79 m) recovered the lower part of the Röt Halite and the whole of the Röt Clay unit including the first few feet of the top Bunter Sandstone, whilst Cores 2, 3, and 4 recovered 166.73 m (547 ft) of the Bunter Sandstone section. All cores were delivered to Weatherford Laboratories (UK) Limited in July, 2013 for core analysis. The core analysis was divided into two parts:

- the conventional (or routine) core analysis; and
- the Special Core Analysis (SCAL).

The RCA involved photographing, CT scanning, spectrographic gamma ray, as well as core plug permeabilty, probe permeametry measurements, porosity, grain density and particle size analysis in addition to plug selection for further SCAL work. A cleaning study to determine the effect cleaning agents had on the halite within the core plugs and Mercury Injection Capillary Pressure tests were also completed.

The SCAL study was preceded by an Interfacial Tension study to determine how synthetic formation water would react with CO_2 at reservoir conditions, as well as a study to determine the effect of critical flow velocity. Subsequently the SCAL study identified irreducible water saturation and relative permeability curve parameters for use in dynamic modelling based on capillary pressure and 1-D core performance modelling results.

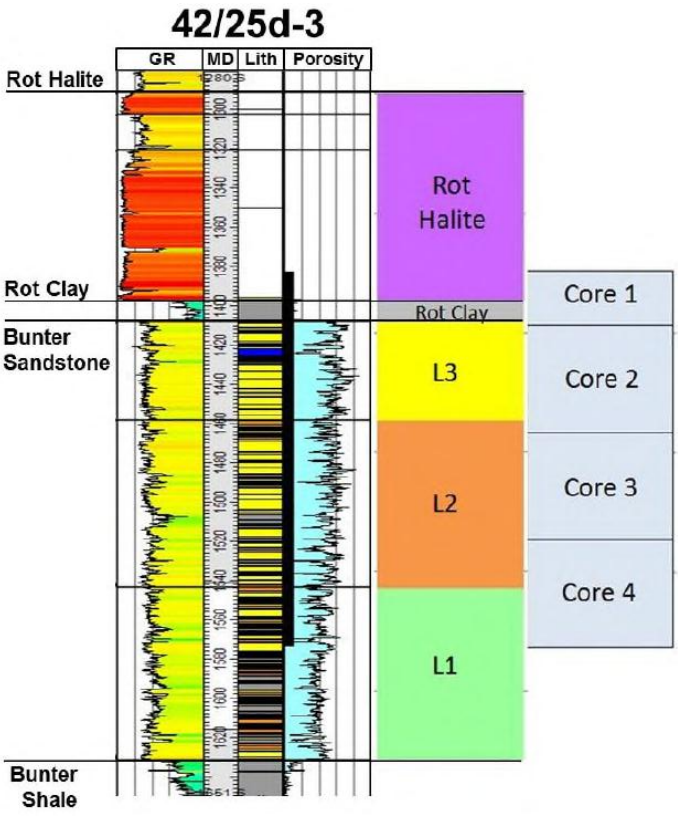

Figure 8.2: 42/25d-3 Well Schematic Showing Cored Interval

8.1.1.1 Conventional Core Analysis

The main objective of the RCA was to determine basic rock properties of the cores recovered from appraisal well 42/25d-3 and to prepare plug samples for use in more specialised core analyses. The basic rock properties measured during RCA include porosity, permeability, grain density and grain size distribution. The following sections give brief summaries of the RCA programme in broadly chronological order:

- Core Preparation;
- Permeability;
- Helium Porosity and Grain Density;
- Klinkenberg Permeability;
- Core Photography;
- Resination;
- Particle Size Analysis; then
- Unconventional RCA Studies.

Core Preparation

Core 1 was cored using 4" diameter half-moon sleeves and delivered to the laboratory cut into 3 ft lengths, immersed in plastic tubes containing a bland mineral oil, capped at each end. Following CT scanning, these were removed from the tubes and transferred to custom made stainless steel troughs, immersed under Isopar L oil. This prevented the core from dehydrating whilst allowing its surface to be viewed as required. Cores 2, 3 and 4 were approximately 3.5" in diameter and arrived at the laboratory in 30 ft aluminium inner sleeves, which were then cut into 3 ft lengths to enable the core sections to be handled. Other operations associated with core preparation were:

- Core Gamma Run;
- CT Scanning;
- Core Handling;
- Samples Preservation;
- Conventional Core Plug Sample Preparation;
- Plugs Preparation; and
- Plug Sample Analysis.

Permeability

Permeability was determined by use of a Weatherford Laboratories DGP-300B Steady State Nitrogen Permeameter at an effective confining pressure of 400 psig. These were used in conjunction with the callipered length and diameter to calculate permeability from Darcy's equation.

As an internal quality control, one in ten plugs was re-run during analysis of the samples, and prior to running the plugs. Check plugs of predetermined permeability covering a range from 0.18 mD to 6000mD were analysed, with each check plug corresponding to a mass flowmeter in the permeameter.

Helium Porosity and Grain Density

Porosity of the clean, dry unsleeved plug samples was determined by direct measurement of grain volume at ambient conditions and bulk volume determined by mercury displacement. The sleeved plugs underwent an additional direct pore volume measurement using a confining pressure of 400 psig.

Grain volume was determined using a Weatherford Laboratories DHP-100 Boyle's Law porosimeter. Bulk volume for the mounted plugs was calculated from the sum of the measured grain volume and direct pore volume. Grain density was calculated from the weight and measured grain volume, taking care that all sleeving materials volume and weight were subtracted. The porosity measurements were repeated to ± 0.02 psi.

Cross plots of horizontal permeability and vertical permeability vs. porosity are presented in Figure 8.3 and Figure 8.4.

Figure 8.3: 42/25d-3 Helium Porosity vs Horizontal Permeability

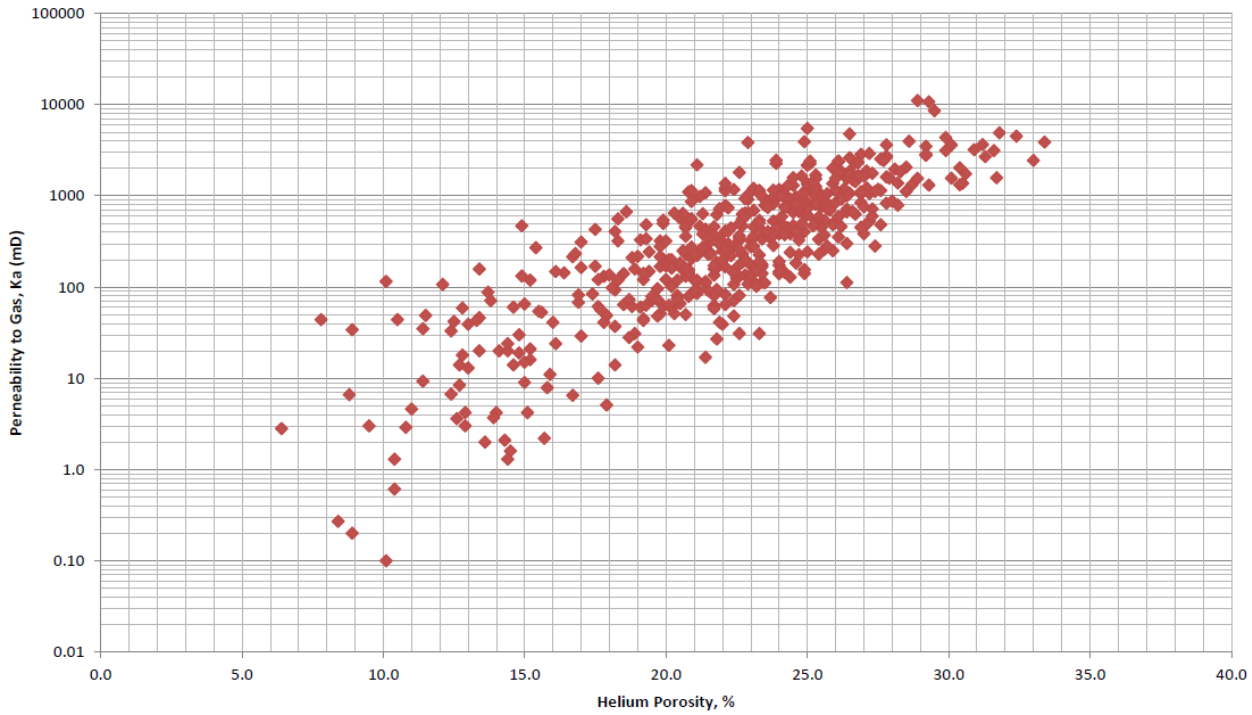

Figure 8.4: 42/25d-3 Helium Porosity vs Vertical Permeability

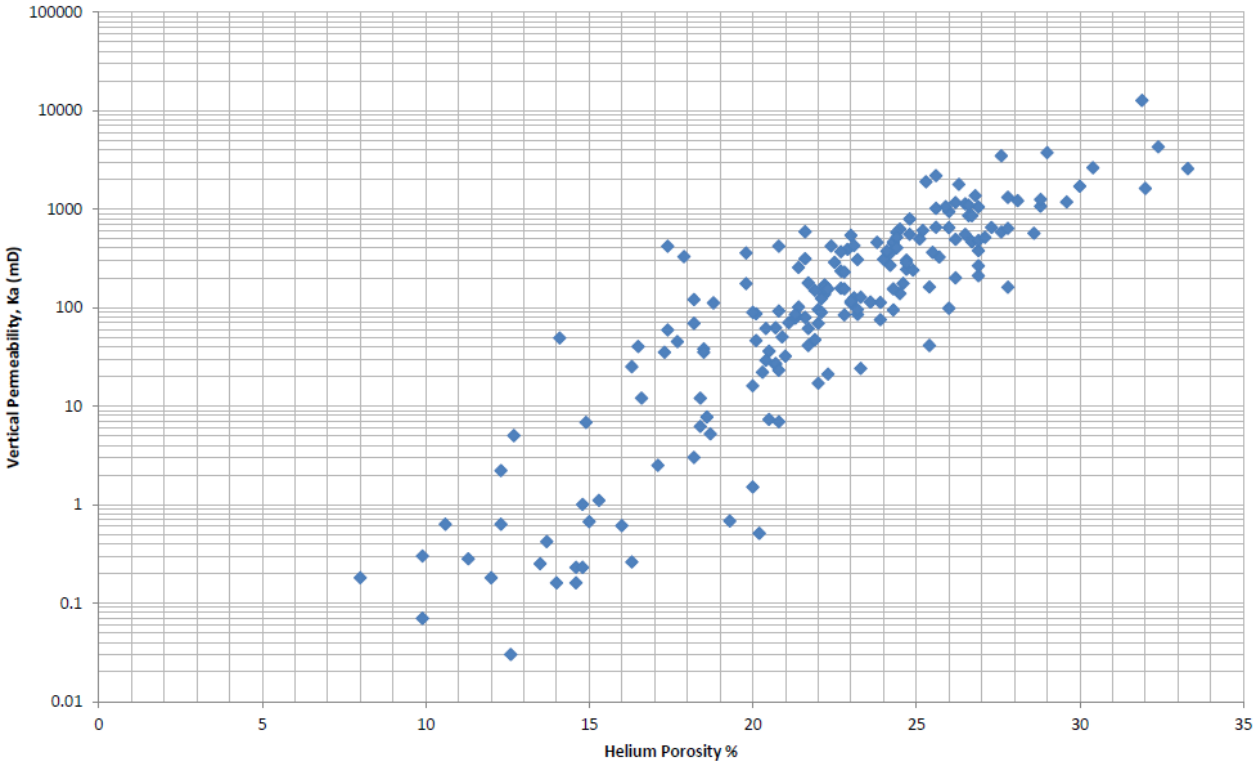

Fifteen plugs were re-measured independently for porosity after an assessment of the original preliminary data showed that the measured porosities for these samples fell outside the accepted error margins in comparison to the calculated length x area porosities. Re-measurement put back the new lengths, diameters and porosities into the accepted error margin. The initial deviations were attributed to plugs misshaped by chipped edges or sides, fractures or slight ridges along plug lengths.

Klinkenberg Permeability

Klinkenberg Permeability was determined by use of a Weatherford Laboratories DGP-300B Steady State Nitrogen Permeameter at two minimum sleeve pressures of 400 psig (28barg) and 2600 psig (179barg).

Measurements were repeated a minimum of four times on each sample at different mean pore pressures to enable the calculation of Klinkenberg permeability (K_L). Permeability to CO_2 was plotted versus 1/mean pore pressure and the best fit line extrapolated to infinite mean pore pressure to provide the K_L.

Example Klinkenberg permeability data is presented in Figure 8.5 and Figure 8.6 for sample 94 (4624.90 ft) at confining pressures of 28barg and 179barg respectively.

Figure 8.5: Klinkenberg Plot for Sample 94 (4624.90 ft) at a Confining Pressure of 28barg

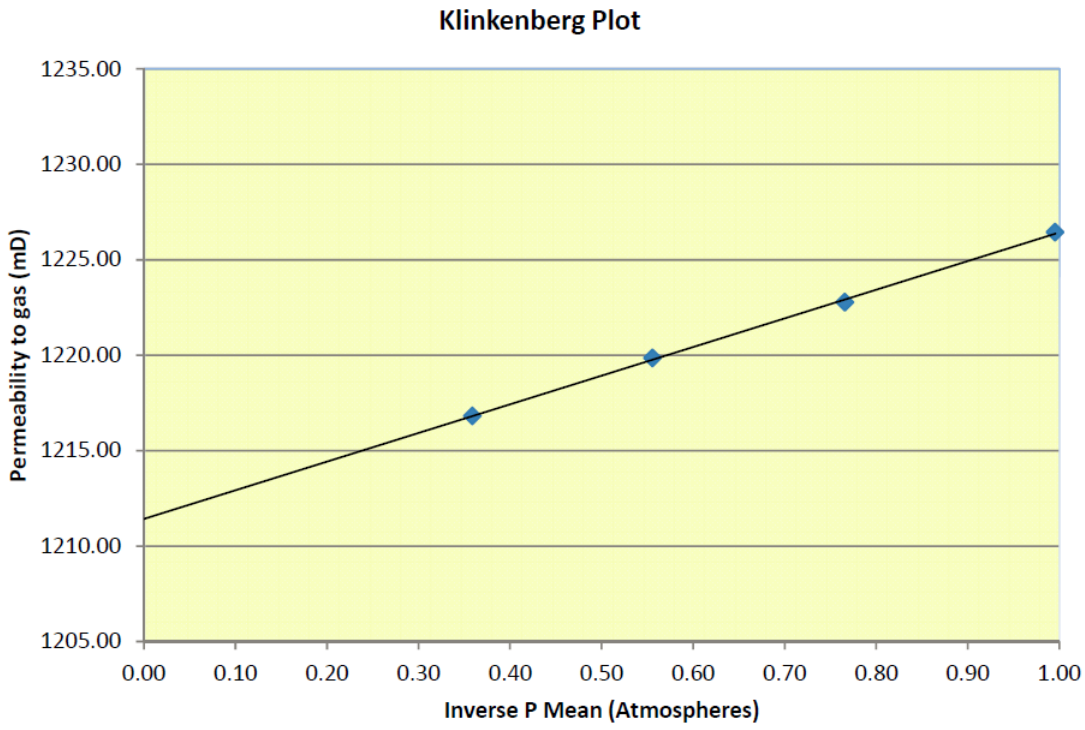

Figure 8.6: Klinkenberg Plot for Sample 94 (4624.90 ft) at a Confining Pressure of 179barg

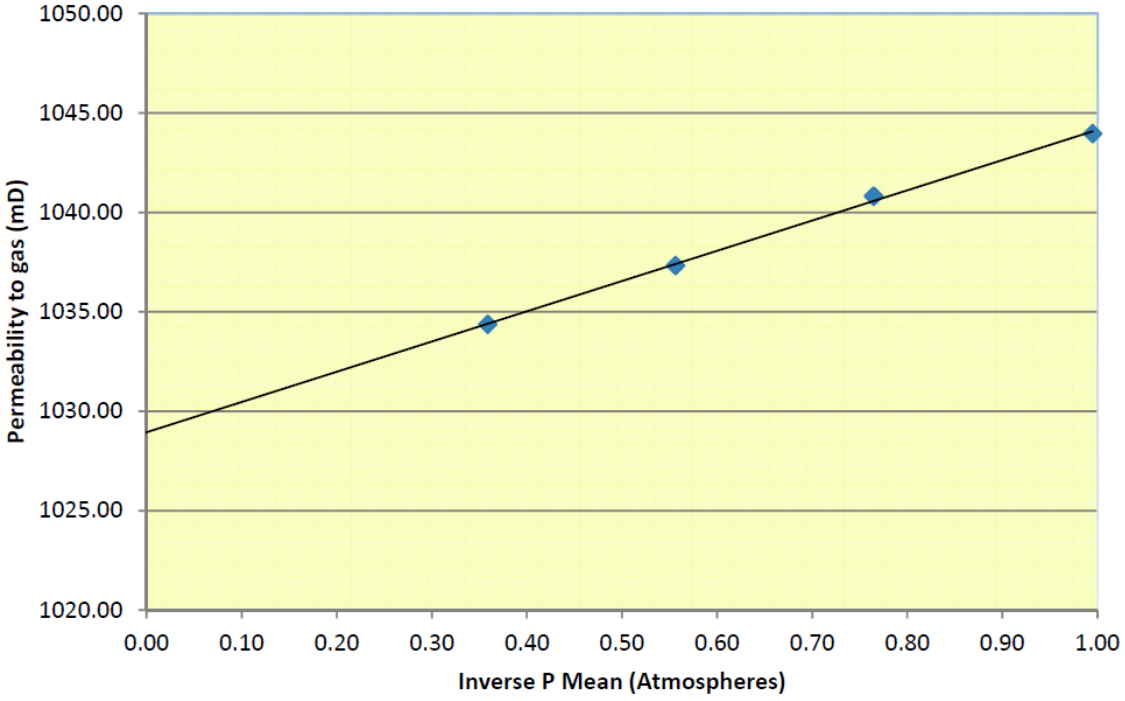

Slabbing

On completion of all sampling and plugging the core was slabbed 1/3 to 2/3 to expose maximum dip dry. The slabbed core was placed into plastic gutters to support it without movement.

Core Photography

Following slabbing, salt was leaching to the surface of the core, obscuring the sedimentological features. In order to improve this, each section was carefully sanded and smoothed prior to quickly taking the core photograph under white light.

Resination

Following core photography, a second slabbing cut was performed. A 2 cm thick “biscuit-slice” was taken along the entire cored interval from the photographed face of the 1/2 cut core section. The slice was placed into plastic presentation trays, labelled with well name, core number, box number, and all routine porosity and permeability data. Clear Epoxy resin was then used to seal the core into the trays for archive purposes.

Particle Size Analysis

Laser particle size analysis and sieve analysis were performed on 17 plug samples. Sieve Analysis is a procedure used to assess the particle size distribution of a granular material by weight whilst Laser Particle Size Analysis (LPSA) is used to assess the particle size distribution of a granular material by laser diffraction.

Sieve analysis is applicable for particles larger than coarse silt (45 microns) whilst LPSA is applicable for particles from 2mm to 0.02 microns.

Graphical LPSA and sieve analyses data is presented in Figure 8.7.

Figure 8.7: - Particle Size Distribution From Laser and Sieve Grain Size Analysis

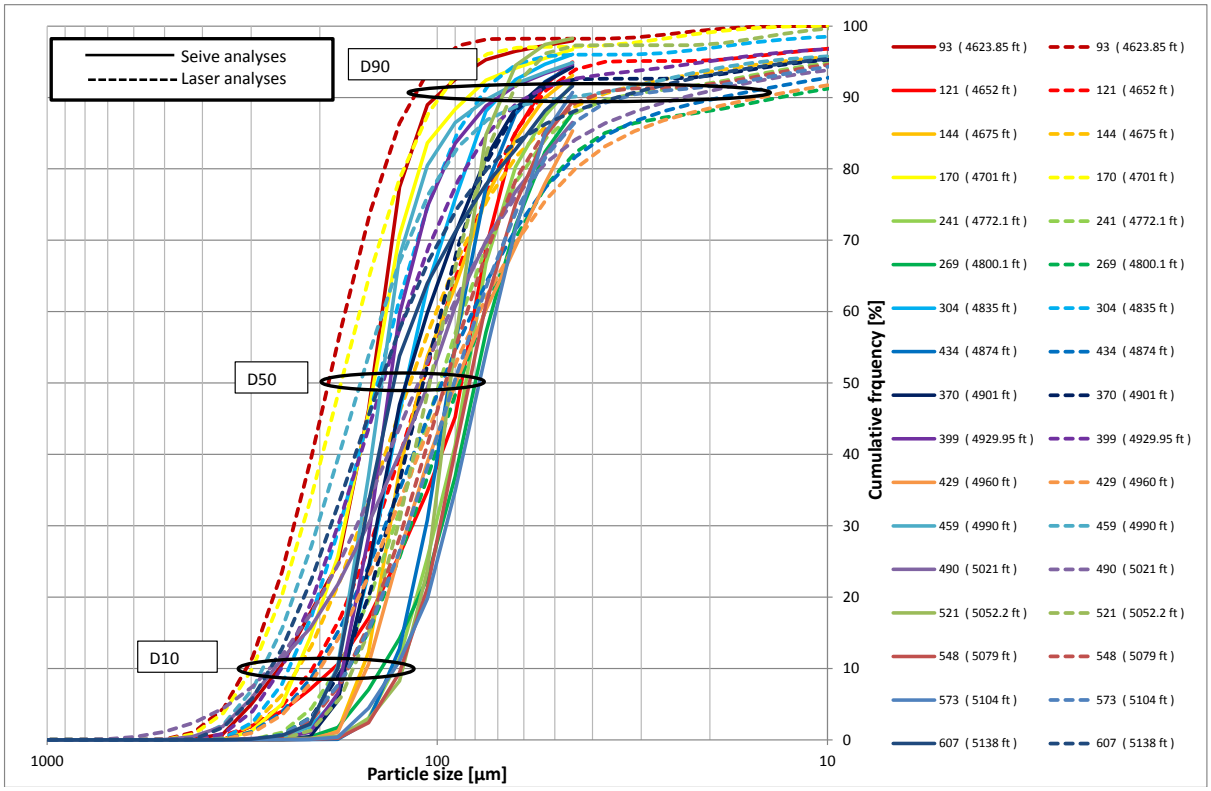

Unconventional RCA Studies

Additional studies (which may be termed unconventional RCA) have been performed at Weatherford Laboratories in Norway to support the RCA carried out in the UK using 30 core plugs, including:

1. Perform a non-standard cleaning study on plug samples and sister end trims, perform basic rock properties on plugs samples, and prepare sister end trims for Scanning Electronic Microscope.

   The Bunter formation contains potential native halite minerals and has highly saline formation water. This study was meant to assess the extent to which the removal of native and/or precipitated salts produced changes in basic rock properties and to ascertain the most appropriate method of cleaning Bunter core for RCA.

   Trims from samples were taken through three cycles of cleaning and basic petrophysical properties determined after each cleaning cycle. All the samples that survived through all cycles of cleaning show a tendency to an increase in permeability but the increase was not significant (see Figure 8.8) Standard cleaning procedures were therefore considered appropriate for cleaning Bunter cores for RCA.

2. Seal unit-cap rock tests meant to determine pore throat size distributions and as a characterisation tool for geological and petrophysical parameters including:

    a. water permeability measurements at 400 psi net confining pressure;
    b. pore squeeze to 2600 psi net confining pressure;
    c. water permeability measurements at 2600 psi net confining pressure;
    d. measurement of bulk volume by Archimedes principal; and
    e. grain volume and porosity measurements.

    This test programme was shared between Weatherford's Stavanger and Trondheim Laboratories. Tests a. to d. was performed at the Stavanger Laboratory, and the remaining at the Trondheim Laboratory. The original test programme at Trondheim Laboratory had to be curtailed because of damage (ranging from complete plug dissolution to fracturing) to all but one of the 19 samples due to prolonged storage in cold isopropanol. It is therefore important to note that even if great care was taken when collecting grains of the damaged samples stored in isopropanol into the thimbles prior to soxhlet cleaning, some grains would have been lost. This will affect the interpretation of the results for grain density and porosity. The results are summarised in Figure 8.9 and Figure 8.10.

3. Capillary pressure by mercury injection or Mercury Injection Capillary Measurements (MICP): This is to determine pore throat size distributions and for use as a characterisation tool for dynamic models.

    Before performing MICP, cleaned Bunter core samples were oven dried and their pore volume, density, and porosity determined.

    Figure 8.11 shows the plot of mercury pressure versus mercury saturation. The pore throat size distribution is given as a plot in Figure 8.12. The pore throat distribution size varies from 0.752 microns to 13.463 microns, corresponding to an injection pressure that varies from 2.52 psia to 62.25 psia. The J-function is plotted against saturation in Figure 8.13.

    Table 8.1 is a summary of the measured petrophysical properties obtained as part of the additional RCA study. The table shows the range (from minimum to maximum values) of each measurement and also indicates the applicable test programme.

Figure 8.8: Klinkenberg Corrected CO_2 Permeability, K_L, Versus Helium Porosity, ϕHe

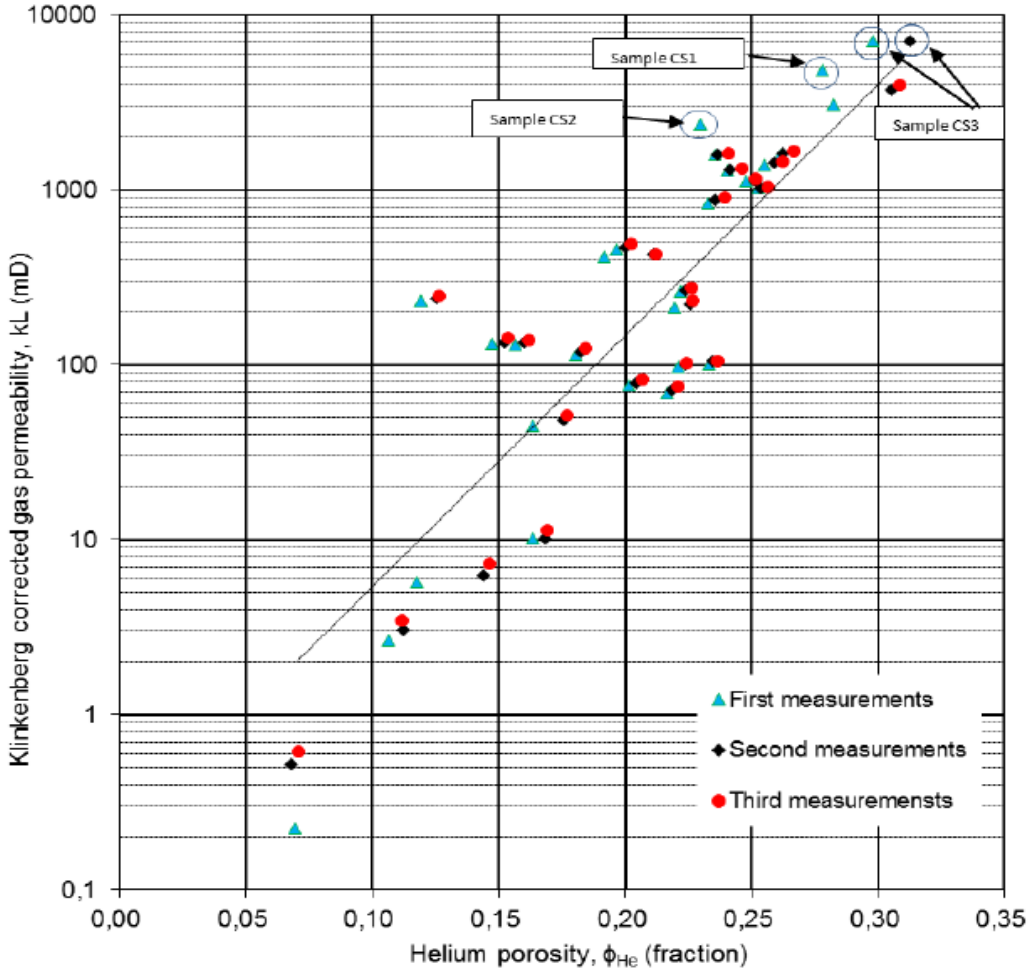

Figure 8.9: K_w at 400 psi NCP versus Porosity Obtained at Trondheim Laboratory

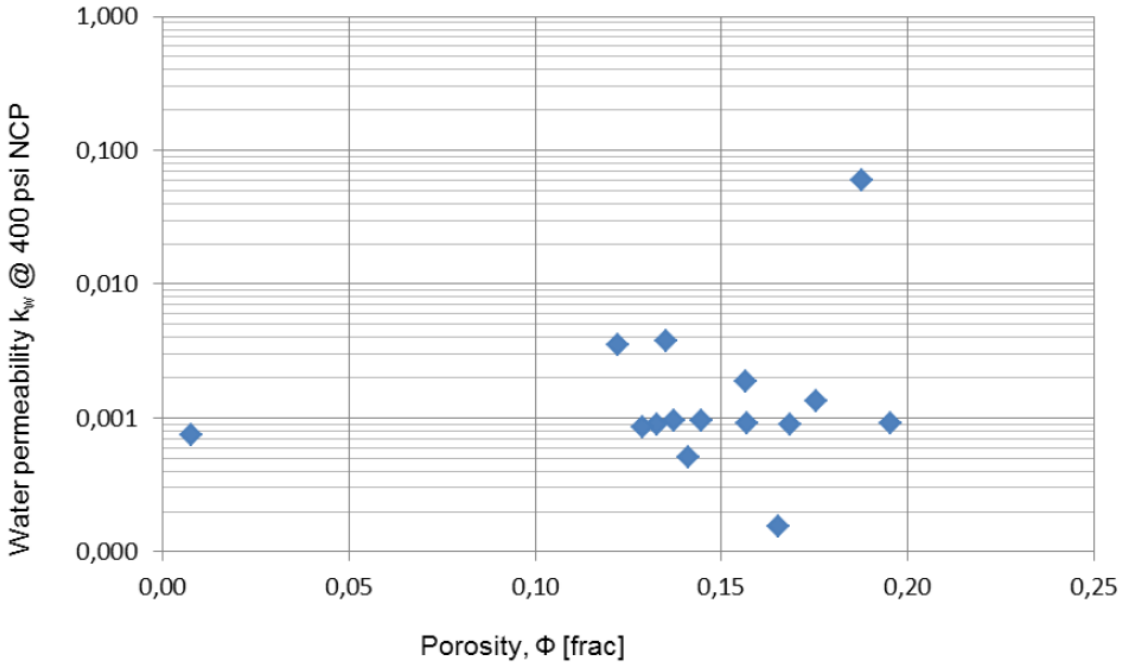

Figure 8.10: K_w at 2600 psi NCP versus Porosity Calculated at 2600 psi NCP

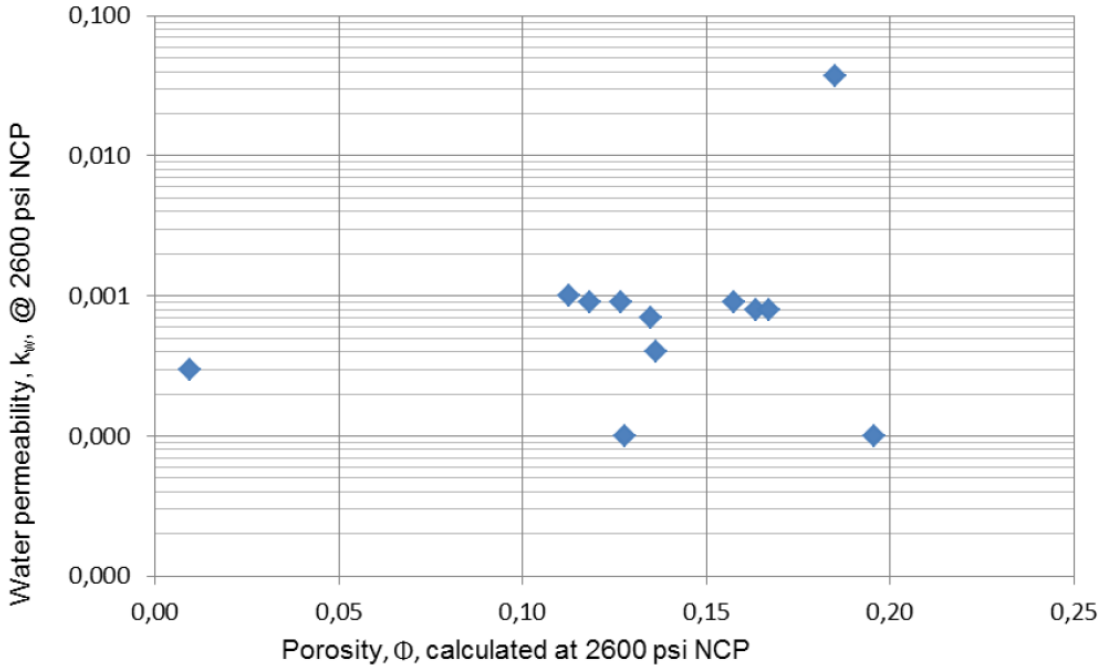

Figure 8.11: Pressure versus Saturation Obtained from MICP

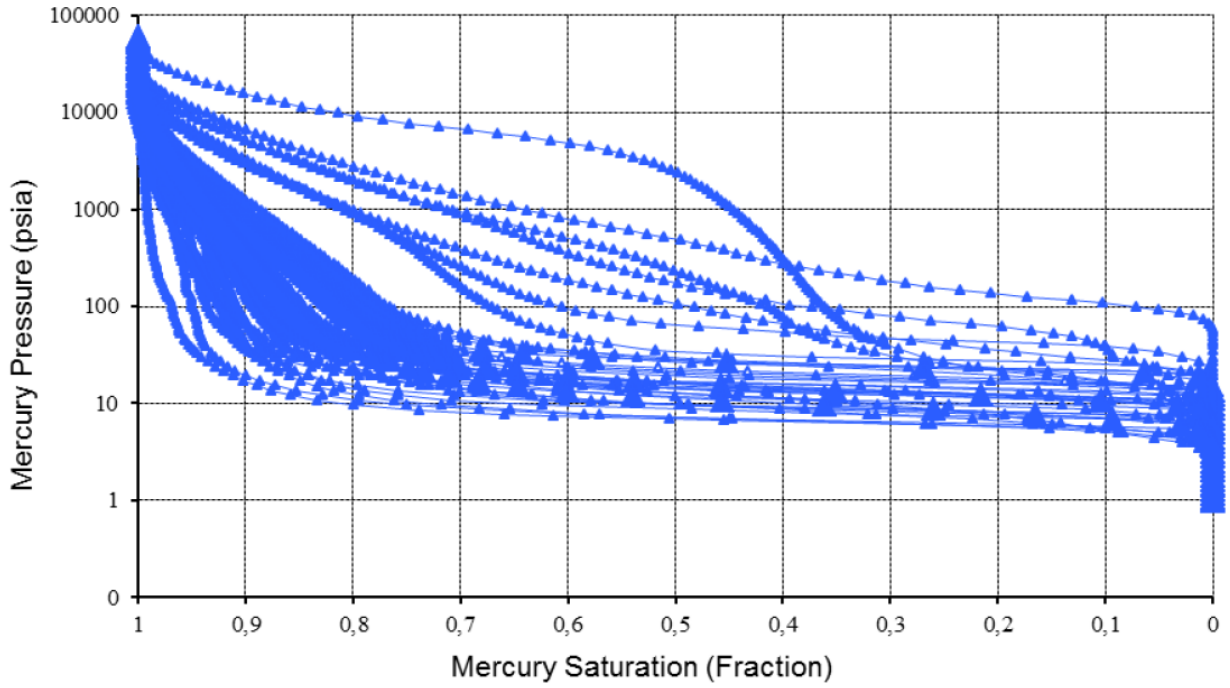

Figure 8.12: dSw/dLog Pore Throat Size versus Pore Throat Size Obtained From MICP

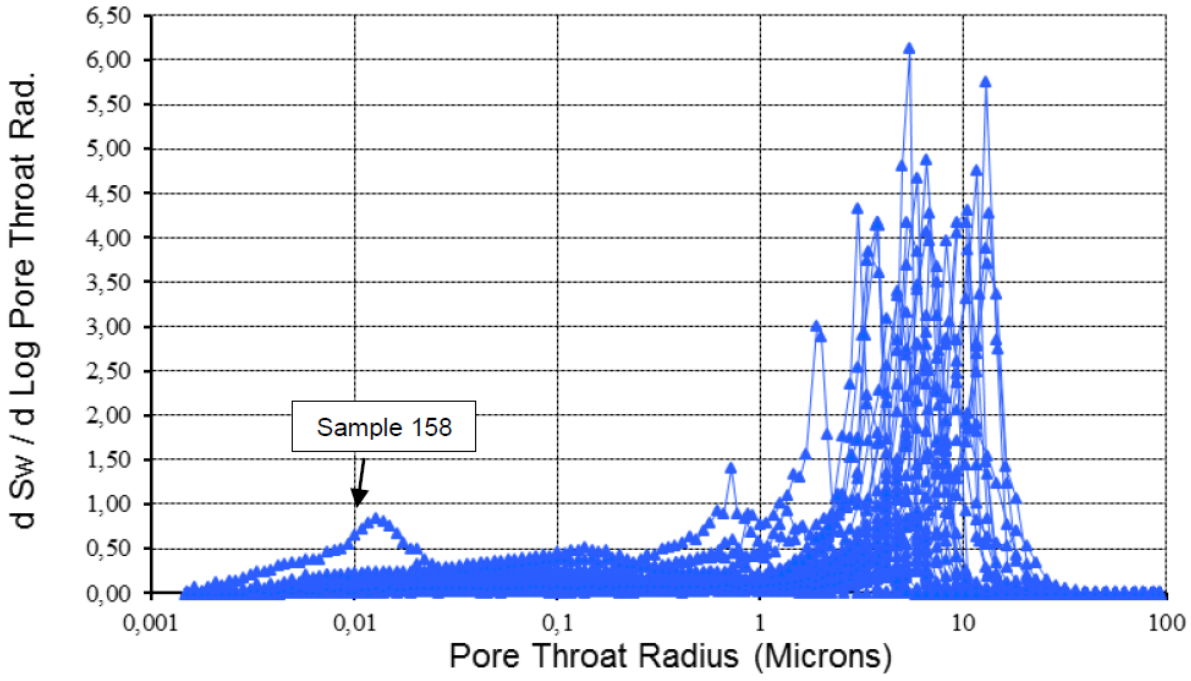

Figure 8.13: J-Function Plot (J(1-SHg) versus Saturation)

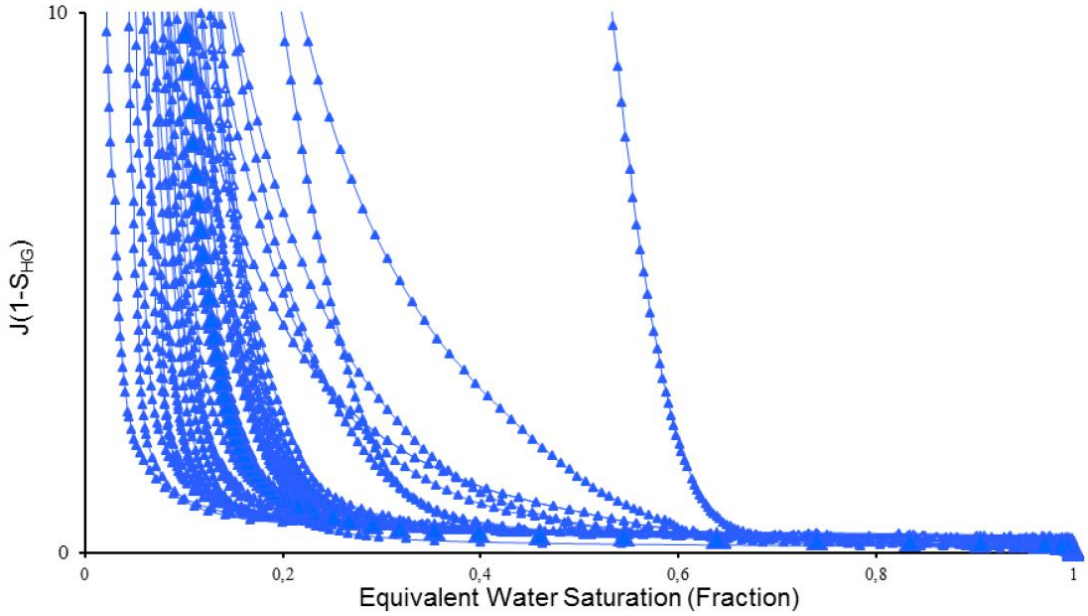

Table 8.1: Measured Petrophysical Properties from Additional RCA study

Petrophyscial Properties	Range	Test Programme
Cleaning study: first measurement Klinkenberg corrected gas permeability, K_L, [MD]	0.225 to 3061	(1)
Cleaning study: first measurement Helium porosity [%]	6.90 to 28.2	(1)
Cleaning study: second measurement Klinkenberg corrected gas permeability, K_L, [MD]	0.519 to 3758	(1)
Cleaning study: second measurement Helium porosity [%]	6.80 to 30.5	(1)
Cleaning study: third measurement Klinkenberg corrected gas permeability, K_L, [MD]	0.615 to 3969	(1)
Cleaning study: third measurement Helium porosity [%]	7.10 to 30.9	(1)
Water permeability @ 400 psi	0.0002 to 2.7	(2)
Porosity at ambient	1.0 to 20.0	(2)
Archemedes bulk volume [ml]	14.93 to 68.77	(2)
Water permeability at reservoir net confining pressure, 260 psi	0.0001 to 0.037	(2)
Porosity at reservoir net confining pressure, 260 psi [%]	0.93 to 15.6	(2)
MICP porosity [%]	2.60 to 30.20	(3)

8.1.1.2 Special Core Analysis

The SCAL programme, shown in Figure 8.14, was undertaken to measure the range of trapped CO_2 saturation, CO_2 and water relative permeability data relevant to dynamic modelling of CO_2 movement in the reservoir. The programme consists of ambient condition tests using centrifuge, unsteady state displacements, together with reservoir condition measurements using supercritical CO_2. For

reservoir condition testing, all measurements were made at a reservoir temperature of 57°C and a reservoir (pore) pressure of 2030 psig (140barg). Analytical grade CO_2 was used as the injection gas.

Figure 8.14: SCAL Experimental Process Description

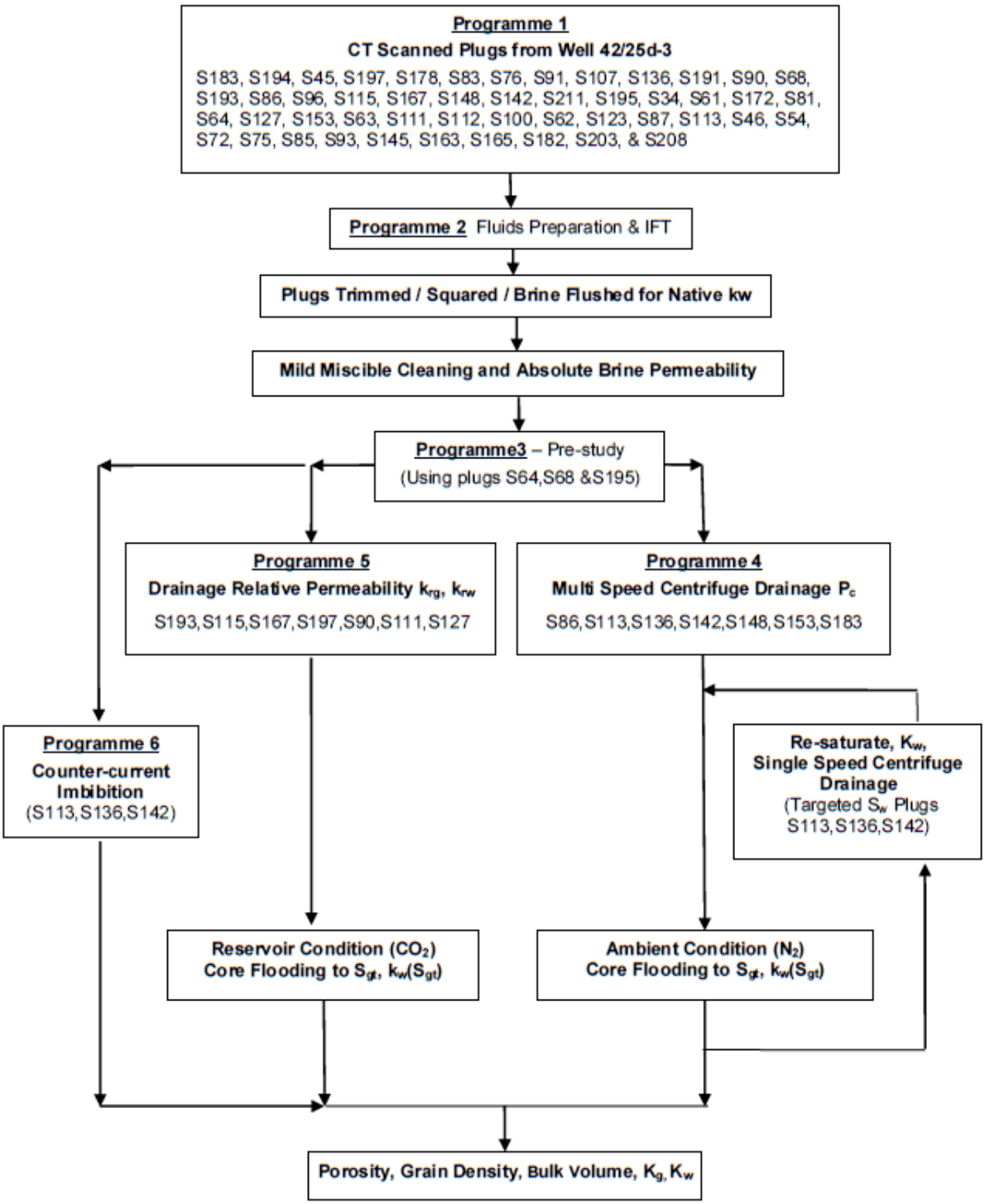

Programme 1 Plug Selection

Plug selection involved:

- Plug CT scanning: 12 of the original 49 samples disqualified after X-ray CT scanning, leaving 37 plugs;
- Native State (as-received) Brine Permeability: Brine permeability was measured for all remaining 37 samples using synthetic formation brine (SFW) and under a confining back pressure of 145 psig (10barg);
- Sample cleaning and RCA: sample cleaning was performed following the procedure described in the cleaning pre-study. The results of the RCA have already been presented in Section 8.1.1.1;
- Brine permeability: dry samples were formation brine saturated, degassed and absolute brine permeability (K_w) measured using a back-pressure of 145 psig (10barg); and
- MICP: measured on 36 samples.

Programme 2 Fluid Preparation

Synthetic formation brine: a laboratory filtered (0.45 µm) and degassed Synthetic Formation Brine (SFW) was prepared according to the salts given in Table 8.2. Data in the table corresponds to SFW density of 1.24 g/cc and salinity of 248, 000 ppm. For measurements using in-situ saturation monitoring, approximately 0.25 mole of CsCl dopant (molar mass 168.36 g/mol) was used to replace 0.25 mole NaCl (molar mass 58.44 g/mol). The doped synthetic brine composition is given in Table 8.3 for reference. The measured density of the doped brine was 1.26 g/cc corresponding to a brine salinity of about 264,300 ppm.

Reservoir fluids: both an impure CO_2 mixture and pure (analytical grade) CO_2 were used at reservoir conditions (57°C at 141bar). The CO_2 mixture was measured to have a density of 0.577 g/cm^3 (at 57°C at 141bar). The CO_2 -brine interfacial tension (IFT) was measured to be 36.8±0.7 mN/m. This compared to a measured (analytical grade) CO_2 density of 0.596 g/cm^3 and CO_2-brine IFT of 39.5±0.8 mN/m at the same test conditions.

Table 8.2: Synthetic Formation Brine

Salt	g/L
NCl	258.13
$CaCl_2.2H_2O$	40.09
$MgCl_2.6H_2O$	31.05
KCl	3.48
$SrCl.6H_2O$	0.42

Table 8.3: Doped Formation Brine

Salt	g/L
NCl	244.24
CsCl	40.00
$CaCl_2.2H_2O$	40.09
$MgCl_2.6H_2O$	31.05
KCl	3.48
$SrCl.6H_2O$	0.42

Programme 3 Pre-Study

Three plugs (S64, S68, S195) were selected for pre-study testing which includes Critical Velocity tests and Acid Brine Sensitivity test. Critical velocity tests were aimed at identifying the potential for fines movement within the plug and its threshold value. The acid brine sensitivity test was to see if the pore matrix was affected by brine that will become acidified when in contact with CO_2 in the reservoir. The results of the critical velocity test was inconclusive whilst for the Acid Brine Sensitivity test, a small reduction in grain volume (0.64cm^3 to 1.14 cm^3) was observed for each plug as a result of acid brine flooding. This corresponds to an increase in porosity of approximately 2 to 6 %. Klinkenberg CO_2 permeability was also observed to increase post-flooding by approximately 10% for S64 and S68 and over 20% for S195.

Scanning Electron Microscopy (SEM): of native pre-test and post-acidified brine flood end-trims were undertaken to determine if there is evidence for pore structural change following exposure to acidified brine. The most notable and common difference between the pre-test and post-test samples was the absence of halite in the post-test samples. No evidence for change in pore structure was observed.

Programme 4 Ambient Temperature Tests

All measurements were performed at a laboratory temperature of 22°C with a pore (back) pressure of around 145 psig (10barg). Analytical grade nitrogen N_2 was used as the injection gas. Primary drainage (air displacing brine) to target S_{wi} was performed by unconfined multi-speed centrifuge tests.

Primary drainage gas-water capillary pressure (P_c) was measured on seven core plugs covering the rock types and permeability ranges for the Bunter Sandstone. These data are shown in Figure 8.15. Plotting of J-function curves showed only samples S153 and S142 of the seven tested plugs as being from the same rock type. Plug S148 was chosen to constrain reservoir condition PC modelling since the base parameters (K, phi) were the closest match available to the composite parameters (S193, S115, S167).

Each plug at S_{wi} was brine flooded to acquire trapped gas saturation and end point brine relative permeability. In-situ saturation monitoring was utilised to quantify both the initial gas saturation and trapped gas saturation. Imbibition end-point data are summarised in Figure 8.16. End-point trapped gas saturation was verified independently using volumetric gas production data and sample (post-study) pore volume measurements.

Targeted brine saturations of 0.30, 0.70 and 0.80 were established on individual plugs, S113, S136 and S142, using the single speed centrifuge method. These plugs were also brine flooded to trapped gas saturation for the measurement of K_{rw} at S_{gt}. The relationship S_{gt} versus S_{gi} correlated as expected, see Figure 8.16, targeted S_w data points, but it was clear from ISSM that the saturation distributions were very non-uniform (Figure 8.17 is an exemplar). Because of the non-uniformity in brine saturation, it is unlikely that measured K_{rw} is representative. This ambient condition work showed that uniform brine saturation profiles cannot be acquired at high values of brine saturation from centrifugation.

Post-study plug characterisation data show that grain volume change was less than 0.1cm^3 for all samples. Significant gas permeability loss was observed for sample S136 but remaining samples were within +/-10% of original values. This was not true for absolute brine permeability which was found to decline by 10% to 30%.

Figure 8.15: Primary Drainage Capillary Pressure, Combined Plot

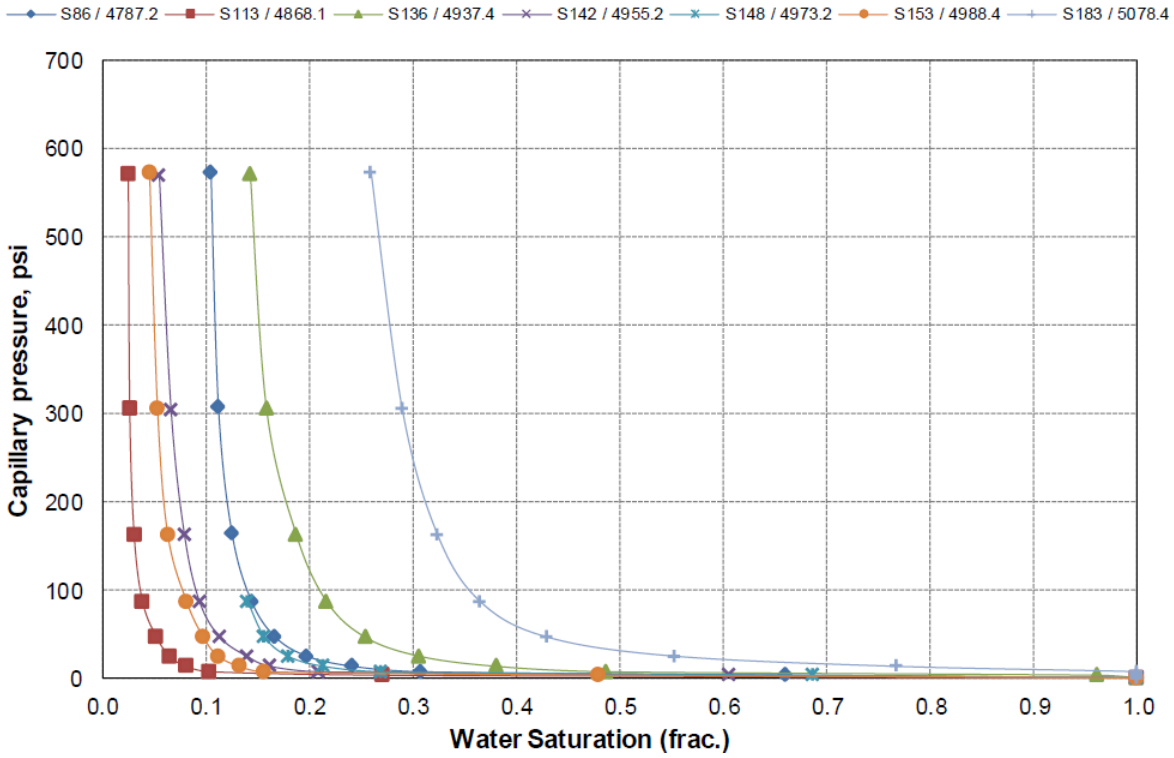

Figure 8.16: Trapped Gas Saturation versus Initial Gas Saturation

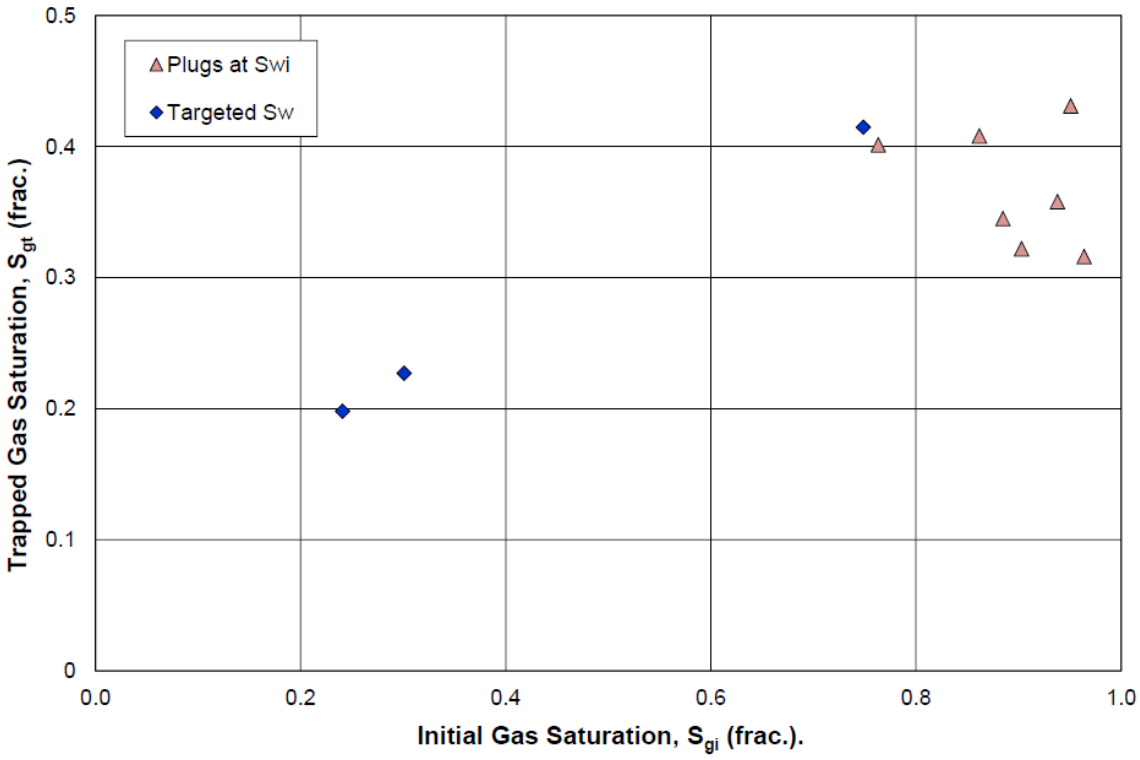

Figure 8.17: Saturation Distribution Targeted S_{wi} 0.3 (Plug S113)

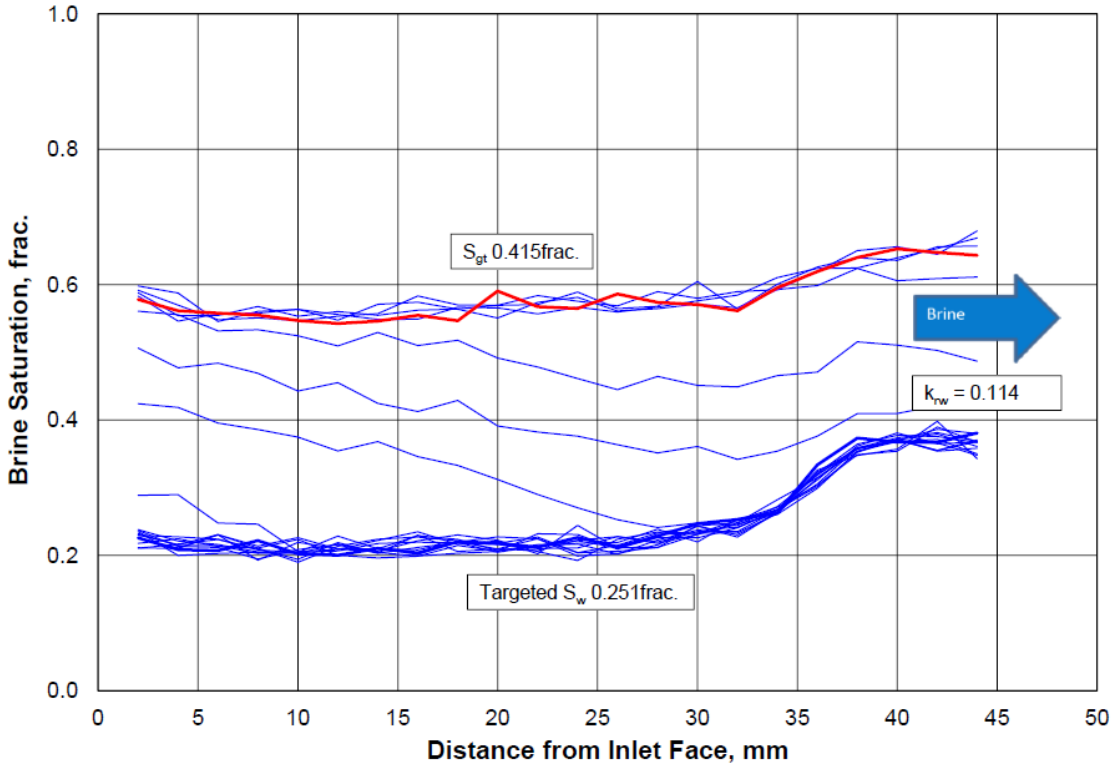

Programme 5 Reservoir Condition Gas-water K_r

Unsteady-state primary drainage gas-water relative permeability was measured using two composites and two single plugs. All measurements were performed at a reservoir temperature of 57°C with a reservoir (pore) pressure of 2,030 psig (140barg), using analytical grade carbon dioxide (CO_2) as the injection gas. The first test used a three plug composite core (Composite S193, S115, S167) with a measured absolute brine permeability of 115.7 mD (porosity 0.253). The brine saturation distribution was influenced by the component plug individual properties and plug butting (see Figure 8.18). Subsequent tests were therefore performed with single plugs, plug S197 (11.6 mD, porosity of 0.152 frac) and plug S90 (77.5mD, porosity of 0.267). The final test however reverted back to a composite core (Composite S111, S127) since the rock type was of high permeability. The measured absolute brine permeability for this composite was 1324 mD (porosity 0.272).

Measured CO_2 relative permeability was similar for plug S90 and composite S111, S127 (K_{rg} 0.158 and K_{rg} 0.184 respectively at S_g 0.560 and 0.556). Higher CO_2 relative permeability was observed for composite S167, S115, S193 and plug S197. The measured analytical end-point CO_2-water relative permeability data for these floods are shown in Figure 8.19.

Imbibition brine flooding to trapped CO_2 saturation was also performed starting from low initial CO_2 saturations ($1-S_{wr}$). Initial CO_2 saturations ranged from $0.424 < S_{gi} < 0.579$ resulting in trapped CO_2 saturation (S_{gt}) ranging from $0.255 < S_{gt} < 0.387$. All trapped CO_2 saturation data including ambient and reservoir condition flooding is summarised in Figure 8.20 which also show the correlations of Spiteri et al. (2008) and that of Land. The alternative data provided on this plot came from Counter-Current Imbibition (CCI) experiments (Programme 6), where the initial saturation is controlled using toluene-CO_2 saturation and imbibition experiments. These are undertaken under purely spontaneous processes, allowing toluene to imbibe into the sample under capillary forces. The corresponding brine relative permeability (K_{rw}) at S_{gt} is shown plotted in Figure 8.21.

As Figure 8.18 shows, coreflood drainage experiments are strongly affected by capillary end effects leading to non-uniformity in saturation distribution along the core length. One way of minimising this effect is by performing experiments at high injection rates. For this study, the CO_2 injection rate ranged between 4 cm^3/h (corresponding to a reservoir advance rate of 1.2 ft/day) to 400 cm^3/h. However, high flow rates are known to induce instabilities at the flood front that are unrepresentative of displacement conditions deep in the reservoir.

To reconcile time and spatially dependent experimental data and generate relative permeability data that is corrected for the effects of laboratory scale capillary pressure, core flood simulation was performed using *Sendra*™. *Sendra*™ is a proprietary simulator based on a two phase 1-D black oil simulation model together with an automated history matching routine. The simulator recreates the balance of forces in the core experiment, taking as input the capillary pressure and relative permeability data, to match measured experimental production and pressure data. Once a satisfactory match has been obtained, a characteristic reservoir relative permeability is then generated that corrects for the laboratory capillary artefacts.

To improve confidence in simulated relative permeability data, it is usually better to employ capillary pressure data from samples within the same rock type. In the case of Bunter data (except for sample

S90), this proved difficult and it became necessary to use an analytical capillary pressure model as an input, where the simulator was given some flexibility to estimate parameters of the capillary pressure model. The model employed is due to Skjaeveland et al (2000) and is as stated in Equation 8.1, recast in terms of water and gas phases. Comparison of Pc generated with the Skjaeveland model and those generated from two laboratory tests – the multi-speed centrifuge capillary pressure (LabPc) and the corrected MICP – are shown in Figure 8.22 through Figure 8.24.

Equation 8.1

$$Pc = \frac{c_w}{\left(\frac{S_w - S_{wR}}{1 - S_{wR}}\right)^{a_w}} + \frac{c_g}{\left(\frac{S_g - S_{gR}}{1 - S_{gR}}\right)^{a_g}}$$

Where:
c and a are constants defining the capillary entry pressure (threshold pressure) and curvature exponent, respectively for water and oil (as denoted by subscripts 'w' and 'o', respectively.

Although this model was designed to allow for mixed-wet capillary pressure data in imbibition and secondary drainage processes, it may still be used for strongly wetting systems in primary drainage, by either negating the gas term or by using cg = 0. Skjaeveland parameters are used as input for each coreflood simulation.

Table 8.5 lists the end points used as input to the simulation model. K_L and K_w represents the Klinkenberg and water permeability respectively. Water permeability was lower than the Klinkenberg permeability and also exhibited a decreasing trend as shown in Figure 8.25. This is uncommon in clean sandstone materials and the anomaly creates unusual CO_2 relative permeability when relative permeability is based on water permeability as the absolute, that is the effective CO_2 permeability at initial water saturation (S_{wi}) become greater than specific water permeability at 100% water saturation, and hence the relative permeability to CO_2 at S_{wi} would be greater than 1.

Although this phenomenon is apparently counter to conventional hydrocarbon system relative permeability behaviour, as referenced in reservoir engineering literature, there are a number of experimental studies reporting similar observed behaviour. These papers incorporate two different potential hypotheses for the phenomenon.

The first theory is that clay minerals may become swollen in the presence of formation water, and that the fresher the water, the more pronounced the effect.

The second theory suggests that turbulent flow may be occurring in a water-filled system due to water flowing over and through tight, rough surfaces – postulating that at irreducible water saturation the gas (or oil) path is free from such turbulence since water continues to fill the rough, clay rich surfaces.

The dominance of Illite in the Bunter clay mineralogy would underpin the first hypothesised mechanism. Illite swells in the presence of brine and can thus reduce the permeability to this phase whilst in the presence of CO_2 the clays will shrink and allow an enhanced permeability.

The second hypothesis has also been described in terms of non-wetting lubrication. Since the CO_2 occupies the largest pores, it is speculated that the CO_2 then sees a reduced drag or surface friction

because it is in contact with smoother surfaces. The Bunter Sandstone is considered (strongly) water-wet and both mechanisms could therefore be complementing one another in the Endurance matrix.

Simulated relative permeability curves were defined using the Corey model which for water relative permeability is defined as:

Equation 8.2 $$K_{rw} = K_{rw_{max}} \cdot S_{wn}{}^{Nw}$$

Where:
K_{rw} is the relative permeability to water
$K_{rw_{max}}$ is the maximum relative permeability to water
Nw is the Corey exponent for water
S_{wn} is normalised water saturation – given as, $S_{wn} = (S_w - S_{wi})/(1 - S_{wi})$, for a primary drainage process

The Corey model for relative permeability to gas (in a gas-water system) is defined as:

Equation 8.3 $$K_{rg} = K_{rg_{max}} \cdot (1 - S_{wn})^{Ng}$$

Where:
K_{rg} is the relative permeability to gas
$K_{rg_{max}}$ is the maximum relative permeability to gas
Ng is the Corey exponent for gas

The Corey exponent for water (Nw) ranged from 4.7 to 6.0, and for gas (Ng) the range was from 2.5 to 3.0. The curves derived from these parameters are presented in Figure 8.26 on Cartesian and semi-log axes (left and right-side, respectively). The curves are also presented as a function of normalised water saturation in Figure 8.27. Figure 8.28 and Figure 8.29 show production and saturation profiles history match for the composite sample S111/S127 using Corey exponents of Nw=4.7 and Ng = 2.7. They show good matches in production, differential pressure and saturation profiles.

Figure 8.18: Primary Drainage In-situ Brine Saturation S115 S167 S193

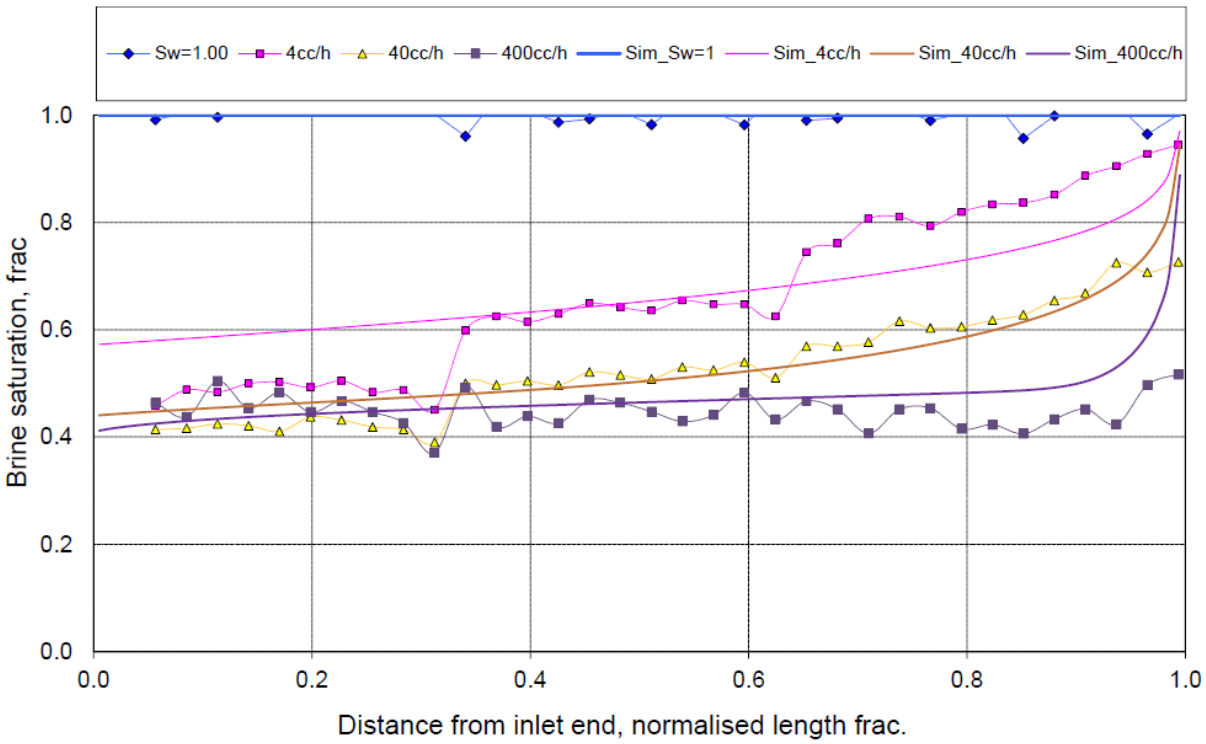

Figure 8.19: Analytical (End-Point) Gas Relative Permeability (Programme 5)

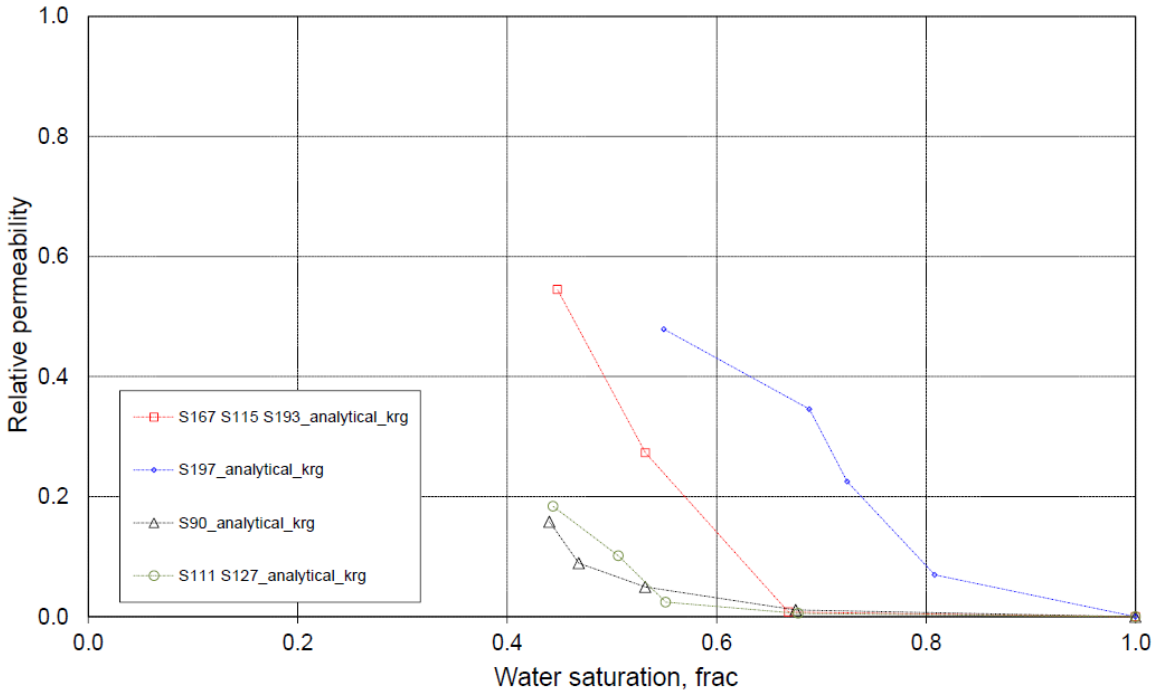

Figure 8.20: Trapped Gas Saturation (S_{gt}) as a Function of Initial Gas Saturation (S_{gi}) – All Methods

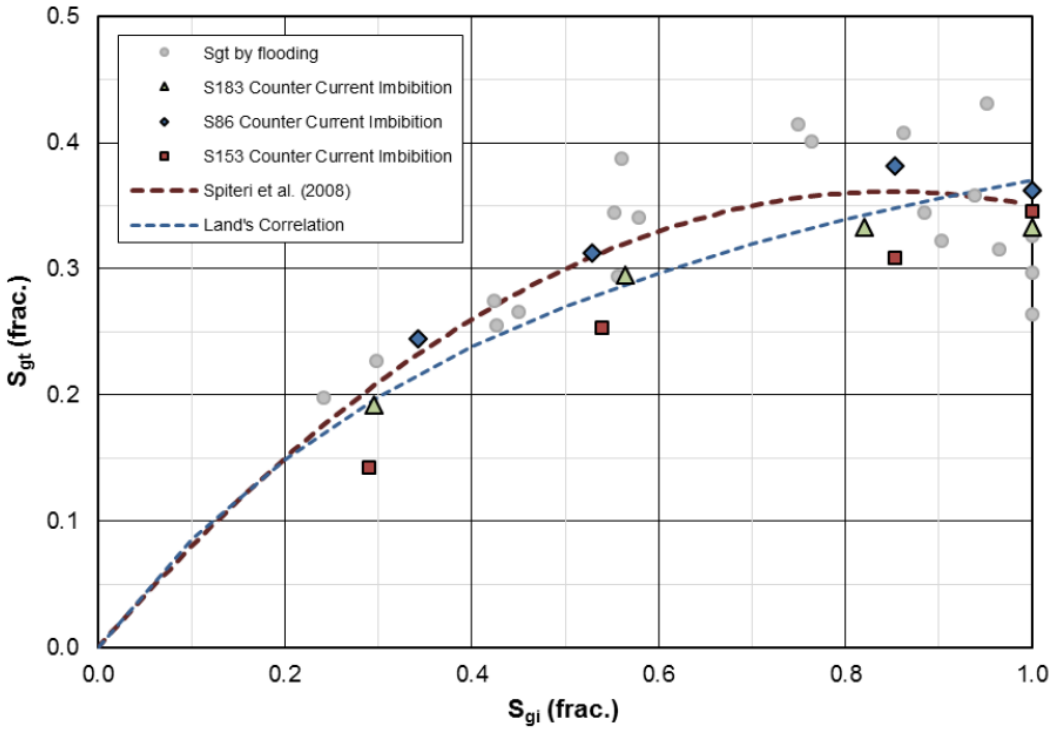

Figure 8.21: Brine Relative Permeability versus S_{w_max} (Programme 5)

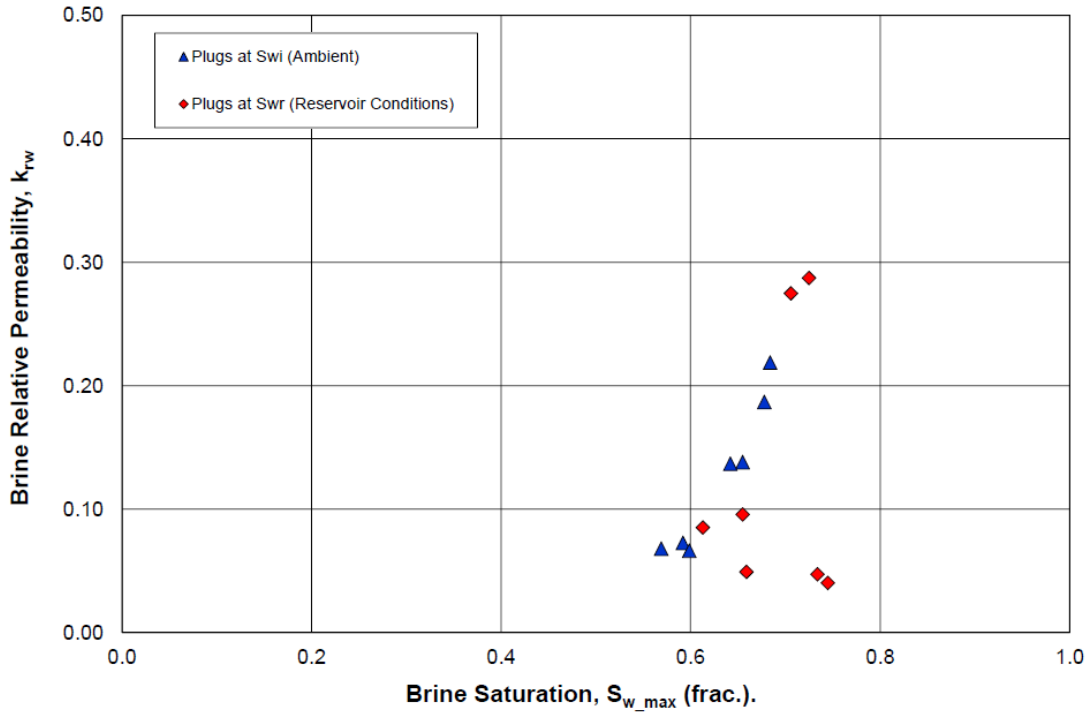

Figure 8.22: Good Correlation of Centrifuge PC (Laboratory PC) and MICP Data (S113 and S153)

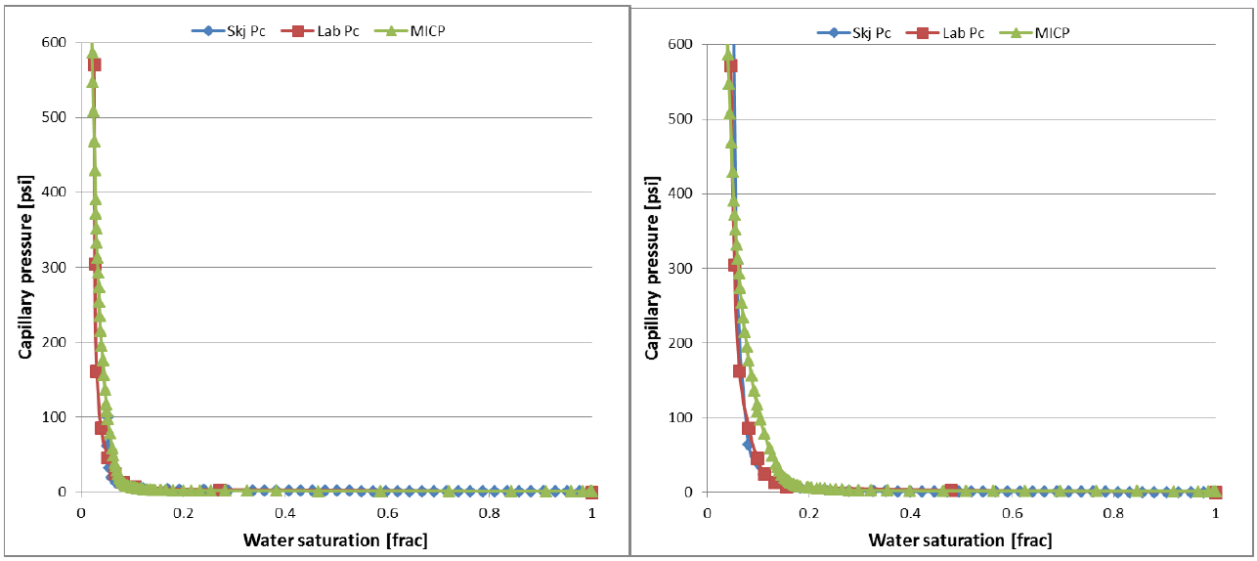

Figure 8.23: Reasonable Correlation between Centrifuge PC (Laboratory PC) and MICP Data (S86, S142 and S148)

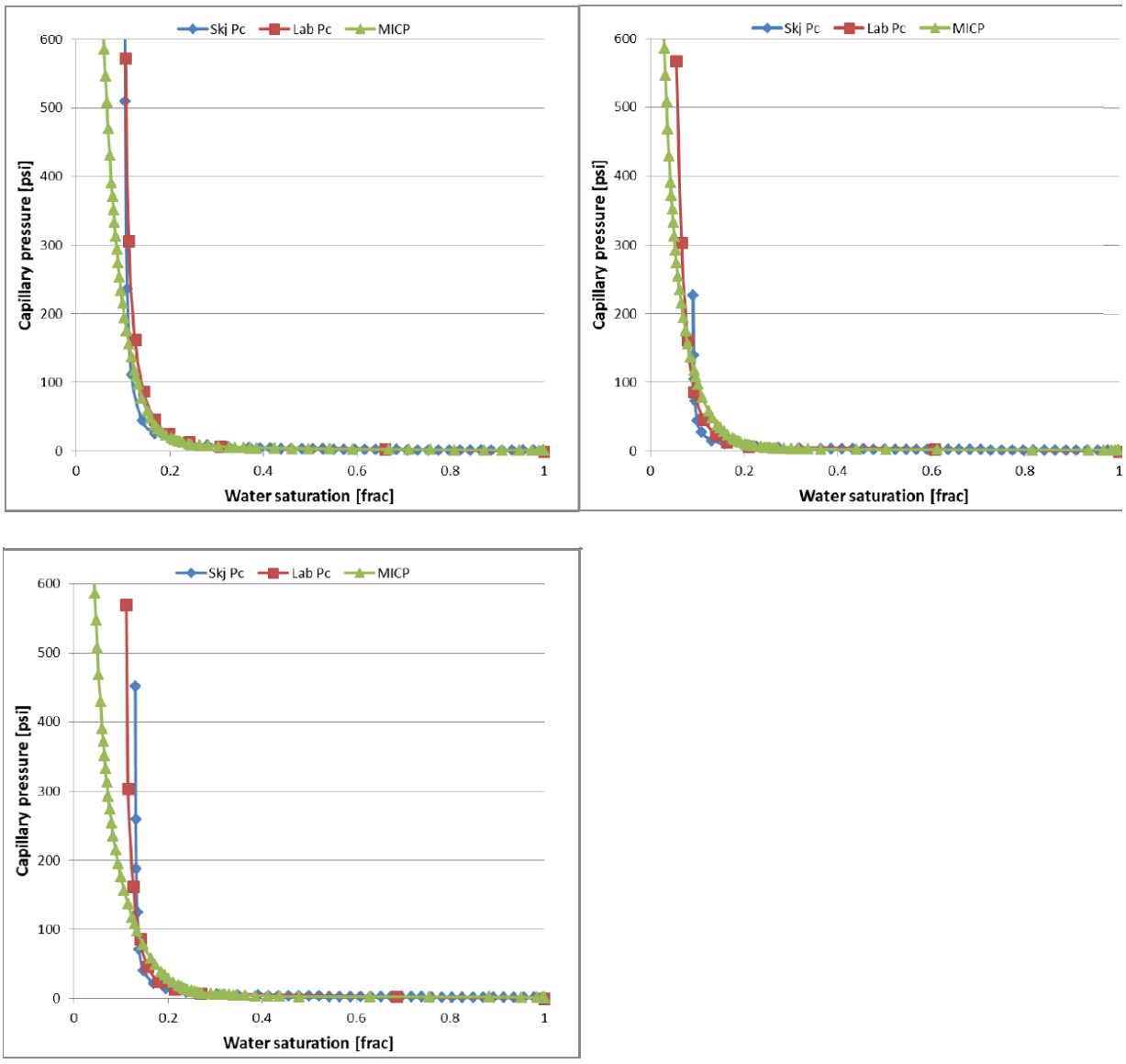

Figure 8.24: Poor Correlation between Centrifuge PC (Laboratory PC) and MICP (S136 and S183)

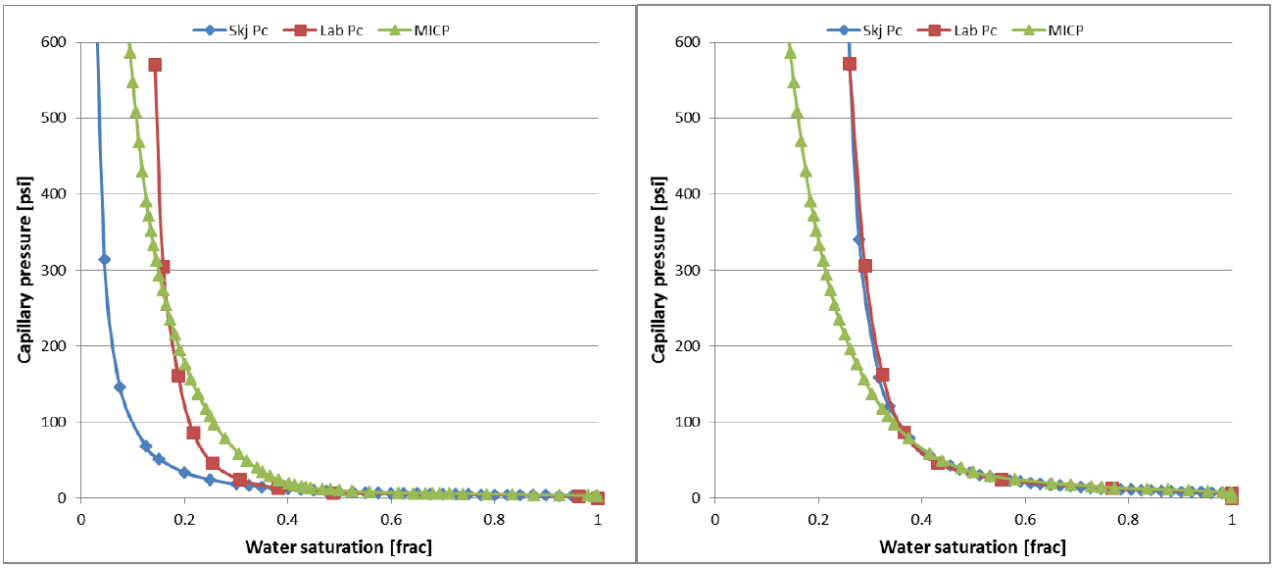

Table 8.4: Skjaeveland PC Model Parameters

Sample	K_L	K_w	K_{rw}_max	K_g@max	K_{rg}_max
S115/S167/S193	275	171	0.620	275	1.000
S197	14	6.75	0.482	14	1.000
S90	173	103	0.596	173	1.000
S111/S127	1583	1136	0.718	1583	1.000

Table 8.5: Endpoint Simulation Inputs

Sample	K_L	K_w	K_{rw}_max	K_g@max	K_{rg}_max
S115/S167/S193	275	171	0.620	275	1.000
S197	14	6.75	0.482	14	1.000
S90	173	103	0.596	173	1.000
S111/S127	1583	1136	0.718	1583	1.000

Figure 8.25: Water Permeability (K_w) versus Klinkenberg Gas Permeability (K_L)

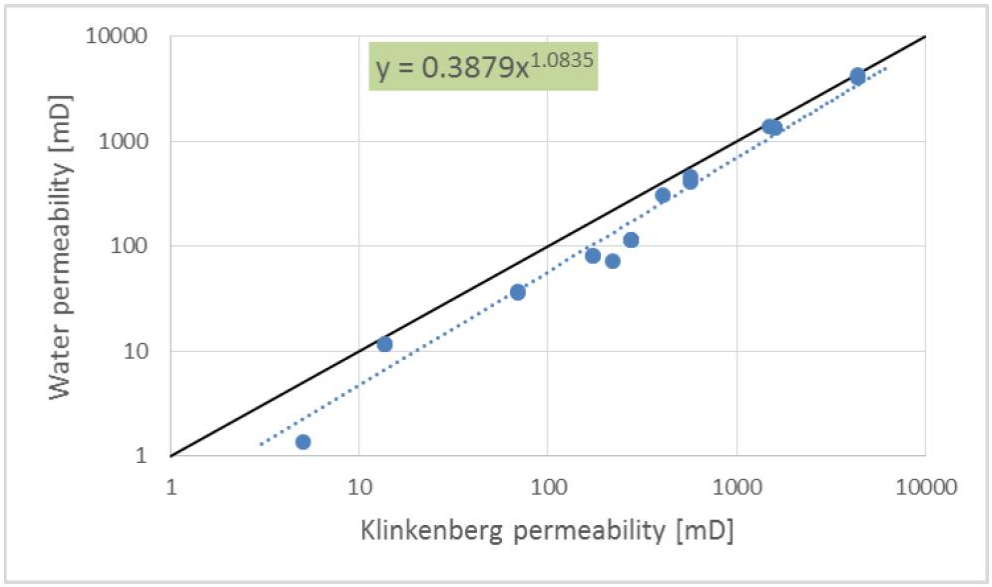

Figure 8.26: Simulated Relative Permeability Curves – Indicating the Observed Exponent Variance

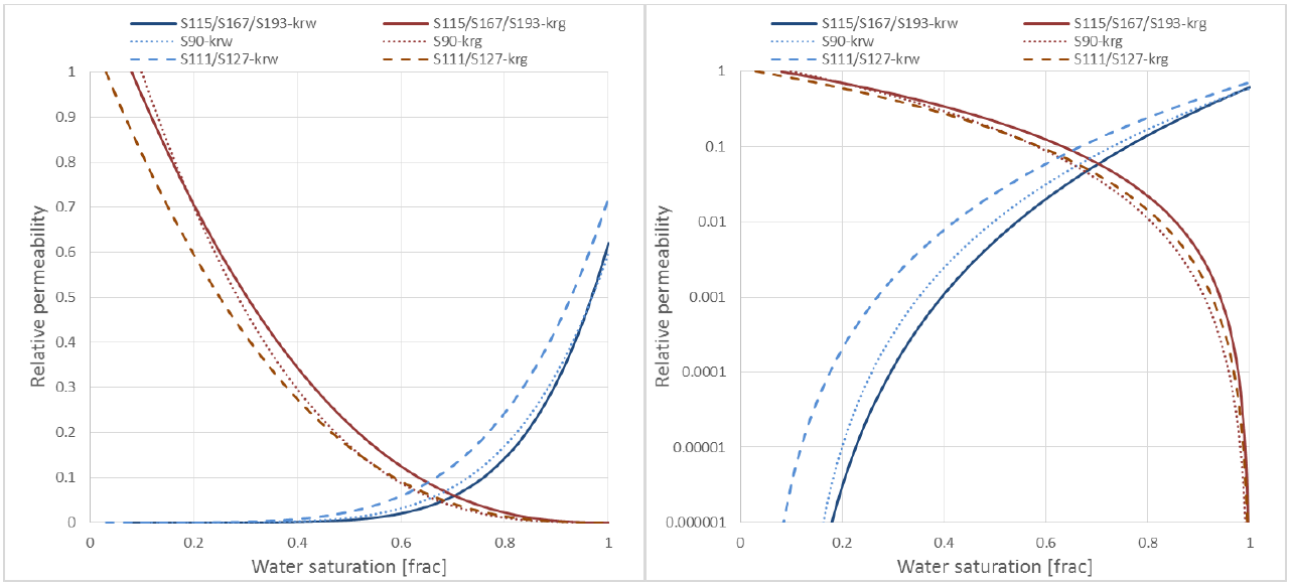

Figure 8.27: Simulated Relative Permeability Curves versus Normalised Water Saturation

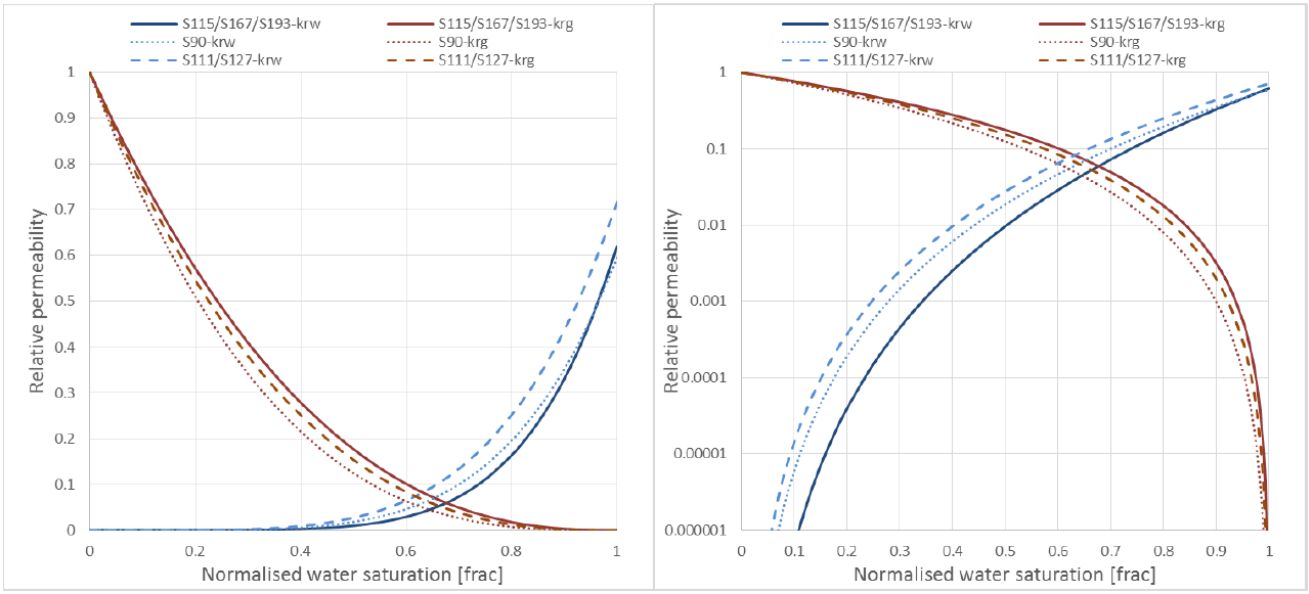

Figure 8.28: Production History Match for S111/S127

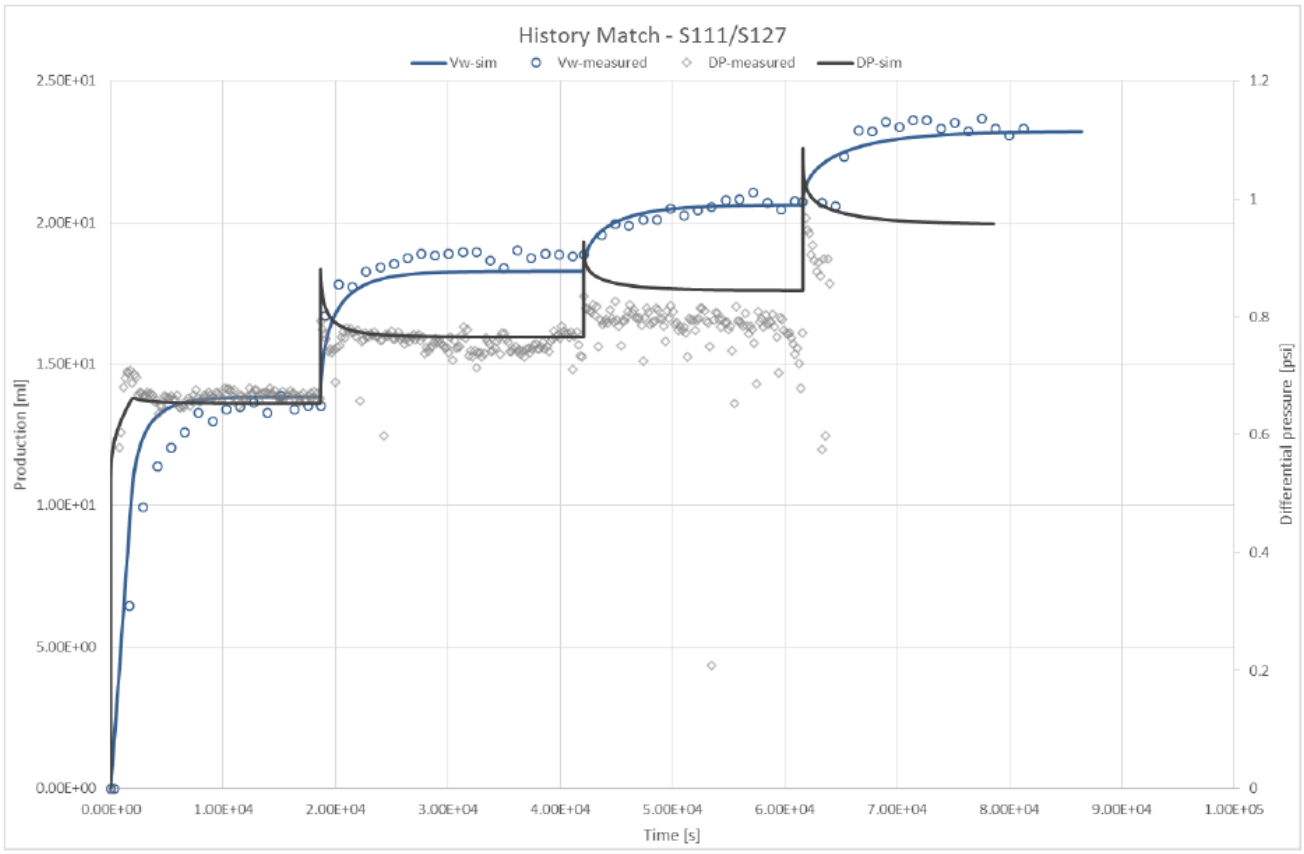

Figure 8.29: Saturation Profiles for S111/S127

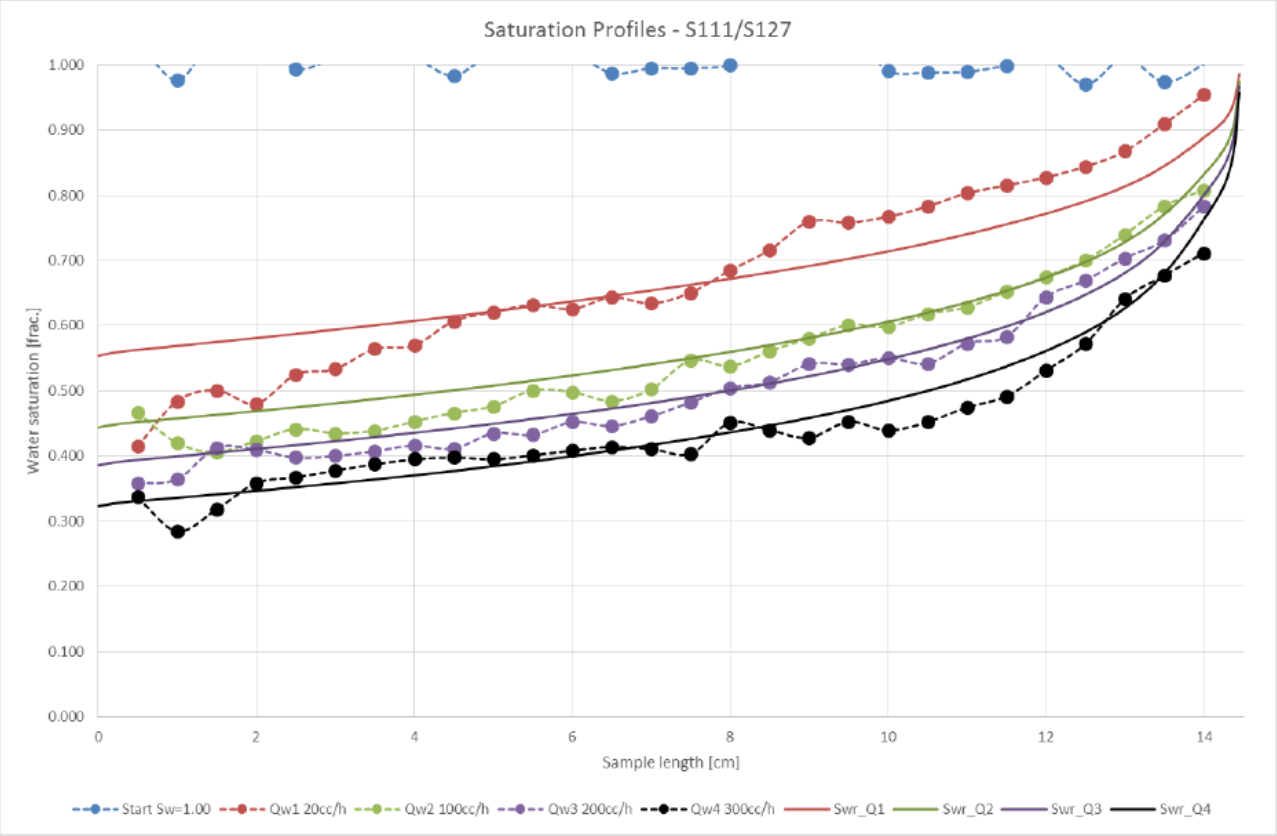

8.1.2 Well Testing and Vertical Interference Test Results

8.1.2.1 Well Test Results

As part of the data gathering programme, a well test was completed over the interval 1396.3 to 1414.3 m TVDSS to achieve the following:

- determine initial reservoir pressure;
- establish key reservoir parameters; permeability, thickness and skin;
- Determine the influence of nearby boundaries and/or heterogeneities within the volume of the reservoir investigated by the test;
- investigate vertical connectivity and estimate K_V/K_H (vertical/horizontal) permeability ratio over the tested interval;
- secure good quality formation water samples for chemical and biological analysis and electrical properties;
- carry out a step rate injection test to prove injectivity of the best practicable analogue to supercritical CO_2 (filtered seawater); and
- investigate (injection) rate dependent skin including any plugging, fraccing or dissolution effects seen during testing.

The testing programme consisted of a production period of approximately 24 hours at a rate of 5000 stb/d (795 m^3/day) using an Electrical Submersible Pump (ESP), followed by a shut-in and pressure build-up for 48 hours. Subsequently a multi-rate injection test using filtered seawater was performed at rates of 5000, 10000 and 15000 stb/d (795, 1590, 2385 sm^3/day), followed by a 12 hour pressure fall-off test.. Note that CO_2 was not used due to safety concerns over handling the fluid in its super-critical state and sourcing a sufficient volume of CO_2) The key results calculated from the test include:

- an initial reservoir pressure of 151.8bar at a depth of 1405.3 m TVDSS. This is in excellent match to the same datum pressure estimated using data from the long duration MDT formation pressure testing on wireline of 152 ±0.5bar at the same datumaverage permeability of 271 mD based on a test interval of 230.4 m; this is an excellent match with reservoir properties derived from porosity-permeability trends;
- a negative skin of -1.1;
- no evidence of boundaries in the volume investigated by the test, which was calculated to extend to a radius of 1.2km;
- a vertical to horizontal permeability ratio (K_v/K_H) of 2.19×10^{-4}, which is considerably lower than that seen on the scales investigated by the Vertical Interference Tests (VIT); this was attributed to the test taking place within a laterally extensive high permeability zone which flows preferentially. K_V/K_H ratio calculated from VIT was used for reservoir simulation;
- multi-rate injection tests generated unexpected results, most likely caused by mechanical blockage of the perforations by debris from the surface equipment;
- a maximum rate-dependent skin of 80; and
- the injection test demonstrated that injection at the specified rates would be possible over the perforated interval despite what was thought to be significant mechanical blockages in the completion.

8.1.2.2 Vertical Interference Test

As part of the wireline programme of the 42/25d-3 appraisal well, three vertical interference tests (VITs) were undertaken at depths of 1580.4, 1522.8 and 1429.8mmD to determine formation permeability and quantify vertical to horizontal permeability ratio (K_V/K_H) to a depth of investigation deeper than would be seen using formation pretests (mini-DST). VIT was also used to identify any barriers to vertical flow over the interval tested.

Each test was planned to use four different pump rates of approximately 30 minutes each, followed by a build-up period of one hour. The VITs were interpreted using Transient Pressure Analysis (TPA) and reservoir simulation.

The mini-DST result for the first station (1429.8 m MD) was successful and recorded a formation permeability of 24 mD from the TPA and 18 mD from the numerical simulation, with a high degree of confidence. Stations two and three (1522.8 and 1580.4 m MD, respectively) could not be taken with similar confidence due to operational reasons; however the estimated results were within the range expected from the porosity-permeability trend. No barriers to vertical flow over the intervals tested could be detected. K_V/K_H ratios were determined from all three stations, ranging from 0.10 to 0.36. This range has informed the choice of the K_V/K_H range of 0.10 to 0.15 for reservoir simulation purposes.

8.2 Extent and Effective Hydraulic Communication of the Aquifer

Two separate reviews, one looking at the geology of the Bunter Sandstone formation in the UK southern North Sea within a RAOI that includes the Endurance storage complex, and the other looking at the historical pressure behaviour at Endurance and the nearby Esmond gas field, suggest that it could be in hydraulic communication with an area approximately 20,000km^2 to 23,000km^2 across.

A triangle drawn to approximate the area of the Bunter Sandstone formation bounded by faults to the west (the Dowsing Fault Zone), north and north-east, and the thinning to the east across the Base Cretaceous Unconformity on the Cleaver Bank High in the Dutch sector of the southern North Sea, was shown to extend to a width of 160km and a height of 240km, giving an area of about 20,000km^2.

Comparison of pressure gradient measurements in the 42/25-1 appraisal well drilled in 1990 and the 42/25d-3 appraisal well drilled in 2013 shows that the pressure in Endurance has fallen by 0.7bar in 23 years. This was probably caused by gas offtake from the Esmond field about 50km north-east of Endurance and the subsequent expansion of the aquifer to replace this void space. A material balance calculation estimated an aquifer with an area of 23,000km^2 to be required to result in the observed pressure decrease. If production from other gas fields in the Esmond Complex (Forbes and Gordon) were taken into account then an aquifer of twice the estimated size or compressibility would be required. It is therefore highly probable that Endurance is connected to a large regional aquifer which can help to limit the pressure increase associated with White Rose CO_2 injection and ensures that the sealing integrity of the cap rock is preserved.

8.3 Dynamic Simulation Models

Dynamic modelling has been performed using the Blackoil ECLIPSE 100 simulator (E100) from Schlumberger. Two classes of simulation models have been built:

1. The Base or Sub-regional simulation model which was used to address issues surrounding general plume development, storage capacity and pressure profile predictions
2. Simplified models consisting of the Simplified AoI simulation model and the Simplified injection model which were developed for the purposes of undertaking various sensitivities in an expeditious manner including the impact of reservoir properties on CO_2 migration and pressure profiles and the impact of completion strategy on CO_2 injectivity

8.3.1 Sub-regional Simulation Model

The dynamic model for simulation covers an area spanning about 42km by 11km, and thereby encompasses and extends beyond the Endurance anticline which measures about 25km long by 8km wide along the 1500m TVDSS contour close to the depth of the most likely spill. The outcrop to the east south-east of the Endurance structure has been included in the simulation model to enable the assessment of the effects of potential hydro-dynamic communication between Endurance structure and the outcrop during CO_2 injection. A Top Bunter depth map view of the resulting grid is shown in Figure 8.30.

Figure 8.30: Grid Model Using 200/400m Cells of Endurance Area of Interest

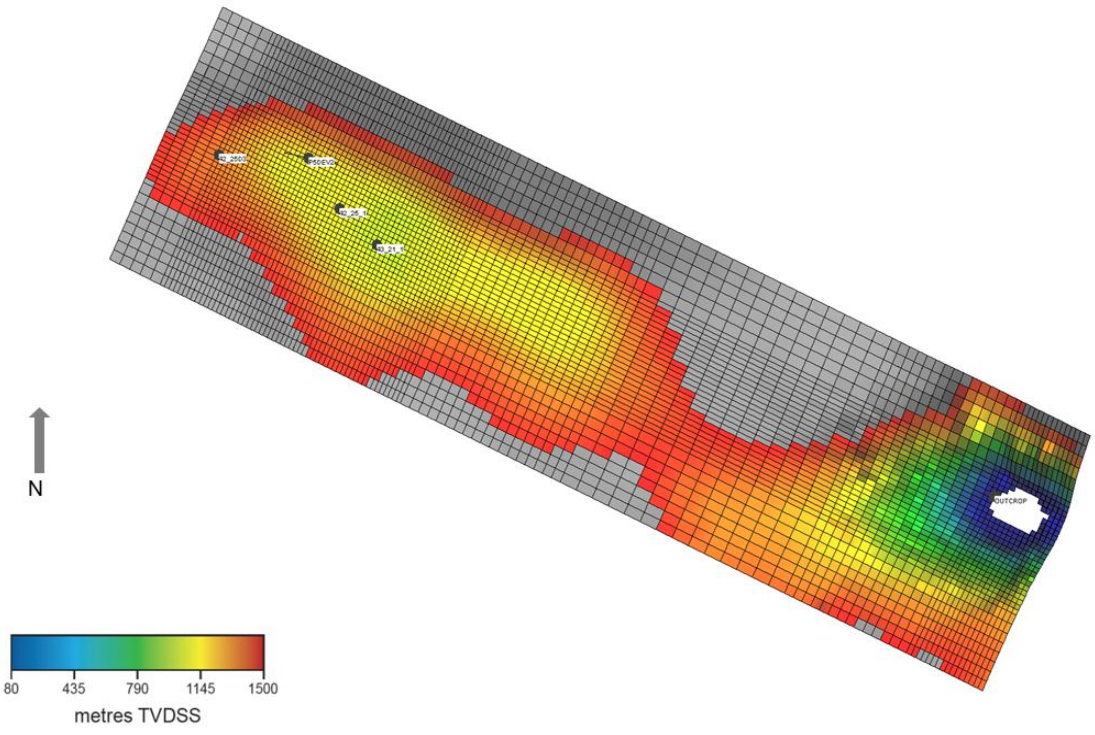

The Bunter Sandstone thickness in the AoI varies between 250 and 300m. The vertical grid cell resolution has been maintained regardless of which aerial resolution was adopted to adequately capture the buoyancy driven migration of injected CO_2. The average vertical grid cell size is about 2 m.

8.3.2 Upscaling for Reservoir Simulation

8.3.2.1 Simulation and Grid Design

A total of 125 cells in the vertical direction (N_z = 125) were used to model the whole Endurance structure volume (an average vertical cell size of 2 m over a 250m interval). Total grid size therefore increases very rapidly once X- and Y-direction grid cells (N_x and N_y) are accounted for. A 200m by 200m X and Y-directions cells would imply $N_{xyz} \approx 1.4$ million cells. It was decided to use relatively fine grids only in the area between the injection points and the crest of the structure to adequately resolve buoyancy-driven CO_2 migration. Control lines have therefore been drawn parallel and perpendicular to the main axis of Endurance to bound the core area of the model and also the outcrop (Figure 8.31).

Figure 8.31: AoI and Control Lines for Hybrid Gridding

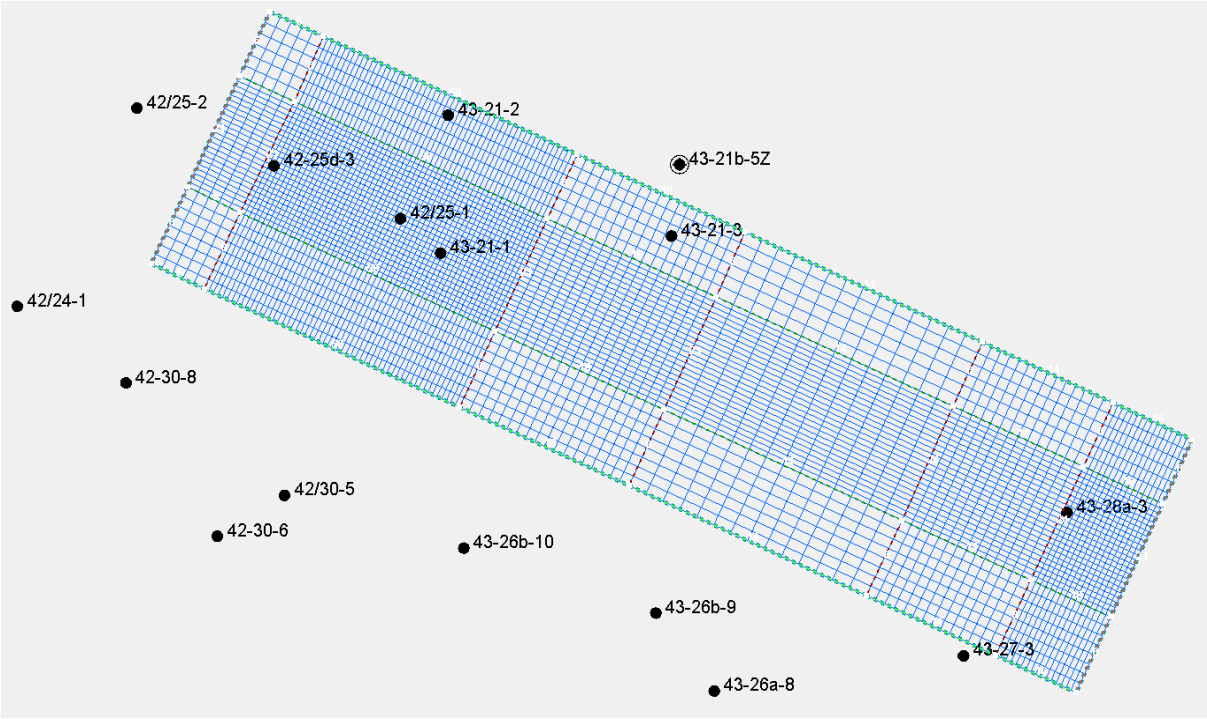

Using these control lines, a hybrid gridding scheme was developed that minimises the overall cell count whilst maximising detail where required. In the core area (and over the outcrop) the finest cell sizes have been implemented, these being:

- 100m by 100m (fine);
- 200m by 200m (intermediate); and

- 400m by 400m (coarse).

Stepping away from the core area in a given direction (X or Y) beyond the control lines, the cell size is allowed to increase by a factor up to two (to minimise material balance errors due to finite difference gradient approximation).

The net result is the total number of grid cells is reduced from $N_{xyz} \approx 1.4$ million to about $N_{xyz} \approx 1.0$ million cells. Whilst this is only a 29% saving in total cells, the reduction in computing time is approximately 80 to 100%. The actual grid dimensions for the three scales considered are shown in Table 8.6.

Table 8.6: Grid Sizes and Dimensions

Case	Core Δ/[m]	(N_x, N_y, N_z)	$N_x N_y N_z$	N_{active}
Fine	100	(258, 82, 228)	4,823,568	2,880,734
Intermediate	200	(129, 41, 228)	1,205,892	734,353
Coarse	400	(66, 21, 226)	313,216	194,896

Comparison of simulated CO_2 breakthrough times (the time for CO_2 to reach the 43/21-1 well at Top Bunter) and peak pressure responses between reservoir models incorporating the three grid sizes showed minor differences. Preference has therefore been given to the coarse or intermediate models for the reservoir engineering modelling runs since they run much quicker, see Table 8.7. Where appropriate, verification runs have been done using the fine scale model.

Table 8.7: CO_2 Time to Crest and CPU Time by Grid Size

Model	Break-Through Time [yr]	CPU Time to 2100 [hr]
Coarse	3.5	0.17
Intermediate	3.9	0.53
Fine	4.2	4.05

8.3.2.2 Up-scaled Parameters

The key parameters required by the simulation model are the NTG ratio, porosity and permeability. NTG and porosity have been upscaled from a fine scale geological model to a coarser scale simulation model using simple pore volume weighted arithmetic averaging. The NTG array depends on the minimum porosity or porosity cut-off below which a volume of rock is considered non-reservoir or non-net. The dynamic effects of porosity cut off was tested on the intermediate grid using the values of minimum porosity shown in Table 8.8 which also shows the resulting average porosity and Water Initially in Place (WIIP).

Table 8.8: Average Porosity and Water Initially in Place versus Porosity Cut-off

Minimum Porosity/[fraction]	Average Porosity/[fraction]	WIIP 10^9 m^3
0.04	0.189	20.8
0.07	0.192	20.5

Minimum Porosity/[fraction]	Average Porosity/[fraction]	WIIP 10^9 m^3
0.12	0.202	18.6

As the minimum porosity is increased, the resulting average porosity increases but the WIIP decreases as more of the GRV is moved from reservoir to non-reservoir. The dynamic pressure profile shows the peak and asymptotic shut-in pressures increasing as WIIP decreased with increase in cut off, see Figure 8.32.

Figure 8.32: Sensitivity of Crestal Pressure to Porosity Cut-Off

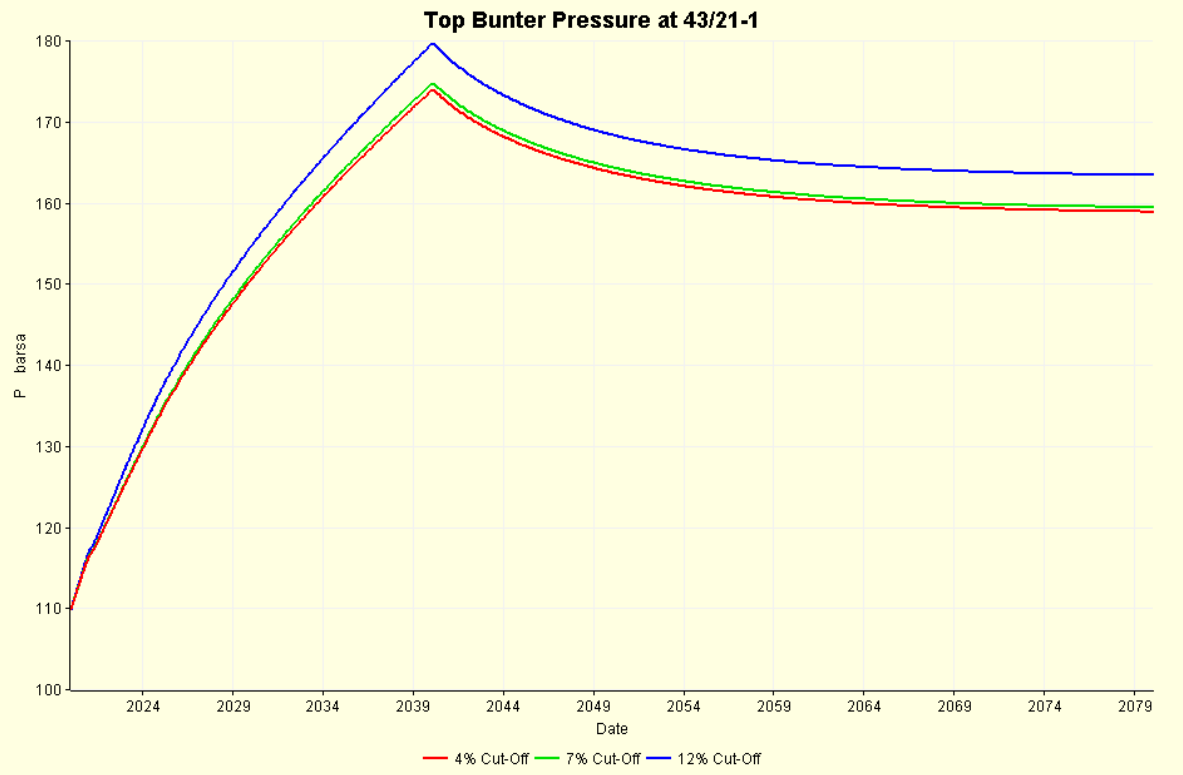

The mid-case porosity cut-off of 0.07 was selected for use in the modelling work.

The Top Bunter porosity map corresponding to that shown in Figure 8.30 is shown in Figure 8.33. Note the minimum porosity here was set to 0.10 and any cells with values less than that are coloured grey. The outline of the seismic phase reversal is clearly visible.

Permeability was distributed based on the upscaled porosity distribution according to Equation 8.4. Regardless of the grid size and permeability upscaling algorithm used, the permeability was multiplied by a factor such that the (arithmetic) average will be close to 271 mD for the pore volume within Endurance above 1500m TVDSS. The Top Bunter X-direction permeability distribution corresponding to that shown in Figure 8.30 is shown in Figure 8.34; note a logarithmic distribution has been used [0.3 to 3000.0mD]. It is assumed that areally permeability is homogeneous; Y-

direction permeability equals X-direction permeability. The average K_V/K_H was taken to be 0.15 as indicated by the VIT run in well 42/25d-3.

Equation 8.4 $$\log_{10} K = 15.6\phi - 0.9$$

Figure 8.33: Top Bunter Porosity Distribution

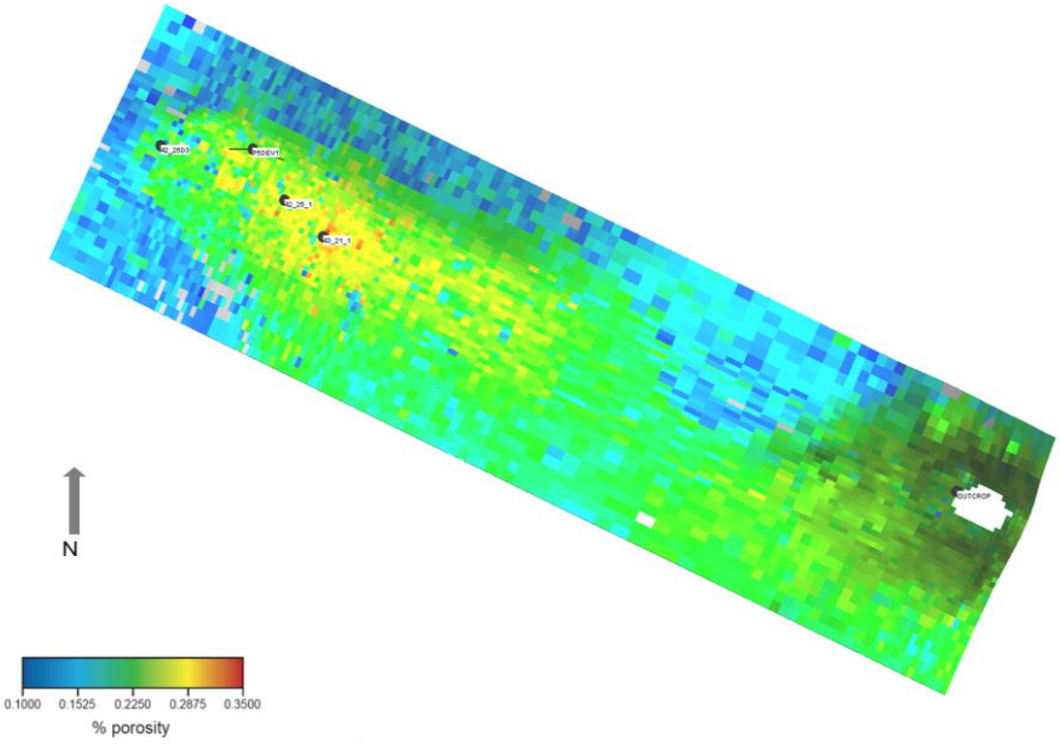

Figure 8.34: Top Bunter Permeability Distribution

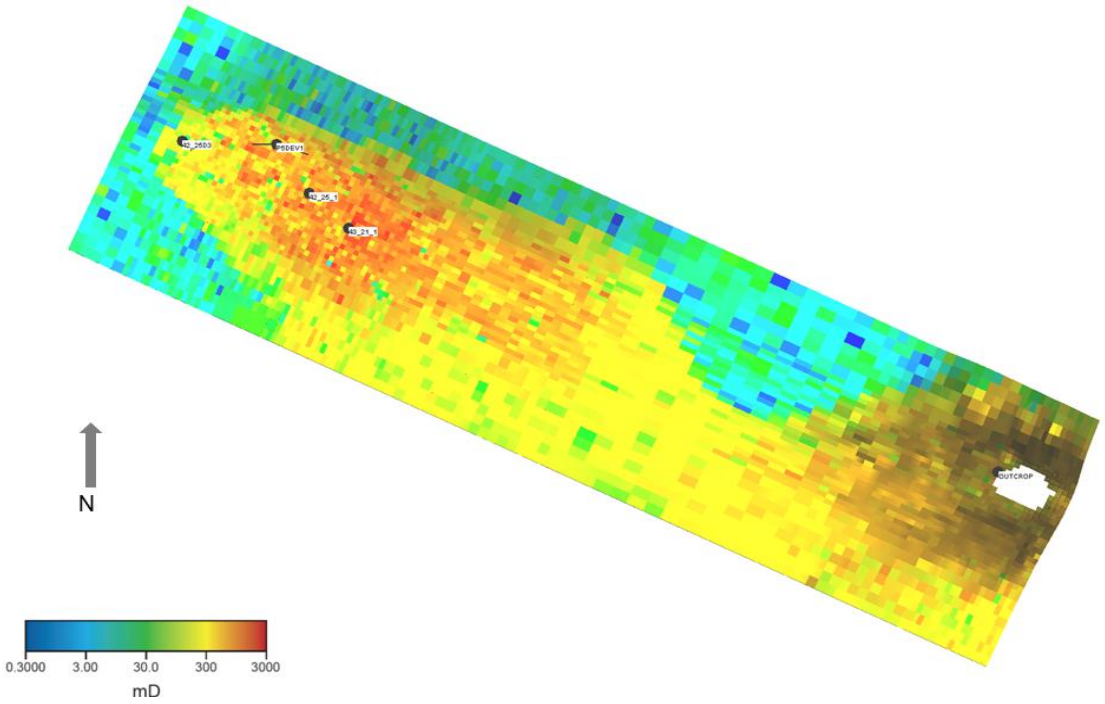

8.3.3 Fluid Properties

All simulations have generally been performed at constant reservoir temperature, assuming immiscible CO_2 and brine with no solid phase. The localised (near well bore) cooling of the reservoir from the injection of cold CO_2 was studied using a simple model, see Section 8.3.16. The possible implications of CO_2 dissolution has been considered separately using somewhat different dynamic modelling methodologies and software other than Eclipse 100. The details of how fluid properties have been modelled under these conditions will be reported accordingly.

8.3.3.1 CO_2

The CO_2 stream composition used in the reservoir simulation model is a typical composition notionally indicative of the commingled stream from multiple prospective CO_2 emitters (power stations). This composition is given in Table 8.9 and conforms to the National Grid Safe Pipeline Transportation Specification for CO_2 Mixtures.

Table 8.9: Notional CO_2 Stream Composition

Component	Mnemonic	Mole Percent
Carbon Dioxide	CO_2	96.0
Argon	Ar	0.6
Nitrogen	N_2	2.0
Hydrogen	H_2	0.6
Oxygen	O_2	0.8

In terms of phase behaviour within the reservoir, the main effect of the impurities is to increase the effective critical pressure and critical temperature of pure CO_2 which are 73.9bar and 31.1°C. As long as the pressure in the system stays above 85.0bar, the mixture will be in its super-critical state.

8.3.3.2 Brine

Brine has been modelled using data derived from brine samples taken in wells 42/25-1 and 42/25d-3. An in situ brine density of 1169.2 kg/m^3 was determined from the RFT (repeat formation tester) pressure gradient measurement of 0.1147bar/m in well 42/25-1. In situ brine salinity was estimated at 243,000mg/kg using the Rowe and Chou correlation, an oil and gas industry standard, which takes in density, pressure and temperature as input. The salinity trend observed from the MDT measurements in 42/25d-3 have also been incorporated into the brine model.

The concentration of anions and cations from the three MDT samples along with the sample depths, pressures and temperatures are shown in Table 8.10.

Table 8.10: Concentration of Anions/Cations from MDT Samples

		MDT Water Samples		
Sample	Unit	1.04	1.09	1.13
MD	ft	5167.5	4722.0	4634.0
MD	m	1575.1	1439.3	1412.4
Pressure	bar	171.48	155.75	152.65
Temperature	C	64.35	60.21	59.39
TDS	mg/kg	253426	242549	241832
pH		6.84	6.61	6.54
Sulphate	mg/kg	296	359	385
Chloride	mg/kg	154146	148780	148164
Fluoride	mg/kg	0.15	0.12	0.10
Bromide	mg/kg	473	460	444
Total BiCarb	mg/kg	51	43	34
Sodium	mg/kg	85512	79664	79953
Potassium	mg/kg	1400	1469	1483
Calcium	mg/kg	8858	8610	8037
Magnesium	mg/kg	2543	3014	3192

8.3.4 Relative Permeability and Capillary Pressure Functions

Both analogue and measured Endurance CO_2-brine relative permeability (Kr) and capillary pressure data were used at different stages in the assessment of the likely dynamic behaviour of the Endurance storage site.

8.3.4.1 Measured Endurance Data

The programme of experiments that has been used to generate relative permeability from core taken from well 42/25d-3 has already been summarised in Section 8.1.1 of this document. As Figure 8.25 shows the Klinkenberg permeability was found to be always greater that measured effective water permeability and this led to the choice of Klinkenberg permeability as the base permeability for calculating the relative permeability in order to avoid the peculiar situation of having CO_2 relative permeability at irreducible waster saturation being greater than 1.0. However, the Endurance storage site is currently brine filled; $S_w = 1$. Therefore, the effective water permeability must be taken to be the absolute permeability K_{abs}, since this is the permeability measured from the dynamic tests undertaken on the 42/25d-3 appraisal well, which include the production well test, the VITs and even the MDT pressure measurements. Because $K_w = K_{abs}$, it means $K_{rw}(S_w=1) = 1$. Selecting (effective) water permeability as the base (absolute) permeability in relation to which relative permeability is defined means the data generated in the SCAL analysis had to be re-based. In Figure 8.35 the re-based relative permeability is compared to the originally generated curve from SCAL laboratory analysis.

Figure 8.35: (a) SCAL Analysis- Water/ CO_2 Relative Permeability Curves and (b) Re-Based Water/CO_2 Relative Permeability Curves

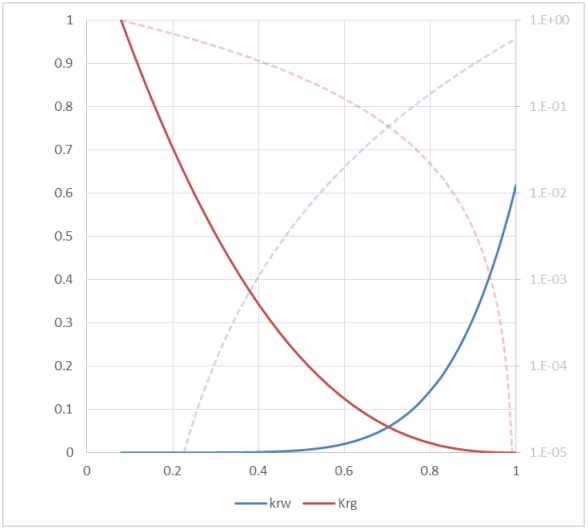

a

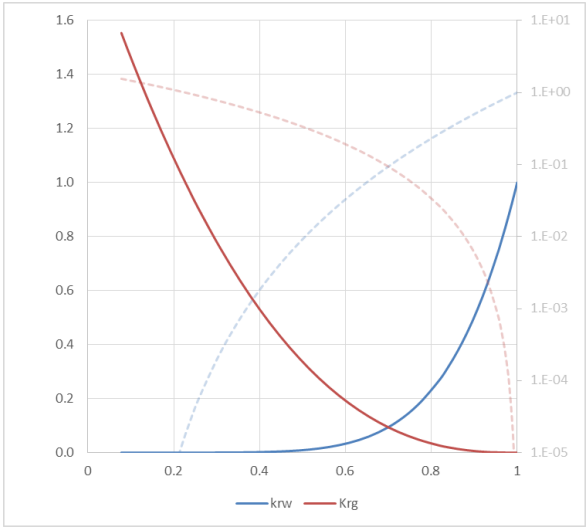

b

Note the dashed lines refer to the logarithmic axis shown as the right-hand y-axis

The Corey exponents and the irreducible water saturation were found to be functions of the Klinkenberg permeability, the Corey exponents being weakly so as Table 8.11 and Figure 8.36 show respectively. The trapped gas saturation S_{gt} is shown in Figure 8.20 to be a function of S_{wi} that is $S_{gi} = 1 - S_{wi}$. The Land model of S_{gi} versus S_{gt} in Figure 8.20 was preferred to the Spiteri model because of the tendency of the Spiteri model to generate a maximum at $S_{gi} < 1$ (giving two values of S_{gi} for a single value of S_{gt}) which could cause numerical problems.

8.3.4.2 Capillary Pressure

MICP and centrifuge methods were used to measure capillary pressure. It was found that the MICP data was best for determining the entry pressure; $P_c(S_w=1) > 0$ whereas the centrifuge data was best at describing the behaviour at low (water) saturation. The final capillary pressure behaviour was generated from a Skjaeveland model:

Equation 8.5

$$P_c = \frac{C_w}{\left(\frac{S_w - S_{wi}}{1 - S_{wi}}\right)^{a_w}}$$

Here the coefficients were determined to be (C_w, a_w) = (1.7, 0.2).

Understanding and quantifying the non-zero entry pressure $P_c(S_w=1)$ was a critical step in determining the relative permeability data shown in Figure 8.35 as in practical terms this data was generated using a core flood simulator called SENDRA using the measured capillary pressure data as one of its sets of input data.

Figure 8.37 shows the drainage and imbibition "base" relative permeability data for CO_2 and brine as well as the capillary pressure curve as implemented in ECLIPSE. Note that the values of the key Corey end-points and exponents have been indicated on the figure. The imbibition water relative permeability follows the drainage curve except that the maximum water saturation is now $1 - S_{gt}$.

The imbibition CO_2 relative permeability curve starts at [S_{wi}, $K_{rg}(S_{wi})$] and terminates at S_{gt}. These dependencies have been modelled using the ECLIPSE End-Point-Scaling functionality (EPS).

Table 8.11: Variation in Endurance Corey Water (Nw) and Gas (Ng) Exponents

Sample	K_L/[mD]	N_w	N_g
S193, S115, S167	276.0	6.0	2.5
S197 *	13.6	4.8	2.4
S90	173.0	5.0	3.0
S111, S127	1583.0	4.7	2.7

* Sample S197 was disqualified based on QC-analysis.

Figure 8.36: Irreducible Water Saturation versus Klinkenberg Permeability

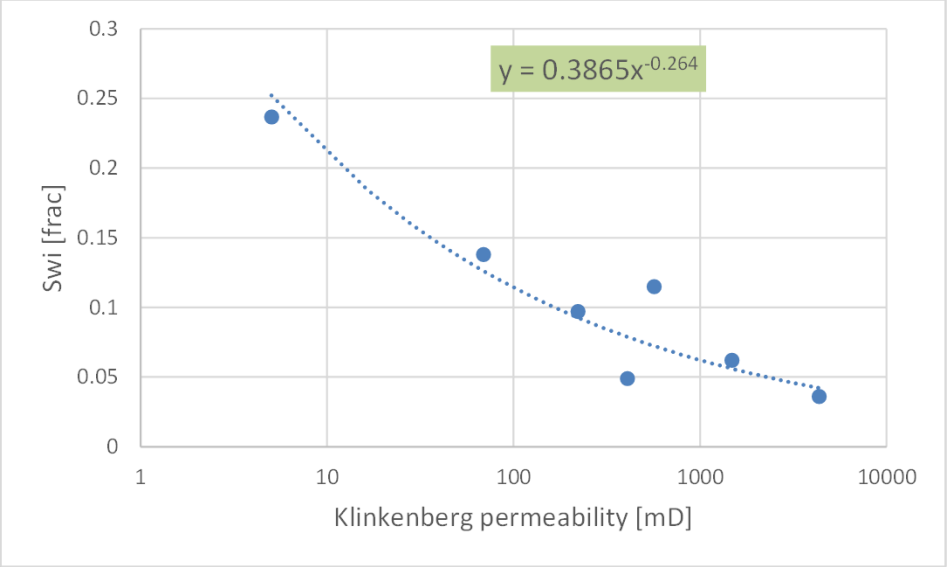

Figure 8.37: Drainage/Imbibition Gas/Water Relative Permeability Data for Endurance

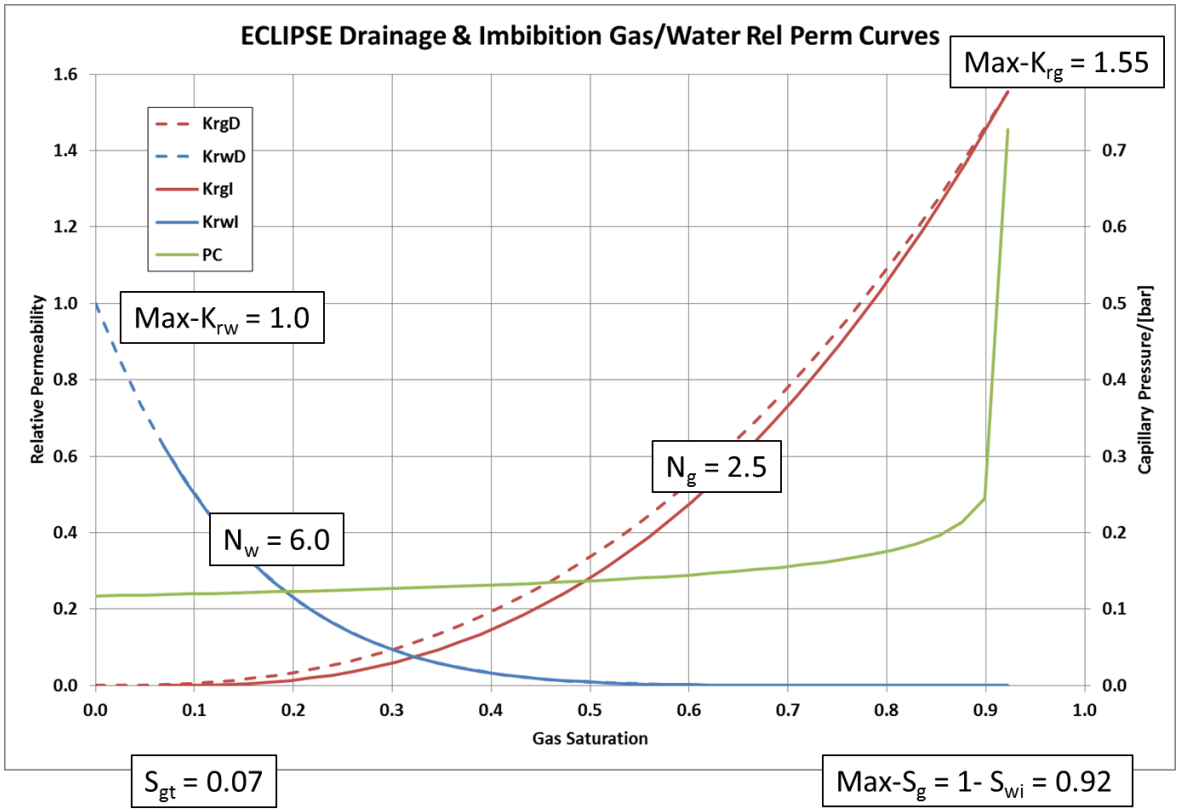

8.3.4.3 Endurance Relative Permeability Analogues

Whilst awaiting Endurance SCAL results, a literature survey was conducted to assess the suitability of published CO_2/brine relative permeability (Kr) and capillary pressure data for use in the reservoir model. The CO_2-brine Kr data determined using a Viking sandstone reservoir sample as reported in Reference 13 in Section 9 and reproduced in Figure 8.38, is a commonly used analogue data for simulation of CO_2 storage in sandstone formations. There is however significant differences between the physical properties of the Viking sandstone formation compared to the Endurance Bunter Sandstone. The Viking sandstone sample was taken from a depth of 1343 m where the pressure and temperature are 86bar and 35°C with an average porosity and permeability of 0.195 and 21.7 mD and a brine salinity of 28,300mg/kg. The Endurance Bunter Sandstone formation on the other hand has average porosity, permeability and salinity of 0.192 (7% cut-off), 271 mD (well test), and 250, 000mg/kg, respectively.

A closer analogue to the Endurance Bunter Sandstone was found in the Ketzin core Kr measurements as shown in Figure 8.39 (reproduced from Reference 8 in Section 9). The Ketzin core was recovered from the Stuttgart formation in the late Triassic Keuper age rocks that overlie the early Triassic Buntsandstein (Endurance Bunter equivalent) formation. In flow tests, the permeability was measured to be between 50 and 100mD whilst tests on core showed values range between 500 and 1000mD. The brine salinity was reported as 220,000mg/kg. The values of the Corey coefficients are reproduced in Table 8.12. Results obtained from these analogue data have been interpreted as model sensitivities on Kr behaviour.

Figure 8.38: Viking Relative Permeability and Capillary Pressure Data

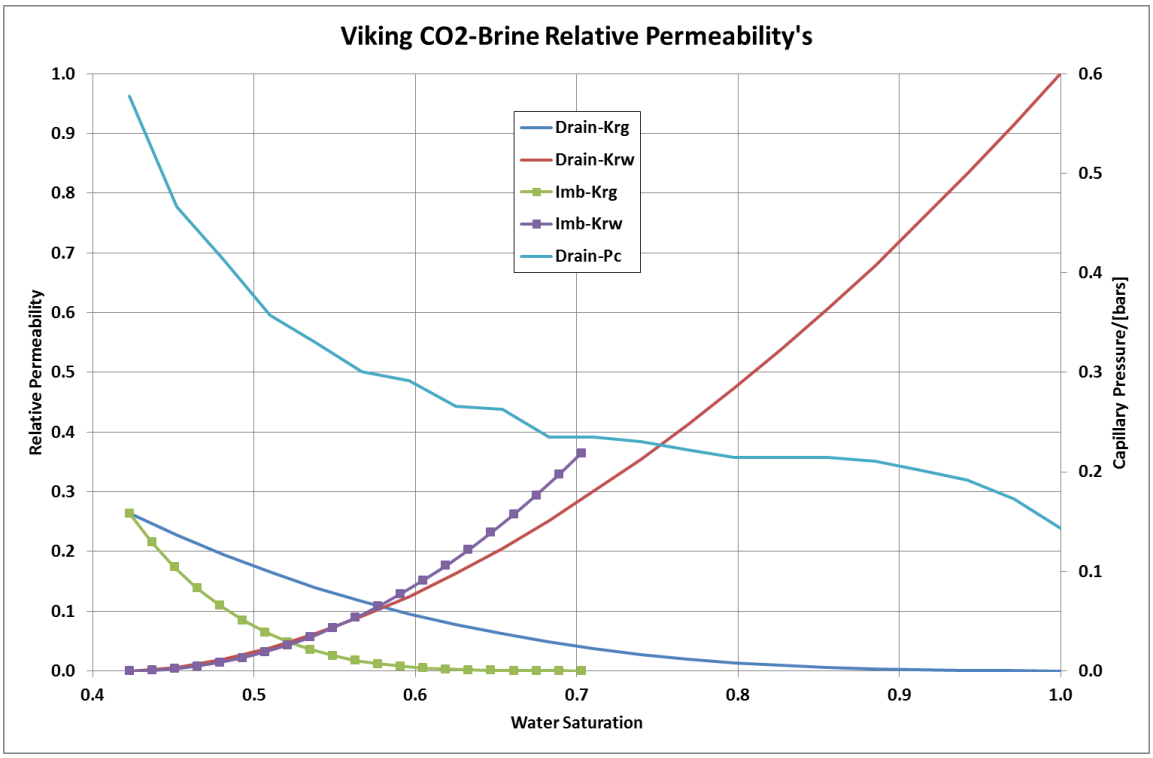

Table 8.12: Ketzin Corey Relative Permeability Coefficients

Parameter	CO_2	Brine
Exponent	1.50	5.50
Drainage-Residual	0.05	0.15
Imbibition-Residual	0.30	0.15

Figure 8.39: – Ketzin Relative Permeability and Capillary Pressure Curves

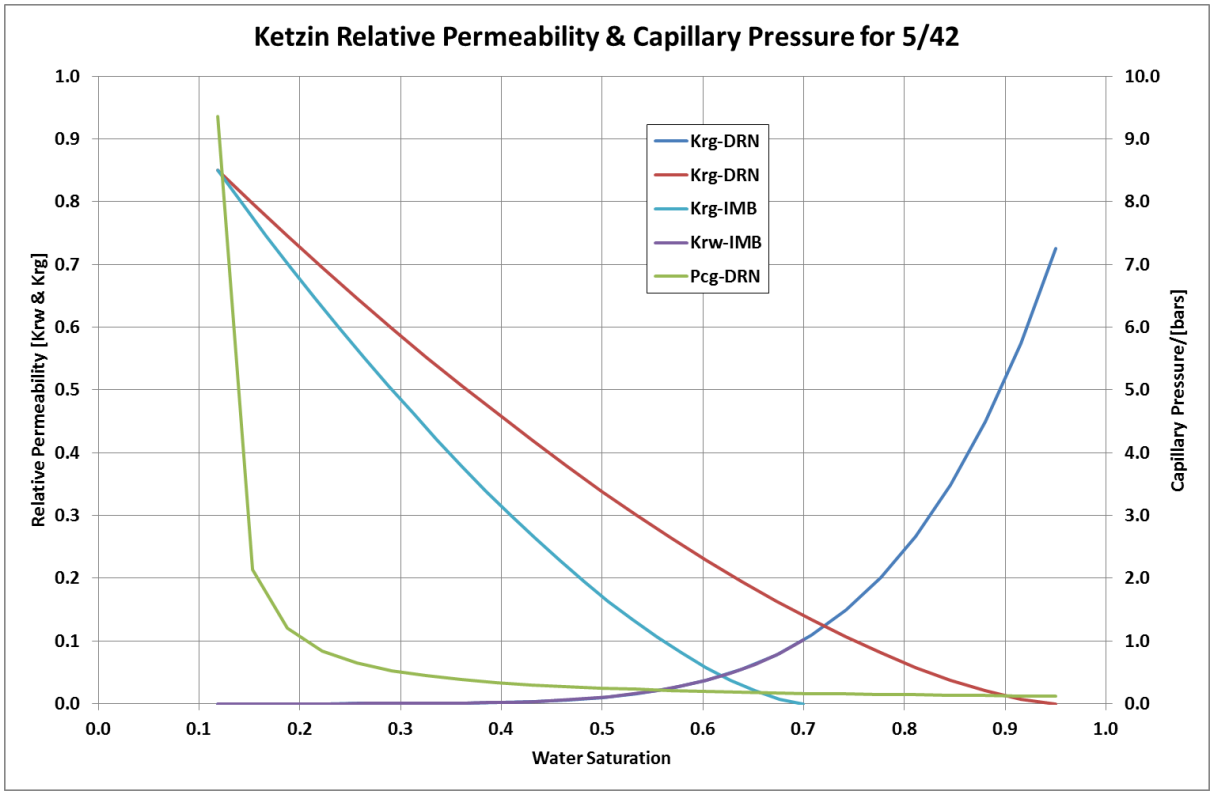

The capillary pressure function is given by:

Equation 8.6

$$P_c = \left(\frac{S_w - S_{wi}}{a} \right)^m$$

Where:
a = 0.096
m = -0.989
Of course Equation 8.6 becomes infinite as $S_w \rightarrow S_{wi}$ so a small offset is introduced to keep P_c finite.

Note the maximum gas (CO_2) relative permeability in Figure 8.39 of K_{rg}^M = 0.85 is 3.2 times larger than the corresponding value in the Viking data (Figure 8.38) and so the CO_2 will move proportionally faster towards the crest of the structure.

8.3.5 Initialisation

Pressure, temperature and salinity (via collection of brine samples) measurements were taken from the 42/25d-3 appraisal well.

8.3.6 Pressure Variation

The model uses a datum pressure of 140.0bar at a reference depth of 1300m TVDSS and the pressure gradient is taken to be 0.115bar/m. These values have been derived from the combined interpretation of RFT and MDT pressure measurements in wells 42/25-1 and 42/25d-3 respectively.

8.3.6.1 Temperature Variation

A reference temperature of 55.9°C at 1300m TVDSS was calculated from a temperature gradient of 0.0305°C/m which was determined from the MDT long duration tests; pressure points and brine sampling.

The CO_2 injected into Endurance will be somewhat cooler than the reservoir given that it will have travelled along a 90km pipeline and the seabed temperature in this part of the UK southern North Sea is known to vary between 5 and 15°C winter to summer. The CO_2 will heat as it travels down the injection wells into the reservoir and this has been estimated to be about 10°C although this will of course depend critically on the flow rate. It has been assumed that the minimum temperature of the CO_2 at the perforations is 15°C (in winter). The injection of CO_2 which is cooler than the reservoir temperature is likely to cause thermal fracturing. For this reason the perforation strategy prescribes the perforation of the deeper sections of the injection wells. A 185 m perforation interval across the L1 zone of the Bunter Sandstone has been shown to support the White Rose maximum design CO_2 injection rate of 2.68MTPA whilst allowing for ample distance between the Röt Clay cap rock and any potential thermally induced fractures in order to provide for future perforating should existing perforations become plugged or collapse, or the near wellbore becomes damaged.

8.3.7 Salinity Variation

Analysis of the MDT brine samples suggests that there is a variation of salinity with depth as shown in Figure 8.40.

Re-arranging the Equation of the fitted trend line gives a Total Dissolved Solids (TDS) (mg/kg) = 74.6 (TVDSS (m) + 1808) so that at the seabed location of the outcrop where TVDSS = 65 m, then TDS ≈ 135,000mg/kg.

It is uncertain whether the outcrop could maintain such a linear gradient in salinity and have a TDS at seabed of around 135,000mg/kg (whilst sea-water salinity is around 35,000mg/kg). Petrographic analysis of cuttings in well 43/28a-3 that passes through the western side of the outcrop suggests flow of meteoric water in the past and also that the high quality Bunter and more recent Quaternary sands are open to flow. The outcrop is by default open to flow and a sensitivity analysis has been performed in which it is considered closed to better characterise its dynamics during and post CO_2 injection.

Figure 8.40: TDS Variation With Depth From 42/25d-3 MDT Samples

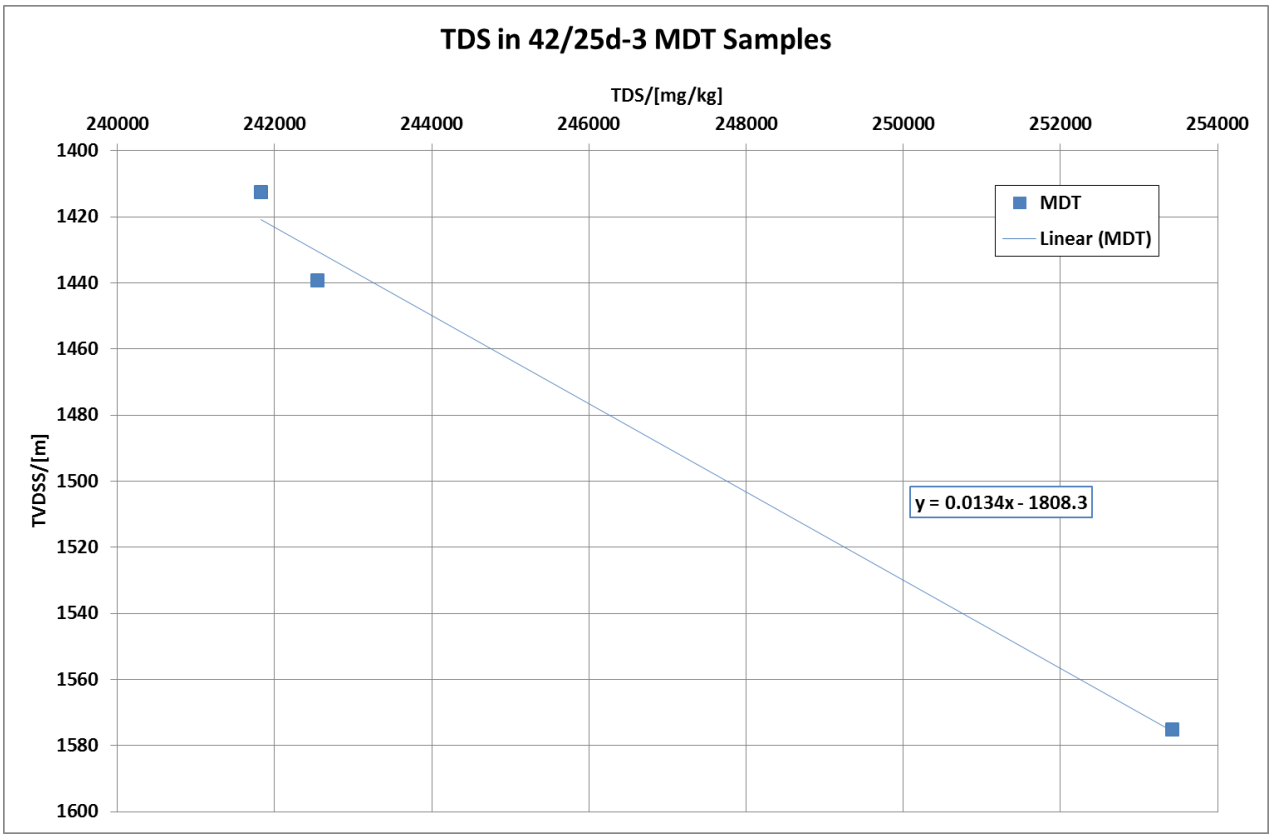

8.3.8 Greater Bunter Size and Properties

Even though an area of about 460km^2 is being considered with a pore volume of around 20.0x10^9 m^3 (the Endurance pore volume measured to the most likely spill is about 4.8x10^9 m^3), it is considered most likely that Endurance is connected to a much larger volume of the Bunter Sandstone formation, see Section 8.2 for a summary of the arguments.

To avoid the prohibitive simulation Central Processing Unit (CPU) requirement, the greater Bunter was not modelled explicitly. Instead, the Carter-Tracy aquifer model in Eclipse has been used. The two parameters which define the model are the time constant τ (with dimensions of time) and the aquifer influx coefficient β (with dimensions of total influx per unit pressure change). These parameters are defined by the following equations:

Equation 8.7

$$\frac{1}{\tau} = c_1 \frac{K_A}{\mu_w \phi_A c_T r_o^2}$$

Equation 8.8

$$\beta = c_2 H f \phi_A c_T r_o^2$$

The variables in Equation 8.7 and Equation 8.8 are defined in Table 8.13 along with values where appropriate. Some of the variables are explained by use of the schematic diagrams shown in Figure 8.41.

Figure 8.41: Schematic of the Carter-Tracy Aquifer Model

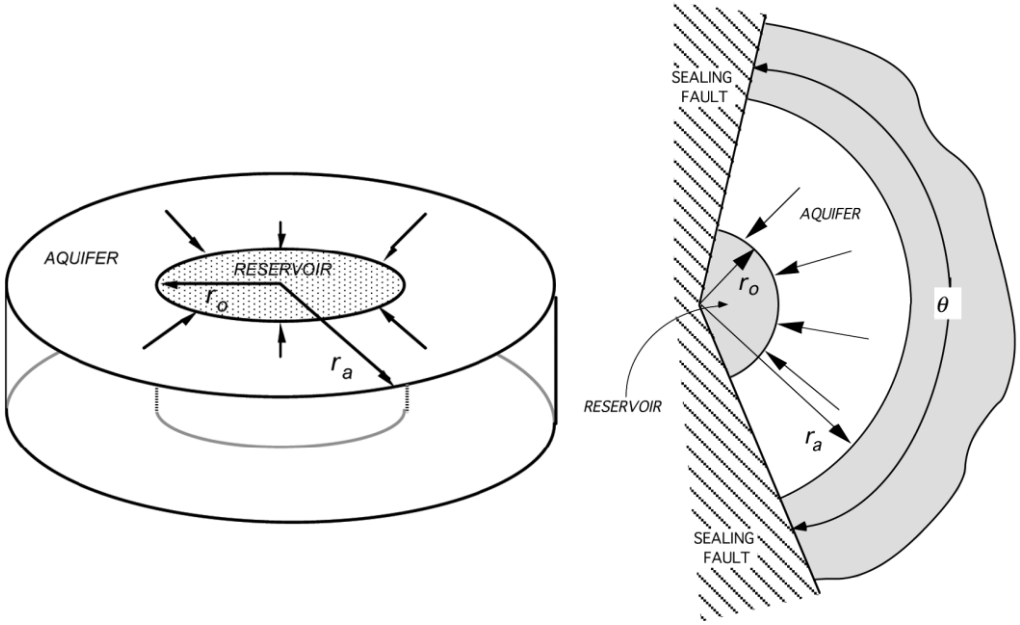

Table 8.13: Parameters in the Carter-Tracy Aquifer Model

Symbol	Parameter	Default Value
K_A	Aquifer Permeability	mD
μ_w	Aquifer Brine Viscosity	1 cP
ϕ_A	Aquifer Porosity	
c_T	Total (Rock and Brine) Compressibility	85×10^{-6} /bar
r_o	Reservoir Radius	11,000m
H	Aquifer Thickness	250m
f	Fraction of Angle Subtended	

For the application of the Carter-Tracy model, rather than a rectangular AoI whose major and minor axes are 40km and 10km, the AOI is considered to be a circle with a radius of 11km; equivalent area (hence the value of r_o shown in Table 8.13). It has been argued that the aquifer attached to 5/4 extends to an area in excess of 20,000km^2. This implies a pore volume of about 1 x 10^{12} m^3, assuming an average thickness of 250m and porosity of 0.19.

8.3.9 The Outcrop

The AoI for the dynamic model has been chosen to explicitly include the outcrop so that sensitivity to whether it is connected to Endurance and open to flow or not can be studied. The geological interpretation of the outcrop bathymetry is shown in Figure 8.42 whilst Figure 8.43 shows the map and sides views of the out crop in the simulation model. Note the area of Bunter Sandstone thought to be exposed at the seabed is around 1.4km^2. Even if only a fraction of this area is open to flow, it is likely to have significant production for minimal pressure increase; a very large Productivity Index (PI).

Allowing the outcrop to flow to the sea if the whole system is pressured up is achieved by defining a super-well at the edge of outcrop within the ring of modelled cells with a transmissibility that is 100 times greater than that of a typical well in order to capture the expected high PI.

Figure 8.42: Geological Interpretation of Outcrop Seabed Bathymetry

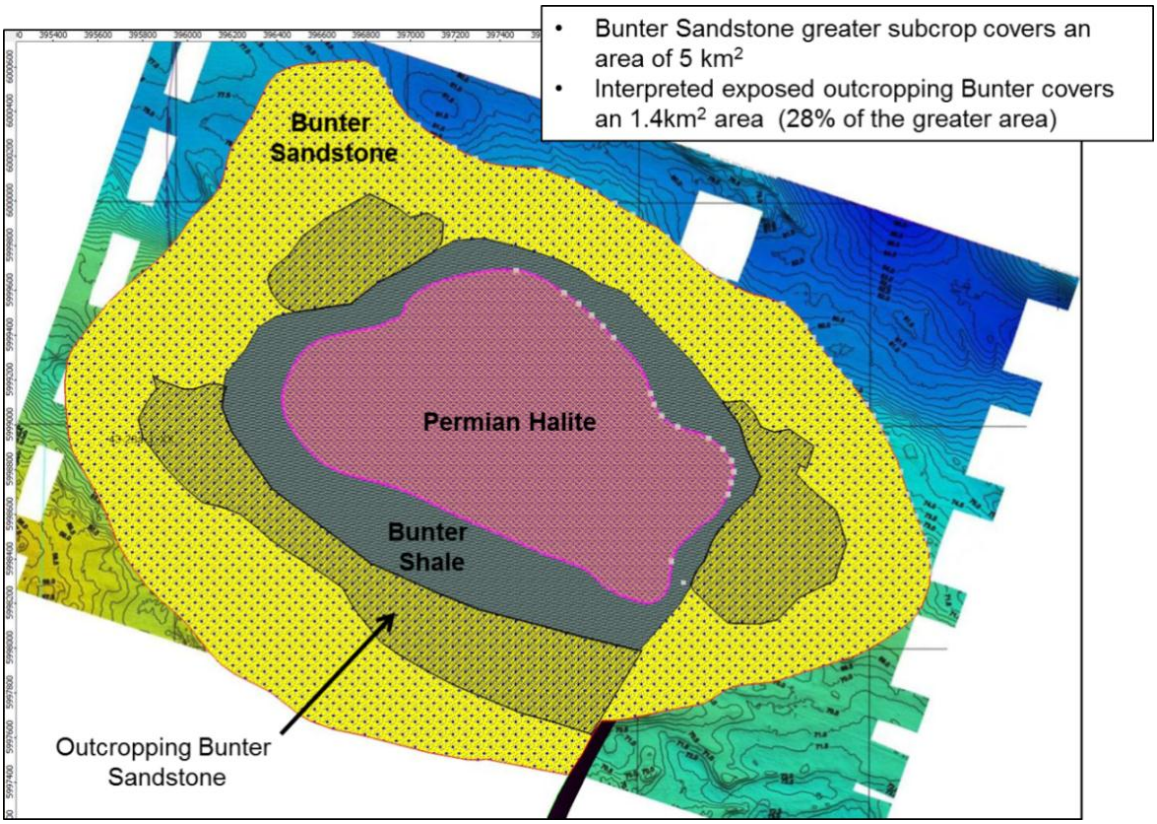

Figure 8.43: Map and Side-Views of the Outcrop in the Simulation Model

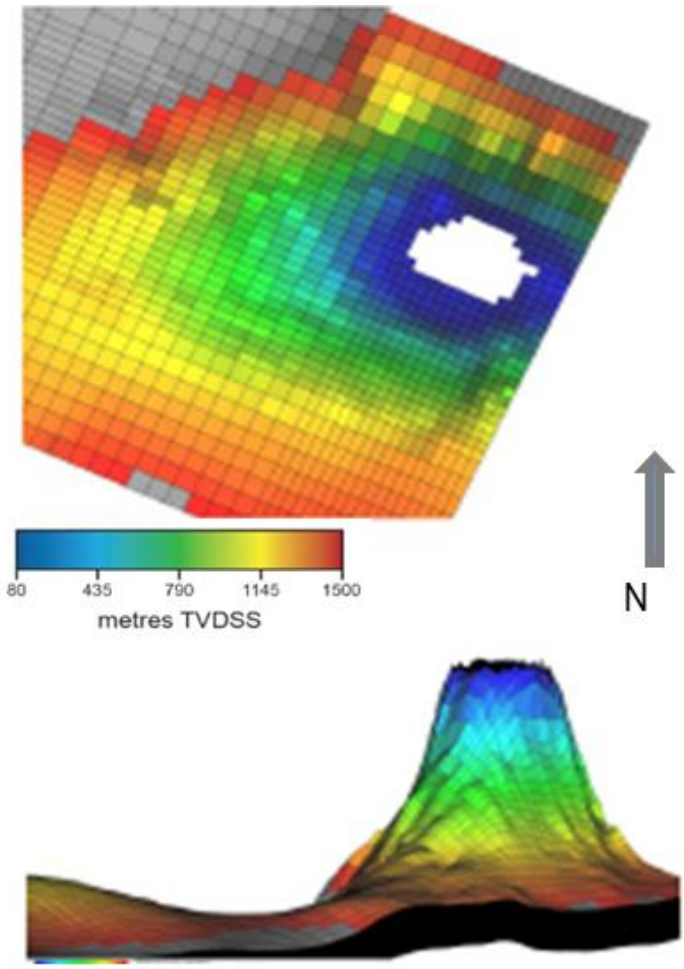

8.3.10 Simplified AoI Simulation Model

To allow more sensitivity runs to be made, a simplified simulation model has been constructed which incorporates the key features of the detailed model. Firstly the model is about 50km long, 12km wide and 250m thick. Porosity is made a linear function of depth with 0.28 at Top Bunter and 0.12 at Bottom Bunter. Horizontal permeability is a function of porosity as per Equation 8.4and vertical permeability is set using $K_V/K_H = 0.15$. The pore volume of the model is adjusted such that the total volume is about the same as the detailed model of 1.9×10^{10m3}. Vertical grid cell resolution is 2 m throughout the 125 layers (to make a total thickness of 250m). The areal grid resolution varies as shown in Figure 8.44.

Figure 8.44: Top Bunter Depth of Simplified Model

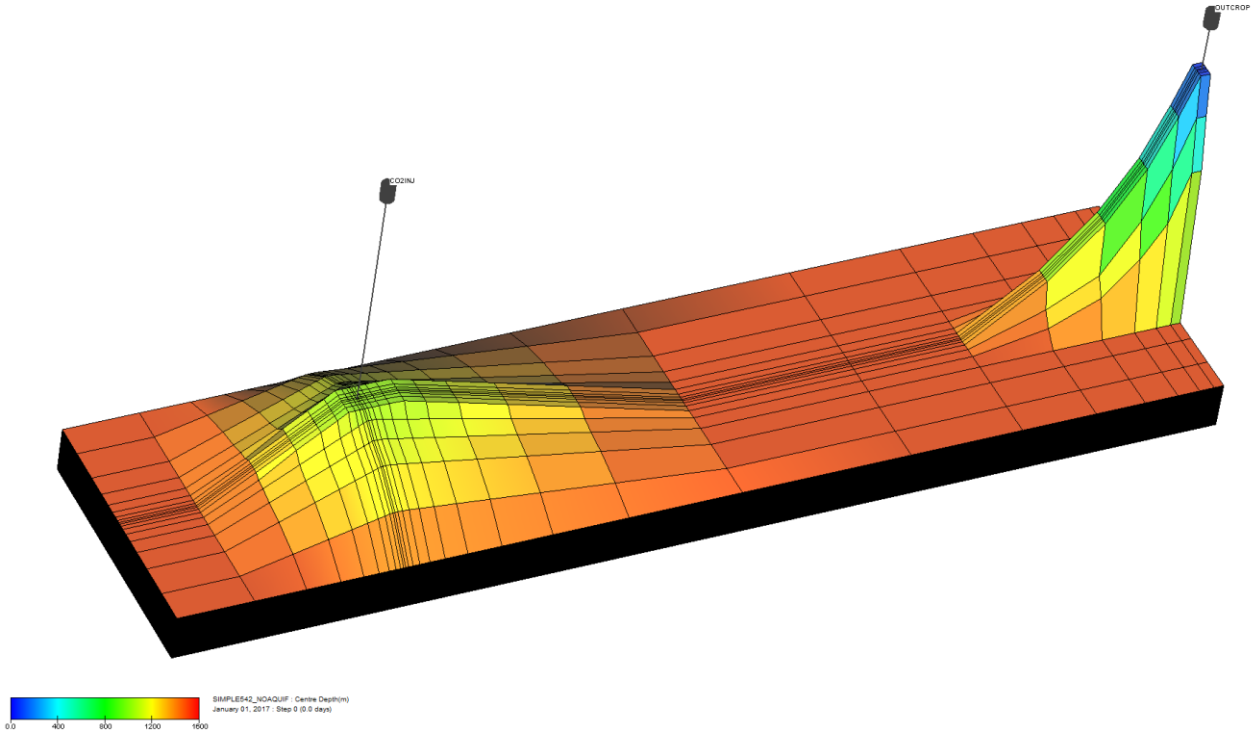

8.3.11 Simplified Injection Model

Even the fine scale grid considered in Section 8.3.2.1 was too coarse for looking at issues surrounding injectivity which are dominated by near well bore effects. Therefore the type of grid developed in the previous section has been modified to study sensitivities around injectivity as discussed in Section 8.3.15.

This model has been developed to study injectivity issues by adding finer grid cells to a core area whose extent has been defined by the horizontal departure of a well drilled through the Bunter sand at 50 to 60^{o} orientation from the vertical. A grid size of (ΔX, ΔY) = (50m, 50m) has been adopted with (N_x', N_y') = (21, 21) cells for this core area. Outside this area, the grid cells are increased by a factor of 1.5 until an area comparable to that of the Greater Bunter in the UK southern North Sea has been covered. A map view of the grid showing the ΔX-values is shown in Figure 8.45 and a cross-section in Figure 8.46

Figure 8.46: West-East Porosity Cross-section through Injection Model

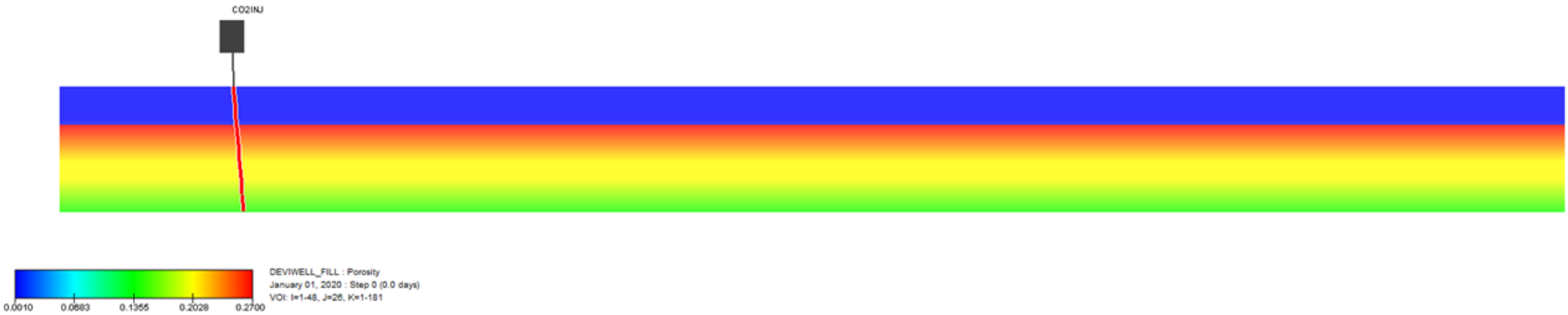

Both Röt Halite and Röt Clay have been included in this model to permit quantification of the conductive cooling created from injecting cold CO_2 through the wells. Porosity and permeability of the halite layers are set to 0.001 and 1 μD whilst the values in the clay are set to 0.005 and 10 μD. The porosity in the Bunter Sandstone is made a linear function of depth with a value of 0.27 at Top Bunter and 0.14 at Bottom Bunter. Permeability of the Bunter Sandstone is calculated using Equation 8.4.

Figure 8.45: Simplified Grid to Study Injection Issues

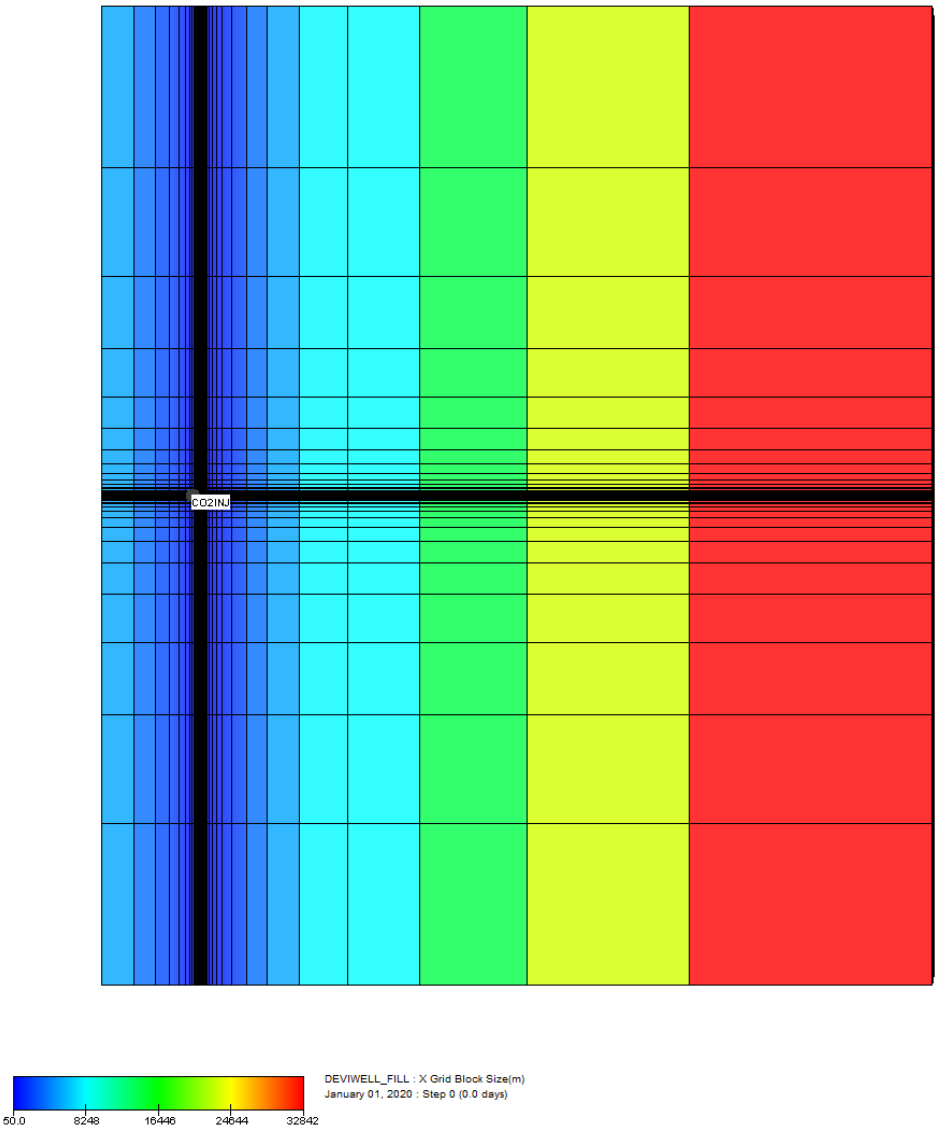

Figure 8.46: West-East Porosity Cross-section through Injection Model

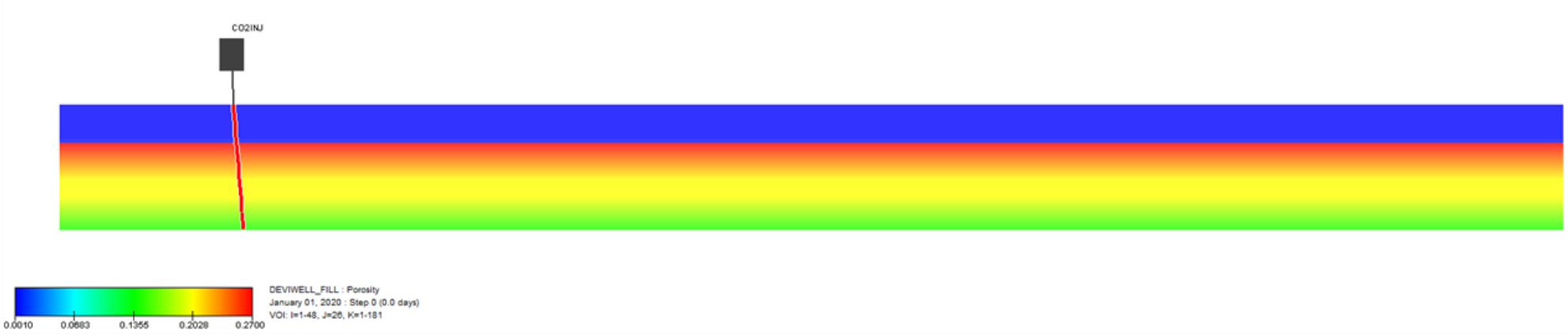

8.3.12 Wells

The injection wells have been designed to ensure ease of access during potential well interventions: wellheads will be located on a platform and a maximum well trajectory of less than 60° has been adopted to ensure operations can be undertaken via wireline. Since all wells will be set on a single platform it is important to perforate as deep as possible to maximise the separation of the plumes generated from each well whilst ensuring the injected CO_2 remains within the confines of the structure defined by the shallowest possible spill point.

Injecting the CO_2 as deep as possible has other advantages, namely:

- maximises the offset from the cap rock; delays the CO_2 arrival time to the crest of the structure;
- maximises opportunity for residual and dissolution trapping; and
- minimises risk of thermal fracturing of the cap rock.

8.3.12.1 Well Locations and Trajectories

The location chosen for the platform is at 366882 m Easting's and 6012790m Northing's in UTM Zone 31 on the ED50 datum.

The deviation of the three specified CO2 injection wells (55o to 60o from the vertical) is shown in Figure 8.47. The red and purple images in the map overlay are overburden faults. Avoidance of overburden faults was one of the criteria which dictated the well placement.

8.3.12.2 Perforation Interval

As stated above, the perforation strategy is to perforate the wells as deep as possible. Whilst the relative buoyancy guarantees that CO_2 will migrate upwards, a decision has been made to set the deepest perforation 30m above the shallowest possible spill point of the structure. It is assumed that the topmost perforation will be set in the middle of the L2-Bunter Sandstone.

Figure 8.47: Well Trajectories from P5 Platform Location

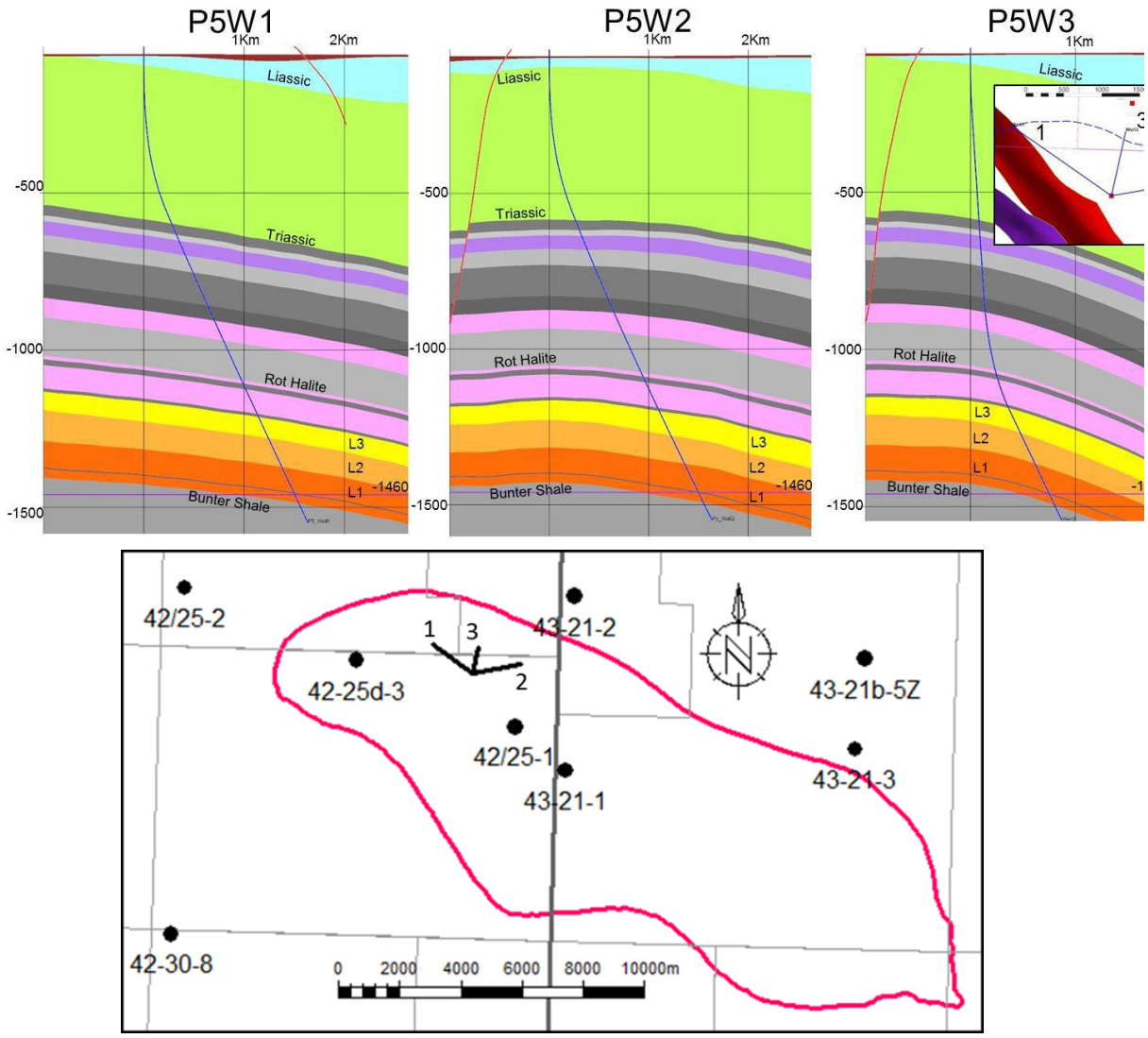

8.3.12.3 Well Switching

Considering the three injection wells discussed above, the standard operating strategy that has been adopted in the dynamic simulations is to split the maximum injection rate of 2.68MTPA between two of the three wells; 1.34MTPA/well and then to cycle between the set of wells every six months so that any given well is injecting for 12 out of every 18 months.

8.3.13 CO_2 Storage Capacity and Reservoir Pressure Profiles

This section describes the determination of the storage capacity within Endurance, bringing together the most up to date interpretation of geophysical and petrophysical data, as well as core analysis data from the 42/25d-3 appraisal well. The most likely net pore volume (NPV) and a mid-case irreducible water saturation are first used to estimate the maximum CO_2 storage capacity within the Endurance and then the implications of White Rose CO_2 injection upon Endurance pressure increase under static and dynamic conditions are explored given assumptions about hydro-dynamic connectivity to the cap rock and the Greater Bunter aquifer.

8.3.13.1 Endurance Maximum CO_2 Storage Capacity

Equation 8.9 has been used to calculate the maximum PV which could be occupied by CO_2

Equation 8.9 $VCO_2 = (1-S_{wi})\ NPV$

Where:
S_{wi} is the irreducible water saturation

The net NPV analysis is based on seven facies and three NTG models over which porosity cut offs are assigned according to the degree of cementation. The low, mid and high NPV are calculated as 4.2 $x10^9$ m^3, 4.6 $x10^9$ m^3, and 5.4 $x10^9$ m^3, respectively. The structural uncertainty was assessed via Petrel uncertainty workflows that calculate the spill point for 500 top structure maps that have been generated stochastically. The current Endurance structural model spill is -1460m with a range of -1416 m to -1553 m resulting from the uncertainty workflow.

Figure 8.36 has been derived from the analysis of cores recovered from the 42/25d-3 appraisal well and shows S_{wi} as a function of Klinkenberg permeability. Using the average permeability interpreted from the 42/25d-3 well test of 271 mD, S_{wi} for the Bunter Sandstone within Endurance is estimated at 0.09. Taking account of measurement uncertainty, a conservative S_{wi} = 0.15 has been used to estimate the CO_2 storage capacity.

Using the mid-case NPV, therefore, V_{CO2} = 3.9 $x10^9$ m^3.

Assuming that the *in-situ* CO_2 density in Endurance is ρCO_2 = 700 kg/m^3, then the mass of CO_2 which could be stored in Endurance is $mCO_2 = \rho CO_2\ VCO_2$ = 2.7$x10^{12}$ kg = 2700Mt. The maximum White Rose CO_2 injection rate is 2.68 Mt/yr for 20 years; a total of 53.6 Mt or less than 2% of the theoretical Endurance capacity. Whilst taking up 2% of the total PV may seem insignificant, it must be remembered that Endurance is presently filled with brine of very small compressibility. The next section describes attempts to estimate the associated pressure increase as a result of injection, firstly using simple material considerations and then using more elaborate dynamic simulation models.

8.3.13.2 Pressure Increase in Endurance Due to White Rose CO_2 Injection

The magnitude of pressure increase within Endurance as a result of White Rose CO_2 injection is strongly dependent on assumptions about pressure communication between the volume enclosed by the most likely structural close contour and the rest of the Bunter Sandstone formation.

8.3.13.2.1 Hydraulically Isolated Endurance

This considers a limit case in which Endurance is a closed volume bounded by an impermeable boundary at the most likely structural close of 1460m.

Equation 8.10 is an expression for the conservation of mass in terms of compressibility factor in which ΔV is the volume of fluid measured at reservoir conditions injected into a closed box of volume V and average compressibility c which as a result of the injection sees an increase of pressure of ΔP.

Equation 8.10

$$\Delta V \approx cV\Delta P$$

or

$$\Delta P \approx \Delta V / cV$$

The compressibility of brine and rock at the conditions of interest is 3.0x10^{-5}/bar and 5.6x10^{-5}/bar, respectively giving a total effective compressibility of $c \approx 85\text{x}10^{-6}$ /bar. The CO_2 density at reservoir condition of 700 kg/m^3 results in a corresponding volume $\Delta V \approx 76.6\text{x}10^6$ m^3; V = *NPV = 4.6* x10^9 *m^3*. Therefore the pressure increase resulting from White Rose CO_2 injection provided by Equation 8.10 is:

$$\Delta P \approx \frac{1}{4.6\times10^{9}}\frac{\left(76.6\times10^{6}\right)}{\left(8.6\times10^{-5}\right)} = 194 \text{ bar}$$

A pressure increase of 194bar equates to an average reservoir pressure of approximately 301bar at the end of White Rose CO_2 injection, which would almost certainly undermine the sealing integrity of the Röt Clay primary seal whose fracture closure pressure has been estimated to be 264bar at 1362.8 m TVDSS. However, multiple sources of evidence ranging from seismic interpretation over the Endurance structure, petrophysical data from surrounding appraisal wells, and analysis of production performance of surrounding gas fields strongly suggests that the assumption of an hydraulically isolated Endurance is an extreme limiting case. Endurance is indeed one of several structural closures of the Bunter Sandstone Formation (BSF) that have been created by salt tectonics within the Triassic southern North Sea basin. To the south-east of the Endurance structure lies a salt diapir that outcrops to the seabed and seismic interpretation suggest that the Bunter Sandstone is continuous in the saddle between the Endurance structure and this diapir, see Figure 5.8.

Pressure history from the Esmond gas field, approximately 40km north of Endurance, as well as pressure measurements within Endurance itself between 1990 and 2013 suggests the existence of an active regional Greater Bunter aquifer whose size has been estimated to be about 50 to 100 times that of the Endurance structure.

Using a 7% porosity cut-off, the total PV of Endurance and the contiguous Bunter Sandstone between it and the outcrop is estimated as $20.5x10^9$ m^3 (note that this does not include the greater Bunter aquifer volume). Substituting the V term in Equation 8.10 results in a maximum Endurance pressure increase due to White Rose CO_2 injection of 43.5bar, well below the fracture pressure of the Röt Clay. Because this is simple material balance estimation, there is the implicit assumption that pressure is transmitted instantaneously across the reservoir during injection. In fact, it takes some time for the total pressure perturbation as a result of a unit volume of CO_2 injection to be felt uniformly across the system and there is always a transient non-uniformity in pressure distribution within the system that peaks just after the end of injection. These dynamic effects have been analysed using more detailed full field simulation models and are discussed below.

8.3.13.3 Dynamic Pressure Profiles Associated with White Rose CO_2 Injection

The model was used to investigate the transient pressure profiles within Endurance during White Rose CO_2 injection using sensitivities that consider:

- Whether the seabed outcrop connected to Endurance is open to flow or not
- The impact of the size and strength of the Greater Bunter attached to Endurance

The question of open/closed outcrop is addressed first as having the outcrop open may obscure questions concerning the aquifer size and strength.

8.3.13.3.1 Outcrop Open/Closed

CO_2 is injected at a rate of 2.68 Mt/yr for 20 years; 53.6 Mt total, followed by a 20 year shut-in period. Initially the model is limited to include only Endurance and the outcrop giving a total PV of $20.5x10^9$ m^3. The pressure calculated at the crest of Endurance that corresponds to the location of 43/21-1 well is shown in Figure 8.48 for when the outcrop is closed and when open, along with the brine production rate in the latter case.

With the outcrop closed the maximum pressure increase is 64.8bar at the end of injection which drops to 49.2bar after shut-in. This shows good agreement between the simulation and the simple material balance model used in the previous section.

With the outcrop open, the maximum pressure at the end of injection is only 0.9bar lower than the closed case, but the pressure then continues to drop as the excess pressure causes flow from the outcrop to continue during the shut-in period. By the year 2500, 460 years after shut-in, the pressure is just 7.8bar over initial pressure.

Brine production starts 2.5 years after the start of CO_2 injection (when the pressure at the outcrop is 0.1bar above its initial pressure), it peaks around $3500m^3$/d about nine years after shut-in and is still over $3000m^3$/d twenty years after cessation of injection. By 2500 the production rate is still more than $30m^3$/d.

For the White Rose project, whether the outcrop is open or closed seems to have little effect on the maximum pressure increase during the injection phase.

Figure 8.48: Pressure Change at Endurance Crest when Outcrop Closed/Open and Water Production

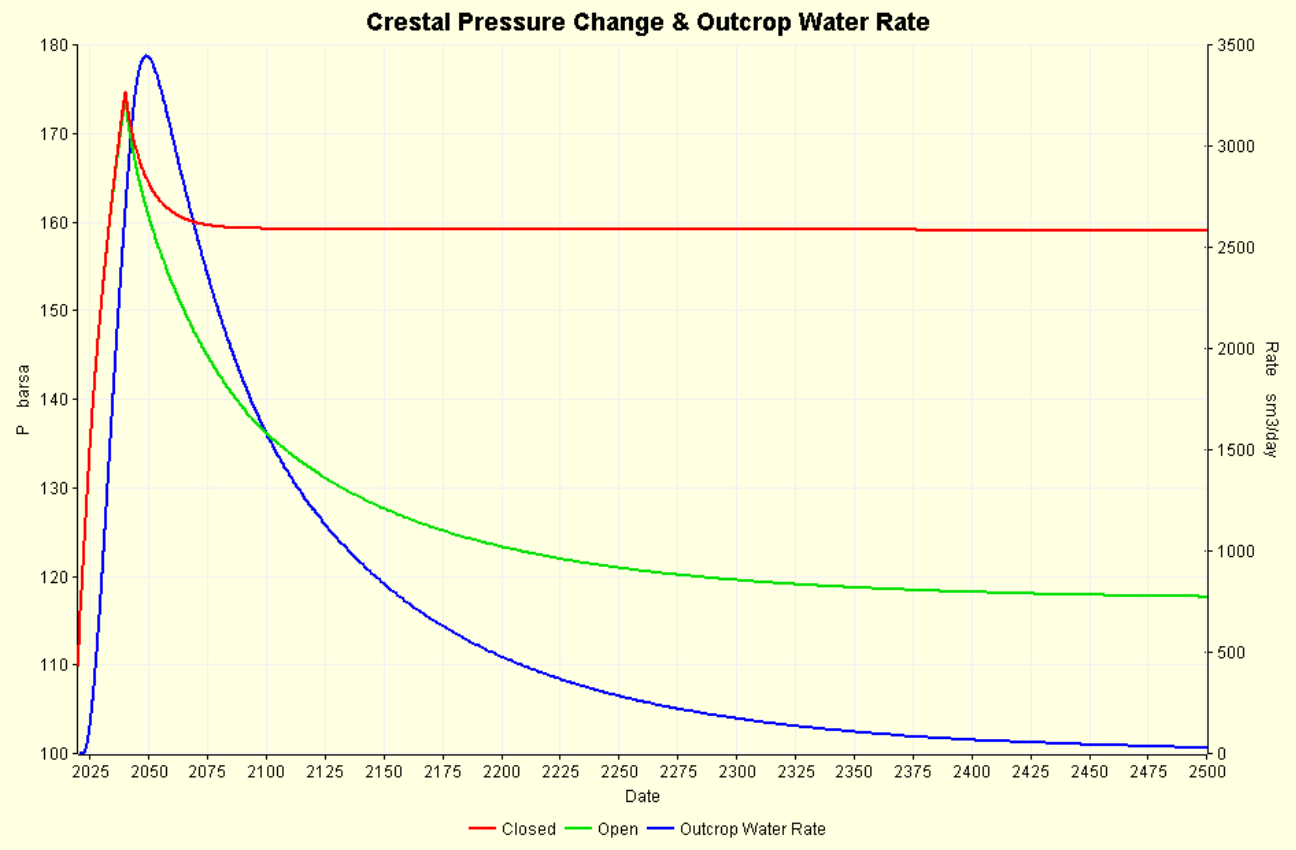

8.3.13.3.2 Greater Aquifer

There is a strong argument that Endurance is in hydrodynamic communication with a much larger volume than itself. However, while there appears to be good evidence over the size of the greater Bunter, the strength by which it couples to Endurance is less clear.

8.3.13.3.3 Aquifer Size

The area of the Endurance structure assuming a spill at 1460m TVDSS is about 25 x 8 = 200km^2. The area of the simulation model is about 42 x 11 = 460km^2. The Greater Bunter area attached to Endurance has been estimated to be probably in excess of 20,000km^2 or 100 times the Endurance area and 43.5 times the area of the simulation model.

To test a range of additional volumes a finite radial aquifer of variable $r_{eD}/r_{eD} = r_a/r_o$, the ratio of aquifer radius to reservoir radius or the dimensional radius, see Figure 8.41, was attached to all the edge cells of the simulation model. The thickness has been set to 250m and an average porosity of 19.2% was used, that being the average porosity assuming 7% cut-off. The proposed porosity yields an aquifer permeability of 125 mD using the poro-perm correlation obtained from interpretation of well logs from 42/25d-3 appraisal well (Equation 8.4). The angle subtended by the aquifer is assumed to

be 360°; full circle, the total compressibility of the rock and brine is $86x10^{-6}$ /bar, the brine has a salt concentration of 250,000mg/kg and the area of the simulation model converts to a circle of radius 11km.

The set of r_{eD} investigated is shown in Table 8.14 along with the resulting area (with respect to the AoI) and the total PV of the AoI and attached aquifer. Note that the first row in the table with r_{eD} = 1.0 means no additional volume attached; the green line in Figure 8.49. The pressure response reported at the crestal location is shown in Figure 8.49. Note that at r_{eD} = 5.0, the total area of the AoI and aquifer system is only 25 times that of AoI alone, somewhat less than the previously speculated size of the Greater Bunter attached to Endurance.

Table 8.14: Size of Aquifer and Resulting Model Area and Pore Volume

r_{eD}	Area With Respect to Model Area	Total PV (10^9 m^3)
1.0	1.00	20.5
1.5	2.25	46.1
2.0	4.00	82.0
3.6	12.96	265.7
5.0	25.00	512.5

Figure 8.49: Sensitivity of Crestal Pressure Increase to Aquifer Size

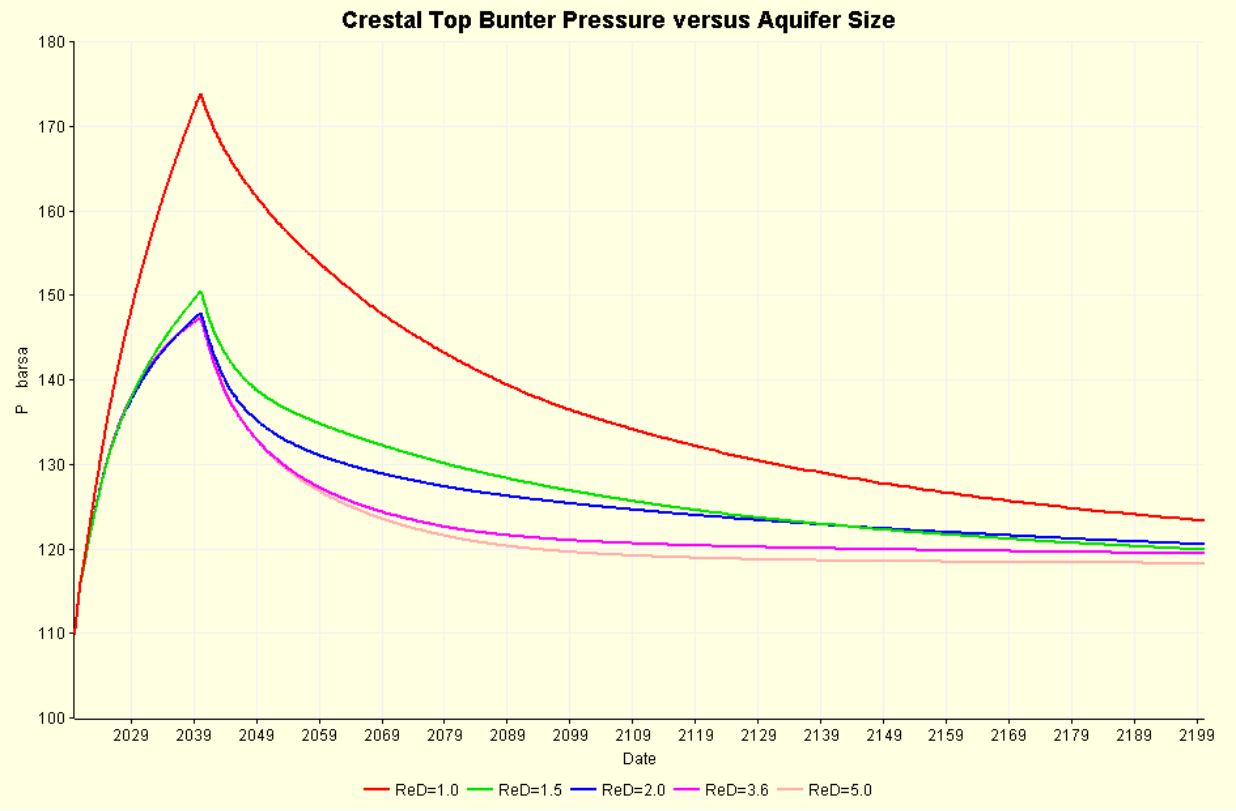

It can be seen once r_{eD} > 2.0 the peak increase in pressure at the crest is not significantly reduced from its value of 38.0bar at r_{eD} = 2.0. Clearly the asymptotic behaviour during shut-in is changed but some of this change is due to the water production rate from the outcrop which has been open to flow in all these cases; the outcrop production rate versus aquifer size is shown in Figure 8.50. As the attached aquifer becomes larger, it can take-up more of the pressure increases caused by injection meaning less pressure at the outcrop and hence less brine production.

It takes 10 to 12 years to differentiate between the r_{eD} = 2 and r_{eD} > 2 cases. It would appear to be nearly impossible to differentiate between the r_{eD} > 2 cases though this may be easier if porosity and permeability are less than the 19.2% and the 125 mD assumed here. This is studied in the next section.

Going forward the r_{eD} = 3.6 aquifer size will be assumed unless notified otherwise.

Figure 8.50: Outcrop Production Rate versus Aquifer Size

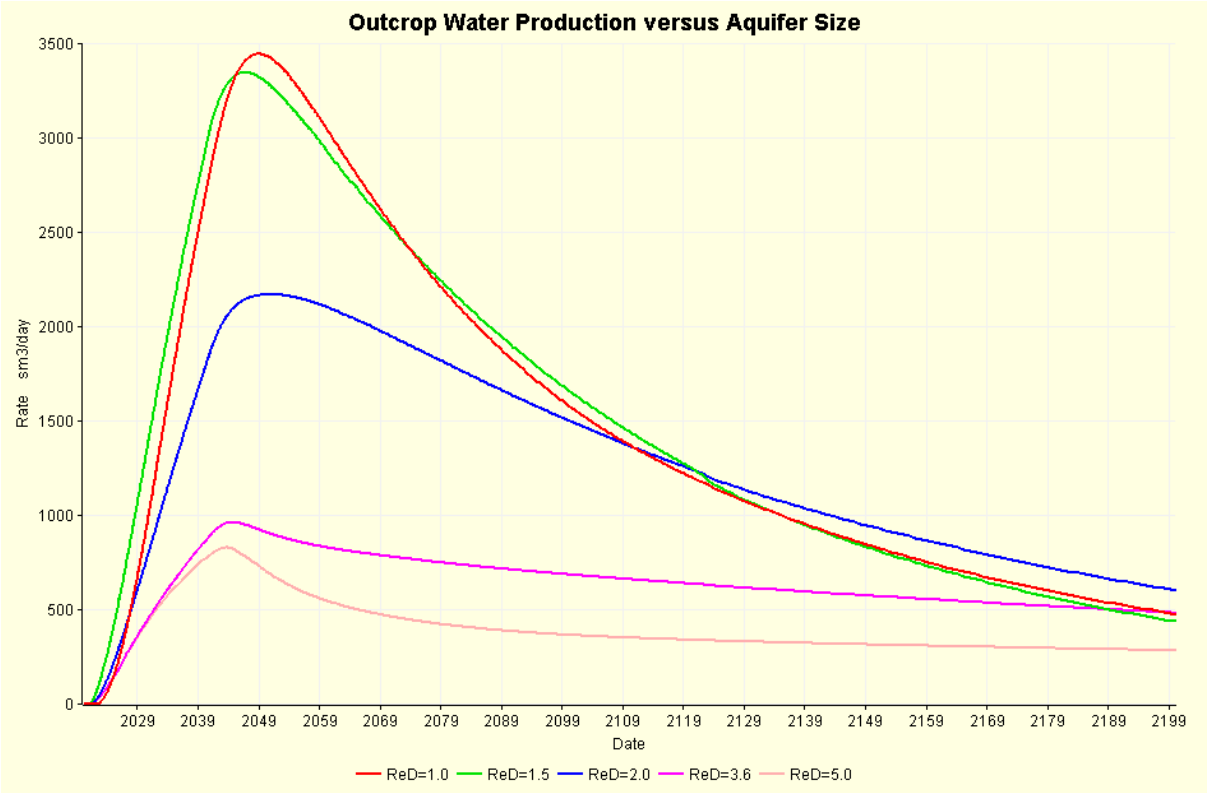

8.3.13.3.4 Aquifer Strength

The properties of the attached aquifer, in particular the related porosity and permeability are clearly unknown. A wide range of permeability values have proposed by various sources that ranged from less than 1 mD to 250mD.

As stated above, the r_{eD} = 3.6 aquifer size has been used, but the porosity and permeability of the Carter-Tracy aquifer are as defined in Table 8.15.

Table 8.15: Porosity and Permeability Used in Aquifer Strength Sensitivity

Porosity [%]	Permeability [mD]
6	1.25
13	12.50
19	125.00
26	1250.00

The results of this sensitivity are shown in Figure 8.51. Reducing the quality of the attached aquifer clearly has a detrimental effect on the injection scheme by increasing the crestal pressure seen at the Top Bunter 43/21-1 location. In particular, relative to the K = 125 mD case, reducing the permeability to 12.5 mD and 1.25 mD makes the peak pressure increase from 37bar to 47bar and 58bar, respectively.

Regarding the most representative aquifer properties, at the Esmond field 45km north-east of Endurance, a Greater Bunter aquifer average permeability of 16 mD was estimated from material balance calculations that used actual production performance and post shut in pressure build up data. However, much wider range of values has been estimated by a number of authors. Reference 9 in Section 9 reported average porosity and permeability for the Greater Bunter of 0.18 and 250mD whilst in Reference 10 in Section 9 the values were 0.20 and 100mD, respectively. Reference 11 in Section 9 estimates the average well porosity for wells in the UK southern North Sea Bunter as 0.187 (from 603 core plugs), although a great variability of porosity within individual wells was observed; from 0.024 in well 42/10a-1 to 0.22 in well 42/25-1. For the 42/25d-3 appraisal well, the average porosity is approximately 0.20 to 0.27 at the top and 0.14 at the base.

There is therefore considerable uncertainty around Greater Bunter aquifer properties. Nevertheless, a Greater Bunter permeability of 125 mD has been used in simulations from here onward unless explicitly stated otherwise as this is consistent with a porosity of 0.19 from the poro-perm function in Equation 8.4.

Figure 8.51: Crestal Pressure Increase versus Aquifer Properties

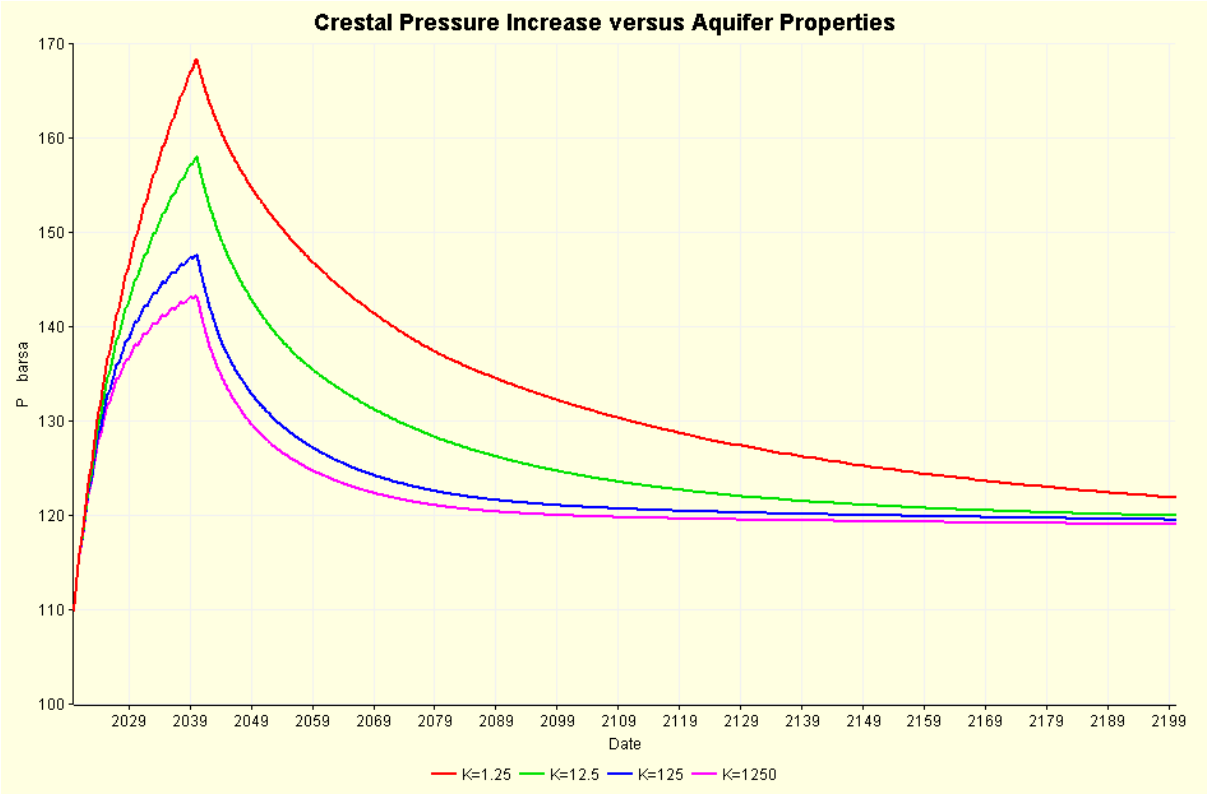

8.3.14 Plume Development

The change in pressure caused by CO_2 injection has been shown to depend mainly on the size and strength of Greater Bunter attached to Endurance. Once the effect of the near wellbore over-pressure required to cause inflow has dissipated, the dense CO_2 will migrate upwards and because of the density difference between it and the native brine, until a seal is encountered. Thereafter CO_2 will flow upwards along the Top Bunter until it pools at the crest of the structure.

The impact of a number of parameters on plume development has been considered and is outlined in the sections that follow.

8.3.14.1 Horizontal Permeability

As with the sensitivity of the aquifer properties analysed in Section 8.3.13.3.2, varying the horizontal permeability of the Endurance rock will change the crestal pressure increase as shown in Figure 8.52. In varying the horizontal permeability, the earlier constraint on average model permeability imposed by the upscaling method has been temporarily relaxed to permit the use of low (135 mD) and high (540mD) case permeability values. The 271mD from 42/25d-3 production well test is taken as the mid case. Note the maximum pressure increase follows the differences seen in Figure 8.51.

Figure 8.52: Crestal Pressure Increase versus Endurance Horizontal Permeability

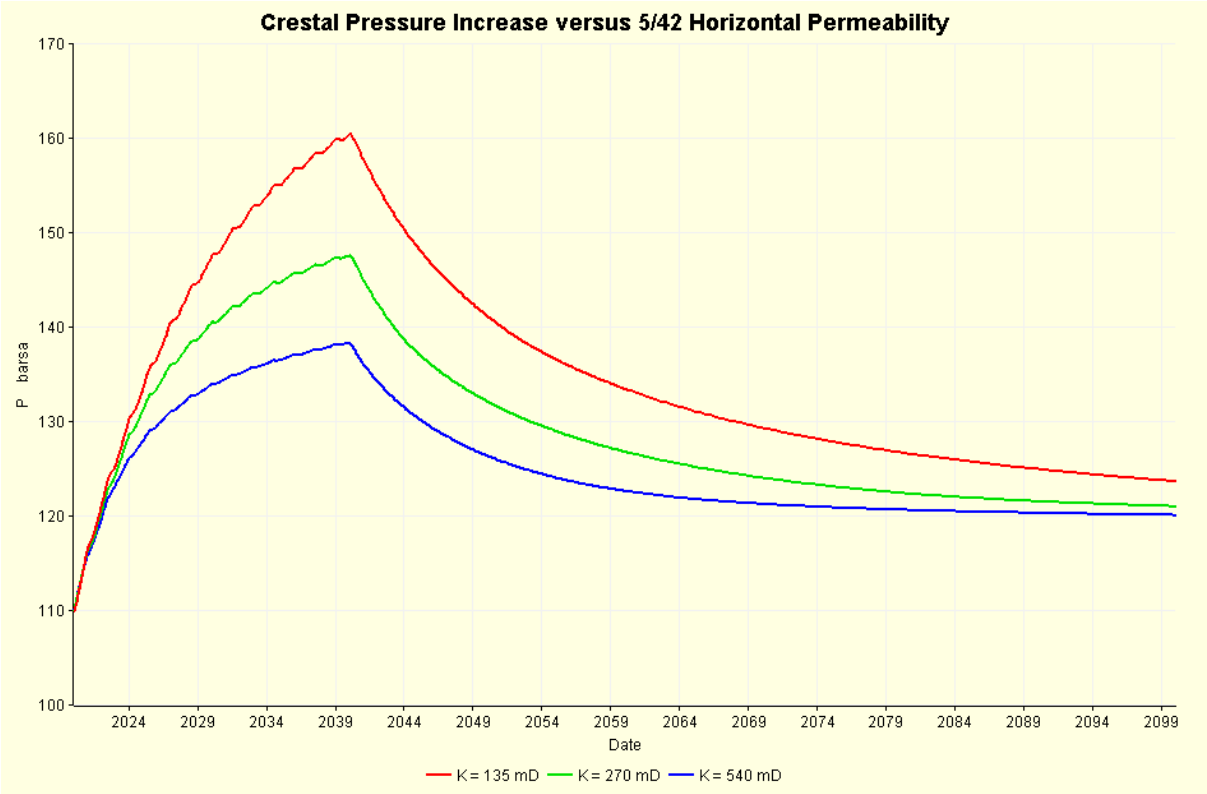

Part of the increase (for K = 135 mD) and decrease (for K = 540mD) in crestal pressure is because of the reduced and increased well injectivity, respectively.

The main effect under study here is the frontal advance of the CO_2 plume because of the reduced/ increased K_H and this is shown in Figure 8.53; the break through time (first CO_2) is listed in Table 8.16.

Table 8.16: Time to First CO_2 at Crest of Endurance versus Permeability

K_H/[mD]	First CO_2/[yr]
135	5.5
270	3.3
540	1.8

A semi-transparent map view of the Top Bunter depth is shown in Figure 8.54 on which a line can be seen from west north-west to east south-east across the crest of the structure. This line denotes the set of cross-section displays that follow. The line includes the DEV1 (north-west) well as well as the 42/25-1 and 43/21-1 wells. The CO_2 saturations in this mid-case (271 mD) cross-section at 6 months after the start of injection, 5 years after, 20 years after (the end of injection) and a further 60 years of shut-in are shown in Figure 8.55, Figure 8.56, Figure 8.57**,** and Figure 8.58 respectively.

Figure 8.53: CO_2 Saturation at Top Bunter 43/21-1 Location

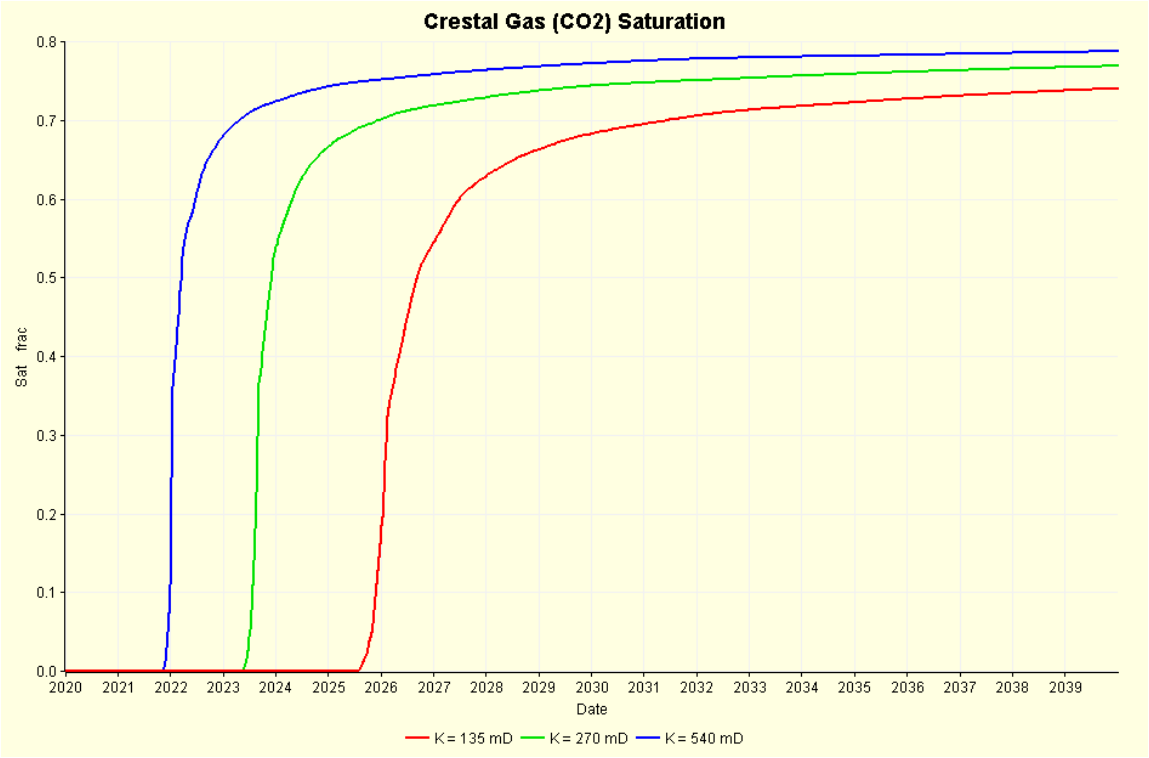

Figure 8.54: Cross-section through DEV1, 42/25-1 and 43/21-1

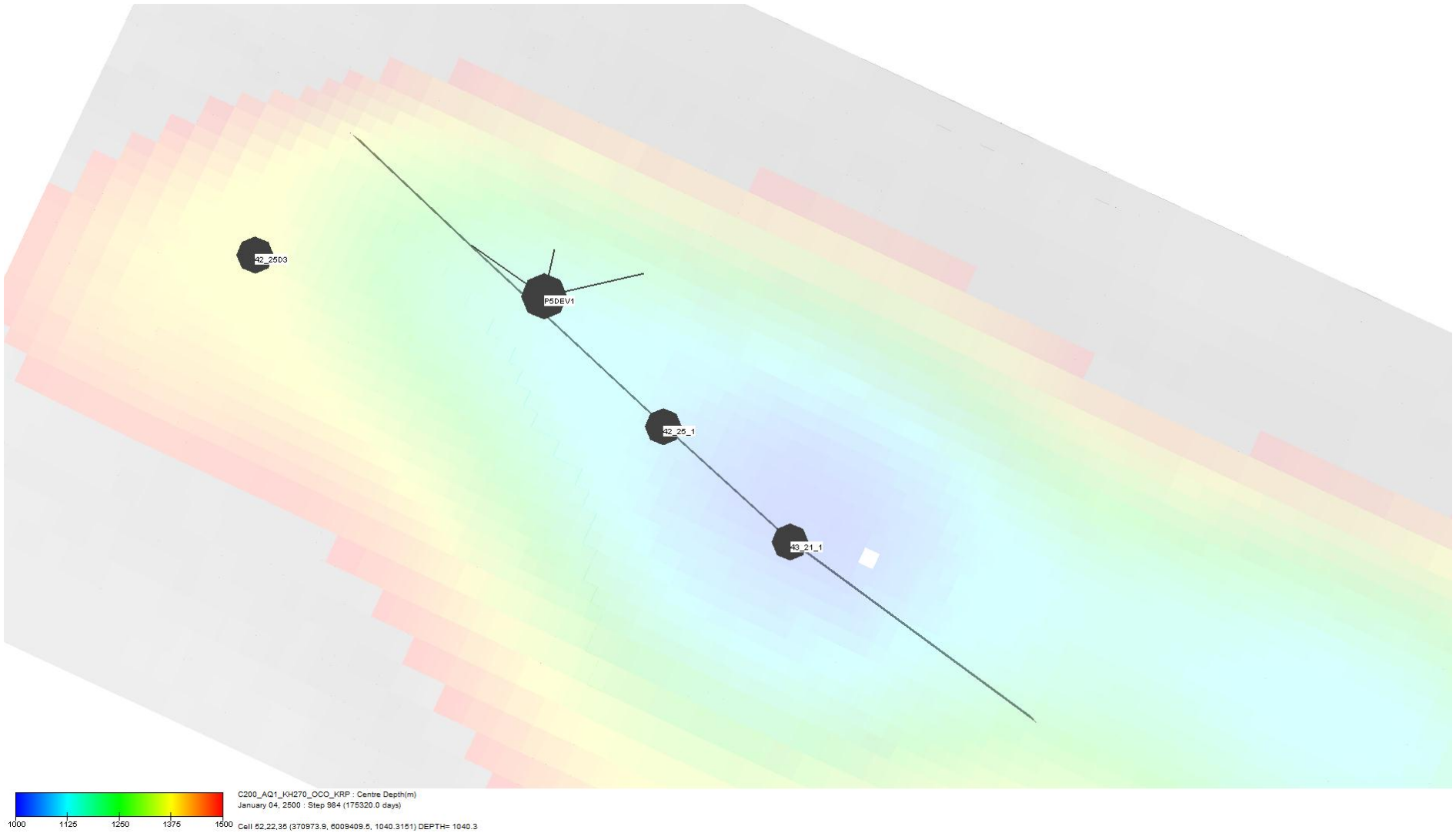

Figure 8.55: CO_2 Distribution after 6 Months of Injection

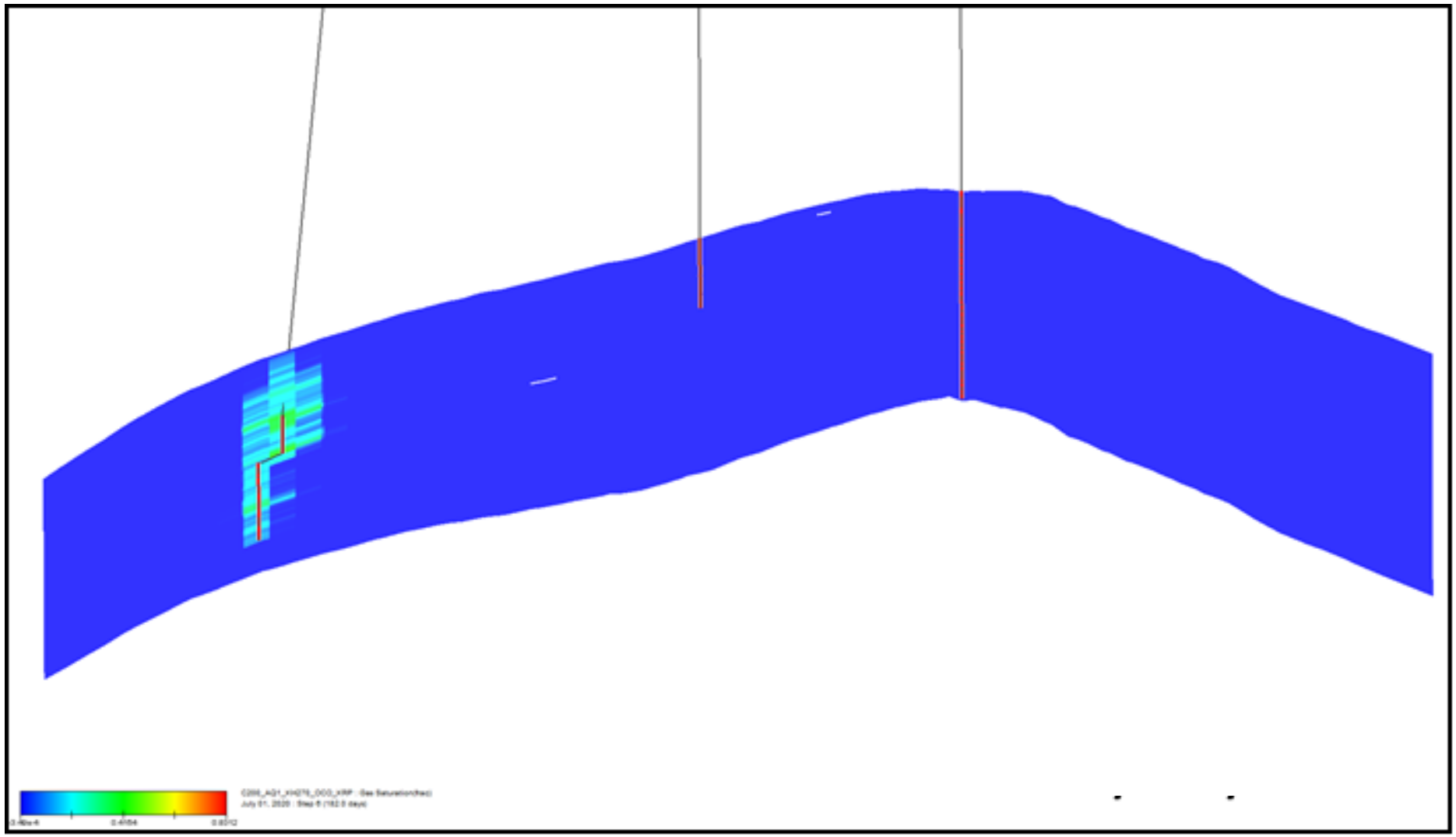

Figure 8.56: CO_2 Distribution after 5 Years of Injection

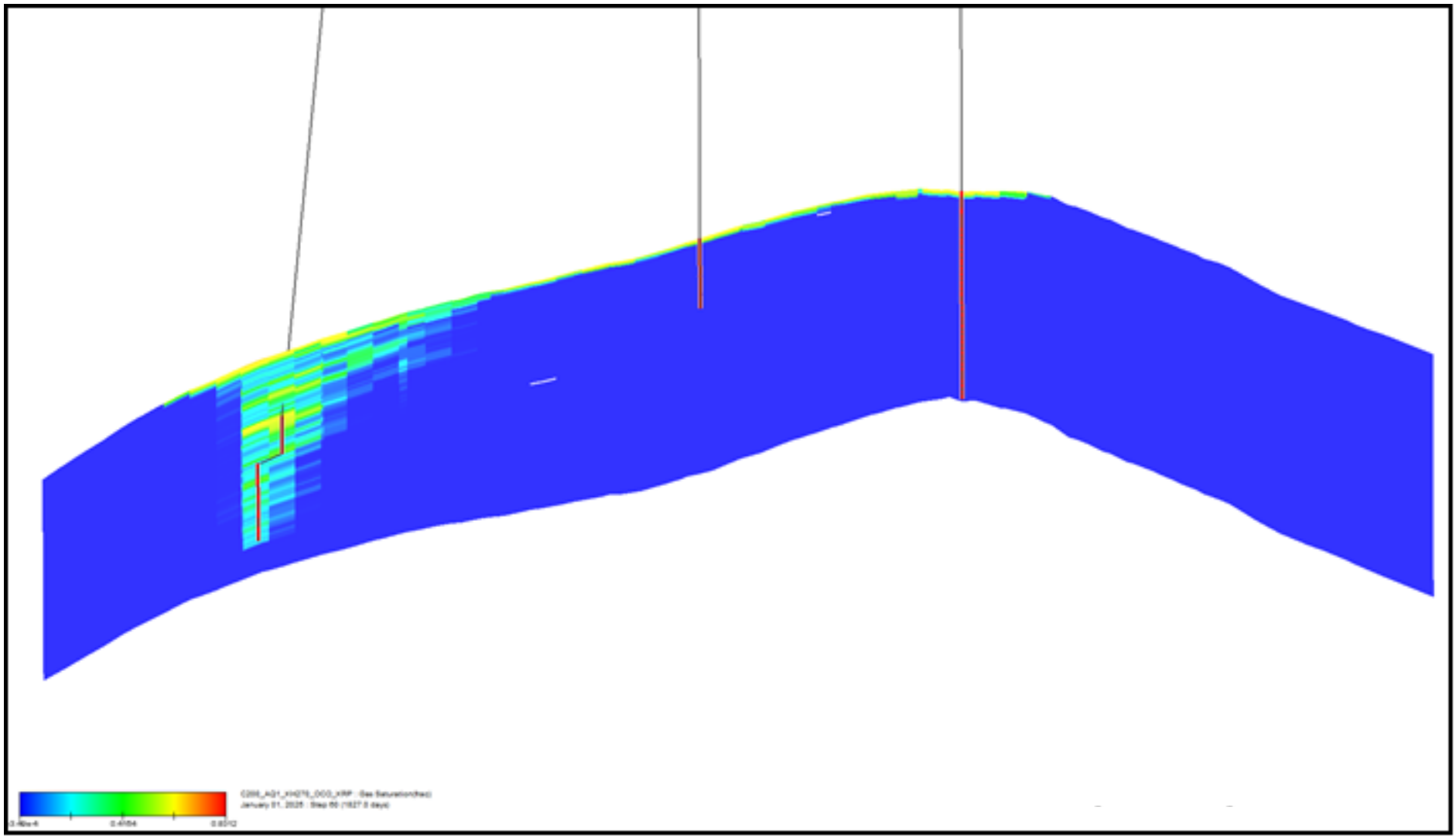

Figure 8.57: CO_2 Distribution after 20 Years of Injection

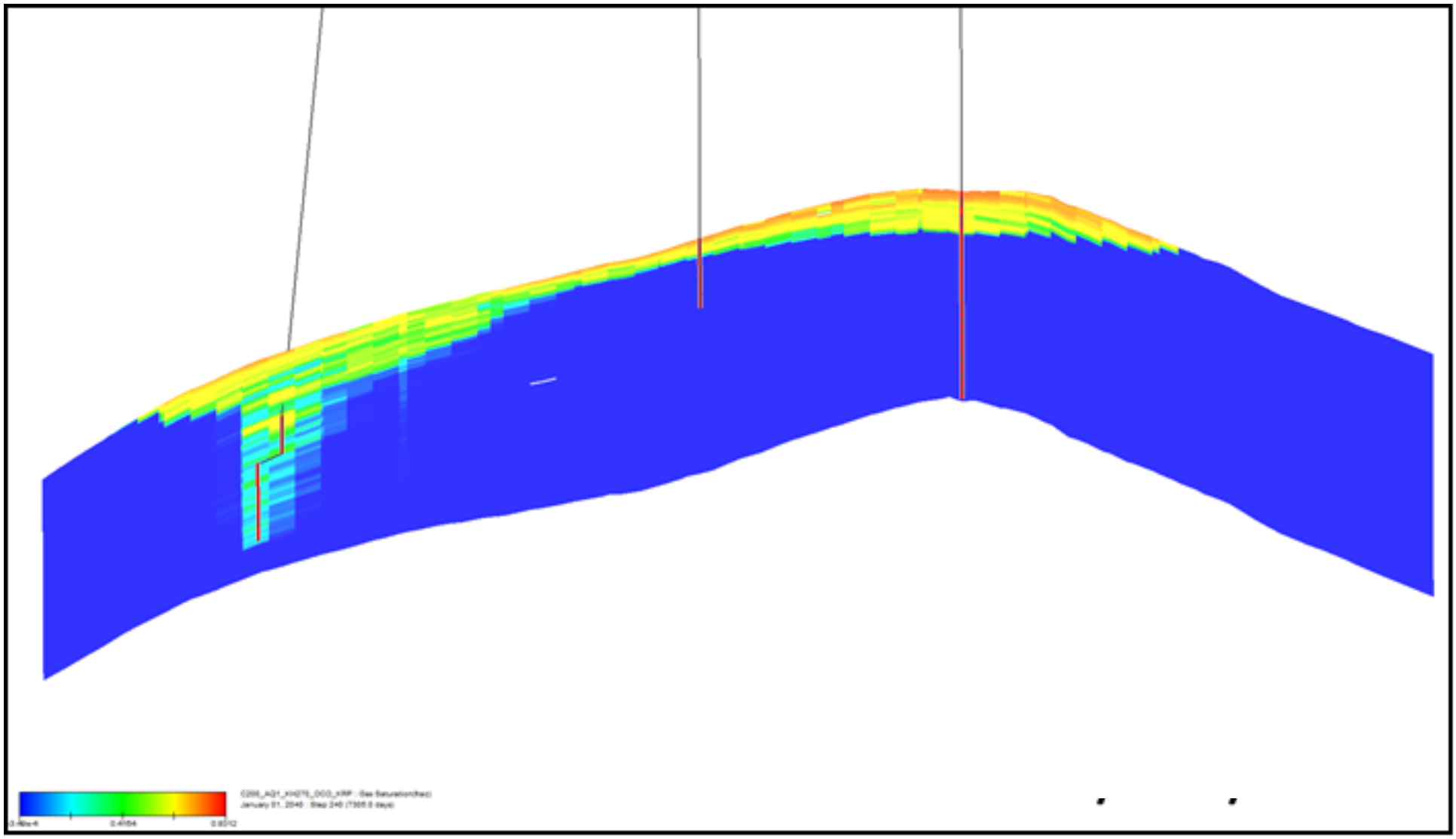

Figure 8.58: CO_2 Distribution after 20 Years of Injection and 60 Years of Shut-In

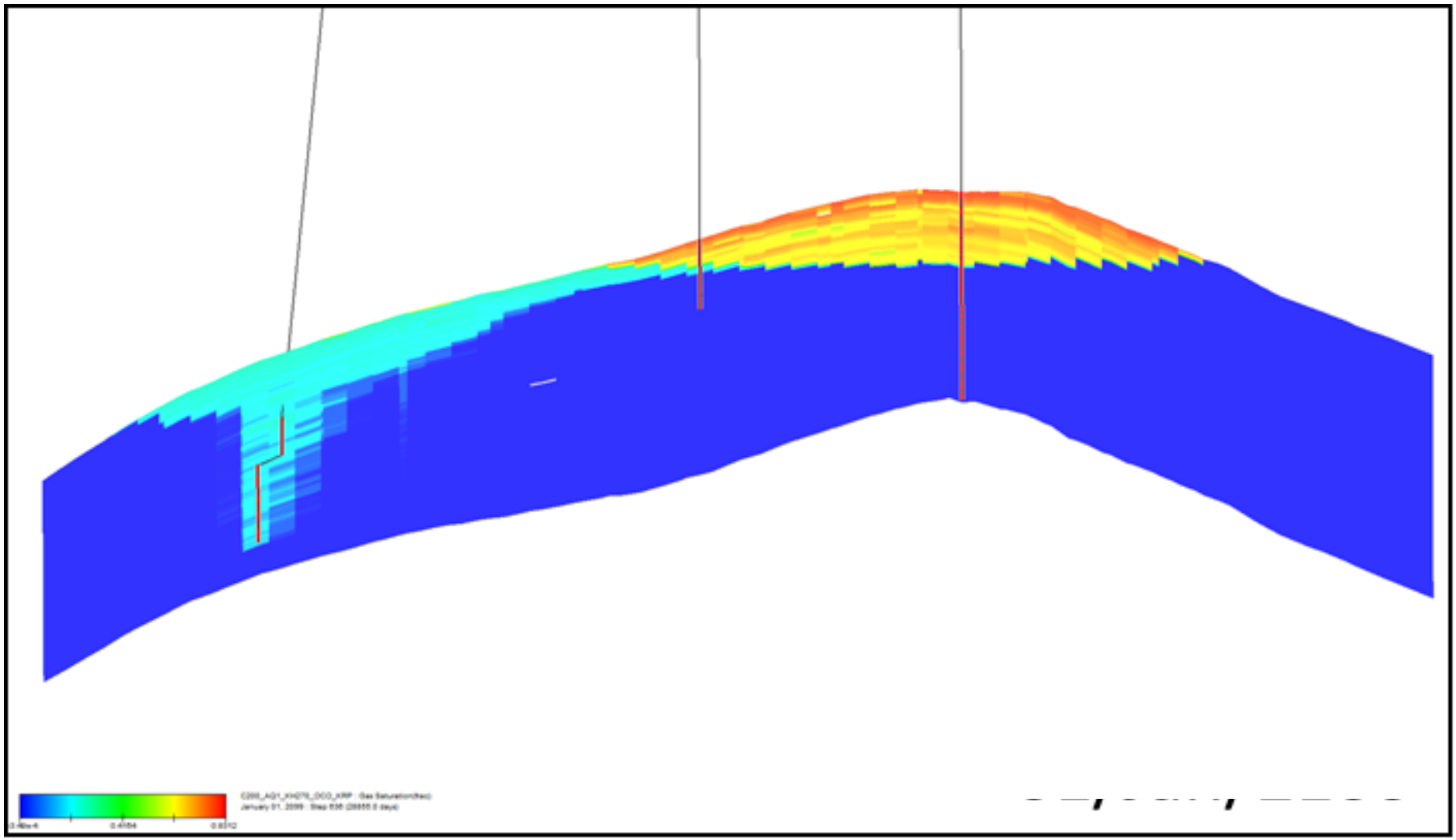

Figure 8.59: CO_2 Distribution after 20 Years of Injection and 460 Years of Shut-In

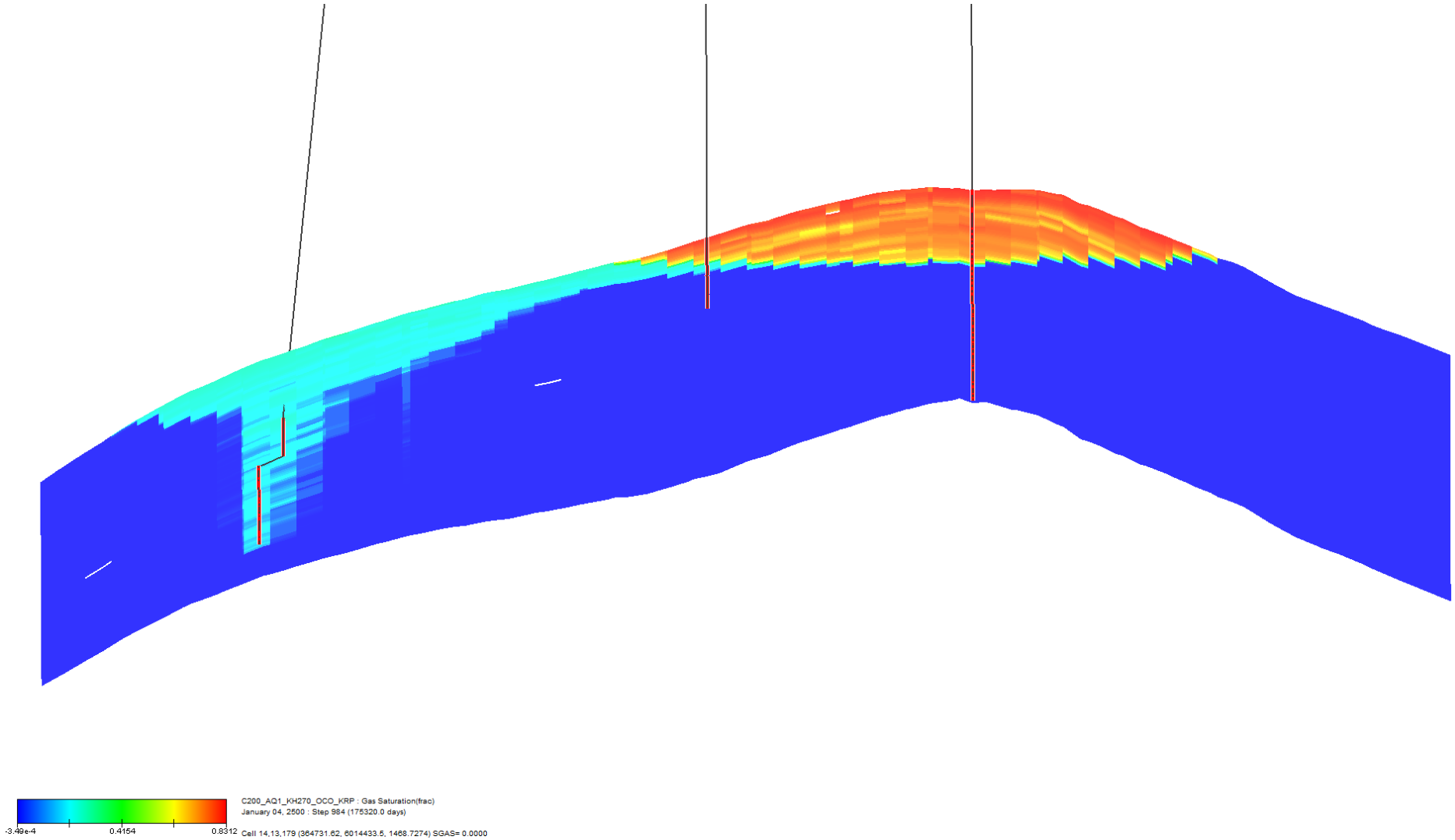

Even though CO_2 is being injected in the lower half of the Bunter Sandstone, it reaches the cap rock in just over 6 months, Figure 8.55. After 5 years, Figure 8.56, the CO_2 cap is starting to become established at the crest of the structure. At the end of injection, Figure 8.57, the area above the DEV1 well shows predominantly green and yellow coloured cells indicating saturations in the range 0.4 to 0.6; well above the imbibition critical gas saturation S_{gt} = 0.3. After shut-in, the mobile CO_2 continues to migrate upward to the cap rock and on to the crest whilst fresh brine imbibes into the area surrounding the well trapping CO_2 at this 0.30 saturation limit as seen in Figure 8.58. The free CO_2 at the crest now approaches its limiting saturation of $S_g = 1 - S_{wc} \approx 0.90$, coloured red in this Figure. Running this model onto 01 Jan 2500, 460 years after shut-in, produces the distribution shown in Figure 8.59. Essentially all the CO_2 is now free at the crest or residually trapped elsewhere.

It is important to remember some of the limitations of this model, namely:

- no CO_2 dissolution in the brine;
- no temperature effects;
- no diffusive flow; and
- no geochemical effects.

Dissolution effects are discussed whilst temperature effects are addressed in Section 8.3.16. In particular, diffusion is thought to be the mechanism by which free CO_2 which has pooled at the crest of the structure can dissolve in the underlying fresh brine generating saturated brine which is slightly denser than fresh brine. This density difference (which will be 0.1 to 0.2% in a 250,000mg/kg brine) can then generate Rayleigh-Taylor instability in which the saturated brine flows down while fresh brine flows up to act as the recipient for additional free CO_2 from the crestal pool. This process in conjunction with long term geochemical reactions between the saturated brine and the rock fabric leading to potential mineralisation of the CO_2 has been suggested by many academic researchers investigating the ultimate fate of the sequestered CO_2. However, all of the experimental research that has been reported has tended to focus on idealised scenarios that use unrepresentative rock matrix and on timescales of days to months rather than thousands of years as is more appropriate for CO_2 sequestration. Whilst modelling and simulation could be used to overcome some of the limitations there is still a great deal of uncertainty as to the accuracy of the results since even the most advanced models are able to account for only a small fraction of the potential geochemical interactions. The approach for investigating the likely dissolution-convection-mineralisation processes as a result of White Rose CO_2 injection into Endurance has been to use 2D sector models to investigate limit cases using proven databases.

8.3.14.2 Vertical/Horizontal Permeability Ratio

Generally vertical permeability K_V is calculated using a multiplier applied to the horizontal permeability K_H; the multiplier is the ratio of K_V/K_H. The mid-case value of K_V/K_H has been presented as 0.15 in Section 8.3.2.2; low and high values for K_V/K_H have been derived as 0.10 and 0.36 respectively from vertical interference test, see Section 8.1.2.1.

The result of this sensitivity had no material effect on the pressure change measured at the crest of the structure. Varying the ratio did not change the horizontal permeability and it was K_H that was used to calculate well injectivity.

The speed at which the CO_2 plume moves is clearly affected by K_V/K_H as shown in Figure 8.60.

Figure 8.60: Crestal CO_2 Saturation versus K_V/K_H

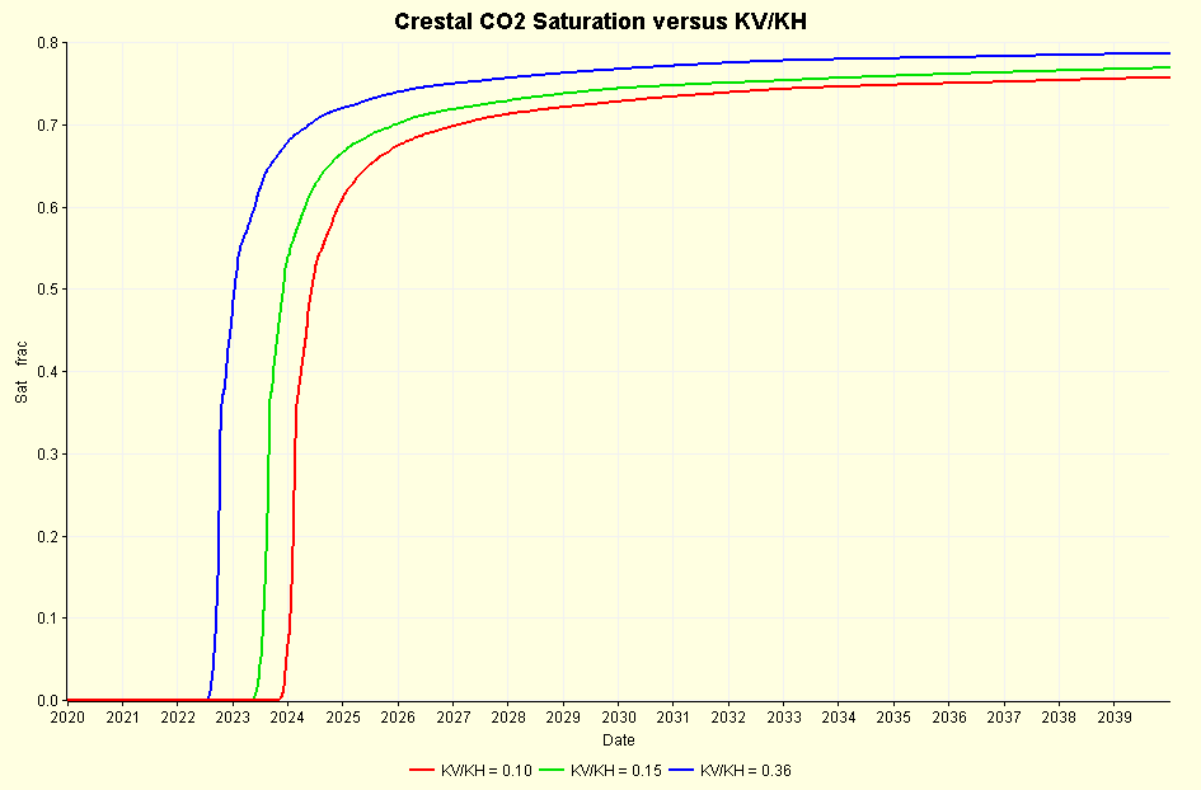

More than doubling the mid-case value from 0.15 to 0.36 does not half the crestal arrival time of the CO_2 but reduced it by around 10 months.

8.3.14.3 Sub-Seismic Baffling

There is no evidence for baffles in any of the three well penetrations nor can faults be seen on seismic within Endurance. This does not preclude the existence of such features being present within the structure.

Therefore, to test the effect of baffles and barriers a simple set of modifications have been employed. First, 1% of the total cells in the intermediate model (representing 7000 cells) were randomly assigned vertical cell-to-cell transmissibility *Tz* of zero. Cells in the intermediate grid have 200m aerial grid spacing over the core of Endurance. The difference between the case without the barriers and that with the 7000 flow barriers is small, with only a slight delay in the arrival time of the CO_2 at the crest of the structure (Figure 8.61).

Two further cases were constructed where the size and then the orientation of the barrier was changed, the results of which (crestal pressure change and CO_2 saturation) are shown in Figure 8.62. Firstly, the set of 7000 horizontal barriers (as applied through a vertical transmissibility multiplier) studied previously were all extended in size. Rather than being the cross-sectional area of a single grid block (200m by 200m), the barriers were made three blocks by three blocks; 600m by 600m. These values are shown as the pair of blue lines (solid line for CO_2 saturation and dashed line for pressure) in Figure 8.62. The green pair of lines shown on the same figure is for a case where the barriers are vertical in their orientation.

Figure 8.61: Crestal Pressure Change and CO_2 Saturation Without and With Horizontal Barriers

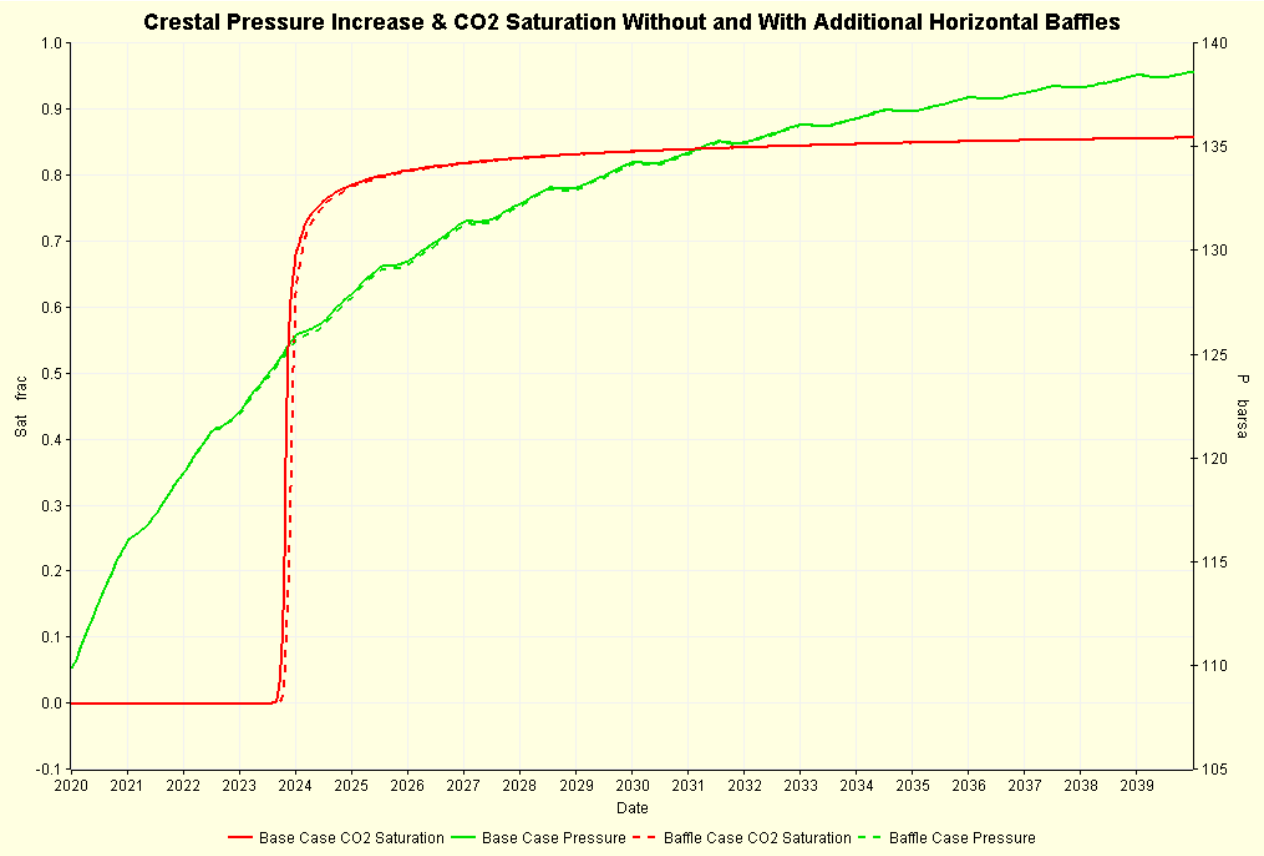

Figure 8.62: Crestal Pressure Change and CO_2 Saturation versus Different Barriers

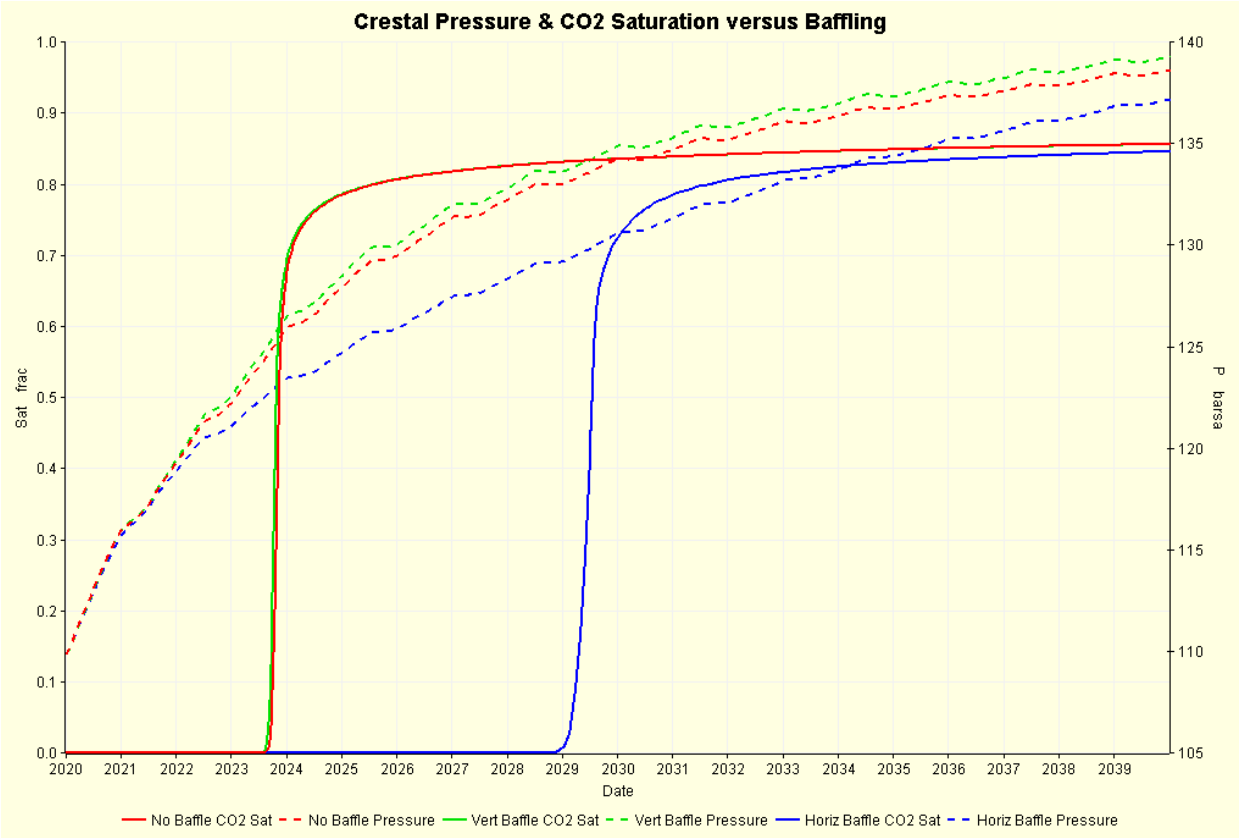

The vertical barriers are three grid blocks wide; 600m and five grid blocks high; 10m. The height is considered to be less than that resolvable on seismic, which is typically 20m. It is noticeable from Figure 8.62 that the vertical barriers (in green) have little impact on the progress of the CO_2.

The effect of larger horizontal barriers (shown in blue) is much more pronounced (also see Figure 8.63 and Figure 8.64). The arrival time of the CO_2 at the crest has been increased from 3.5 years to over 9 years whilst the increase in pressure is also reduced although this difference is gets smaller toward the end of the 20 year injection period.

Figure 8.63: No Baffle CO_2 Cross-section after 9 Years

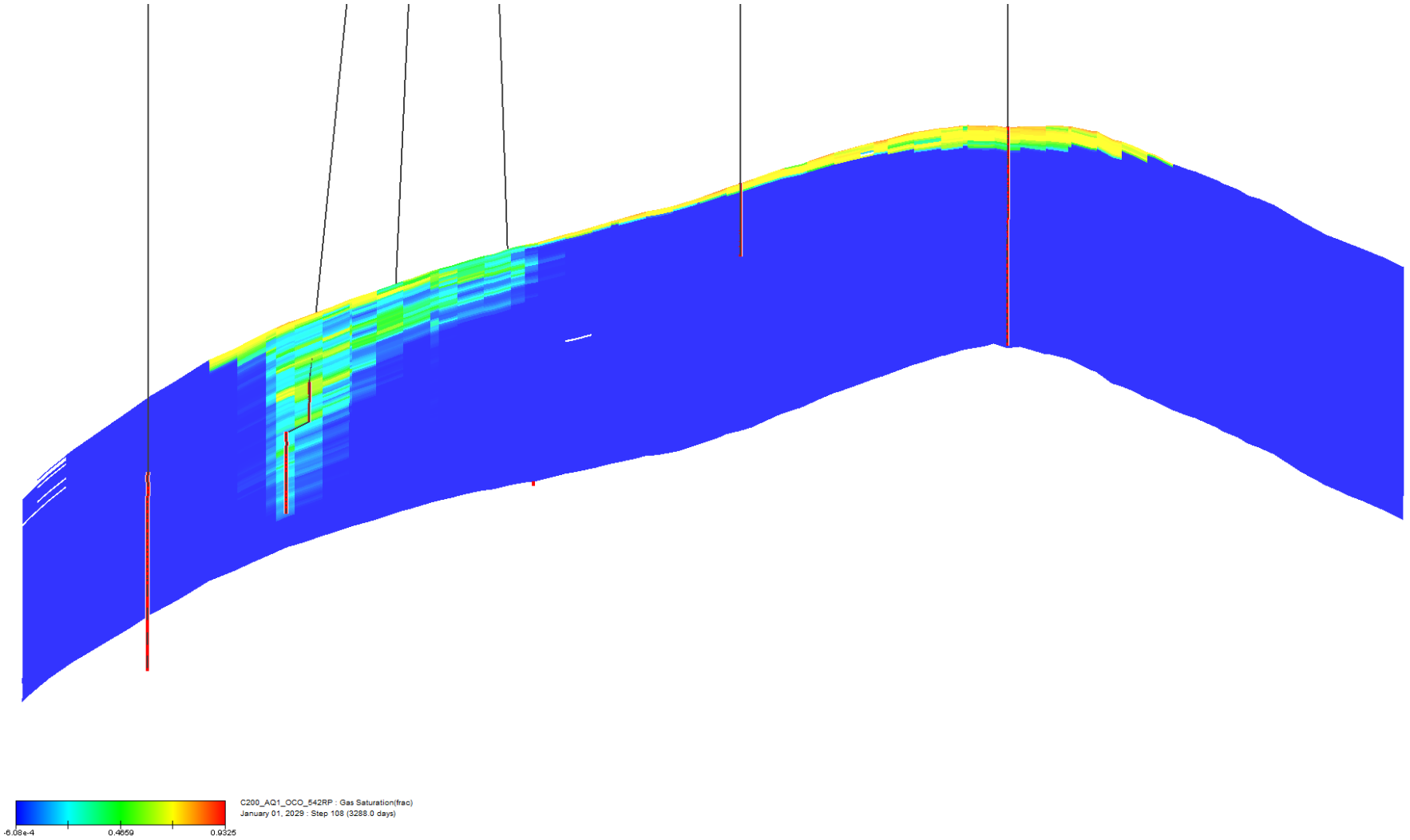

Figure 8.64: Vertical Baffle CO_2 Cross-section after 9 Years

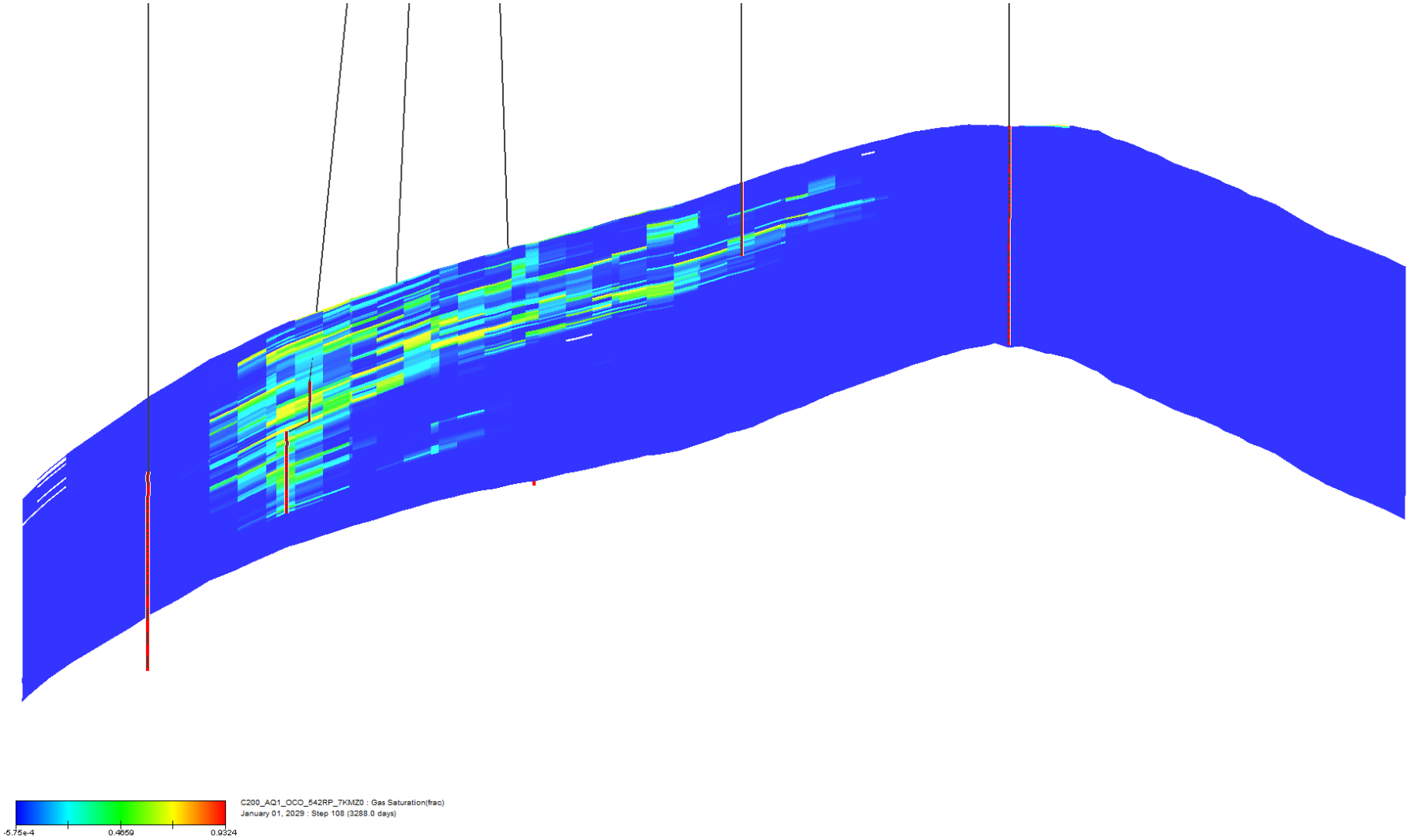

It must be stressed there is little geological evidence for either of the barrier cases presented here, horizontal or vertical; there is evidence for barriers in the Caister Bunter field. That said, most reservoirs are usually found (late in the field life) to be more heterogeneous than first thought.

8.3.14.4 Impact of Relative Permeability Data on Model Behaviour

The behaviour of the mid-case Ketzin data (dashed lines) is compared with that of the Endurance relative permeability data (solid lines) in Figure 8.65, which shows the CO_2 saturation and pressure at the crest of the structure. The difference in the pressure response was predicted to be minimal. The asymptotic value of CO_2 saturation was higher for the Endurance data because of the low irreducible water saturation for Endurance at the crest of the structure where the CO_2 is pooling.

One of the interesting results is the delayed arrival of CO_2 at the crest (by 3 months) when using the measured Endurance data set compared to the Ketzin data set. This has been attributed to the CO_2 Corey exponent for the Endurance data (N_g = 2.5) being higher than that used in the Ketzin data (N_g = 1.5). The Corey exponents control the curvature of the relative permeability curve, comparing Figure 8.39 for the Ketzin data and Figure 8.37 for the Endurance data the CO_2 relative permeability is observed to be lower for the Endurance data when the CO_2 saturation is less than 50% because of the increased curvature.

Figure 8.65: Crestal CO_2 Saturation and Pressure versus Relative Permeability Set

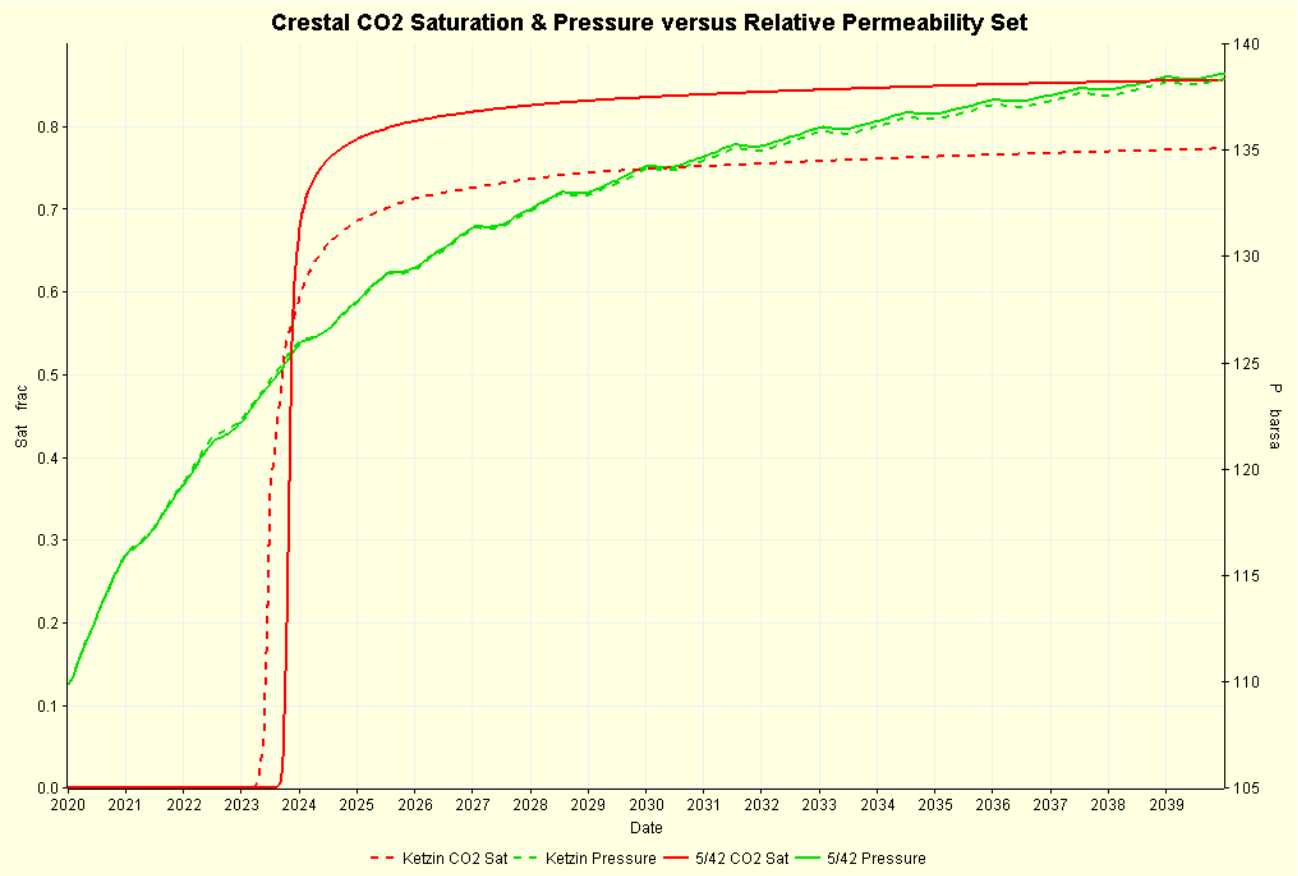

The CO_2 saturation after 20 years of shut-in (following 20 years of injection) along the west north-west – east south-east cross-section is shown in Figure 8.66 using the Ketzin data and in Figure 8.67 using the Endurance data; note both figures use the same range of 0.01 to 0.85 hence most cells are greyed-out; zero CO_2 saturation.

Figure 8.66: CO_2 Saturation Cross-section after 20 years of Shut-In: Ketzin Rel Perm

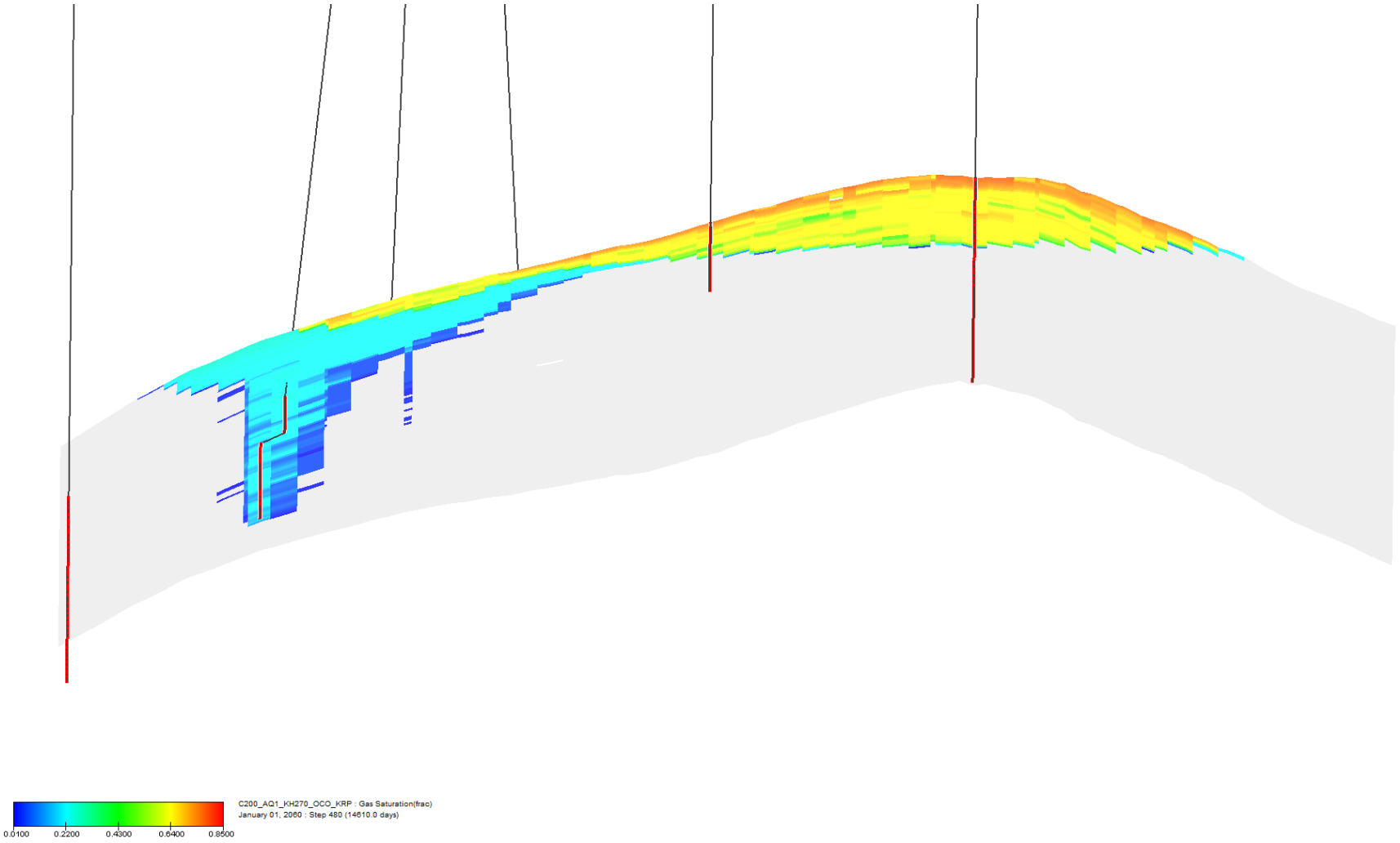

Figure 8.67: CO_2 Saturation Cross-section after 20 years of Shut-In: Endurance Rel Perm

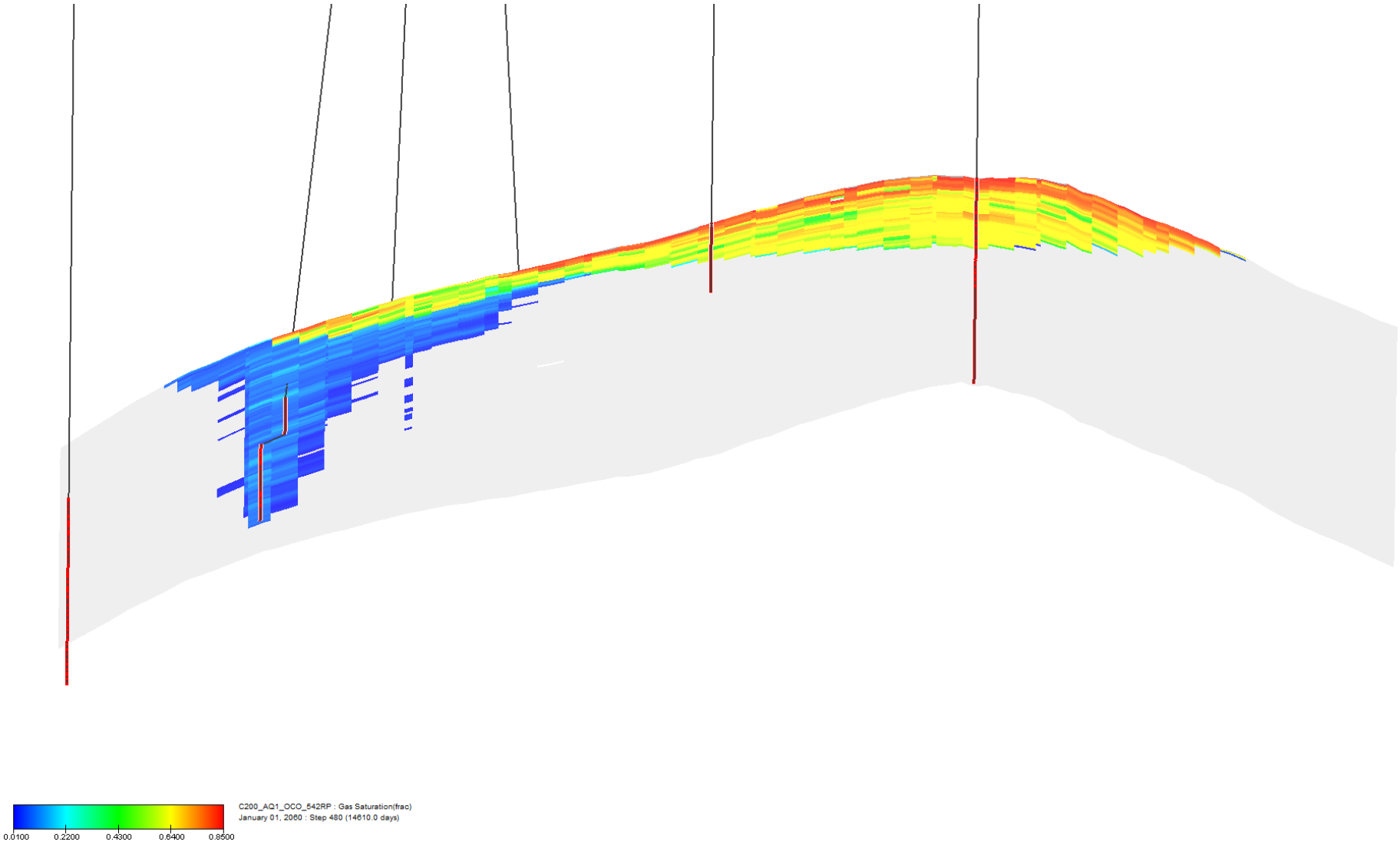

Note the shape of the plume is very similar. What differs is the trapped gas saturation which is lower using the Endurance data as shown by the darker blue colours in the vicinity of the injection wells. Whilst there appears to be significant differences between the analogue Ketzin and measured Endurance relative permeability data, in terms of the overall model performance there is little difference between the two.

8.3.14.5 Maximum Gas Relative Permeability

In Figure 8.41 the maximum gas relative permeability is shown as being $K_{rg}^{M} = 0.85$; this has been taken as the mid-case value. Low and high values have been set to 0.5 and 1.0, respectively, and the resulting crestal CO_2 saturations are shown in Figure 8.68. The effect is as expected and it replicates the changes seen by varying K_H and K_V/K_H.

Figure 8.68: Crestal CO_2 Saturation versus Maximum-K_{rg}

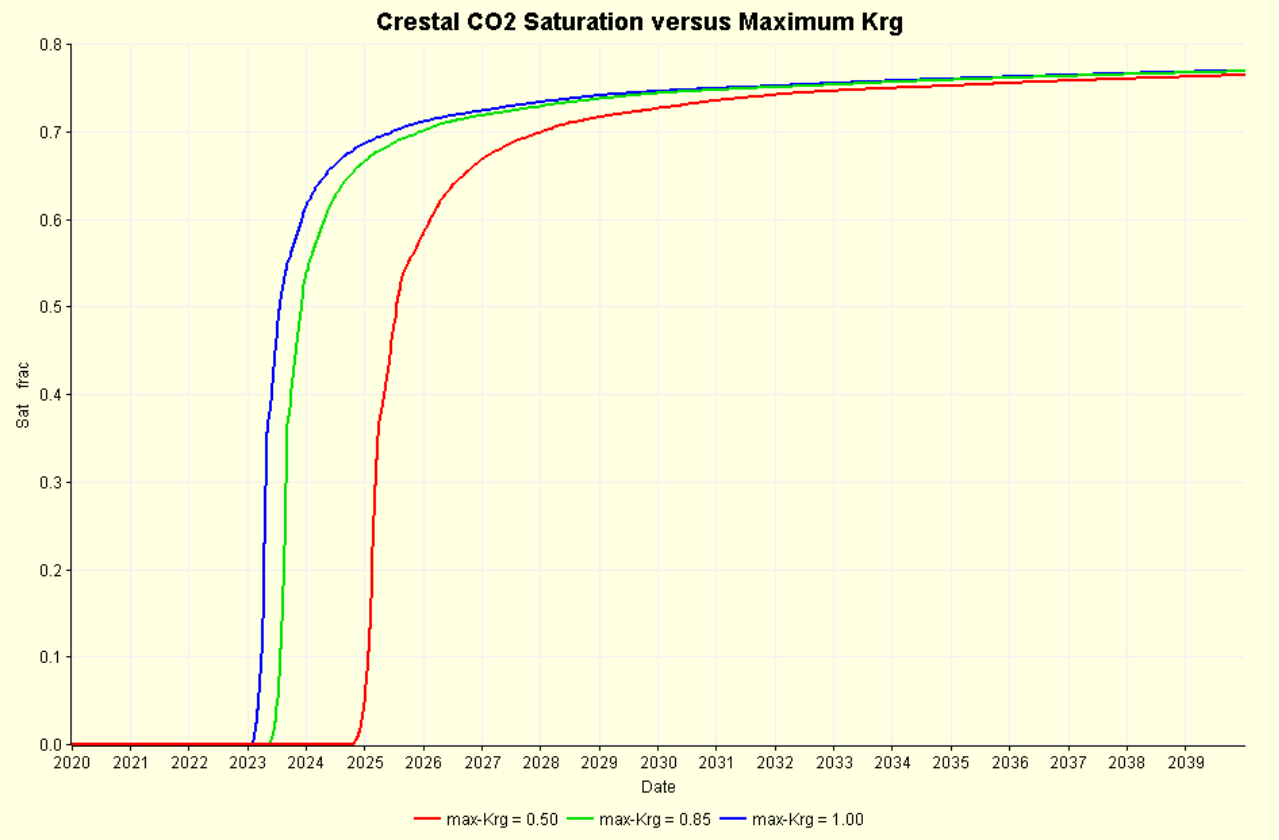

There is a change in the maximum pressure increase seen at the crest but the difference between the 0.50 and the 0.85 and 1.00 cases is less than 2.0bar.

8.3.14.6 Drainage Critical Gas Saturation

The default (mid-case) drainage critical gas saturation S_{gc} has been set to 0.05 from Table 8.12. For a low case S_{gc} = 0.0 and a high case S_{gc} = 0.1. The resulting crestal CO_2 saturation profiles are shown in Figure 8.69. Clearly setting S_{gc} = 0.0 means the CO_2 does not have to wait in a grid cell for its saturation to rise before it is free to move onto the next grid cell. This sensitivity has no discernible effect on the maximum pressure increase.

Figure 8.69: Crestal CO_2 Saturation versus Drainage Critical Gas Saturation

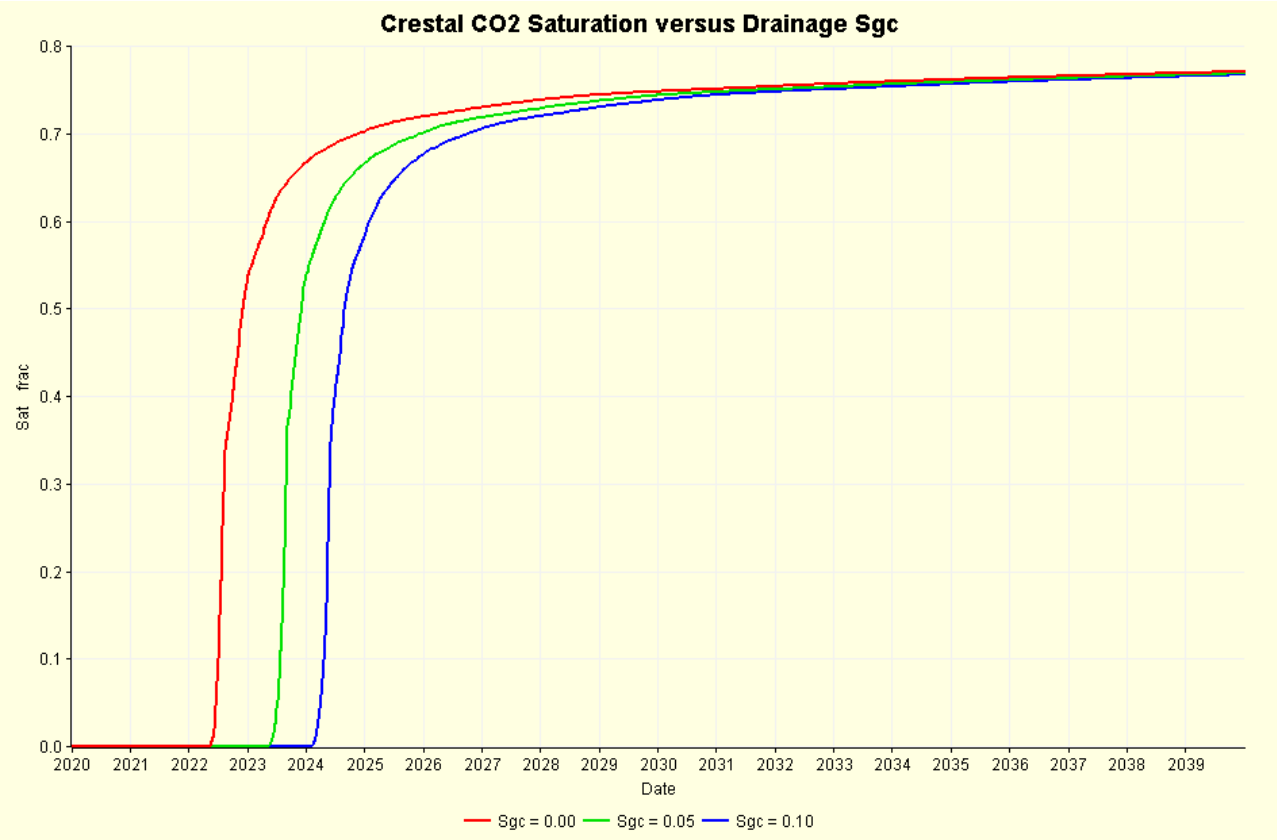

8.3.14.7 Imbibition Critical Gas Saturation

The mid-case value adopted in Table 8.12 has been S_{gt} = 0.30; low and high case values were 0.20 and 0.40 respectively. There was no discernible difference in crestal pressure increase or CO_2 arrival time as a result of this sensitivity.

8.3.14.8 Critical Water Saturation

The drainage (and imbibition) critical water saturation S_{wc} quoted in Table 8.12 was 0.15. For sensitivity to critical water saturation the mid-case S_{wc} used was 0.118. Low and high case values of

0.05 and 0.20 were selected and the resulting crestal CO_2 saturation profiles are shown in Figure 8.70.

Varying this parameter does not affect the time at which the CO_2 reaches the crest, rather it changes the maximum saturation $S_g = 1 - S_{wc}$. There is no effect on the pressure change from this sensitivity.

Figure 8.70: Crestal CO_2 Saturation versus Critical Water Saturation

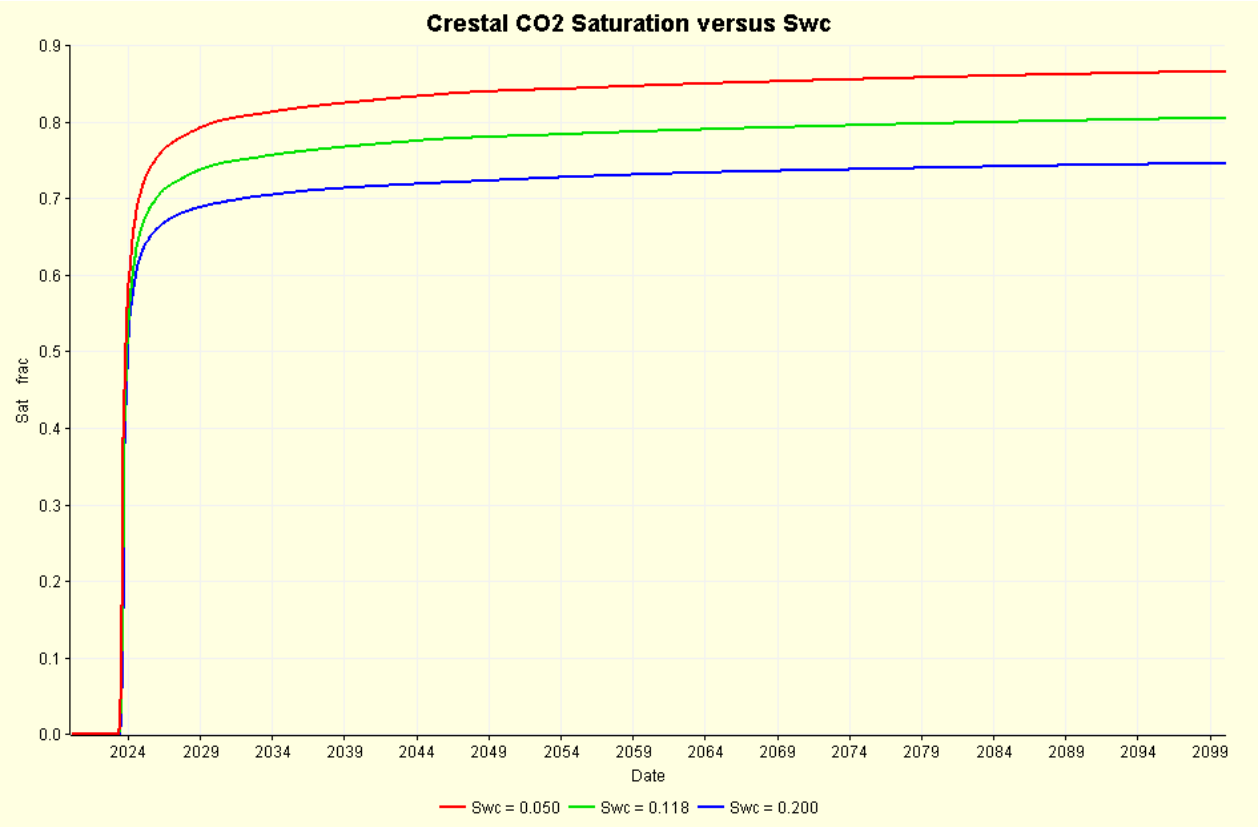

8.3.14.9 Reservoir Location of White Rose CO_2

The downhole (reservoir) volume occupied by the White Rose CO_2 mass of 53.6 Mt of CO_2 (being 2.68MTPA for 20 years) is predicted to be 84.9×10^6 m^3 from the mid case model. Assuming no dissolution or residual trapping and a critical water saturation of $S_{wi} \approx 0.15$, the pore volume required to store this volume is about 100×10^6 m^3 CO_2.

Figure 8.71: West North-West - East South-East Depth Cross-section through the Core of Endurance

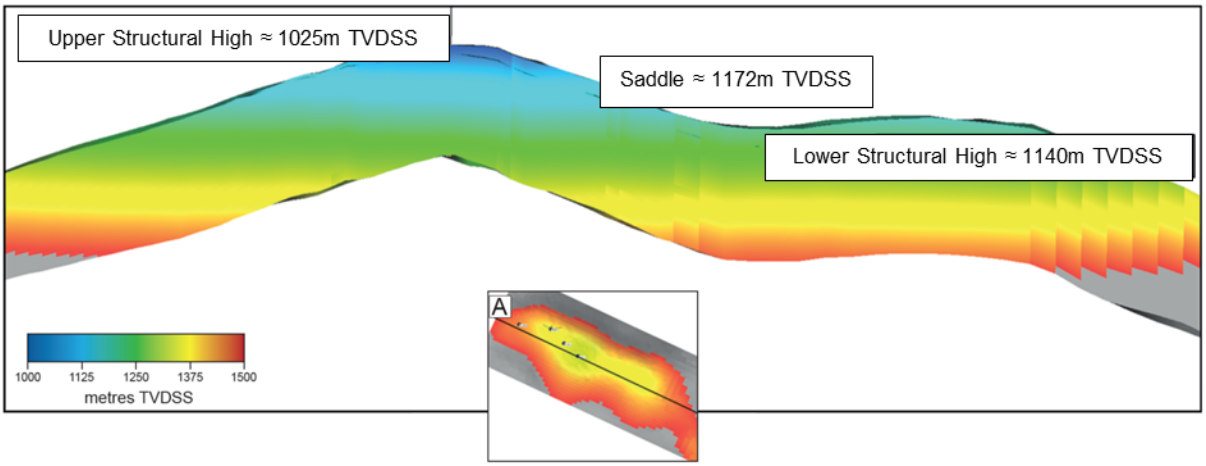

Figure 8.71 shows a cross-sectional depth display along the spine of Endurance. Note the depth of the upper peak (corresponding to the location of the 43/21-1 exploration well), the depth of the lower peak and the saddle between them. The pore volume contained in the upper peak to the spill at the saddle depth of 1172 m TVDSS is 362x10^6 m^3; 3.6 times larger than the White Rose volume. So, consideration is given here to whether there is any way CO_2 can get to any part of Endurance other than the upper peak given the current injection locations to the north-west of the structure.

It is pertinent here to consider Darcy's Law applied in the vertical direction:

Equation 8.11

$$v_z = \frac{K_V K_{rC}}{\mu_C} \frac{dP}{dZ}$$

Where:
v_Z is the vertical velocity (in m/s)
K_V is the vertical permeability (in m^2)
K_{rC} is the CO_2 relative permeability
μ_C is the CO_2 viscosity
dP/dZ is the vertical pressure gradient
The effect of capillary pressure and gravity head has been ignored

The pressure gradient is driven by the density difference between the native brine of $\rho_B \approx 1170$ kg/m^3 and the CO_2 density in the reservoir which varies between $600 \leq \rho_C \leq 800$ kg/m^3; a mid-case density of $\rho_C \approx 700$ kg/m^3 is assumed here to give a density gradient of $dP/dZ \approx (\rho_B - \rho_C).g$ = (1170 – 700) (9.81) = 4610 Pa/m (0.0461bar/m).

The average vertical permeability can be estimated from $K_V = K_H (K_V/K_H)$ = (271) (0.15) (10^{-15}) = 41x10^{-15} m^2, where $K_V/K_H \approx 0.15$, $K_H \approx 271$ mD, and 1 mD ≈1x10^{-15} m. At typical reservoir conditions the CO_2 viscosity $\mu_C \approx 0.06$x10^{-3} Pa.s.

The vertical velocity of CO_2 can then be estimated to be $v_Z = 3.15\text{x}10^{-6}\ K_{rC}$ m/s, where K_{rC} is the maximum CO_2 relative permeability which when set to 0.85 gives $v_Z = 2.68\text{x}10^{-6}$ m/s. The injection rate of 2.68MTPA is equivalent to a reservoir conditions volumetric rate of 11,500m^3/d or Q = 0.133 m^3/s. Therefore the horizontal velocity will be $v_H = Q/(2\pi RH)$ where R is the radial distance from the well where the velocity is being calculated and H is the perforated length through which the fluid is being injected. With the injection wells being deviated 60^o from the vertical, the perforated length in the reservoir is about 250m so that $v_H \approx Q/(1500\ R) = 90\text{x}10^{-6}/R$ m/s. Therefore, at around 30m from the injection wellbore the (near-constant) vertical velocity will always exceed the falling horizontal velocity so even if one or more of the wells intersected an extremely high permeability streak, the CO_2 cannot avoid its ultimate fate of pooling under the upper peak. A further reinforcing consideration is that the injection rate of 2.68MTPA is a maximum value (of flow from the power station) unlikely to be reached in practice for any extended period of time.

8.3.15 Injectivity

One of the key objectives of the flow test performed on the 42/25d-3 appraisal well was to assess injectivity. The test (summarised in Section 8.1.2.1) demonstrates that injection at the specified rates would be possible over the perforated interval although the large pressure spike observed about 1200 s after the start of injection give cause for caution. The timing is significant as it corresponds to the time required for the sea-water from the surface to reach the perforations (at 795 m^3/d) given the Internal Diameter (ID) of the well tubing.

The pressure spike is thought to have been caused by some contamination carried with the injected sea water. The pressure spiked until a fracture was created and as the injection test continued, and the rate was increased in two further increments, the effect of the blockage was gradually reduced. There is a possibility that the blockage was caused by an interaction between the native brine and the sea-water or as a temperature effect.

8.3.15.1 CO_2 Injection Wells Injectivity

To maximise the opportunity for residual trapping as well as keep colder CO_2 away from the cap rock it is proposed to perforate the lower half of the three injection wells drilled from the P5 platform location. One downside of the lower half perforation strategy is the quality of the Bunter Sandstone formation degrades with depth so that while porosity at the top of the Bunter often exceeds 0.25, at the bottom of the Bunter it can be less than 0.15, with consequent effect on permeability via Equation 8.4. This has been investigated using the simplified injection model developed in Section 8.3.14.1.

Equation 8.12

$$Q = I_I \Delta P$$

In Equation 8.12 ΔP is the (depth corrected) pressure difference between the Bottom Hole Pressure (BHP) and (average) reservoir pressure into which the (total) rate Q is being injected and I_I is the Injectivity Index.

To assess injectivity two simulations were performed with one having the well shown in Figure 8.65 perforated through the whole of the Bunter Sandstone and the other having the well just in the lower half. The resulting well Injectivity Index for the two cases is shown in Figure 8.72.

The units for II in Figure 8.72 are m^3/day/bar which E100 does not append to the outputted property. After the transient (pressure and saturation) changes have declined, the pseudo-steady-state II is over three times lower for the case where the whole well has been perforated.

The variation of BHP however needs to be considered in conjunction with the differences in Injectivity Index. In Figure 8.73 the BHP variations for the three CO_2 injection wells are shown for the mid-case model. Note the cyclic nature of the wells which are injecting half the total rate of 2.68MTPA for 12 months out of every 18 months (see Section 8.3.12.3 for summary of well switching scheme).

The transient spike in BHP at the start of each well's 12-months of injection is a relative permeability effect. In the grid cells containing the well completions, the CO_2 saturation and hence the CO_2 relative permeability is low initially. This in turn means the mobility is small and a high pressure difference is required to achieve the desired flow rate. The transient spike is almost the same on the first injection cycle for all three wells. All the wells see an increase in the transient pressure on the second cycle of injection. Thereafter the transient pressure for P5DEV2 is greater than P5DEV3 which is greater than P5DEV1.

Figure 8.72: Well Injectivity Index in Simplified Model

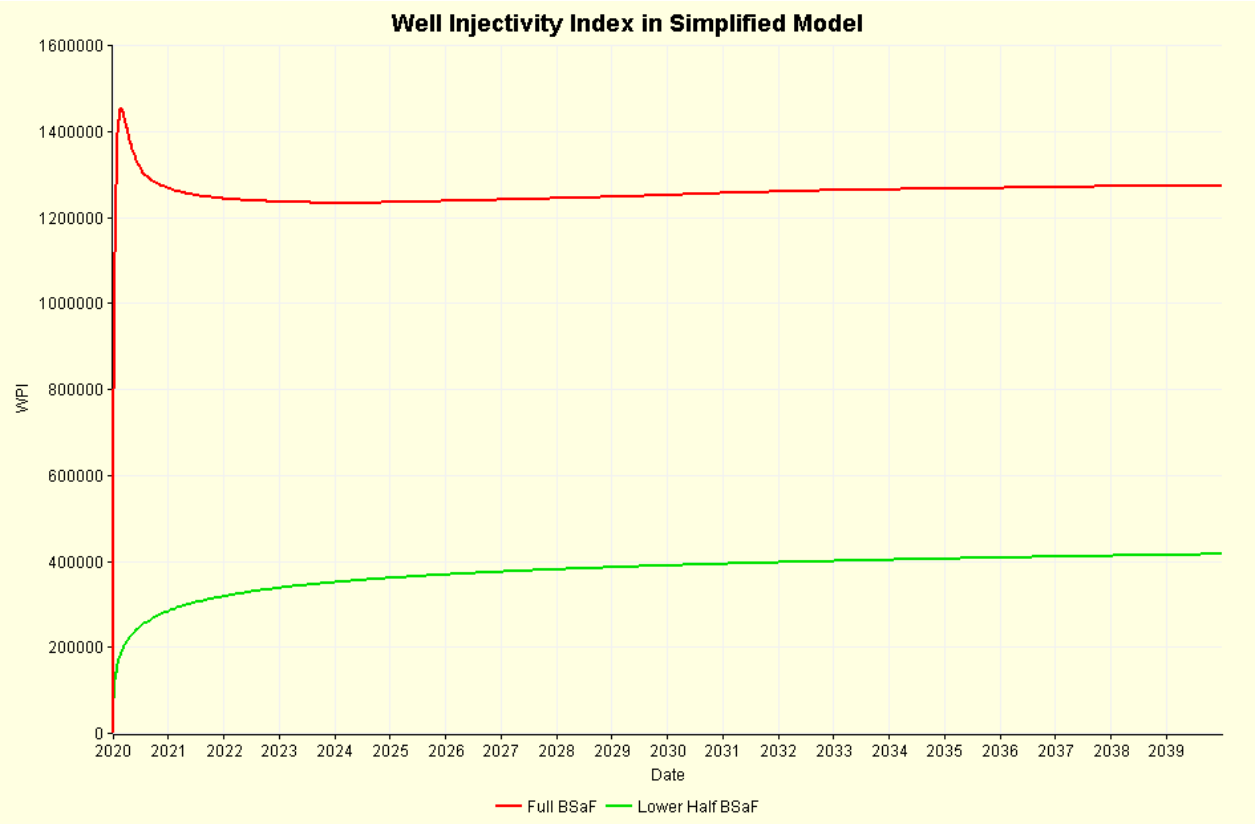

The jump in the transient pressure spike between the first and second cycles of injection occurred during the six months period that the well is shut-in, the buoyant CO_2 migrates up-structure and fresh brine imbibes into the vicinity of the shut-in well, trapping CO_2 at a saturation of about S_{gt} = 0.30. When CO_2 injection resumes, a new drainage (of the brine) phase begins but with a lower effective

CO_2 relative permeability and hence the need for a larger BHP to achieve the required flow rate. After the third and fourth cycles the pattern settles down. Note that the Ketzin Kr data (Figure 8.39) which incorporates the extreme limit of S_{gt} was used for this simulation. In contrast the measured Endurance Kr data (Figure 8.37) has in contrast S_{gt} ~ 0.10 which would likely cause a smaller change in CO_2 mobility after fresh brine imbibition and hence reduce the pressure spikes predicted in Figure 8.72.

The differences between the BHP responses of the three wells are due to their relative locations and the way in which CO_2 and brine move during the 12-month injection period and 6-month shut-in period of each well. CO_2 injected in P5DEV1 and P5DEV3 migrates upward in the plane of the wells before heading toward the crest, thereby leaving higher CO_2 saturation behind, whereas the CO_2 injected in P5DEV2 move tangentially away from this well's trajectory toward the crest (Figure 8.72 and Figure 8.75).

Figure 8.73: BHP Variations from Mid-Case Model

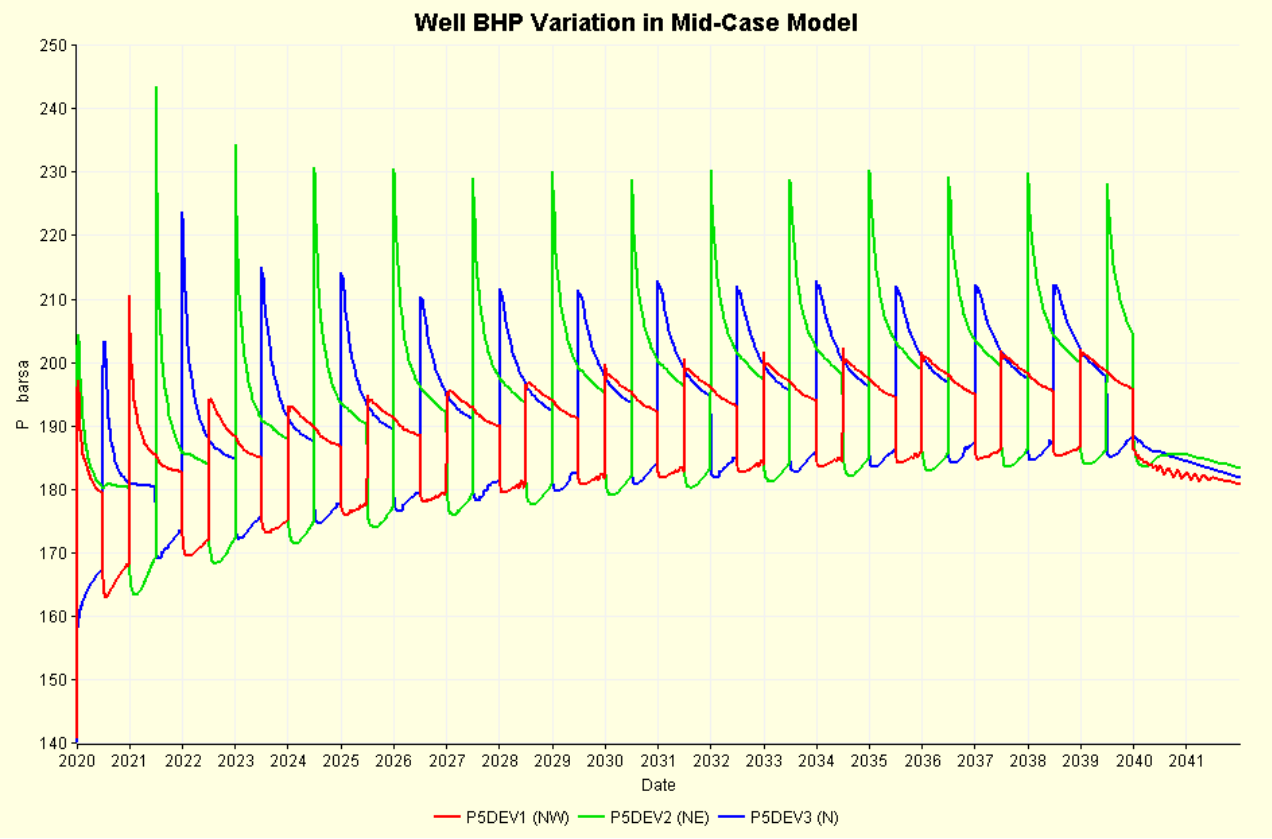

Figure 8.74: Line of Cross-section through Injection Wells

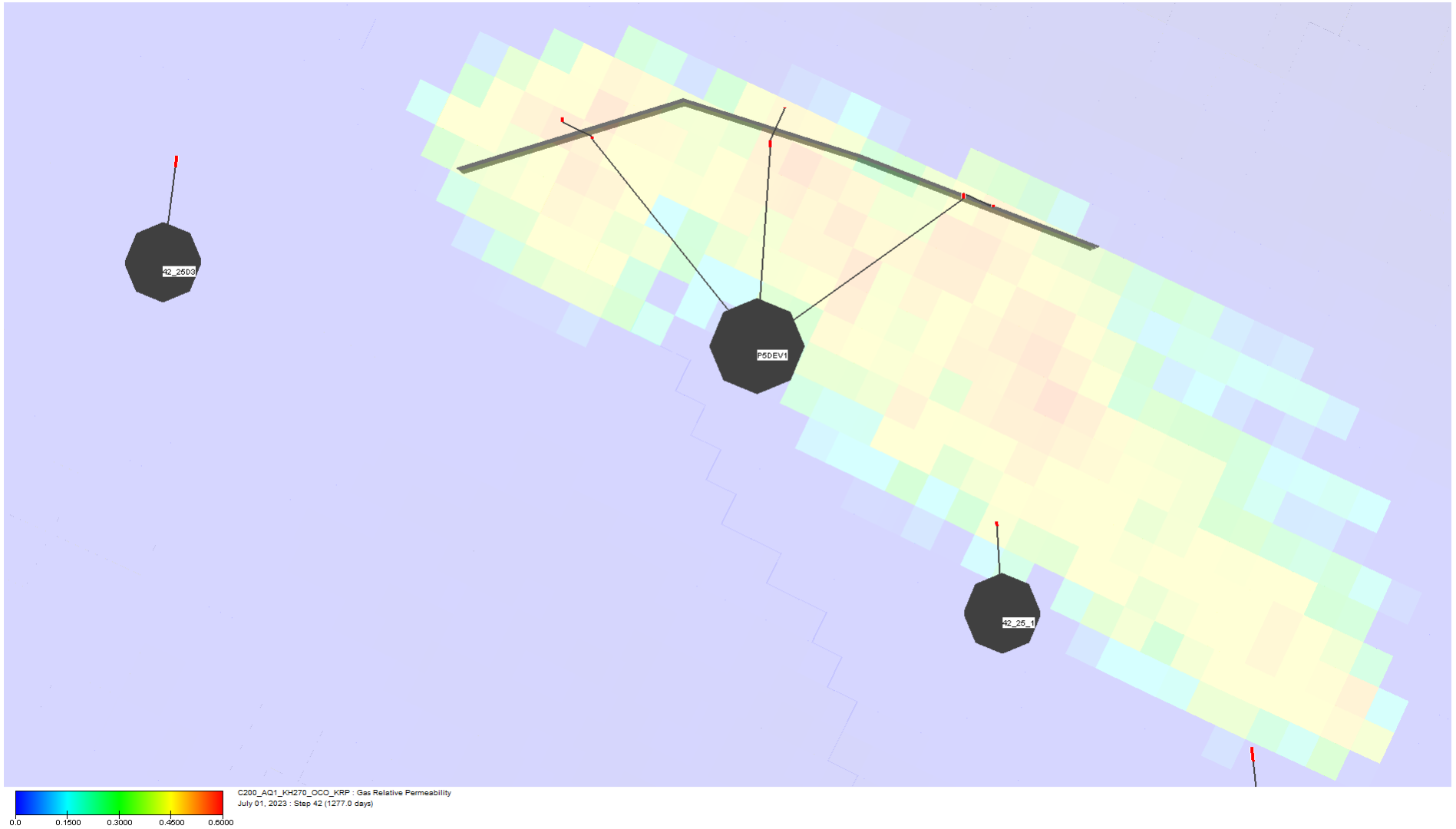

Figure 8.75: CO_2 Relative Injectivity shown on Cross-section Defined in Figure 8.74

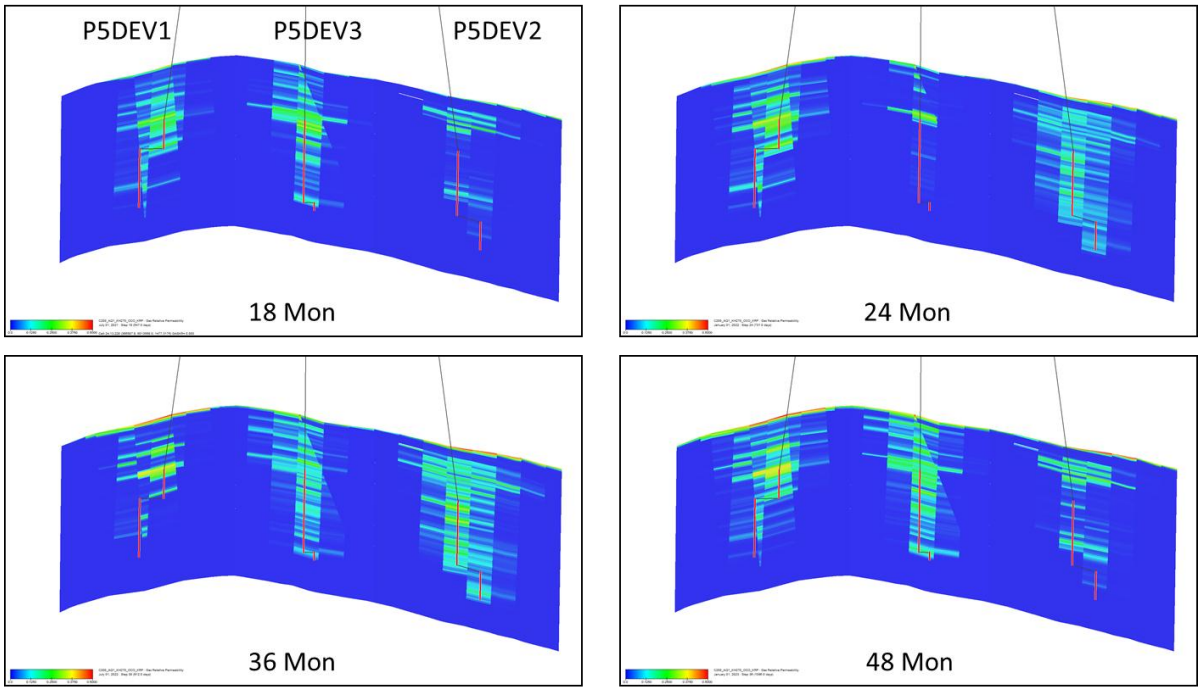

8.3.15.2 Skin Factor

The default skin applied to all the wells is zero. There is a case to suggest that the skin in the actual wells could be negative as a result of thermal fracturing caused by relatively cold CO_2 cooling the rock in the near wellbore; note that the perforation strategy will prevent any thermal fracturing near the Röt Clay cap rock by confining perforations to the deeper zones of the Bunter formation. Alternatively, positive skin may result due to mechanical blockage as was seen in the injection phase of the 42/25d-3 well test. For the purposes of understanding the range of possible effects a beneficial case has been simulated using a skin of S = -2 applied to all perforations whereas a detrimental case has been simulated using S = +5; the mid-case being S = 0.

There is no effect of changes in skin (of the range of magnitudes investigated) in terms of the crestal pressure increase or the time taken for the CO_2 to reach the crest of the structure. Skin clearly has an effect on well BHP and the difference is shown in Figure 8.76 for the P5DEV1 only. The other two wells show a similar response.

The beneficial effect of the negative skin (red line) is relatively modest but again it must be stressed the value of S = -2 has been assessed based on experience of realistic negative skins rather than detailed modelling.

The detrimental effect of the positive skin (blue line) is potentially of more concern as the assessed value of S = +5 is not considered particularly high and yet the second cycle transient response is close to the maximum pressure that would be tolerated to avoid hydraulic fracturing.

Figure 8.76: P5DEV1 BHP versus Skin-Factor

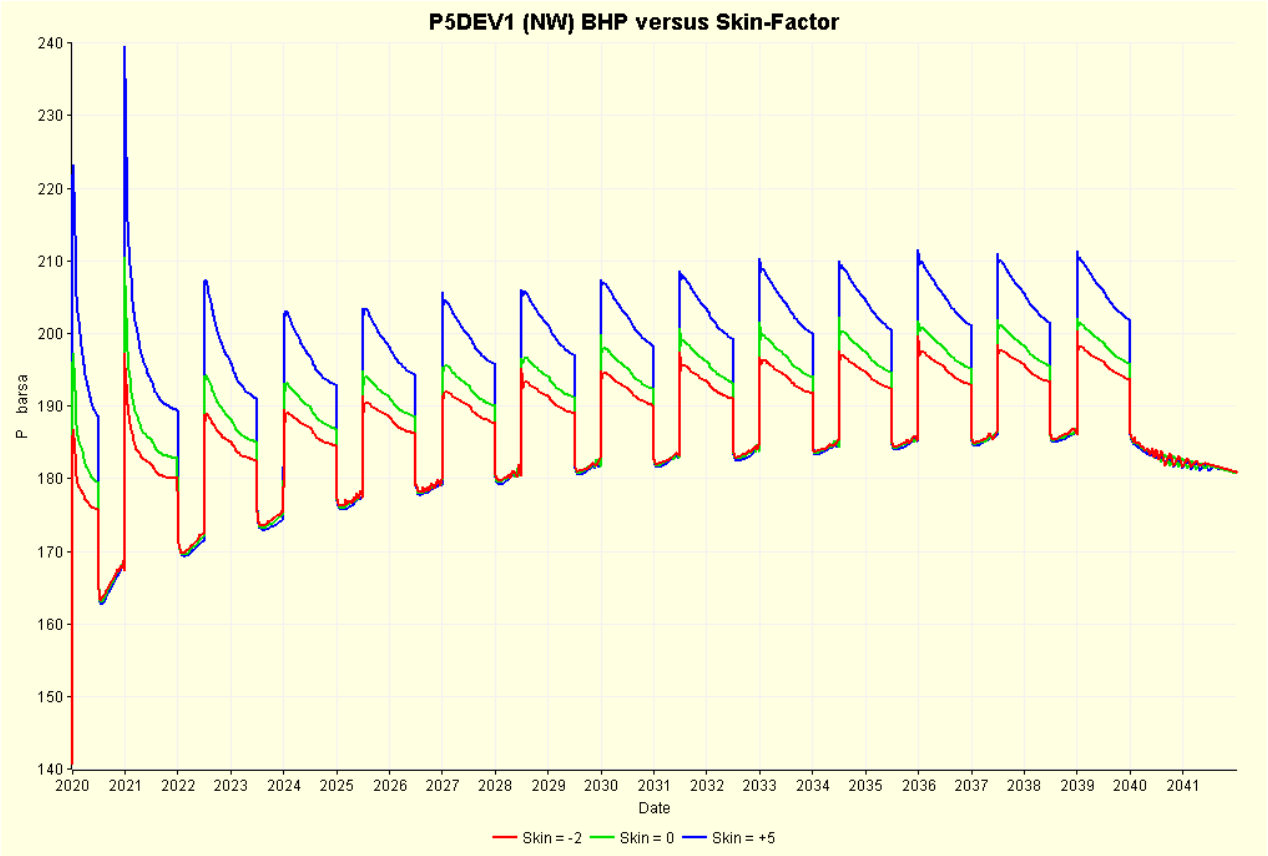

8.3.16 Temperature Effects

The simplified injection model was used to examine how temperature profiles within Endurance might change as a result of injection of cold CO_2.

The CO_2 will be transported to Endurance through a 90km 24in pipeline and so will cool to the seabed temperature which will vary between 5°C and 15°C winter to summer. Using the steady-state Prosper modelling, it is estimated that the CO_2 will heat by about 10°C between wellhead and the perforations meaning the lowest sandface temperature is estimated to be 15°C compared with a reservoir temperature of about 55°C (the specified CO_2 injection wells are up-structure of 42/25d-3).

Two cases of the simplified injection model have been considered here. The first considers the whole Bunter interval is perforated so see the effect of putting cold CO_2 against the cap rock, see Figure 8.77. The second case is thought to be more likely as only the lower half of the well has been perforated, see Figure 8.78.

Figure 8.77: Temperature Cross-section after 20 Years, All Bunter Perforated

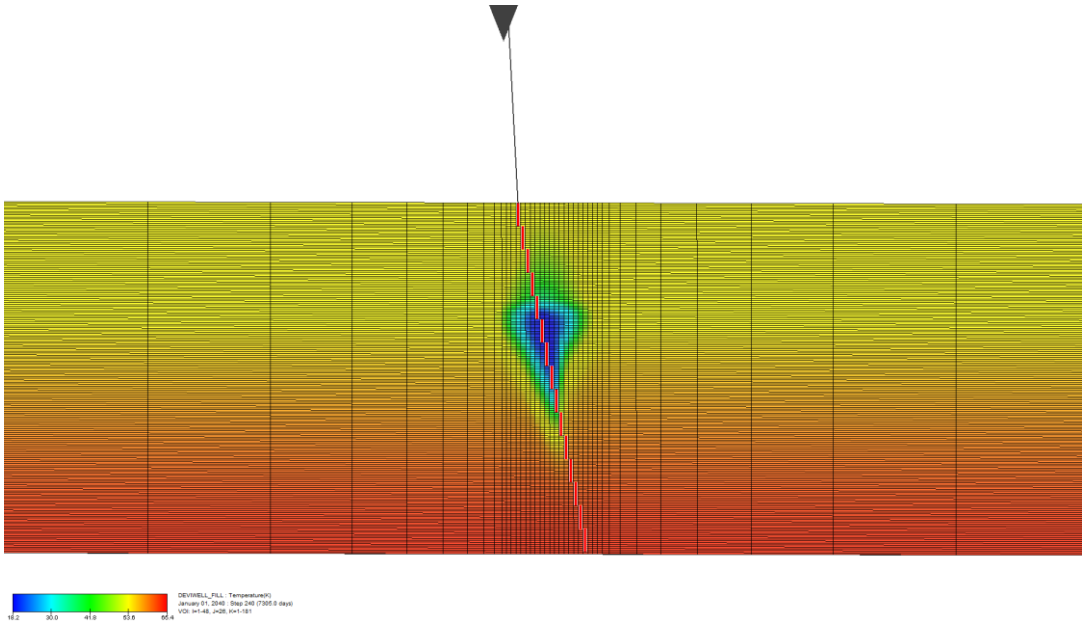

Figure 8.78: Temperature Cross-section after 20 Years, Lower Bunter Perforated

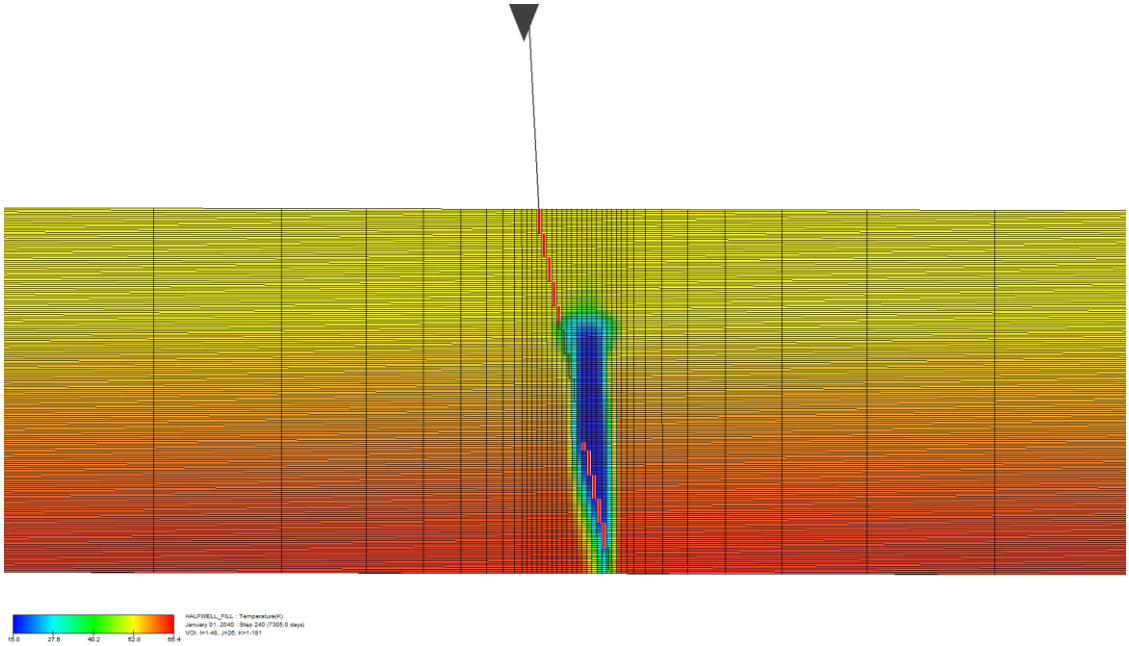

The convective cooling effect of placing cold CO_2 against the cap rock is felt immediately if the top of Bunter Sandstone is perforated as is seen in Figure 8.77. This should be compared with the gradual cooling that would be achieved by injecting deeper in the Bunter Sandstone. With reference to the detailed simulation models it is noted that the CO_2 takes between 6 to 12 months to flow from top perforation to the cap rock. Therefore the 20 year profile shown in Figure 8.78 would take many months to develop in practice.

8.4 Simulation of the Diffusion-Dissolution-Convection Process

The four main CO_2 trapping mechanisms during CO_2 sequestration include:

- structural trapping in which CO_2 accumulates beneath an impermeable cap rock;
- residual trapping in which part of the migrating CO_2 plume gets detached and ultimately trapped by capillary forces;
- solubility trapping in which both structurally and residually trapped CO_2 dissolves in the brine via diffusion and convective processes; and
- mineral trapping in which the dissolved CO_2 reacts with the brine and the host rock to produce solid minerals.

Section 8.3.14 has already dealt with structural and residual trapping. Only the characterisation of solubility trapping has not been presented so far.

The full field simulation approach used in the prediction of CO_2 plume development, specifically the use of analytical aquifer models, does not permit direct modelling of the dissolution of CO_2 in brine under dynamic flow conditions. An alternative scheme that uses a 2D XZ sector model of Endurance has therefore been used to quantify solubility trapping and thereby gain a better insight into the long term fate of White Rose CO_2.

8.4.1 Diffusion-Dissolution-Convection Process Overview and Simulation Model Set-up

CO_2 dissolution in brine occurs by molecular diffusion across the CO_2-brine interface and this process would take place wherever a CO_2-brine interface exists; both CO_2 trapped by capillary forces and CO_2 trapped under the cap rock will undergo dissolution over time. Since the Endurance relative permeability measurement suggests that less than 10 % of White Rose CO_2 is likely to be trapped in residual form, the Diffusion-Dissolution-Convection (DDC) modelling has focused on dissolution of the CO_2 cap at the crest of the Endurance structure.

Dissolution of CO_2 increases the brine density (by approximately 2.5 kg/m^3), creating a denser brine layer below the plume. This layer eventually becomes gravitationally unstable so that fingers of dense CO_2-rich brine propagate downward and transport the aqueous CO_2 away from the interface. This density-driven convection increases the rate of mass transport from the free CO_2 phase into the brine phase and is typically orders of magnitude faster than pure diffusion.

The E100 black oil simulator with the diffusion option has been used for modelling the DDC process. The grid is a 2D XZ sector model of Endurance, 2500m × 200m across and consisting of 100, 000 cells (Figure 8.79). The central portion (500m) of the model is assumed to capture the extent of the CO_2 plume predicted by the full field model (Figure 8.79a). The left and right hand sides are for the reservoir section outside the CO_2 plume footprint area. The simulation model is given a dip angle of 2.3^o by varying the depth of cells on the left and right hand sides at the top layer as shown in Figure 8.79. The key parameters for this model are:

- Cell number (N_x, N_y, N_z) = (500, 1, 200)
- ΔX = 5 m
- ΔY = 3000m
- ΔZ = 1 m

The top layer of the model is used to represent the CO_2 plume in the crest of the reservoir structure at a depth of 1299 m TVDSS. Using a pore volume multiplier of 20, the top layer has a free CO_2 initially in place of 2.24 billion sm^3, which is about $1/10^{th}$ of the CO_2 at the crest of Endurance at the end of injection. The 2D sector model is therefore considered scalable to the CO_2 storage in Endurance.

Porosity and permeability were distributed across the model in the manner described in Section 8.3.2.2. Firstly porosity was defined as a linear function of depth with a value of 0.27 at the top and 0.14 at the base. Then horizontal permeability was defined from Equation 8.4 with an approximate value of 2020mD at the top and 19 mD at the base of the model. Additionally, a small random variation in permeability is also applied to initiate the development of the dense brine fingers as described in. Fluid and rock properties pertinent to the simulation are listed in Table 8.17. The PVT inputs such as viscosity and solubility are generated based on the correlations found in the technical literature.

Figure 8.79: Construction of the DDC Model: (a) Full Field Model, (b) 2D Slice, X-Direction and (c) Full DDC model

(a) Full Field Model

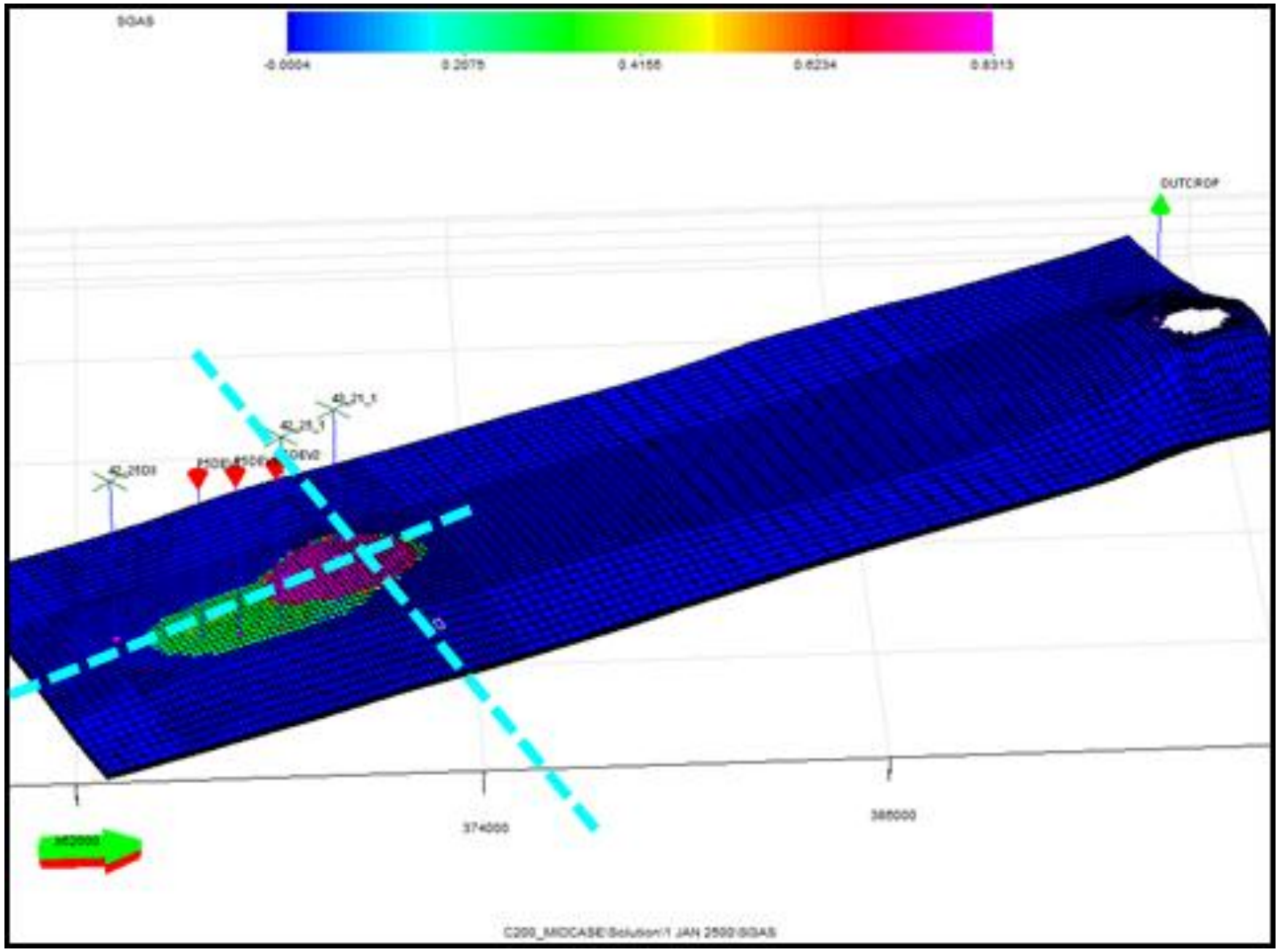

(b) 2D Slice, X-Direction

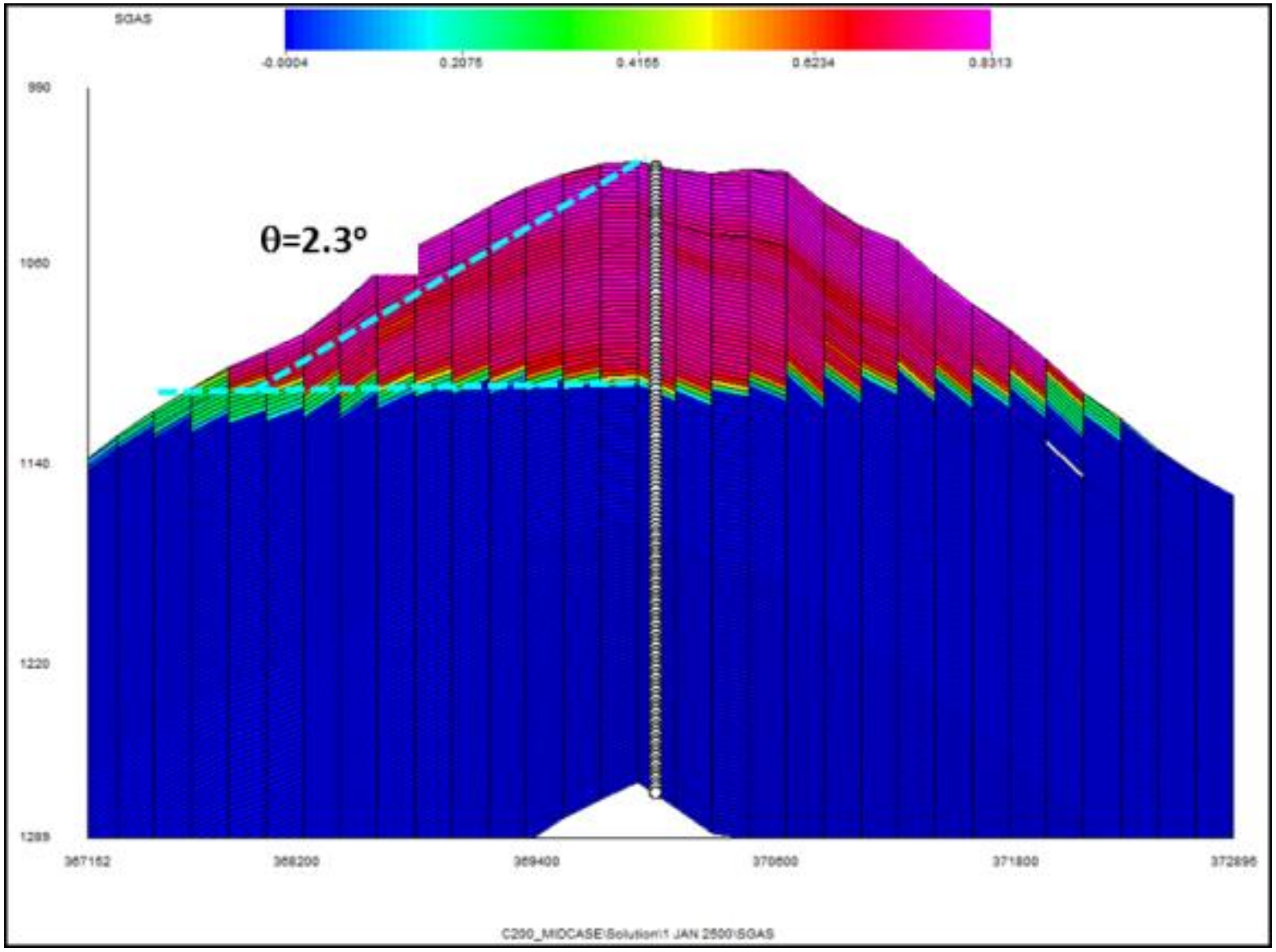

c) Full DDC model

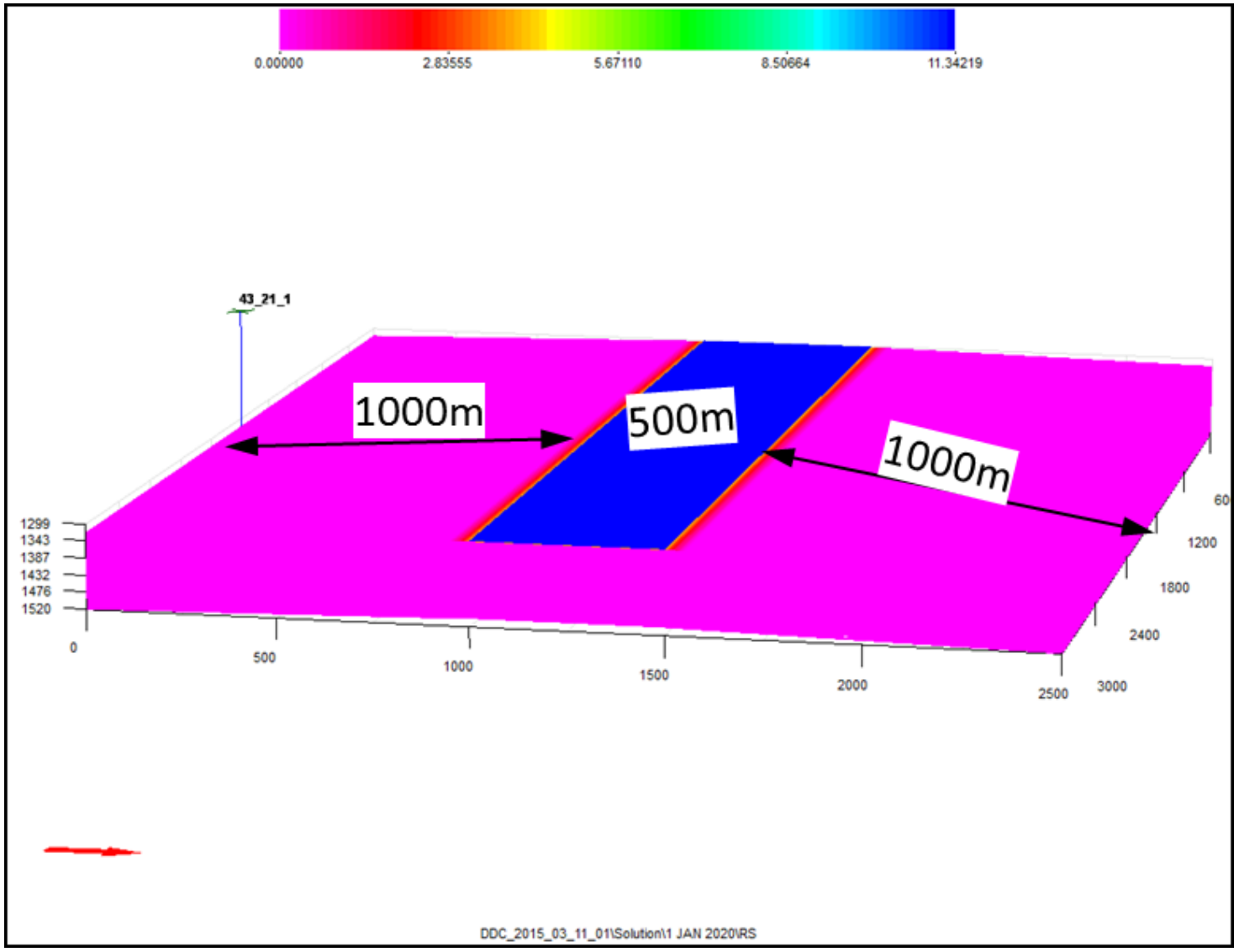

Table 8.17: Critical Parameters of DDC using Typical Bunter Properties

Attribute	Value	Unit	
Temperature	56	C	
Reservoir pressure	141	Bar	
Salinity	250, 0000	Mg/kg	
Viscosity	$9.0x10^{-4}$	Pa.s (kg/s/m)	0.9 cP
Diffusion coefficient	$2.0x10^{-9}$	m^2/s	
K_V/K_H	0.15		

8.4.2 Diffusion-Dissolution-Convection Process Simulation Results

The CO_2-in-Brine concentration (in m^3 of CO_2 per m^3 of brine, both at standard conditions) is shown in Figure 8.80. The eight cross-sections are shown at 01/January/YYYY where YYYY is the year shown.

The onset of convective fingers is discernable 100 years post injection. The process starts out with multiple fingers which then broaden and coalesce as CO_2-laden brine propagate downward whilst the lighter brine flows upward, a phenomenon that has been widely reported by several researchers.

The plume of saturated brine does not reach the base of the model until 01/Jan/12000; about 10,000 years after the cessation of injection, at which time about 25% of the initial CO_2 in place had dissolved.

Figure 8.80: CO_2-in-Brine Distribution at Stated Years

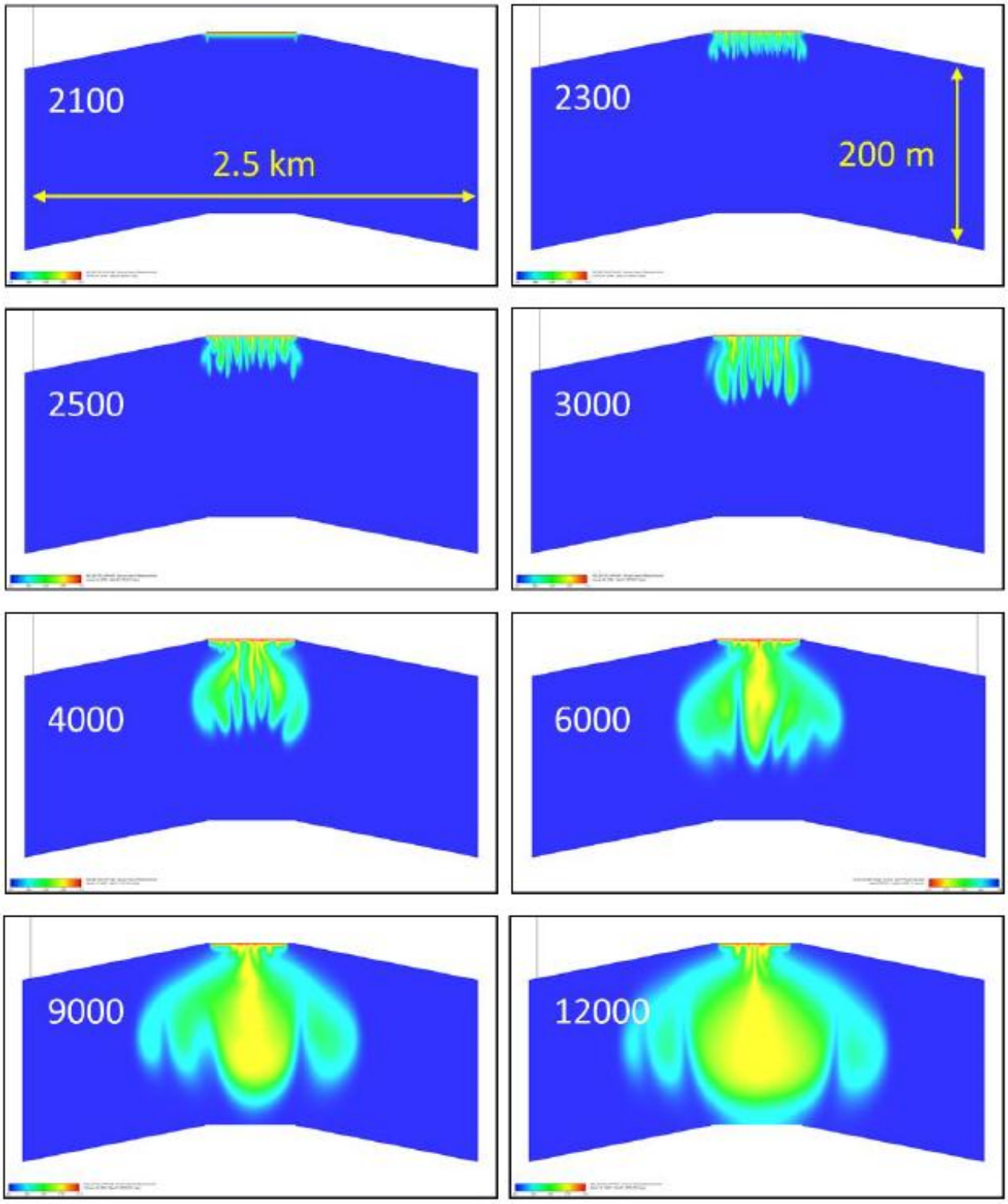

8.5 Possible Influence and Effects on Regional Hydrocarbon Developments

Hydrocarbon developments in the southern North Sea that are likely to be influenced by CO_2 injection into Endurance are fields producing (or that previously have produced) gas from the Bunter Sandstone formation. Table 8.18 shows the production data from the eight gas fields within the potential Regional Area Of Influence (RAOI) around Endurance and Figure 6.3 their locations. As gas is produced from a gas reservoir and the reservoir depressurises, water encroaches from the underlying aquifer into the reservoir to provide pressure support. Any process that increases the pressure of the underlying aquifer such as CO_2 injection will increase this pressure support. Although the gas fields listed in Table 8.18 produce wholly or partly from the Bunter Sandstone formation, only a subset (Esmond, Caister-Bunter, Forbes and Gordon) show evidence of hydraulic connectivity to a shared aquifer with Endurance and close enough to receive any significant transient pressure support from CO_2 injection into Endurance.

The Hewett field is the dominant producer but only 35% of its production comes from the Bunter Sandstone formation (the rest is from Hewett Sandstone and Zechstein Carbonates). Moreover, water influx into the Hewett Bunter Sandstone formation interval has been shown to be limited due to local faulting in this area and this applies also to the Little Dotty reservoir. Both Hewett and Dotty are therefore probably not in hydraulic communication with Endurance.

Figure 6.3 shows that Orwell is located just south of the Cleaver Bank Zone where the Bunter Sandstone is partially eroded; thus limiting any potential pressure communication with Endurance. Data on the dynamic behaviour of the Hunter field is not available and would probably be of little value in properly assessing its hydraulic connectivity to Endurance given the insignificant production from this field relative to other fields within the regional area of influence.

To summarise, the influence of CO_2 injection into the Endurance storage site upon regional hydrocarbon developments is likely to be non-existent or immeasurably small. The gas fields that share a common aquifer with Endurance have either ceased producing or have too weak hydraulic connectivity to the sector of the Bunter aquifer within the potential regional area of influence to receive any measureable pressure communication with Endurance.

Table 8.18: Cumulative Production from Bunter Gas Fields

Field	Cumulative Gas Production to 2013 Msm^3	Date Production Ceased
Caister-Bunter	3,202	-
Esmond	8866	Mar 1995
Forbes	1473	Feb 1993
Gordon	3994	Feb 1995
Hewett[1]	122,378	Still Flowing
Hunter	41	-
Little Dotty[2]		
Orwell	8618	Jan 2000

Hewett Field has reservoirs in Upper Bunter (BSF), Lower Bunter or Hewett Sandstone and Zechstein Carbonates. Little Dotty production is through Hewett 48/29-A platform.

8.6 Conclusions

The Bunter Sandstone formation is extensive in the UK southern North Sea with an area in excess of 20,000km^2, an average thickness of 250m and an average porosity of 19% implying a PV of 1000x10^9 m^3 or more. How much of this volume is connected to Endurance is unknown, but the post-production pressure history of the Esmond Gas field and pressure measurements taken in Endurance between 1990 and 2013 provide some evidence to suggest they are connected.

The seabed outcrop of the Bunter Sandstone formation to the east of Endurance is seen to be more of an opportunity than a threat. Geological arguments favour the outcrop is both in hydrodynamic communication with Endurance and open to flow to the seabed; thus forming a natural pressure relief well. Thermodynamic considerations would suggest the brine salinity in the upper portion of the outcrop is more like that of seawater than that of Endurance, so any expulsion of fluid should have minimal effect on the seabed. In the worst case of minimal extra aquifer volume, the maximum flow rate from the outcrop will be approximately 3500m^3/d which is comparable to what might be expected from a single high-rate high water-cut well in a mature North Sea oil field.

A simple material balance model suggests the pressure increase in Endurance from injecting the first load of 53.6 Mt of CO_2 over a twenty year period in excess of 194bar; probably enough to fracture the reservoir and cap rock. However, it is believed Endurance is connected to a much larger volume which could be in excess of 1000x10^9 m^3. Even if this were the case, because of the distances involved, not all this volume can be expected to react in the timescales of the injection and it is suggested that no additional benefit is derived from a volume in excess of 100x10^9 m^3, that is 20 times that of Endurance itself. The pressure increase expected at the crest of the structure from injecting first load is between 25bar and 65bar with a most likely value of 40bar

The speed at which the CO_2 will flow from the perforations of the injectors, assumed to be in the Lower Bunter, in the north-west of Endurance to the crest depends on: horizontal and vertical permeabilities, maximum gas (CO_2) relative permeability, drainage critical gas saturation, and the presence or not of horizontal baffles or barriers.

It is expected that the time from injector to crest is two to five years with a most likely value of three and a half years. The only parameter listed which might conceivably slow the progress of the CO_2 plume is the presence of horizontal baffles of barriers. No direct evidence for such features is seen on seismic over Endurance or present in any of the well logs in the structure although these were seen in the Caister gas field in the Bunter Sandstone formation.

Current understanding suggests that 4D seismic monitoring will be able to track the CO_2 plume.

The relative permeability measurements undertaken on core taken from Endurance have produced what may appear to many as being anomalous results in that the maximum gas relative permeability (at irreducible water saturation) $K_{rg}(S_{wi}) > 1$. However, this result is far from anomalous and could have been predicted.

The injection of the Phase 1 maximum mass of 53.6 Mt is expected to pool at the crest of the structure and no scenario can be envisaged where the CO_2 can get beyond the spill of the

Endurance structure. In fact there is no known mechanism by which the CO_2 can get out of the upper peak and into the eastern lower peak of Endurance.

Cooling of the reservoir by the cold CO_2 is thought to be highly localised to the near wellbore region although the work done here has not been able to consider conductive cooling of the cap rock as the CO_2 flows down through the well. The geomechanical modelling done in parallel to this study suggests the biggest risk to the failure of the seal is more likely due to cooling than pressurising-up from the Phase 1 loading.

The Bunter Sandstone formation in Endurance is considered to be fair to good to very good in terms of reservoir quality; hence there should be more than enough permeability in the Lower Bunter to allow well perforations to be set deep thereby maximising the opportunity for residual trapping although the relative permeability data indicate the amount of residual trapping might be quite low. It had been thought this strategy would also keep the cold injectant away from the cap rock where it could lead to thermal fracturing.

The dynamic modelling work reported here confirms that Endurance is an extremely strong candidate for a CO_2 store. The modest Phase 1 loading into such a large structure with what is thought to be a large and strong connected volume will allow the operator to gain invaluable experience of CO_2 storage operations that can be shared with operators of similar projects in the future.

.

9 References

1. Hassanzadeh, H., Pooladi-Darvish, M., Elsharkawy, A.M., Keith, D.W., and Leonenko, Y., "Predicting PVT data for CO_2-brine mixtures for black-oil simulation of CO_2 geological storage", International J. Greenhouse Gas Controls, 2, (2008), pp. 65-77.
2. Glennie, K. W. And Boergner, P. L. E.. Sole Pit Inversion Techtonics. In Illing, L.V., and Hobson, D.G., eds., Petroleum Geology of the Continental Shelf of North-west Europe: Special Publication, Institute of Petroleum, London, p. 110-120.1981.
3. Dubrule, O. Geostatistics in Petroleum Geology, Continuing Education Course Notes Series #38. American Association of Petroleum Geologists, 1998.
4. Hottman, C. E., and Johnson, R. K., "Estimation of Formation Pressures from Log-Derived Shale Properties", J Pet Technology, 17 (6), 717 – 722. SPE-1110-PA. doi:10.2118/1110-PA, 1965.
5. Pennebaker, E.S., "An Engineering Interpretation of Seismic Data", SPE 2165, presented at the Fall Meeting of the Society of Petroleum Engineers of AIME Houston, Texas, 1968.
6. Tang, H., Luo, J., Qiu, K., Chen, Y., and Tan, C. P., "Worldwide Pore Pressure Prediction: Case Studies and Methods", SPE 140954, presented at 2011 SPE Asia pacific Oil and Gas Conference and Exhibition, Jakarta, Indonesia.
7. Terzaghi, K., and Peck, R., Soil mechanics in engineering practice. New York, Wiley, 1948.
8. Wiese, B., Nimitz, M., Klatt, M. and Kühn, M., "Sensitivities of injection rates for single well CO_2 injection into saline aquifers", Chemie der Erde – Geochemistry, 70, Suppl. 3, pp. 165-172, (2010).
9. Heinemann, N., Wilkinson, M., Pickup, G.E., Haszeldine, R.S. and Cutler, N.A., "CO_2 storage in the offshore UK Bunter Sandstone Formation", International Journal of Greenhouse Gas Control, 6, pp. 210-219, (2012).
10. Noy, D.J., Holloway, S., Chadwick, R.A., Williams, J.D.O., Hannis, S.A. and Lahann, R.W., "Modelling large-scale carbon dioxide injection into the Bunter Sandstone in the UK southern North Sea", International Journal of Greenhouse Gas Control, 9, pp. 220-233, (2012).
11. Brook, M., Shaw, K., Vincent, C., and Holloway, S., "Gestco case study 2a-1: Storage Potential of the Bunter Sandstone in the UK sector of the southern North Sea and the adjacent area of Eastern England", British Geological Survey commissioned report CR/03/154N, Keyworth, Nottingham, 2003.
12. Jolley, S. J., Fisher, Q. J., Ainsworth, R. B., Vrolijk, P. J. and Delisle, S. (eds) Reservoir Compartmentalisation. Geological Society, London, Special Publications, 347, 1–8. DOI: 10.1144/SP347.1 0305-8719/10/$15.00 # The Geological Society of London 2010.
13. Bennion, D.B., and Bachu, S.: "Supercritical CO_2 and H_2S – Brine Drainage and Imbibition Relative Permeability Relationships for Intergranular Sandstones and Carbonate Formations", SPE Paper Number 99326, 2006.
14. Blackbourn, G 2014. Sedimentology, Petrography and Burial History of the Cored Triassic Section in National Grid Carbon Well 42/25d-3, UK North Sea. Blackbourn Consulting Report", prepared for National Grid Carbon.
15. Spiteri, E. J., Juanes, R., Blunt, M. J., & Orr, F. M. (2008, September). "A New Model of Trapping and Relative Permeability Hysteresis for All Wettability Characteristics. SPE Journal, 277-288.
16. Skjaeveland, S. M., Siqveland, L. M., Kjosavik, A., Hammervold-Thomas, W. L., & Vimovsky, G. A. (2000, February). "Capillary Pressure Correlation for Mixed-Wet Reservoirs". SPE Reservoir Evaluation & Engineering, 3(1), 60-67.

10 Glossary

Abbreviations	Meaning
%	Percentage
ϕHe	Helium Porosity
4D	Four Dimensional (3D and Time)
5/42	Former name of the White Rose Storage Endurance Site
°C	Degrees Celsius
AoI	Area of interest
Ar	Argon
Atm	Atmosphere
barg	(Gauge Pressure) Pressure reading relative to current atmospheric pressure
BCU	Base Cretaceous Unconformity
BHP	Bottom Hole Pressure
BOC	British Oxygen Company
Br	Bromide
BSF	Bunter Sandstone Formation
CCF	Completion Connection Factor
CCI	Counter-Current Imbibition
CCS	Carbon Capture and Storage
CH_4	Methane
Cl	Chloride
C_L	Land constant
CO_2	Carbon Dioxide
CPL	Capture Power Limited
CPU	Central Processing Unit
D	Darcy
DECC	UK Government's Department of Energy and Climate Change
DST	Drill Stem Test
DVHM	Diffuse Vertical Hardground region Model
E100	Blackoil ECLIPSE 100 simulator
EOR	Enhanced Oil Recovery
EPS	End Point Scaling
ETHM	Easterly Trending Hardground Model
EU	European Union
FEED	Front End Engineering Design
FVF	Formation Volume Factor
GR	Gamma Ray
GRV	Gross Rock Volume
GRFS	Gaussian Random Function Simulation
H_2S	Hydrogen sulphide
H_2	Hydrogen
H_2O	Water
ID	Internal Diameter
K_H	Horizontal permeability

Abbreviations	Meaning
K_L	Klinkenberg permeability
K_V	Vertical permeability
K_w	Absolute brine permeability
$K_{rg}M$	The maximum gas (CO_2) relative permeability
K_{rw}	Water relative permeability
K_r	Reservoir Condition Gas-Water
KSC	Key Sub-Contract
LPSA	Laser Particle Size Analysis
mD	milli Darcy (1 darcy $\approx 10^{-12} m^2$) measure of permeability
MD	Measured Depth
MDT	Modular Dynamic Tester (a Schlumberger wireline tool used for measuring formation pressure and collecting reservoir fluid samples)
MICP	Mercury Injection Capillary Pressure
MMscf	Million standard cubic feet
Mt	Million tonnes (conventional numerically identical definition is megatonne)
MTPA	Million Tonnes Per Annum
N_2	Nitrogen
NaCl	Sodium chloride (salt)
NO_x	Generic term for the mono-nitrogen oxides, and nitric oxide (NO) and nitrogen dioxide (NO_2)
NGC	National Grid Carbon Limited
NPV	Net Pore Volume
NTG	Net To Gross ratio
O_2	Oxygen
OBC	Ocean Bottom Cable
OPP	Oxy Power Plant
pH	A numeric scale used to specify the acidity or alkalinity of an aqueous solution
PHM	Patchy Hardground Model
PI	Productivity Index
ppmv	parts per million by volume
PRP	Phase Reversal Polygon
PV	Pore Volume
PVT	Pressure, Volume and Temperature and refers to the physical properties shown by hydrocarbon fluids
TPA	Transient Pressure Analysis
RAOI	Regional Area Of Influence
RCA	Routine conventional Core Analysis
RFT	Repeat Formation Tester (wireline tool used for measuring formation pressure and collecting reservoir fluid samples)
S_g	CO_2 saturation
S_{gc}	The critical gas saturation
S_{gi}	Initial gas saturation
S_{gt}	The trapped gas (on imbibition) saturation

Abbreviations	Meaning
S_{wi}	The irreducible water saturation
SCAL	Special Core AnaLysis
SEM	Scanning Electron Microscopy
SFW	Synthetic Formation Brine
SIS	Sequential Indicator Simulation
SNS	Southern North Sea
SPR	Seismic Phase Reversal
TDS	Total Dissolved Solids
TGS	Truncated Gaussian Simulation
TVDSS	True Vertical Depth Sub-Sea
UK	United Kingdom
VHM	Vertical Hardground region Model
VIT	Vertical Interference Test
VLP	Vertical Lift Performance
WIIP	Water Initially In Place

11 Nomenclature and Jargon

Term	Explanation
Acidification	A preparation technique to determine metal in water samples
Aeolian Processes	Also spelled eolian or æolian, pertain to wind activity in the study of geology and weather and specifically to the wind's ability to shape the surface of the Earth (or other planets)
Analogue	Real example
Anhydrite	A mineral—anhydrous calcium sulphate, $CaSO_4$
Anion	An ion with more electrons than protons, giving it a net negative charge
Anisotropic Variogram	A geometrical term to define when the spatial correlation pattern changes with the direction of orientation of pairs of sites within a variogram
Anthropogenic	Originating in human activity
Anticline	A fold that is convex up and has its oldest beds at its core
Areal Permeability	Area of permeability
Authigenic	An authigenic mineral or sedimentary rock deposit is one that was generated where it is found or observed. Authigenic sedimentary minerals form during sedimentation by precipitation or recrystallisation instead of being transported from elsewhere (allogenic) by water or wind
Base Quaternary horizon	Refers to the geological time scale
Black oil model	A reservoir simulation computer models used to predict the flow of fluids (typically, oil, water, and gas) through porous media
Brine	A solution of salt (usually sodium chloride) in water
Büchner flask	Also known as a vacuum flask, filter flask or side-arm flask
Bunter sandstone	Sandstone deposits containing colourful rounded pebbles, widespread across central Europe
Calcareous	Mostly or partly composed of calcium carbonate, in other words, containing lime or being chalky
Cap rock	A combination of clay rock and rock salt (Halite) which overlies the Bunter sandstone formation
Carbon capture	Collection of carbon dioxide (CO_2) from power station combustion process or other facilities and its process ready for transportation
Carter-Tracy model	A realistic unsteady-state model that attempts to simulate the complex pressure changes that gradually occur within an aquifer and between an aquifer and reservoir
Cation	An ion with fewer electrons than protons, giving it a positive charge
Cementation	Where new minerals crystals grow around sediment grains and bond them together. One of the processes by which sediments are changed into rock.
Chemostratigraphy	Also known as Chemical stratigraphy; is the technique of sediment characterisation and correlation using subtle variations in the elemental composition of the sediments
Clast	A fragment of geological detritus, chunks and smaller grains of rock broken off other rocks by physical weathering. Geologists use the term clastic with reference to sedimentary rocks as well as to particles in sediment transport whether in suspension or as bed load, and in sediment deposits
Compositional analysis	quantitative descriptions of the parts of some whole, conveying exclusively relative information, can be expressed as molar concentrations of each component
Connate	In geology and sedimentology, connate fluids are liquids that were trapped in the pores of sedimentary rocks as they were deposited.
Core sample	A cylindrical section of sediment obtained by drilling with a hollow steel tube, the sample is pushed more or less intact into the tube and removed from the tube in

Term	Explanation
	the laboratory
Darcy	The measure of permeability named after Henry Darcy, with symbol D, where 1 Darcy is approximately $10^{-12}m^2$
Diagenetic	The change of sediments or existing sedimentary rocks into a different sedimentary rock during and after rock formation (lithification), at temperatures and pressures less than that required for the formation of metamorphic rocks
Diapir	A geologic intrusion in which a more mobile and ductily deformable material is forced into brittle overlying rocks
Distal	Relating to or denoting the outer part of an area affected by geological activity
Drill Stem Test	A procedure for isolating and testing the pressure, permeability and productive capacity of a geological formation during the drilling of a well
ECLIPSE	Reservoir simulation computer model
Electrofacies	Represents a unique set of log responses which characterizes the physical properties of the rocks and fluids contained in the volume investigated by the logging tools
Endurance aquifer	The offshore saline aquifer (reservoir) identified for permanent storage of CO_2
Facies	Sedimentary facies are bodies of sediment recognisably different from adjacent sediment deposited in a different depositional environment. Generally, facies are distinguished by what aspect of the rock or sediment is being studied
Feldspars	A family of silicate minerals which occur in igneous rocks
Freephase CO_2	CO_2 that remains in the gas (or supercritical fluid) phase
Full chain	The complete process from the capture of the CO_2 at the emitter plant to its injection into the storage reservoir
Gravimetry	Analytical methods in which the analytical signal is a measurement of mass or a change in mass
Halite	Rock salt, mineral form of salt
Heterolithic bedding	A sedimentary structure made up of interbedded deposits of sand and mud. It is formed mainly in tidal flats but can also be formed in glacial environments.
Illite	A clay mineral, a hydrous silicate of potassium, aluminium, iron, and magnesium; swells considerably on wetting and shrinks proportionately on drying
Imbibition	Absorption of liquid by a solid or a semisolid material
Immiscible	Not forming a homogeneous mixture when mixed
Inductively coupled plasma atomic emission spectroscopy	An analytical technique used for the detection of trace metals. It is a type of emission spectroscopy.
Ion chromatography	A process that allows the separation of ions and polar molecules based on their affinity to the ion exchanger.
Ion selective electrode	A transducer (or sensor) that converts the activity of a specific ion dissolved in a solution into an electrical potential, which can be measured by a voltmeter or pH meter
IP365	International standard which specifies a method for the determination of density
Isochore map	Displays lines of equal thickness in a layer where the thicknesses are measured vertically. Isochore maps in geology are also referred to as True Vertical Thickness (TVT) maps
Isotopes	The atoms of an element with different numbers of neutrons. They have the same proton number, but different mass numbers
J-Function	A dimensionless function of water saturation describing the capillary pressure used for correlating capillary pressure data for rocks with similar pore types and wettability, but with different permeabilities
Ketzin CO_2SINK project	Europe's first onshore CO_2 project

Term	Explanation
Lithology	The general physical characteristics of a rock or rock formation
Microbial	A microorganism, especially a bacterium that causes disease; a minute life form
Microbiological analysis	The detection and identification of microbes in the environment, to indicate metabolic activity, and assist with the determination of structural composition and integrity
Nitrogen quads	Manifold pack holding nitrogen cylinders connected to one outlet
Offset well	An existing wellbore that may be used as a guide for planning a well. Many offsets could be referred to in the planning of a well, to identify subsurface geology and pressures.
Ooids	Small (≤2mm in diameter), spheroidal, "coated" (layered) sedimentary grains, usually composed of calcium carbonate, but sometimes made up of iron- or phosphate-based minerals
Permeability	Measure of the ability of a material (such as rocks) to transmit fluids
Permian	A geologic period and system which extends from 298.9 ± 0.15 to 252.17 ± 0.06 million years ago
Petrography	A branch of petrology that focuses on detailed descriptions of rocks. The mineral content and the textural relationships within the rock are described in detail
Petrophysical	Pertaining to physical and chemical rock properties and their interactions with fluids
Phase Partition	Where a substance is distributed between two phases in a dynamic equilibrium
Physicochemical analysis	A method of investigating systems that makes possible a determination of the nature of the interactions between its components through a study of the relations between the system's physical properties and composition
Physicochemical parameters	Parameters that are dependent on the joint action of both physical and chemical processes
Playa Lake	Dry lake
Porosity	Measure of the void spaces in a material as a fraction or percentage
Potentiometric titration	A volumetric method in which the potential between two electrodes is measured (referent and indicator electrode) as a function of the added reagent volume
Radiological analysis	Measurements of radioactivity using radioanalytical methods and mass spectrometric methods
Radionuclide	Radioactive nuclide
Reservoir	Containment in suitable pervious rock formations located under impervious rock formations usually under the sea bed
Resistivity	A measure of the resisting power of a specified material to the flow of an electric current
Sedimentology	Encompasses the study of modern sediments such as sand, silt, and clay, and the processes that result in their formation (erosion and weathering), transport, deposition and diagenesis
Sheetflood	Generally produced by cloudbursts, sheetfloods are of brief duration, and they commonly move only short distances. They involve the detachment of soil particles by water flowing overland as a sheet where a uniform layer of fine particles is removed from the entire surface of an area, sometimes resulting in an extensive loss of rich topsoil. Sheet erosion commonly occurs on recently ploughed fields or on sites with poorly consolidated soil material with scant vegetative cover
Skin (Wellbore) Factor	A numerical value used to analytically model the difference from the pressure drop predicted by Darcys Law due to skin a zone of reduced permeability adjacent to the wellbore
Skjaeveland Model	Relationship between capillary pressure, saturation, and interfacial area

Term	Explanation
Spill Point	Point where the reservoir is open to the seabed
Spiteri Model	Calculation of hysteresis in the relative permeability of the hydrocarbon phase in a two-phase system
Stochastically	Statistics Involving or containing a random variable or process
Stratigraphic Column	A representation used in geology and its subfield of stratigraphy to describe the vertical location of rock units in a particular area. A typical stratigraphic column shows a sequence of sedimentary rocks, with the oldest rocks on the bottom and the youngest on top
Supercritical CO_2	CO_2 above its critical temperature (304.25 K) and pressure (72.9 atm or 7.39 MPa) - A supercritical fluid expands to fill its container like a gas but with a density like that of a liquid
Tedlar bag	A sample bag made of a special film with good stability for volatile organic compounds, sulphur compounds, carbon monoxide, carbon dioxide, methane, and sulphur hexafluoride
Thermodynamics	A branch of physics concerned with heat and temperature and their relation to energy and work
Triple point	The temperature and pressure of a substance at which the three phases (gas, liquid, and solid) of that substance coexist in thermodynamic equilibrium
Well bore	The hole that forms the well
White Rose Transport and Storage FEED Project	CPL and NGC have entered into a key sub-contract agreement where NGC will perform this project which will meet that part of CPL's obligations under the FEED Contract which are associated with the transport and storage assets
Zechstein	A unit of sedimentary rock layers of Middle to Late Permian (Guadalupian to Lopingian) age located in the European Permian Basin which stretches from the east coast of England to northern Poland
Zone	The thickness interval between stratigraphically defined horizons

12 Appendix A

Figure 12.1: Composite Top Triassic TWT Interpretation

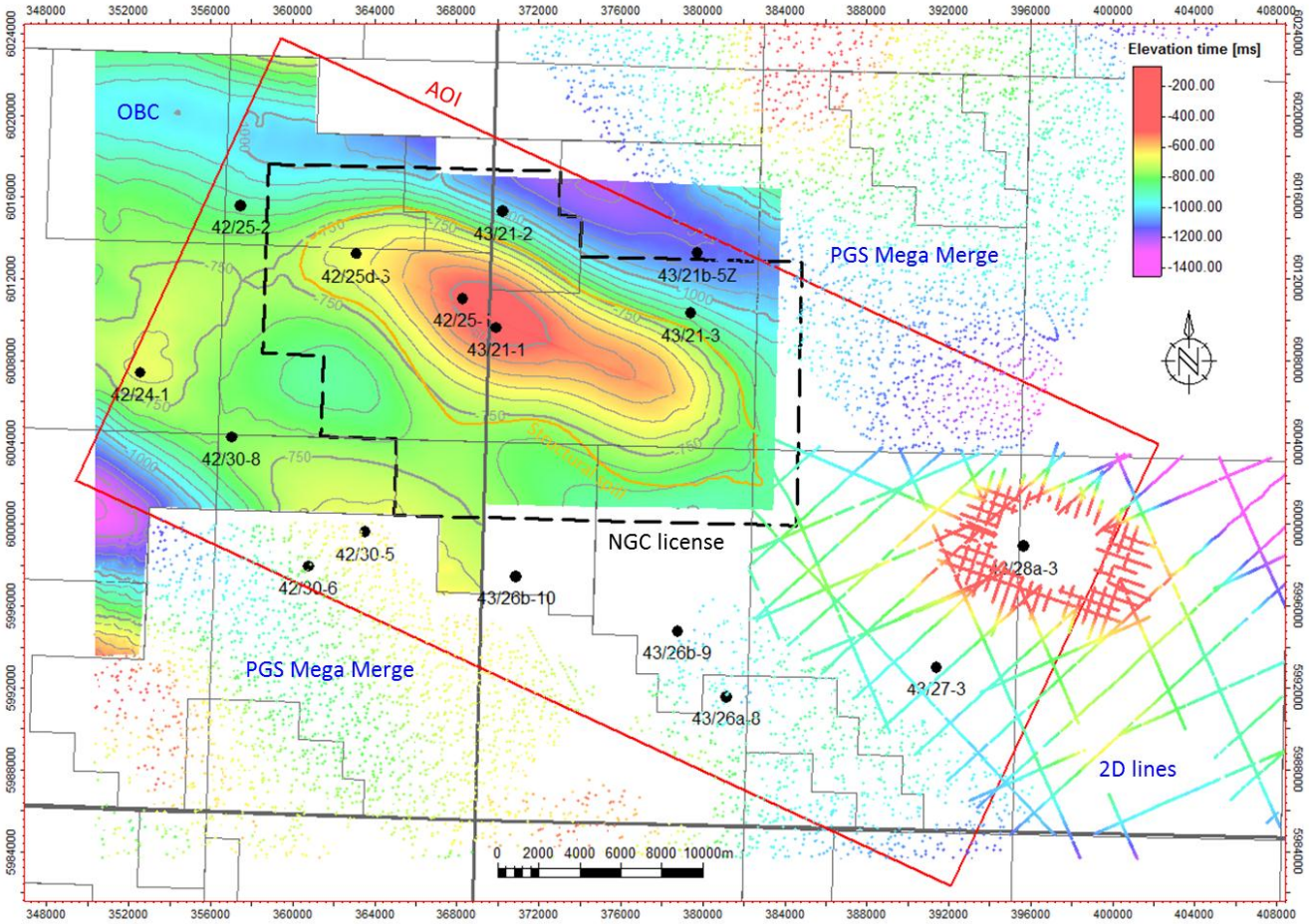

Figure 12.2: Composite Top Bunter Sand TWT Interpretation

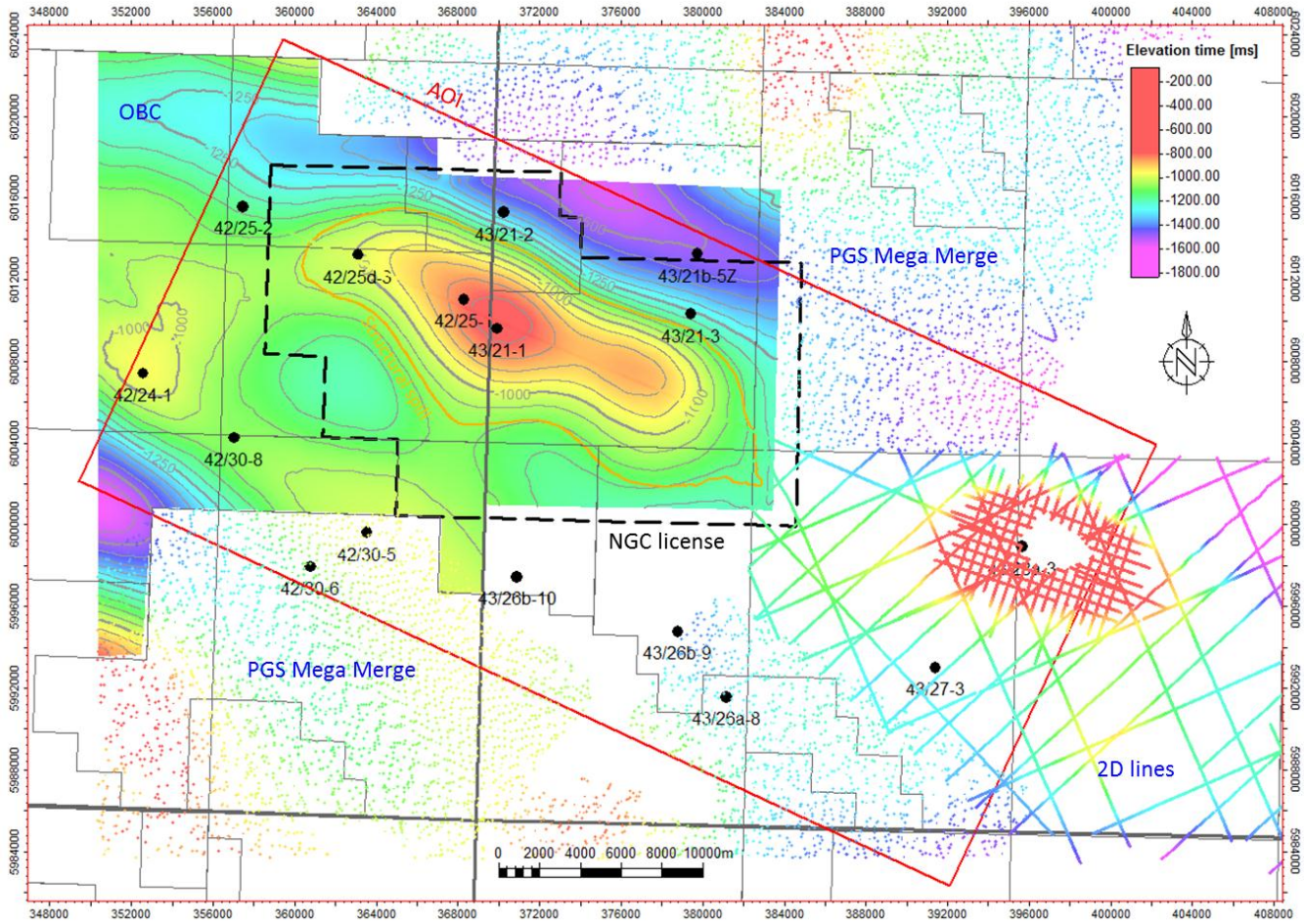

Figure 12.3: Composite Top Zechstein TWT Interpretation

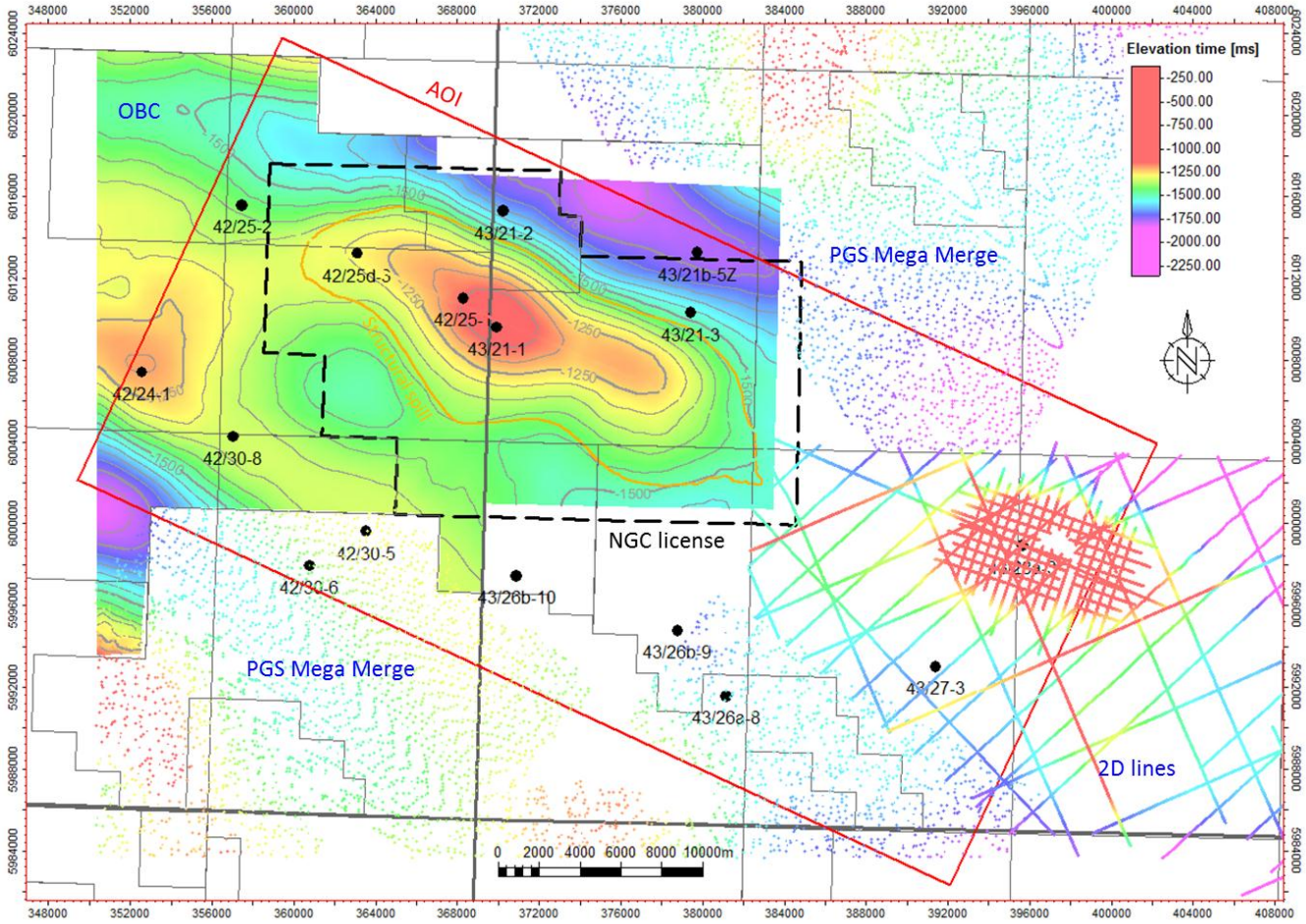

Figure 12.4: Composite Top Rotliegend TWT Interpretation